LBL-29357

In-Beam Studies of High-Spin States of Actinide Nuclei

Mark A. Stoyer

Ph. D. Thesis

Department of Chemistry
University of California
Berkeley, CA 94720

and

Nuclear Science Division
Lawrence Berkeley Laboratory
Berkeley, CA 94720

November 15, 1990

This work was supported in part by the Director, Office of Energy Research, Division of Nuclear Physics of the Office of High Energy and Nuclear Physics of the U.S. Department of Energy under Contract DE-AC03-76SF00098.

In-Beam Studies of High-Spin States of Actinide Nuclei

by
Mark A. Stoyer

Abstract

High-spin states in the actinides have been studied using Coulomb-excitation, inelastic excitation reactions, and one-neutron transfer reactions. Experimental data are presented for states in ^{232}U, ^{233}U, ^{234}U, ^{235}U, ^{238}Pu and ^{239}Pu from a variety of reactions. Energy levels, moments-of-inertia, aligned angular momentum, Routhians, gamma-ray intensities, and cross-sections are presented for most cases. Additional spectroscopic information (magnetic moments, $\frac{M1}{E2}$ mixing ratios, and g-factors) is presented for ^{233}U. One- and two-neutron transfer reaction mechanisms and the possibility of band crossings (backbending) are discussed. A discussion of odd-A band fitting and Cranking calculations is presented to aid in the interpretation of rotational energy levels and alignment. In addition, several theoretical calculations of rotational populations for inelastic excitation and neutron transfer are compared to the data. Intra-theory comparisons between the Sudden Approximation, Semi- Classical, and Alder-Winther-DeBoer methods are made. In connection with the theory development, the possible signature for the nuclear SQUID effect is discussed.

Dedication

This thesis would have been impossible without the support of the following people:

(1) To all those many people I've had the fortune of interacting with during my learning experiences while performing this and related work–too many to acknowledge individually, but certainly not forgotten.

(2) To Dr. Richard A. Meyer who welcomed me to my first job in Nuclear Chemistry, pointed me in the right direction at Berkeley, and whom I consider a good friend.

(3) To my brother, Dale, who first provoked in me the curiousity of a scientist; to my new sister-in-law, Janice, whose only connection with this thesis was a concern that I not recite it at her wedding; and to my parents, Lyn and Dorothy, who, though it is probably still somewhat of a mystery to them, nevertheless gave me the support and encouragement to "do whatever it is I do".

(4) And lastly, to Dr. John Rasmussen, whom it has been an honor to work for during my graduate studies. His patience, kindness, creativity, and guidance have been generous during my stay at LBL, and I am eternally in his debt.

Acknowledgements

The author would like to acknowledge the Dr. John Rasmussen and Dr. Ken Crowe group (Dr. Roy Bossingham, Dr. Helmut Bossy, Dr. Felipe Canto†, Dr. Dean Chacon, Dr. Raul Donangelo†, Dr. Aminah Farhan†, Richard Hodge, Marvin Justice, Dr. Peter Ring†, Dr. Quiyun Shao†, Dr. Adnan Shihab-Eldin†, Krysta Wyatt, Dr. Yongwen Xu†, Dr. Yanglin Ye†), the Dr. Doug Cline group at the University of Rochester (Karl Helmer, Dr. Alex Kavka, Dr. Warnick Kernan, Ehrenfried Vogt, Dr. Ching Yen Wu), and the Dr. Mike Guidry group at ORNL/University of Tennessee (Wayne Kincaid, Dr. Xin Tao Liu) for help with the experimental aspects of this thesis. The author would also like to acknowledge Dr. Richard A. Meyer, Dr. Dan Decman, Dr. Eugene Henry, and Dr. Wolfgang Stöffl of LLNL for help with the spectral fitting software, and the Dr. Darleane Hoffman group at LBL (Dr. Diane Bennett, Carolyn Gannett, Dr. Ken Gregorich, Dr. Howard Hall, Dr. Roger Henderson, Dr. John Leyba) as well as Ken Biscay and Glenn Garabedian of EH&S for help with the target making.

This work was supported in part by the Director, Office of High Energy Research, Division of Nuclear Physics of the Office of High Energy and Nuclear Physics of the U.S. Department of Energy under Contract DE-AC03-76SF00098.

† Visiting scholar

Contents

A. Experimental 1

1 Introduction **1**

2 Experimental Methods **5**

2.1 General Description 5

2.1.1 ^{58}Ni + ^{235}U Reaction at ORNL 13

2.1.2 ^{206}Pb + ^{233}U Reaction at LBL 17

2.1.3 ^{58}Ni + ^{233}U Reaction at UOR 20

2.1.4 ^{90}Zr + ^{239}Pu Reaction at ORNL 20

2.2 Data Analysis Techniques 24

3 Results and Discussion **33**

3.1 ^{58}Ni + ^{235}U Reaction 33

3.2 ^{206}Pb + ^{233}U and ^{58}Ni + ^{233}U Reactions 39

3.3 ^{90}Zr + ^{239}Pu Reaction 72

3.3.1 ^{239}Pu 77

3.3.2 ^{238}Pu 89

B. Theoretical 116

4 Introduction **116**

5 Discussion of Relevant Theories **120**

5.1 Sudden Approximation 122

5.2 Alder-Winther-deBoer modified method 128

5.2.1 General Description 128

5.2.2 Coulomb Excitation 131
5.2.3 Inelastic excitation 132
5.2.4 Neutron Transfer 135

6 Comparison of Theory with Experimental Data 144
6.1 Brief SQUID Results 145
6.2 ^{233}U Results 152
6.3 ^{90}Zr + ^{239}Pu Results 158
6.3.1 ^{239}Pu Inelastic Excitation 158
6.3.2 ^{238}Pu One-Neutron Transfer Results 166

7 Conclusions 179

A Target Construction 183
A.1 General Apparatus 183
A.2 ^{233}U Target Preparation 186
A.3 ^{239}Pu Target Preparation 187

B FITEK Program 189

List of Figures

2.1 Schematic diagram of generic experimental configuration. . . 6

2.2 Calibration of particle scattering angles in a PPAC. 10

2.3 Diagram of ^{58}Ni + ^{235}U experimental setup. 14

2.4 Diagram of ^{206}Pb + ^{233}U experimental setup. 18

2.5 Diagram of ^{90}Zr + ^{239}Pu experimental setup. 22

2.6 Mass spectrum from one PPAC for the ^{206}Pb + ^{233}U reaction. 27

2.7 ^{152}Eu calibration spectrum for a Ge detector. 28

2.8 The top figure is an uncorrected Ge E_γ spectrum. The middle figure is the same Ge E_γ spectrum with Doppler corrections, and the bottom figure is the Ge timing spectrum. 30

2.9 NaI(Tl) timing spectrum showing the neutron-γ-ray separation for the ^{90}Zr + ^{239}Pu reaction for events depositing $2-16$ MeV in the detector. 31

3.1 Ge γ-ray spectrum for the ^{58}Ni + ^{235}U reaction 35

3.2 Total E, M plot for the ^{58}Ni + ^{235}U reaction where the dashed line indicates the approximate Yrast line for ^{234}U assuming no excitation of the ^{58}Ni. 37

3.3 Total γ-ray spectrum for the ^{206}Pb + ^{233}U reaction 40

3.4 Level diagram for both signatures of the ground-state band in ^{233}U 41

3.5 Moments-of-inertia for ground-state band in ^{233}U 44

3.6 Plot of $\frac{E_I - E_{I-1}}{2I}$, the inverse moment-of-inertia $(\frac{\hbar^2}{2\Im^{(1)}})$ for $\Delta I = 1$ transitions, vs. $2I^2$ showing the magnitude of the staggering term. 45

3.7 A comparison between experimental energy levels and theoretical energy levels for the ground rotational band in ^{233}U. The theoretical energy levels are calculated using the cranking model described in the text and the standard Kumar and Baranger parameters. 49
3.8 A comparison of extracted aligned angular momentum for the ground rotational band in ^{233}U between experiment and cranking model calculations 52
3.9 Experimental Routhians for the ground-state band in ^{233}U. . . 62
3.10 Routhians from cranking calculation for the ground-state band in ^{233}U. 64
3.11 Routhians from cranking calculation for the ground-state band in ^{233}U including a slight γ-deformation. 66
3.12 Total Ge γ-ray spectrum for the ^{90}Zr + ^{239}Pu reaction. 73
3.13 Neutron multiplicity for the ^{90}Zr + ^{239}Pu reaction. 74
3.14 Total two dimensional Ge γ-γ coincidence spectrum for the ^{90}Zr + ^{239}Pu reaction showing relationships between γ-rays in this experiment. Both inelastic ^{239}Pu γ-rays and one-neutron transfer ^{238}Pu γ-rays are present. 76
3.15 Total (H, K) spectrum for the ^{90}Zr + ^{239}Pu reaction. 78
3.16 Projection of a) H and b) K for the ^{90}Zr + ^{239}Pu reaction. . 79
3.17 Ge γ-γ spectrum for the ^{90}Zr + ^{239}Pu reaction gated on the 201.1-keV $\frac{17}{2}^+ \rightarrow \frac{13}{2}^+$, 212.1-keV $\frac{19}{2}^+ \rightarrow \frac{15}{2}^+$, 288.3-keV $\frac{25}{2}^+ \rightarrow \frac{21}{2}^+$ and 299.7-keV $\frac{27}{2}^+ \rightarrow \frac{23}{2}^+$ transitions. 80
3.18 Moments-of-inertia for the ground-state band in ^{239}Pu. 82
3.19 Inverse moment-of-inertia, $\Im^{(1)}$, for the ground-state band in ^{239}Pu showing the magnitude of the staggering between the favored and unfavored signatures. 84
3.20 Aligned angular momentum (i_α) for the ground-state band in ^{239}Pu. 85
3.21 Experimental Routhians for the ground-state band in ^{239}Pu. . 87
3.22 Theoretical Routhians for ^{239}Pu as a function of ω. 88
3.23 Inelastic (H, K) spectrum for the ^{90}Zr + ^{239}Pu reaction. . . . 90
3.24 Projections of a) H and b) K for the ^{90}Zr + ^{239}Pu reaction. . 91

3.25 The γ-ray spectrum gated on three known ^{238}Pu transitions, the 307-keV $12^+ \rightarrow 10^+$, 349-keV $14^+ \rightarrow 12^+$ and 389-keV $16^+ \rightarrow 14^+$ transitions for the one-neutron transfer reaction. . 92

3.26 Kinematic (open circles) and dynamic (•) moments-of-inertia for the ground-state band in ^{238}Pu. 94

3.27 Experimental Routhians for ^{238}Pu. 96

3.28 Transfer (H, K) spectrum for ^{238}Pu. 98

3.29 Projections of a) H and b) K for the transfer reaction. 99

3.30 Differential cross-sections for one-neutron transfer as a function of distance of closest approach in the lab. 102

3.31 Differential cross-sections for one-neutron transfer as a function of distance of closest approach in the center-of-mass frame. . 103

3.32 Reduced differential cross-sections for one-neutron transfer as a function of distance of closest approach in the lab. 104

3.33 One-neutron transfer probability as a function of distance of closest approach. The solid line represents a simple theory based on equation (3.34). 106

3.34 Ge γ-ray spectrum gated on the "mystery" transition at 145 keV in the ^{90}Zr + ^{239}Pu experiment. 108

3.35 Ge γ-ray spectrum gated on the "mystery" transition at 185 keV in the ^{90}Zr + ^{239}Pu experiment. 109

3.36 Ge γ-ray spectrum gated on the "mystery" transition at 226 keV in the ^{90}Zr + ^{239}Pu experiment. 110

3.37 Ge γ-ray spectrum gated on the "mystery" transition at 268 keV in the ^{90}Zr + ^{239}Pu experiment. 111

5.1 Definition of geometry of systems under investigation. 121

6.1 Theoretical calculation of the rotational population probability for states in the ground band in the neutron pair transfer reaction ^{208}Pb + ^{160}Dy reaction. 148

6.2 Theoretical calculation of the rotational population probability for states in the ground band in the neutron pair transfer reaction ^{208}Pb + ^{158}Dy reaction. 149

6.3 A comparison of the experimental rotational population yields extracted from the reaction ^{156}Gd + ^{206}Pb with the calculations of theory from Section 5.2.4 for the reactions ^{208}Pb + ^{160}Dy and ^{208}Pb + ^{158}Dy. 150
6.4 Rotational population pattern for the ^{58}Ni + ^{233}U Coulomb excitation experiment. 153
6.5 Rotational population pattern for the ^{206}Pb + ^{233}U inelastic excitation experiment. 156
6.6 Inelastic excitation rotational population pattern in the ground band of ^{239}Pu. 159
6.7 Inelastic rotational population pattern for the ground band in ^{239}Pu extracted from the γ-γ coincidence spectrum gated on Yrast transitions. 161
6.8 Theoretical calculation of rotational population probability for the inelastic excitation experiment ^{90}Zr + ^{239}Pu. 167
6.9 Rotational population pattern for the states populated in ^{238}Pu in the one-neutron transfer reaction. 168
6.10 Several theoretical calculations of the rotational population patterns in ^{238}Pu from one-neutron transfer using deformation $\eta = 6$.170
6.11 Same as Figure 6.10 but for deformation $\eta = 4$. Pure Coulomb excitation is not shown in this figure. 171
6.12 Best theoretical calculation of the rotational population patterns in ^{238}Pu from one-neutron transfer. 172
6.13 Parts of the surface form factor $F_{I'I}$ for ^{239}Pu. 176
6.14 Comparison of the best theoretical calculation of the rotational population patterns in ^{238}Pu from one-neutron transfer with experimental data. 177

A.1 Schematic of electrodeposition apparatus. 184

List of Tables

2.1 Isotopic composition of target for ^{58}Ni + ^{235}U experiment . . 15
2.2 Lab detector positions for ^{58}Ni + ^{235}U experiment 15
2.3 Lab detector positions for ^{58}Ni + ^{235}U experiment 16
2.4 Isotopic composition of target for ^{206}Pb + ^{233}U experiment . 17
2.5 Lab detector positions for ^{206}Pb + ^{233}U experiment 19
2.6 Isotopic composition of target for ^{90}Zr + ^{239}Pu experiment . . 21
2.7 Lab detector positions for ^{90}Zr + ^{239}Pu experiment 23
2.8 Lab detector positions for ^{90}Zr + ^{239}Pu experiment 23

3.1 Observed transitions in ^{233}U 39
3.2 Orbitals used as basis for Cranking model calculations 47
3.3 Main parts of the ground-state band wavefunction for ^{233}U in Cranking model 50
3.4 ^{233}U rotational band fit parameters (keV) 57
3.5 Apparent g-factors deduced from cascade-to-crossover transition ratios for ^{233}U 71
3.6 Observed transitions in ^{239}Pu 81
3.7 Observed transitions in ^{238}Pu 93
3.8 Peak assignments for the Ge γ-ray spectrum gated on the 268-keV "mystery" transition observed in the ^{90}Zr + ^{239}Pu experiment 114

6.1 Relative spot intensities for the probability of populating a given spin in ^{239}Pu including a gate to exclude side-feeding. 162
6.1 Continuation of relative spot intensities for ^{239}Pu 163
6.1 Continuation of relative spot intensities for ^{239}Pu 164
6.1 Continuation of relative spot intensities for ^{239}Pu 165

6.2 Relative spot intensities for the probability of populating a given spin in ^{238}Pu including a gate to exclude side-feeding. 169

B.1 Comparison of FITEK results and raw integration methods . . 196

Experimental

Chapter 1

Introduction

Nuclear physicists and chemists have long been concerned with the fundamental building blocks of our world. Because we have no tools to directly "see" these fundamental building blocks of nature, one has to resort to indirect observation. Nuclear reactions are performed with a variety of probes to try to elucidate, from the resulting debris, something about the initial characteristics of the system. It is interesting to perturb a nucleus, study it under extreme conditions, and perhaps learn something about the underlying structure of the system. Two of the extreme conditions that are among the most studied today are high temperature and high pressure. Researchers collide nuclei at the highest possible energies, and use huge detector systems to study the resulting plethora of particles produced, and try to determine, for instance, the possible existence of the quark-gluon plasma. This thesis, however, is concerned with

a third possible extremum, high angular momentum.

It is well known that spheroidally deformed nuclei exhibit rotational quantum states characterized by spin angular momentum states. For an even-even nucleus, the energy levels are given by the well-known equation $E_{rot} = \hbar^2 I(I+1)/2\Im$, where I is the spin of the nucleus, and $\Im$ is the moment-of-inertia. Rotational states have been studied in the deformed rare earth region for the better part of 40 years by a variety of reactions [1],[2],[3],[4],[5],[6],[7]. Transfer reactions in the rare-earth region have yielded much information, not only on rotational states, but also on transfer mechanisms. One-nucleon transfer has been demonstrated to be a selective probe of single-particle and single-hole states [8] and two-nucleon transfer probes nucleon-nucleon correlations and pairing effects [9]. The earliest transfer reactions studied used light ion probes ((d,p) reactions) [10],[11],[12].

With the development of better heavy-ion accelerators, heavy-ion induced transfer reactions enjoyed growing success. Early work concentrated on light nucleus-nucleus systems [13],[14]. The development of even heavier beams allowed study of transfer reactions from rotationally excited states [15]. The largest difference in the physics of heavy-ion transfer reactions is the Coulomb excitation, caused by the large Z of the projectile and target [16]. Since

the Coulomb force is long range, and nucleon transfer occurs with highest probability near the distance of closest approach, transfer is likely to occur between rotationally excited states [17]. Few-nucleon transfer experiments combine the selectivity of studying one- and two-particle correlations with the selectivity of Coulomb excitation to add a new dimension to the study of nuclear structure [18]. Many experiments have been performed in the rare-earth region (cf [19],[20],[21],[22],[23],[24],[25],[26]), some in the actinides (cf [20],[27],[28]) and some on spherical nuclei (cf [29],[30]).

Work by von Oertzen et al. [31] for Sn on Sn systems, and by Sapotta et al. [32] for Ni on ^{208}Pb systems shows the expected slope dependence on neutron transfer as a function of distance of approach for spherical systems. Indeed, the one-neutron transfer with deformed systems [33] also shows normal behavior. It is two-neutron transfer with deformed systems that shows enhanced transfer at large distances. Enhancement factors have been measured for several systems [26].

Coulomb excitation has also been used in the regions between closed-shell spherical nuclei and well-deformed nuclei, or transitional regions. For instance, collective effects in the Se region [34] and in the Pt region [35] were investigated using Coulomb excitation.

In the actinide region, however, most of the information on rotational states (high-spin states) has been from Coulomb excitation [36],[37],[38],[39],[40] and from (α,xn) reactions [41] and [42]. Transfer reactions have been extended into the actinide region [27]. This thesis will discuss high-spin states in the actinide region populated by heavy-ion inelastic excitation and neutron transfer reactions. Chapter 2 will discuss the experimental setups, Chapter 3 will discuss the results of the experiments and Chapter 6 shows the comparison between experimental rotational population patterns and theory. Chapters 4 and 5 are concerned with theories.

Chapter 2

Experimental Methods

2.1 General Description

This section will describe the experimental setup for inelastic excitation reactions and neutron transfer reactions. A sample experimental configuration is shown in Figure 2.1. The exact details for each experiment will be given in later sections. Most experiments described in this work were done at Oak Ridge National Laboratory's (ORNL) Holifield Heavy Ion Research Facility (HHIRF) in the Spin Spectrometer. Some of the work was done at the SuperHILAC facility at Lawrence Berkeley Laboratory (LBL) in the High Energy Resolution Array (HERA). All experiments had the following common features: (1) large number of Compton-suppressed intrinsic Ge detectors for detecting γ-rays with high resolution, and (2) position-sensitive parallel-plate avalanche

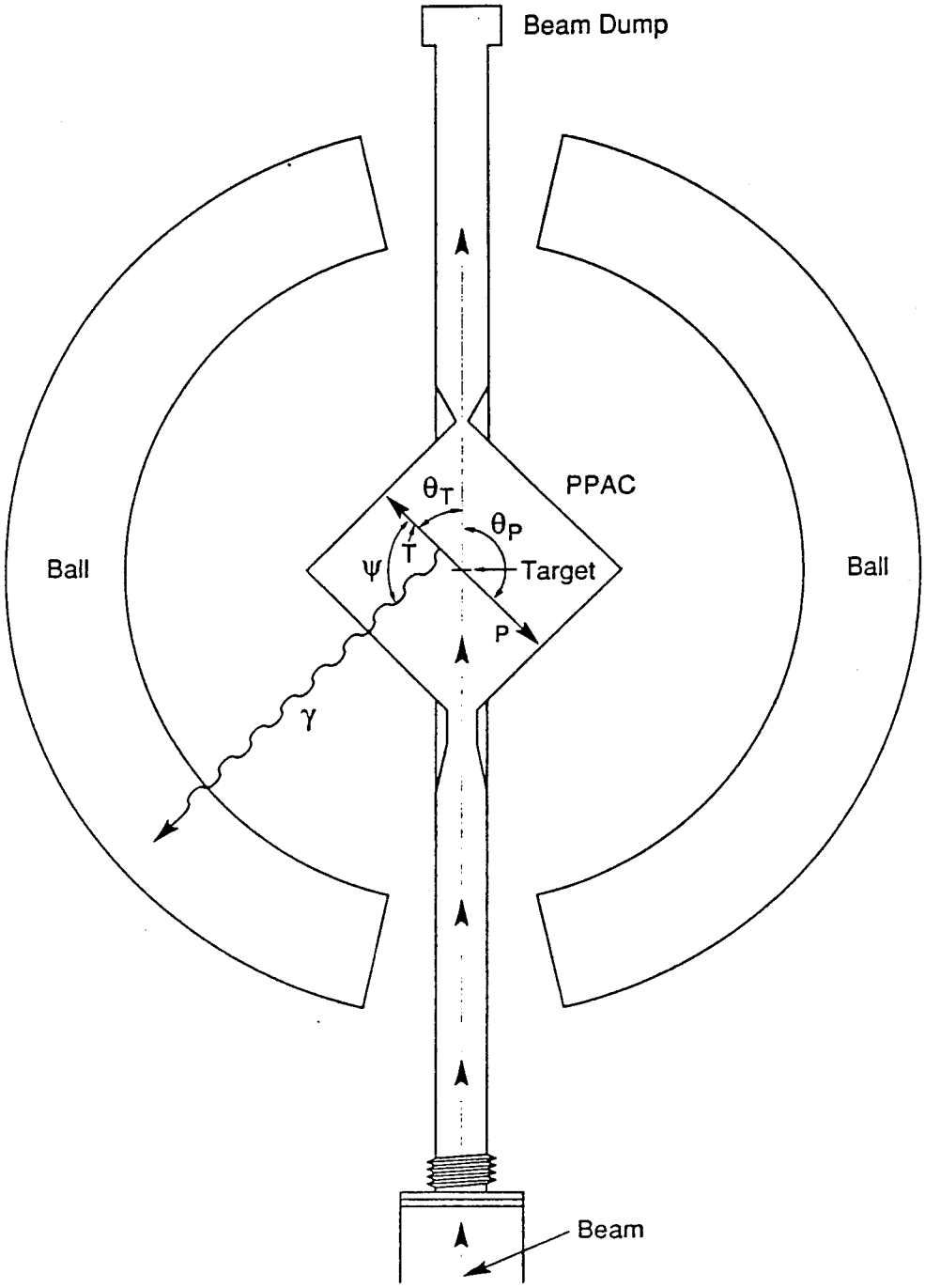

Figure 2.1: Schematic diagram of generic experimental configuration.

counters (PPACs) for detecting projectile-like and target-like charged-particle reaction products. In addition, the ORNL experiments had a large number of NaI(Tl) scintillator detectors arranged in a ball covering $\sim 4\pi$ solid angle.

The study of heavy-ion transfer and scattering reactions poses severe problems for charged-particle spectroscopy, because, even though thin targets are used in the experiments, the multiple scattering and energy loss in the target degrades the energy resolution of the charged-particle detectors. The rotational energy levels of deformed nuclei are typically on the order of 100's of keV apart, requiring higher resolution methods. Thus, a particle-particle-γ coincidence method is used, where the PPAC detectors give scattering angles and times-of-flight (TOF) of the target-like and projectile-like fragments in the lab (allowing a reconstruction of the kinematics of the reaction), and the Ge detectors give γ-ray energy information on the population of final product states. Because the γ-rays are emitted from a moving source (up to $\sim$ 10% the speed of light), the positional information from the PPACs allows for a Doppler correction of the γ-rays on an event-by-event basis to minimize the Doppler broadening and Doppler shift. In addition, the scattering angles also determine the distance of closest approach and impact parameters of the event. In the experiments at ORNL, the Spin Spectrometer NaI(Tl) array provided

total energy and multiplicity information for the event, and allowed for the separation of neutrons and γ-rays based on TOF. A more complete description of each of these elements of the experiments is given below.

A thin target, typically $\sim 400\ \mu g/cm^2$ target material deposited on $\sim 100\ \mu g/cm^2$ Ni backing facing upstream, is used to minimize the disturbance of the kinematics. The PPACs are located approximately 10 cm from the target, and form the walls of the University of Rochester scattering chamber. PPACs are chosen because of the high counting rates inherent in these experiments. The angular coverages of the PPACs are given in the detailed discussion of each experiment. The PPACs contain flowing isobutane at 4 Torr and are separated from the evacuated target chamber by $\sim 50\ \mu g/cm^2$ polypropylene film. Because of the polypropylene film, there is a low-energy threshold for charged particles to be detected in the PPAC of ~ 50 keV. The PPACs outside walls are $\sim \frac{1}{16}$" aluminum to minimize absorption of γ-rays. The cathodes are printed-circuit boards with 2° θ stripes. The θ stripes are interconnected with delay chips linking the stripes in a long chain, such that the difference in recorded times of a signal travelling to both ends of the cathode yields the θ position of the particle. The PPAC is calibrated in θ by placing an aluminum mask slotted at known angular positions in front of the polypropylene window

of the counter that stops all scattered particles except for those at the known angles. A sample PPAC calibration spectrum is shown in Figure 2.2. The anodes are stretched aluminized polypropylene foils sectioned to yield ϕ information (resolution $\approx 15°$) and spaced 3 mm from the cathodes. The anode is kept at +400 V and provides a prompt timing signal for a charged particle traversing the detector. Because the main decay mode of the radioactive targets used in this study is $5 - 8$ MeV α-particles, the voltage is chosen to suppress the significant background source of α-particles from the targets. A potential of +500 V makes the PPACs sensitive to α-particles. From the time difference between the particles and the reconstructed kinematics the mass of each particle can be determined. The mass resolution of a PPAC, $\sim 10 - 15$ amu, is insufficient for resolving particles differing by only one or two neutrons (as in the case of neutron transfer reactions), but sufficient for resolving an actinide-like particle from a lighter projectile-like particle. The outside wall of the PPAC stops all particles except neutrons.

The PPACs and scattering chamber are positioned inside a ball of Ge detectors (and at ORNL also NaI(Tl) detectors) for detecting γ-rays in coincidence with a projectile-like and target-like fragment. From fourteen to eighteen $\sim 25\%$ efficient intrinsic n-type Ge detectors plus either bismuth ger-

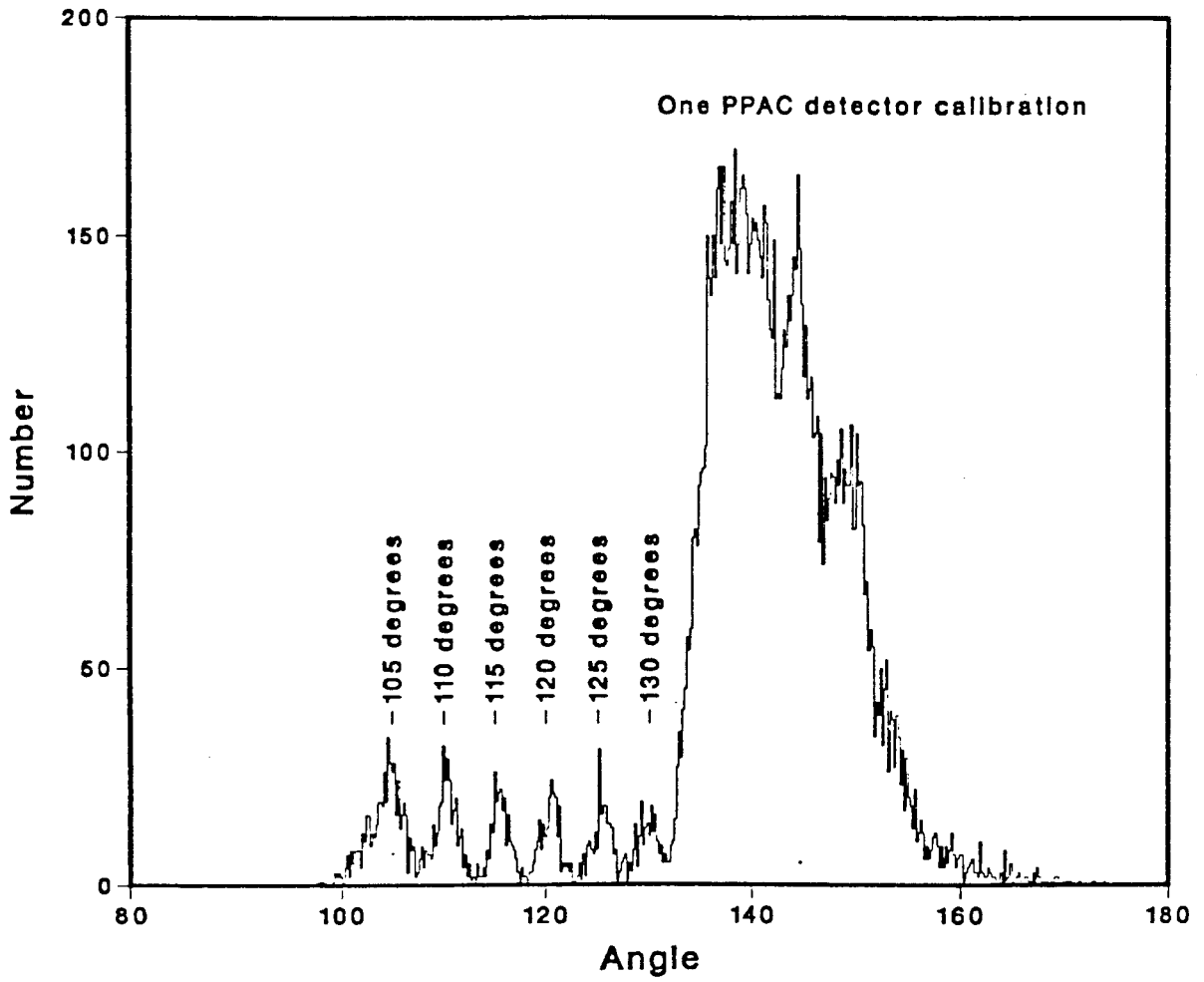

Figure 2.2: Calibration of particle scattering angles in a PPAC.

manate (BGO) or NaI(Tl) anti-coincidence Compton shields were typically used. Any event depositing some energy in the Compton shield was rejected. This substantially reduces the background. These detectors were placed ~ 20 cm from the target. Absolute energy and efficiency calibrations were made with standard radioactive γ- ray sources of ^{182}Ta, ^{152}Eu, ^{60}Co and a mixed source of ^{125}Sb, ^{125}Te, ^{155}Eu, and ^{154}Eu. The angular locations are given in the detailed descriptions of the experiments. The Ge detectors had a typical energy resolution of 1.7 keV at $E_\gamma = 1$ MeV and an efficiency of $\sim 1\%$ at 200 keV. Ta ($\sim$ 0.005"), Cu ($\sim$ 0.007") and Sn ($\sim$ 0.010") absorbers were placed in front of the Ge detectors to absorb the low-energy γ- and x-rays (mostly background x-ray radiation from the target). Thus, many low-energy rotational transitions like the $2^+ \rightarrow 0^+$ and $4^+ \rightarrow 2^+$ ^{238}Pu transitions were impossible to detect in our experimental setup because of the low-energy cut-off, and also because of the high conversion rates of these transitions. There was no attempt to detect conversion electrons, e^-.

For the experiments at ORNL, up to 55 NaI(Tl) detectors in the Spin Spectrometer ball were also used in addition to Ge γ-ray detectors. These detectors were placed ~ 18 cm from the target, and were used to detect γ-rays with high efficiency, and neutrons with lower efficiency. The slower neutrons

were detected by (n,γ) reactions in the NaI(Tl), and can be separated from prompt γ-rays by TOF. Because of the high segmentation of the array, the ball yields information about the total energy of the reaction ($H = \sum_{NaI} E_\gamma$), total γ-ray multiplicity (K = number of NaI(Tl) fired), and total neutron multiplicity (K_n) for an event. The H, K matrix can be transformed to (E, M) (total de-excitation energy, multiplicity $\rightarrow$ spin) through a procedure of "unfolding" with a ball response function. The ball response function was constructed with standard radioactive γ-ray sources of ^{60}Co, ^{207}Bi, ^{88}Y, ^{75}Se and ^{232}Th, and corrects for NaI(Tl) efficiency, double hits in the detectors, and γ-rays "lost" through spaces between the adjacent detectors. Jääskeläinen et. al. [43] characterized the response function for this particular detector setup. Figure 17 in reference [43] shows the multiplicity projections for the system for an experimental test with a given number of 1 MeV γ-rays. For $K = 30$, the distribution is a Gaussian centered about a detected multiplicity of 30 γ-rays; however, for $K = 40$, the distribution is centered about a detected fold of 35 γ-rays. As a rule of thumb then, for the Spin Spectrometer, as long as the total event multiplicity is less than or equal to half the number of NaI(Tl) detectors used in the experiment, the number of double hits in detectors approximately cancels the γ-rays that go undetected between detectors. However, if the average

multiplicity is larger than half the number of NaI(Tl) detectors, corrections for double hits in the detectors become severe ($\sim 20 - 25\%$). Figure 18 in reference [43] shows the detected total energy for a given number of 1 MeV γ-rays. For 20 γ-rays, the $E_{tot} \approx 20$ MeV, however, for 30 γ-rays the energy is only ~ 25 MeV. Thus, the total energy detected deviates from the actual total energy deposited in the ball by about 20% when half the detectors fire in the ball. The response function for the Spin Spectrometer is discussed in reference [43].

2.1.1 ^{58}Ni + ^{235}U Reaction at ORNL

This experiment was carried out using 325-MeV ^{58}Ni ions bombarding a 300 μg/cm^2 ^{235}U target with 110 μg/cm^2 Ni backing in the Spin Spectrometer at ORNL, which consisted of 55 NaI(Tl) and 14 Ge detectors. Figure 2.3 shows a schematic diagram of the experimental configuration. The target composition is given in Table 2.1. Surrounding the target were four PPACs, covering lab angles of 8° to 78° and 104° to 162° in the θ direction, and $-35°$ to 35° and 145° to 215° in the ϕ direction; the + z-axis is the beam direction, θ is the angle measured from the z-axis, and ϕ is the azimuthal angle measured

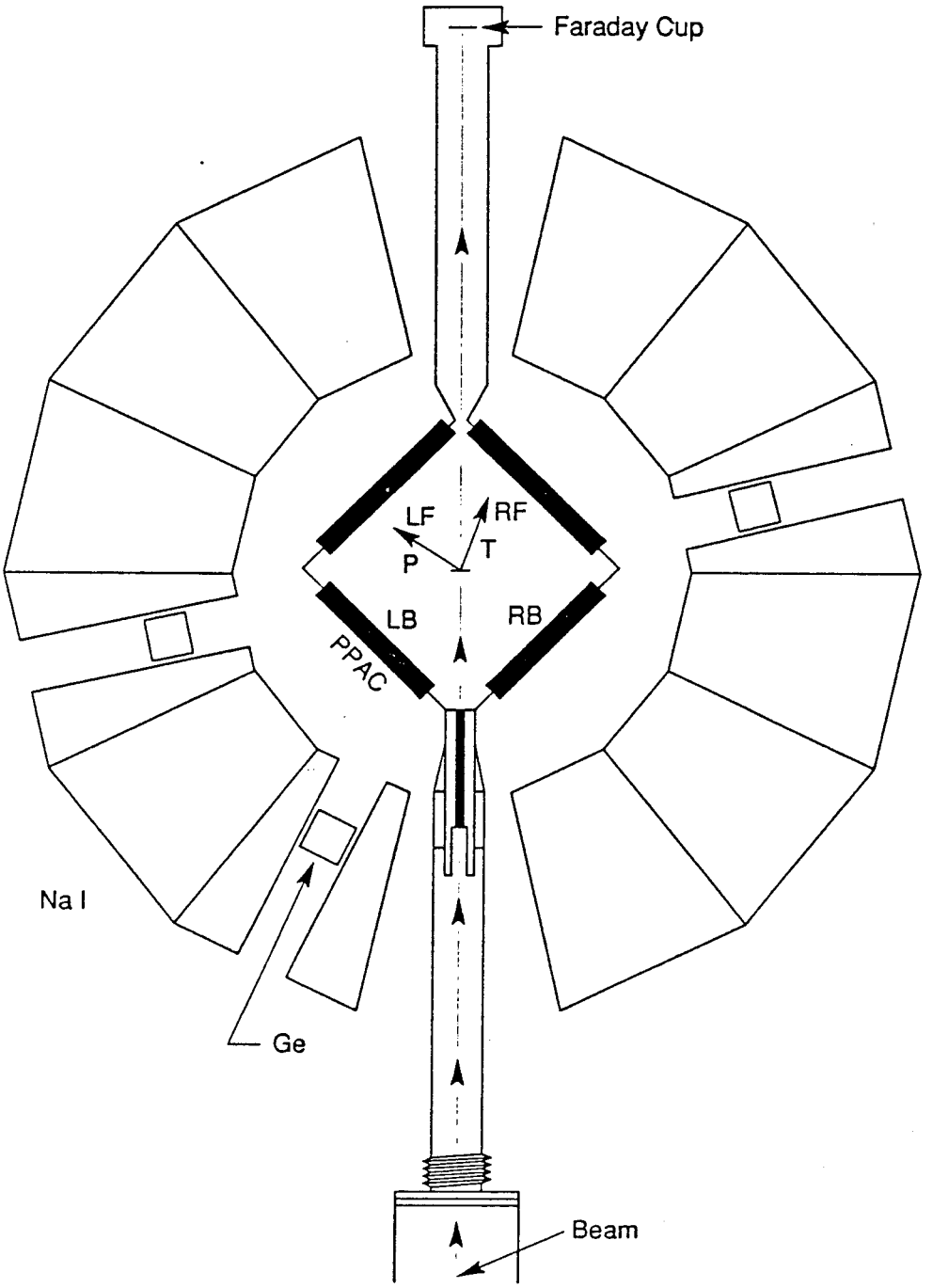

Figure 2.3: Diagram of ^{58}Ni + ^{235}U experimental setup.

Table 2.1: Isotopic composition of target for ^{58}Ni + ^{235}U experiment

Isotope	Percentage
^{235}U	99.85 %
^{234}U	0.034 %

from the axis perpendicular to the horizontal plane in the lab. The PPACs are arranged as the sides of a cube and form the walls of the target chamber. Both the projectile-like and the target-like particles are detected. The lab angles of the Ge and NaI(Tl) detectors are given in Tables 2.2 and 2.3, respectively. The principle reaction studied was the one-neutron pickup reaction ^{235}U(^{58}Ni,^{59}Ni)^{234}U (Q_{react} = 3.73 MeV, V_c = 323.4 MeV, where V_c is the Coulomb barrier height).

Table 2.2: Lab detector positions for ^{58}Ni + ^{235}U experiment

Ge detector positions (angles in lab)								
No.	θ	ϕ	No.	θ	ϕ	No.	θ	ϕ
1	155.6°	−4.9°	2	116.6°	18.0°	3	63.4°	−18.0°
4	63.4°	126.0°	5	116.6°	−54.0°	6	24.4°	4.9°
7	116.6°	−126.0°	8	116.6°	162.0°	9	138.4°	176.0°
10	63.4°	−162.0°	11	41.6°	−176.0°	12	130.5°	−6.3°
13	63.4°	54.0°	14	24.4°	148.9°			

Table 2.3: Lab detector positions for ^{58}Ni + ^{235}U experiment

NaI(Tl) detector positions (angles in lab)								
No.	θ	ϕ	No.	θ	ϕ	No.	θ	ϕ
2	24.4°	76.8°	4	24.4°	-67.1°	5	24.4°	-139.1°
7	63.4°	-90.0°	8	87.3°	-95.4°	9	67.9°	-116.4°
10	41.6°	-104.0°	11	49.5°	-65.7°	12	77.5°	-68.7°
14	87.3°	-23.4°	15	67.9°	-44.4°	16	41.6°	-32.0°
17	49.5°	6.3°	18	77.5°	3.3°	20	87.3°	48.6°
21	67.9°	27.6°	22	41.6°	40.0°	23	49.5°	78.3°
24	77.5°	75.3°	26	87.3°	120.6°	27	67.9°	99.6°
28	41.6°	112.0°	29	49.5°	150.3°	30	77.5°	147.3°
32	87.3°	-167.4°	33	67.9°	171.6°	35	49.5°	-137.7°
36	77.5°	-140.7°	38	155.6°	-76.9°	40	155.6°	67.1°
41	155.6°	139.1°	42	155.6°	-148.9°	43	116.6°	90.0°
44	92.7°	95.4°	45	112.1°	116.4°	46	138.4°	104.0°
47	130.5°	65.7°	48	102.5°	68.7°	50	92.7°	23.4°
51	112.1°	44.4°	52	138.4°	32.0°	53	130.5°	-6.3°
54	102.5°	-3.3°	56	92.7°	-48.6°	57	112.1°	-27.6°
58	138.4°	-40.0°	59	130.5°	-78.3°	60	102.5°	-75.3°
62	92.7°	-120.6°	63	112.1°	-99.6°	64	138.4°	-112.0°
65	130.5°	-150.3°	66	102.5°	-147.3°	68	92.7°	167.4°
69	112.1°	-171.6°	71	130.5°	137.7°	72	102.5°	140.7°

2.1.2 ^{206}Pb + ^{233}U Reaction at LBL

This experiment was carried out using 1566-MeV ^{206}Pb ions (1200-MeV at the center of the target) from the SuperHILAC bombarding a 430 μg/cm^2 ^{233}U target with a 2.1 mg/cm^2 Be backing in HERA at LBL, which consisted of fourteen Ge detectors. Figure 2.4 gives a schematic diagram of the experimental configuration. The target composition is given in Table 2.4, and target construction is discussed in detail in Appendix A. Surrounding the target were

Table 2.4: Isotopic composition of target for ^{206}Pb + ^{233}U experiment

Isotope	Percentage
^{233}U	99.8 %
^{232}U	< 0.0038 %

six PPACs covering lab angles of 15° to 75° in the θ direction, and −25° to 25°, 35° to 85°, 95° to 145°, 155° to 205°, 215° to 265° and 275° to 325° in the ϕ direction. The PPACs are arranged as the sides of a pyramid with its apex on the beam axis, and both projectile-like and target-like particles are detected. The lab angles of Ge detectors are given in Table 2.5. The principle reaction studied was the inelastic excitation reaction ^{233}U(^{206}Pb,^{206}Pb$'$)^{233}U$'$ (V_c = 1220 MeV).

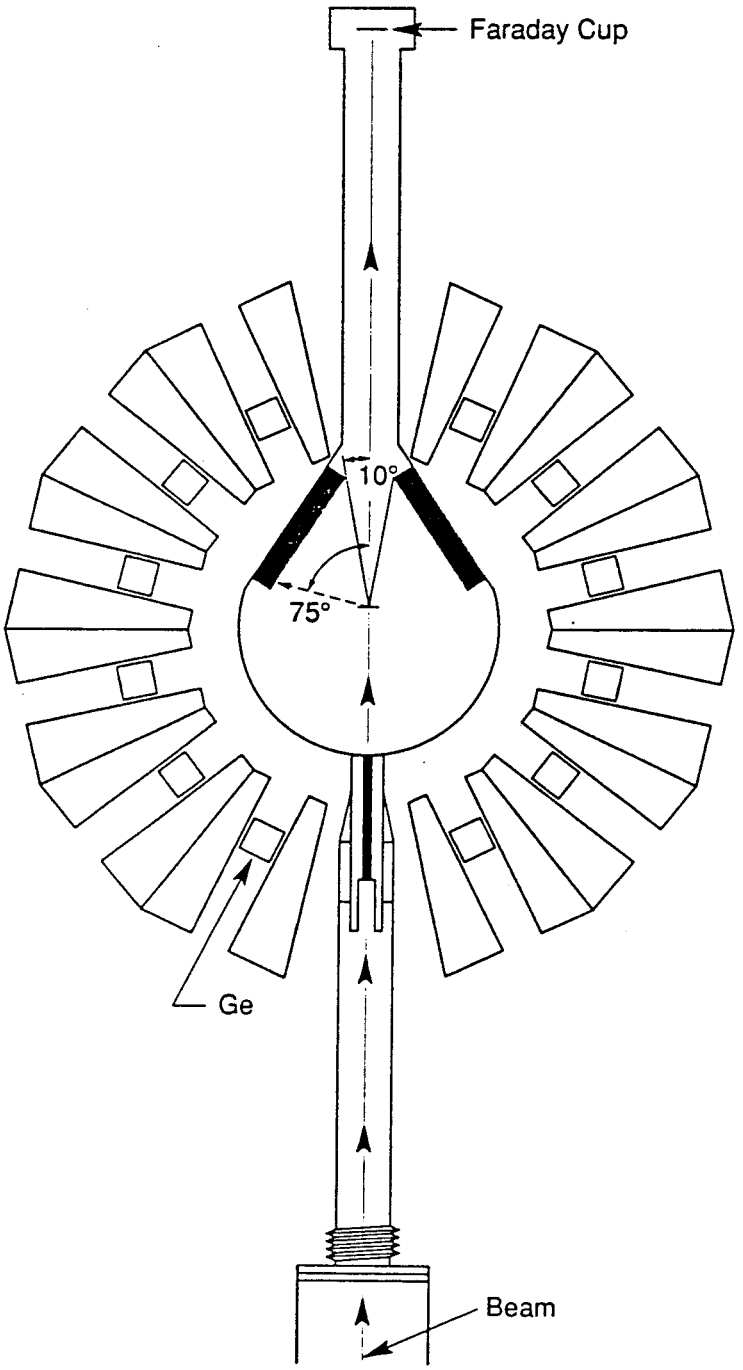

Figure 2.4: Diagram of ^{206}Pb + ^{233}U experimental setup.

Table 2.5: Lab detector positions for ^{206}Pb + ^{233}U experiment

Ge detector positions (angles in lab)								
No.	θ	ϕ	No.	θ	ϕ	No.	θ	ϕ
1	41.4°	0.0°	2	20.5°	−55.4°	3	21.1°	54.6°
4	159.6°	0.0°	5	138.6°	37.7°	6	138.6°	−37.3°
7	180.0°	90.0°	8	159.6°	180.0°	9	138.6°	127.3°
10	180.0°	270.0°	11	48.3°	180.0°	12	75.0°	207.6°
13	140.0°	218.3°	14	75.0°	117.6°			

2.1.3 ^{58}Ni + ^{233}U Reaction at UOR

This counting experiment was carried out using 249-MeV ^{58}Ni ions bombarding a 430 μg/cm^2 ^{233}U target with 135 μg/cm^2 Ni and 4.0 mg/cm^2 Cu backing at the University of Rochester (UOR) Nuclear Structure Research Laboratory's Tandem Accelerator. The target was viewed by one BGO Compton-suppressed Ge detector located at $\theta = 0°$, two Ge detectors located at $\theta = \pm 90°$, and a Si particle detector covering 135° to 170° in the θ direction. Backscattered Ni ions were detected in the Si detector, and the ^{233}U was allowed to recoil through the target backing, emerging with approximately 30 MeV (a loss of about 120 MeV in the backing). Doppler shifts at 0° were decreased due to this slowing of recoils in the target backing, and the Doppler broadening of the lines was small in this experiment. The principle reaction studied was the Coulomb excitation reaction ^{233}U(^{58}Ni,^{58}Ni$'$)^{233}U$'$.

2.1.4 ^{90}Zr + ^{239}Pu Reaction at ORNL

This experiment was carried out using 500-MeV ^{90}Zr ions bombarding a 356.3 μg/cm^2 ^{239}Pu target with a 170 μg/cm^2 Ni backing in the Spin Spectrometer at ORNL, which consisted of 52 NaI(Tl) and 18 Ge detectors. Fig-

ure 2.5 gives a schematic diagram of the experimental configuration. The target composition is given in Table 2.6, and the target construction is discussed in Appendix A. Surrounding the target were two PPACs covering lab

Table 2.6: Isotopic composition of target for ^{90}Zr + ^{239}Pu experiment

Isotope	Percentage
^{239}Pu	93.826 %
^{238}Pu	0.012 %
^{240}Pu	5.913 %
^{241}Pu	0.222 %
^{242}Pu	0.027 %
^{241}Am	< 1 %
^{237}U	$\ll 1$ %

angles of 104° to 162° in the θ direction, and −35° to 35° and 145° to 215° in the ϕ direction. The PPACs were arranged as the upstream two sides of a cube and formed the walls of the scattering chamber. Only backscattered Zr ions were detected in this experiment; the Pu scattering angle was inferred from the scattering kinematics. The lab angles of the Ge and NaI(Tl) detectors are given in Tables 2.7 and 2.8, respectively. The principle reaction studied was the one-neutron pickup reaction ^{239}Pu(^{90}Zr,^{91}Zr)^{238}Pu (Q_{react} = 1.58 MeV, V_c = 493.9 MeV), but the inelastic excitation reaction ^{239}Pu(^{90}Zr,^{90}Zr$'$)^{239}Pu$'$ was also studied in this setup.

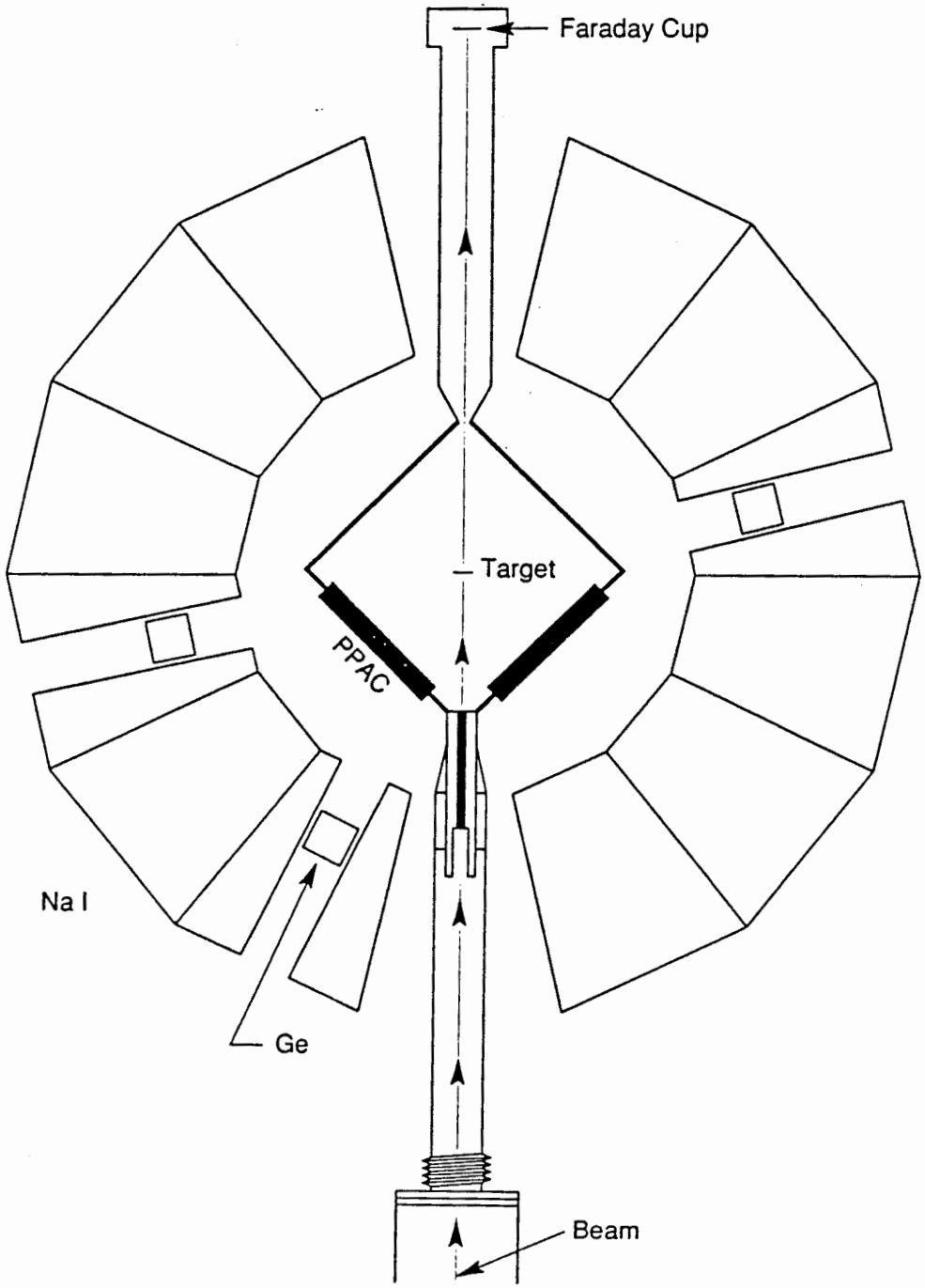

Figure 2.5: Diagram of ^{90}Zr + ^{239}Pu experimental setup.

Table 2.7: Lab detector positions for $^{90}Zr + ^{239}Pu$ experiment

Ge detector positions (angles in lab)								
No.	θ	ϕ	No.	θ	ϕ	No.	θ	ϕ
1	63.4°	−162.0°	2	92.7°	23.4°	3	155.6°	−148.9°
4	116.6°	162.0°	5	63.4°	−18.0°	6	155.6°	139.1°
7	116.6°	−126.0°	8	63.4°	126.0°	9	24.4°	148.9°
10	24.4°	−139.1°	11	63.4°	54.0°	12	116.6°	18.0°
13	24.4°	−67.1°	14	116.6°	−54.0°	15	155.6°	−4.9°
16	138.4°	176.0°	17	49.5°	6.3°	18	138.4°	32.0°

Table 2.8: Lab detector positions for $^{90}Zr + ^{239}Pu$ experiment

NaI(Tl) detector positions (angles in lab)								
No.	θ	ϕ	No.	θ	ϕ	No.	θ	ϕ
2	24.4°	76.8°	3	24.4°	4.9°	7	63.4°	-90.0°
8	87.3°	-95.4°	9	67.9°	-116.4°	10	41.6°	-104.0°
11	49.5°	-65.7°	12	77.5°	-68.7°	14	87.3°	-23.4°
15	67.9°	-44.4°	16	41.6°	-32.0°	18	77.5°	3.3°
20	87.3°	48.6°	21	67.9°	27.6°	22	41.6°	40.0°
23	49.5°	78.3°	24	77.5°	75.3°	26	87.3°	120.6°
27	67.9°	99.6°	28	41.6°	112.0°	29	49.5°	150.3°
30	77.5°	147.3°	32	87.3°	-167.4°	33	67.9°	171.6°
34	41.6°	-176.0°	35	49.5°	-137.7°	36	77.5°	-140.7°
38	155.6°	-76.9°	40	155.6°	67.1°	43	116.6°	90.0°
44	92.7°	95.4°	45	112.1°	116.4°	46	138.4°	104.0°
47	130.5°	65.7°	48	102.5°	68.7°	51	112.1°	44.4°
53	130.5°	-6.3°	54	102.5°	-3.3°	56	92.7°	-48.6°
57	112.1°	-27.6°	58	138.4°	-40.0°	59	130.5°	-78.3°
60	102.5°	-75.3°	62	92.7°	-120.6°	63	112.1°	-99.6°
64	138.4°	-112.0°	65	130.5°	-150.3°	66	102.5°	-147.3°
68	92.7°	167.4°	69	112.1°	-171.6°	71	130.5°	137.7°
72	102.5°	140.7°						

2.2 Data Analysis Techniques

An event written on raw data tapes consisted of uncalibrated energies and time signals from the PPACs, NaI(Tl) and Ge detectors. These tapes were then scanned on an event-by-event basis and rewritten on prescan tapes which recorded the new and calibrated parameters. An event on the prescan tape consisted of scattering angles θ, ϕ of the particles in the lab, timing information between the left and right PPACs, Doppler-corrected and energy-calibrated Ge and NaI(Tl) E_γ spectra; and new parameters calculated from the observables, mass observed in a given PPAC, neutron multiplicity (K_n), number of Ge detectors firing (K_{Ge}), sum of NaI(Tl) energies (H) and the number of NaI(Tl) detectors firing (K). Doppler corrections to the Ge spectra were made for both the projectile-like and target-like fragments. The Doppler corrected γ-ray energy for the target-like fragment is given by:

$$E'_\gamma = \frac{E_\gamma}{1 + \beta(DOPP)}, \tag{2.1}$$

where E_γ is the raw, uncorrected γ-ray energy, and β and $DOPP$ are defined in the following manner:

$$\beta = \frac{p}{A_T}\frac{1}{931.5016}, \tag{2.2}$$

where A_T is the mass number of the target-like fragment, and the momentum is defined in the usual way

$$p = \frac{p_{tot} \sin \theta_T}{v_{trans}}. \tag{2.3}$$

p_{tot} is the total initial momentum of the projectile, or

$$p_{tot} = \sqrt{2E_{beam} A_P}. \tag{2.4}$$

In the ^{90}Zr + ^{239}Pu case, p_{tot} = 9156.1 MeV/c. The lab scattering angle of the target-like fragment is θ_T, and the transverse velocity, v_{trans}, is given by:

$$v_{trans} = \sin \theta_P + \theta_T, \tag{2.5}$$

where θ_P is the lab scattering angle of the projectile-like fragment. The Doppler shift is given by:

$$DOPP = \hat{x}_{Ge} \cdot \hat{p}_x + \hat{y}_{Ge} \cdot \hat{p}_y + \hat{z}_{Ge} \cdot \hat{p}_z, \tag{2.6}$$

where $\hat{x}_{Ge}, \hat{y}_{Ge}$, and $\hat{z}_{Ge}$ are unit vectors denoting the x, y and z direction in the lab of the Ge detectors (the target being defined as the origin with the beam direction the + z-axis), and

$$\begin{aligned} \hat{p}_x &= \sin \theta_T \cos \phi_T \\ \hat{p}_y &= \sin \theta_T \sin \phi_T \\ \hat{p}_z &= \cos \theta_T. \end{aligned} \tag{2.7}$$

Similar equations exist for the Doppler correction of the projectile-like fragment. The Doppler correction is made on an event-by-event basis for each Ge detector individually. Doppler corrections for the NaI(Tl) detectors were made in some cases, however, in general the Doppler corrections for a NaI(Tl) detector are negligible compared to the resolution of the scintillator (Doppler shifts are on the order of 2-5 keV, NaI(Tl) resolution $\sim$ 50 keV).

For the reactions studied in which both the target-like recoil fragment and the projectile-like scattered fragment were detected, the beam energy, entrance channel masses, TOFs, angles of the trajectories, and timing difference between the particles are enough to calculate the mass of a particle observed in a PPAC, assuming two-body kinematics. A mass spectrum for the ^{206}Pb + ^{233}U reaction is shown in Figure 2.6. As Figure 2.6 shows, the mass resolution of the PPACs is insufficient to resolve particles A and A+1, but a Pb-like and U-like separation can clearly be made. As mentioned previously, θ calibrations were determined by placing an Al mask with known slits over the PPACs and running the reaction for a short time. Figure 2.2 shows a sample calibration spectrum for the ^{90}Zr + ^{239}Pu reaction. A linear least-squares fit for the angular calibration is used.

Figure 2.7 shows a ^{152}Eu calibration spectrum for one Ge detector. Peak

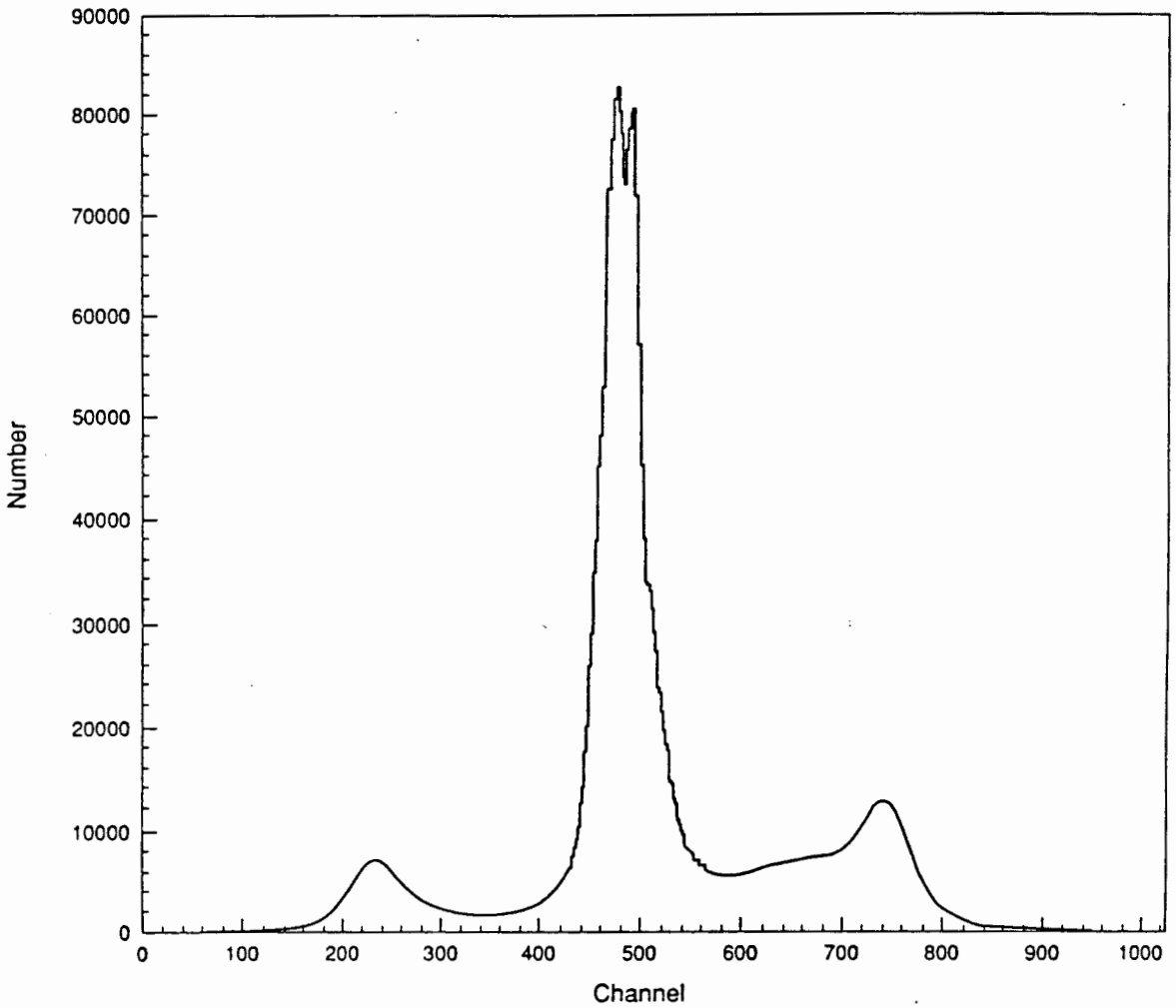

Figure 2.6: Mass spectrum from one PPAC for the ^{206}Pb + ^{233}U reaction.

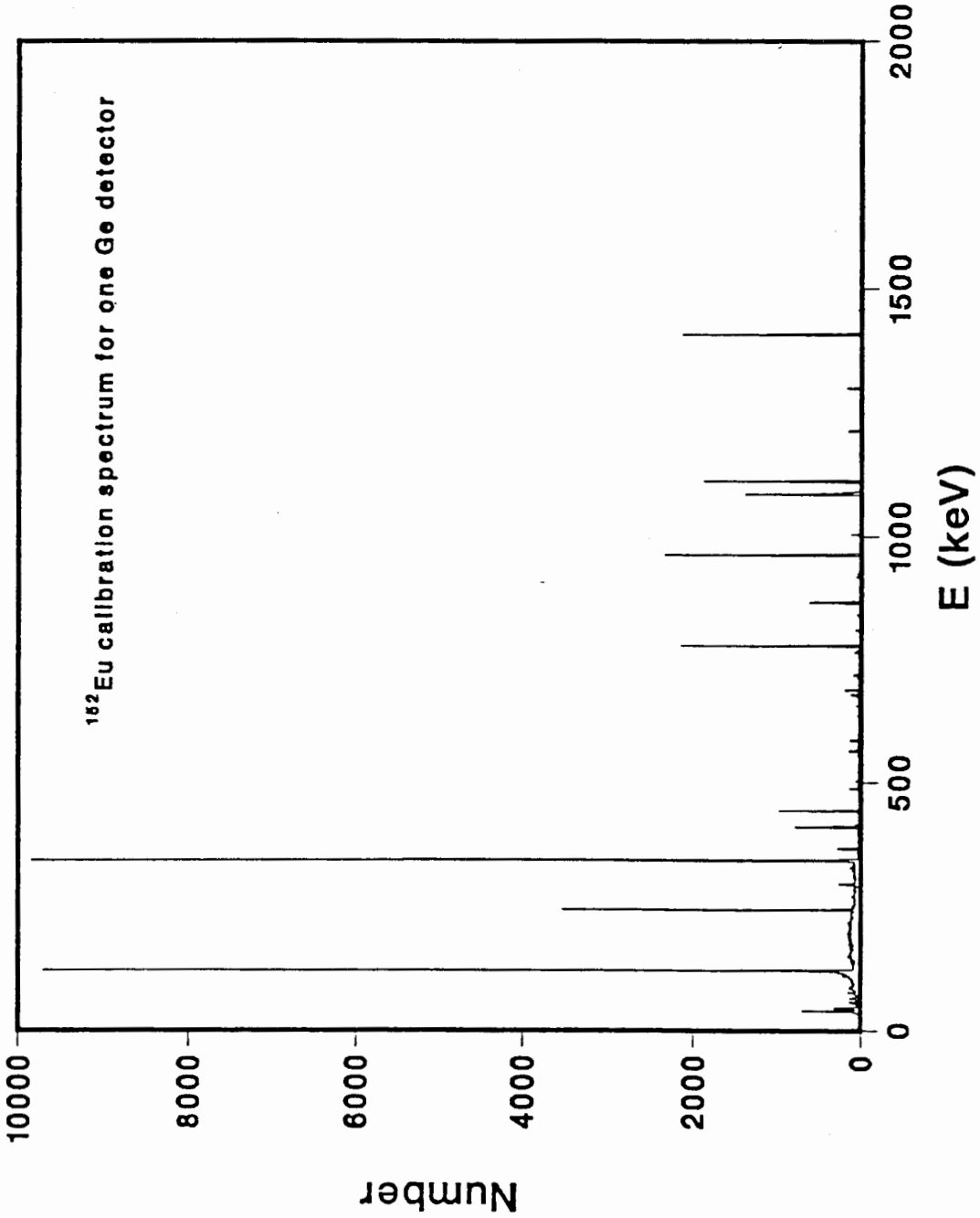

Figure 2.7: ^{152}Eu calibration spectrum for a Ge detector. The detector resolution and background suppression should be noted.

positions and intensities were obtained using the Gaussian least- squares fitting program FITEK. The FITEK program was developed by Dr. Wolfgang Stöffl at Lawrence Livermore National Laboratory (LLNL) and is discussed further in Appendix B. Using ~ 20 standard reference γ-rays from radioactive sources, linear least-squares energy calibrations are obtained for all Ge detectors. In addition, all Ge timing spectra are corrected. Figure 2.8 shows a typical uncorrected Ge E_γ spectrum, a Doppler corrected E_γ spectrum, and a Ge timing spectrum for the ^{90}Zr + ^{239}Pu reaction. Timing resolution is 8 ns full-width-half-maximum (FWHM).

Doppler corrections and energy calibrations were performed again for experiments with NaI(Tl) detectors, ie., at the ORNL Spin Spectrometer. In addition, for detectors with sufficient timing, neutrons and γ-rays are resolved from each other via the TOF of the neutrons. Figure 2.9 shows an example of a timing spectrum for a NaI(Tl) detector in the ^{90}Zr + ^{239}Pu reaction for events depositing $2 - 16$ MeV in the detector. The NaI(Tl) timing is energy dependent, with a neutron-gamma separation impossible to make below 200 keV. The time separation between the γ-rays and the neutrons is 5 ns, which is about the same FWHM NaI(Tl) timing resolution ($4 - 5$ ns). Only detected γ-ray energies are added to the total energy spectrum. In addition, for most

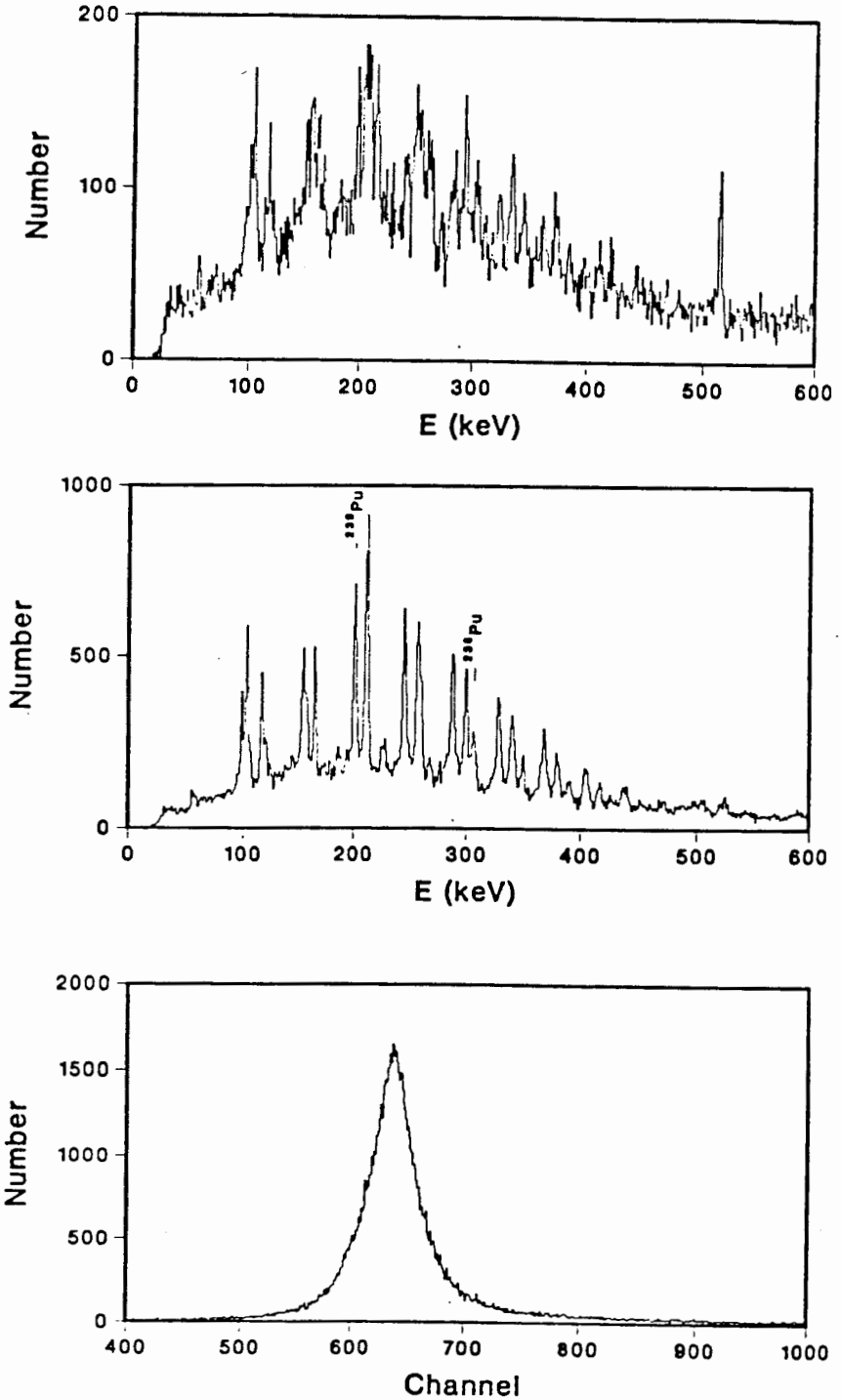

Figure 2.8: The top figure is an uncorrected Ge E_γ spectrum. The middle figure is the same Ge E_γ spectrum with Doppler corrections, and the bottom figure is the Ge timing spectrum.

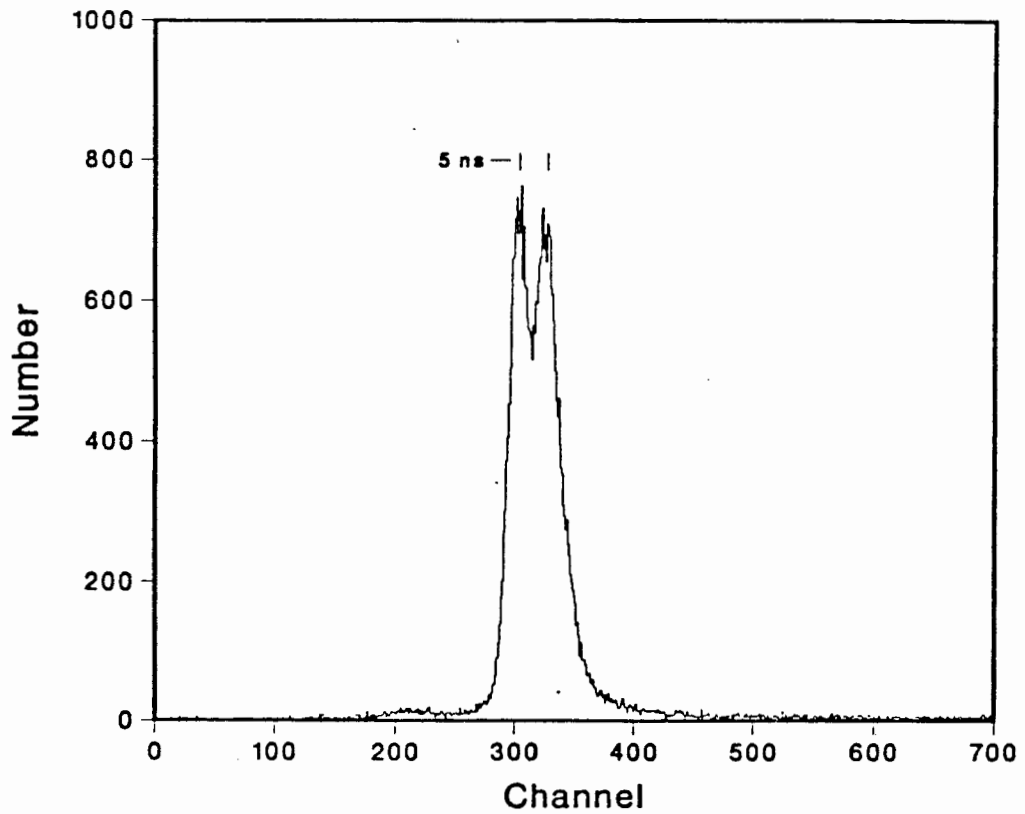

Figure 2.9: NaI(Tl) timing spectrum showing the neutron-γ-ray separation for the ^{90}Zr + ^{239}Pu reaction for events depositing 2 – 16 MeV in the detector.

cases in the remainder of this thesis, except where otherwise noted, a $K_n = 0$ gate is used when analyzing events any further. This insures that the reaction being studied is not contaminated with neutron evaporation or fission events. As expected, NaI(Tl) detectors with high rates of neutron events were the ones located at forward angles in the lab, as both fission and neutron evaporation would occur from sources moving downstream.

Any parameter on the prescan tapes can then be histogrammed for further analysis. In addition, a variety of gates (different reaction conditions) or cuts could be applied to the data. Parameters could be histogrammed in a two-dimensional matrix versus other parameters to study correlations between different quantities. The results of these analyses are presented in Chapter 3.

Chapter 3

Results and Discussion

3.1 ^{58}Ni + ^{235}U Reaction

The LBL/UOR/UTK/ORNL collaboration performed this experiment in the actinides as an exploratory effort to test the effectiveness of the heavy-ion "cold" one-neutron transfer technique, as a high-spin spectroscopic tool. The "cold" transfer mechanism is characterized by population of states in the product nucleus on or near the Yrast line. The actinide region, as mentioned earlier, is a difficult region in which to obtain data, as stable targets do not exist. In addition to the natural radioactivity of the targets, fission is expected to be a dominant exit channel for any reaction above the fission barrier ($\sim$ 5 MeV in the light actinides). Consequently, our first effort was more along the lines of proving the usefulness of the method, and a longer-lived ^{235}U target was used.

Figure 3.1 shows the Ge spectra; Figure 3.1a is the total γ-ray spectrum summed over all 14 Ge detectors with appropriate Doppler corrections, Figure 3.1b is a $\gamma - \gamma$ coincidence two-fold γ-ray spectrum gated on the previously known $8^+ \rightarrow 6^+$, $10^+ \rightarrow 8^+$ and $12^+ \rightarrow 10^+$ transitions in ^{234}U, and Figure 3.1c is the γ-ray spectrum gated on the (H, K) spectrum from the NaI(Tl) detectors ($H > 2.9$ MeV, $K > 4$). Figure 3.1a shows a γ-ray spectrum dominated by ^{235}U inelastic transitions and ^{234}U neutron transfer transitions. No appreciable fission competition was observed. The differential cross-section for the one-neutron pickup reaction was about 20 mb/sr at the grazing angle ($\sim 130°$ in the lab).

Figure 3.1b clearly separates the ground rotational band of ^{234}U from inelastic contamination, although the spectrum suffers from the traditional lack of statistics associated with the $\gamma - \gamma$ coincidence methods. Nevertheless, the $22^+ \rightarrow 20^+$ ^{234}U transition can clearly be identified. Figure 3.1c, gated on (H, K) in a region where one-neutron transfer should dominate, clearly shows the $24^+ \rightarrow 22^+$ ^{234}U transition. With some imagination, there is a candidate for the $26^+ \rightarrow 24^+$ ^{234}U transition. It should be noted, that this is $6 - 8$ units of angular momentum higher than the highest spins populated by Coulomb excitation with ^{58}Ni ions in this region [36]. Also, the statistics are much

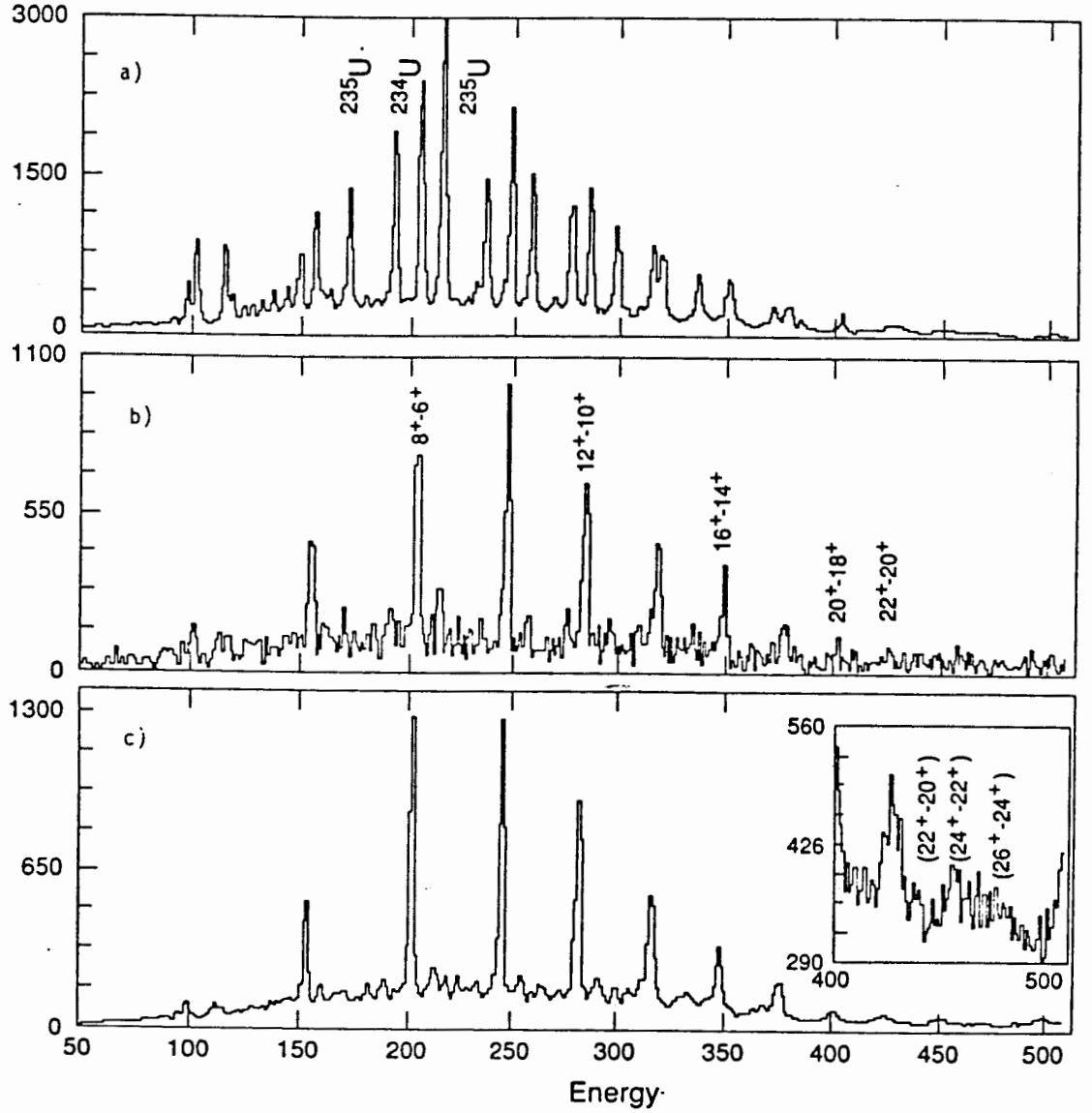

Figure 3.1: Ge γ-ray spectrum for the ^{58}Ni + ^{235}U reaction; a) is the total γ-ray spectrum of all 14 Ge detectors summed together; b) is a $\gamma-\gamma$ coincidence spectrum gated on three previously known ^{234}U transitions; and c) is the γ-ray spectrum gated on the (H, K) spectrum. Transitions from the $24^+(26^+)$ level can clearly be identified in the inset to c).

better in this method of using the NaI(Tl) ball to separate the transfer exit channel from the inelastic exit channel.

Figure 3.2 shows the total E, multiplicity, M, spectrum for the one-neutron transfer. It was produced by summing again on gates of the $8^+ \rightarrow 6^+$, $10^+ \rightarrow 8^+$, and $12^+ \rightarrow 10^+$ transitions in ^{234}U in the Ge detectors. The dashed line indicates the approximate Yrast line for ^{234}U assuming no ^{58}Ni excitation, and a conversion scale to spin, $I/\hbar$, is provided. Two maxima in the contour plot are observed, the lower one lying approximately on the Yrast line at $E = 0.5$ MeV, $M = 1.5$. Inelastic events from target impurities are less than 10% of this peak. The upper maximum is centered at $E = 3$ MeV, $M = 3.5$ and is 80% of the strength of the lower maximum. The upper maximum is ~ 2 MeV above the Yrast line, still relatively low in excitation energy.

Figure 3.2 clearly indicates that the reaction is "cold" and populates states on or within 2 MeV of the Yrast line. They can be understood through a mechanism in which kinematic and binding energy favors population near the Yrast line, and structure effects favor population of the rotationally aligned states. The lower bump is interpreted as population of states following the pickup of the odd neutron (the unpaired $j_{\frac{15}{2}}$ neutron), ie., the direct population of the ground-state band. The upper bump represents the population of states

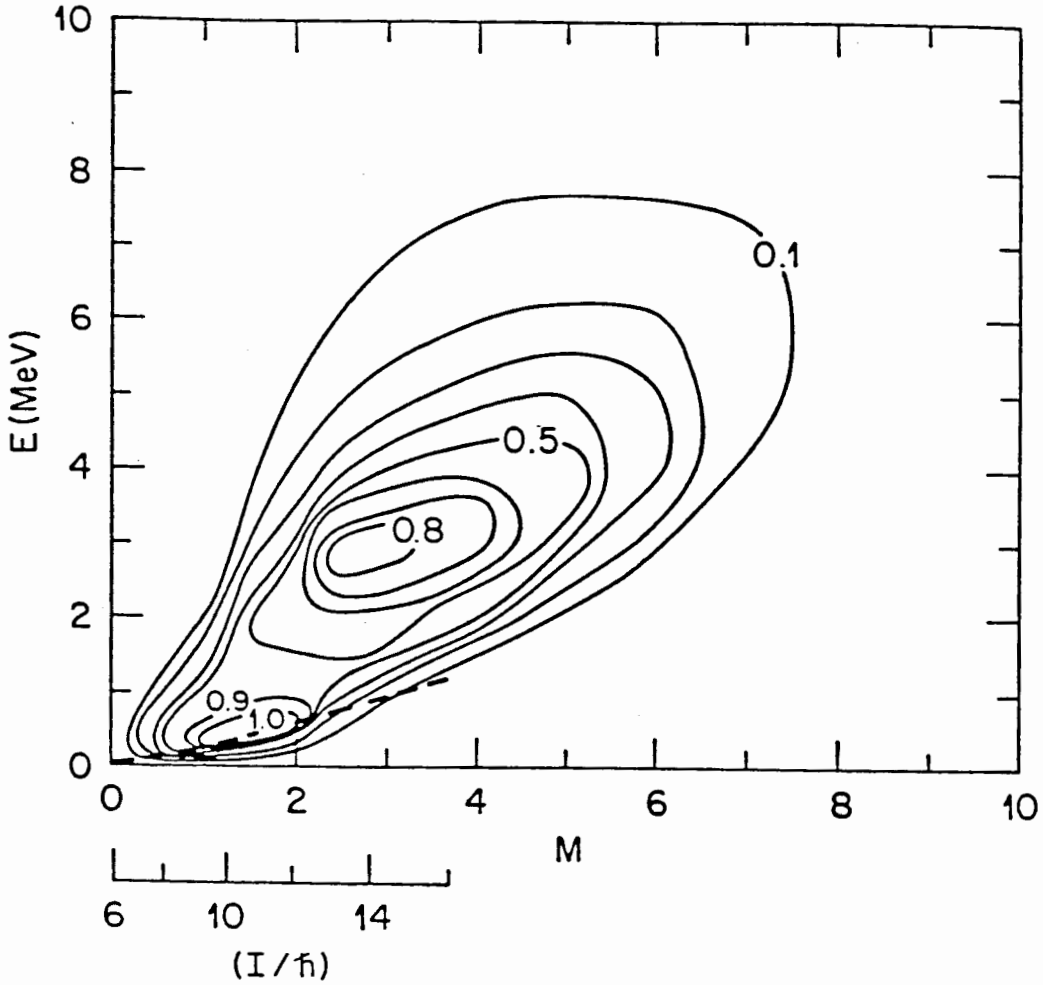

Figure 3.2: Total E, M plot for the ^{58}Ni + ^{235}U reaction where the dashed line indicates the approximate Yrast line for ^{234}U assuming no excitation of the ^{58}Ni.

following the pickup of a paired neutron after the pair is broken leading to a two-quasiparticle state of higher excitation energy (hence the ~ 2 MeV above the Yrast line). The average alignment for each state populated in the two-quasiparticle region is about 6, accounting for the multiplicity difference of about 3 between the upper and lower bumps in the (H, K) spectrum if the de-excitation is by $E2$ transitions. It should be pointed out that population of states with spin ≥ 26 is most certainly occurring, but that a lack of statistics prevents identification of the discrete γ-rays.

The data presented here clearly establish this method as excellent for studying high-spin states in the actinides. The "cold" reaction mechanism minimizes fission competition. One-neutron transfer reactions populate higher spin states than does Coulomb excitation. Spins up to $24^+(26^+)$ in ^{234}U are seen for the first time in this experiment. In Coulomb excitation experiments with Pb projectiles, states with spins $\sim 30\hbar$ have been reached in the actinides [40],[44],[45],[46]. This suggests that discrete states with spins higher than $30\hbar$ could be populated in one-neutron transfer reactions using Pb projectiles. This directly led to the experiments described in the next section.

3.2 ^{206}Pb + ^{233}U and ^{58}Ni + ^{233}U Reactions

A total inelastic excitation γ-ray spectrum (sum of 14 Ge detectors all appropriately Doppler corrected) from the SuperHILAC experiment is shown in Figure 3.3. Rotational transitions up to $\frac{49}{2}^+ \rightarrow \frac{45}{2}^+$ in ^{233}U are observed. In addition, the $8^+ \rightarrow 6^+$ transition in ^{232}U from the one-neutron transfer reaction ^{233}U(^{206}Pb,^{207}Pb)^{232}U is observed. Insufficient statistics and contamination from ^{233}U lines precluded γ-γ gating studies of other ^{232}U rotational transitions. Table 3.1 and Figure 3.4 contain a more complete presentation of both branches or signatures of the ground-state band transitions observed in ^{233}U from both experiments. Figure 3.4 shows the two signatures separately;

Table 3.1: Observed transitions in ^{233}U

Transition	Energy (keV)	Transition	Energy (keV)
$\frac{11}{2}^+ \rightarrow \frac{7}{2}^+$	113.0(2)	$\frac{13}{2}^+ \rightarrow \frac{9}{2}^+$	137.6(2)
$\frac{15}{2}^+ \rightarrow \frac{11}{2}^+$	160.1(2)	$\frac{17}{2}^+ \rightarrow \frac{13}{2}^+$	181.6(2)
$\frac{19}{2}^+ \rightarrow \frac{15}{2}^+$	203.1(2)	$\frac{21}{2}^+ \rightarrow \frac{17}{2}^+$	223.6(2)
$\frac{23}{2}^+ \rightarrow \frac{19}{2}^+$	243.0(2)	$\frac{25}{2}^+ \rightarrow \frac{21}{2}^+$	262.5(2)
$\frac{27}{2}^+ \rightarrow \frac{23}{2}^+$	281.9(2)	$\frac{29}{2}^+ \rightarrow \frac{25}{2}^+$	299.3(2)
$\frac{31}{2}^+ \rightarrow \frac{27}{2}^+$	316.7(2)	$\frac{33}{2}^+ \rightarrow \frac{29}{2}^+$	334.1(4)
$\frac{35}{2}^+ \rightarrow \frac{31}{2}^+$	349.5(4)	$\frac{37}{2}^+ \rightarrow \frac{33}{2}^+$	366.9(4)
$\frac{39}{2}^+ \rightarrow \frac{35}{2}^+$	381.2(4)	$\frac{41}{2}^+ \rightarrow \frac{37}{2}^+$	397.6(4)
$\frac{43}{2}^+ \rightarrow \frac{39}{2}^+$	409.8(4)	$\frac{45}{2}^+ \rightarrow \frac{41}{2}^+$	423.2(4)
$\frac{47}{2}^+ \rightarrow \frac{43}{2}^+$	436.5(4)	$\frac{49}{2}^+ \rightarrow \frac{45}{2}^+$	448.7(4)

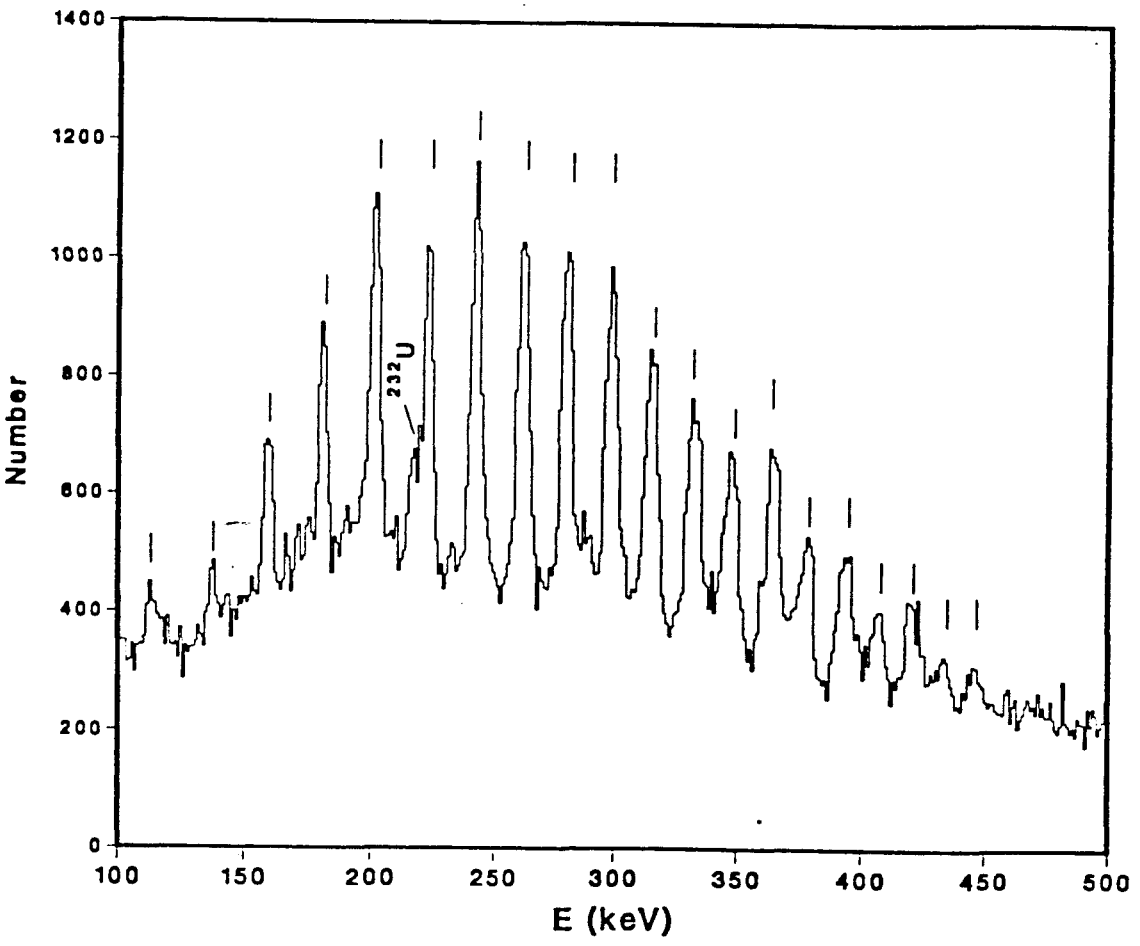

Figure 3.3: Total γ-ray spectrum of ^{206}Pb(^{233}U,^{233}U$'$)^{206}Pb$'$ inelastic excitation reaction with beam energy of 1566 MeV. The spectrum is a sum of 14 Ge detectors, all appropriately Doppler corrected, and is gated on scattering angles of 45–70° in the lab. The ^{233}U transitions are marked with dashes. Particle ϕ information was lost in some PPAC's resulting in broadening of lines. Note the transition at 217.4-keV that is identified as the $8^+ \rightarrow 6^+$ transition in ^{232}U, which is from the one-neutron transfer reaction.

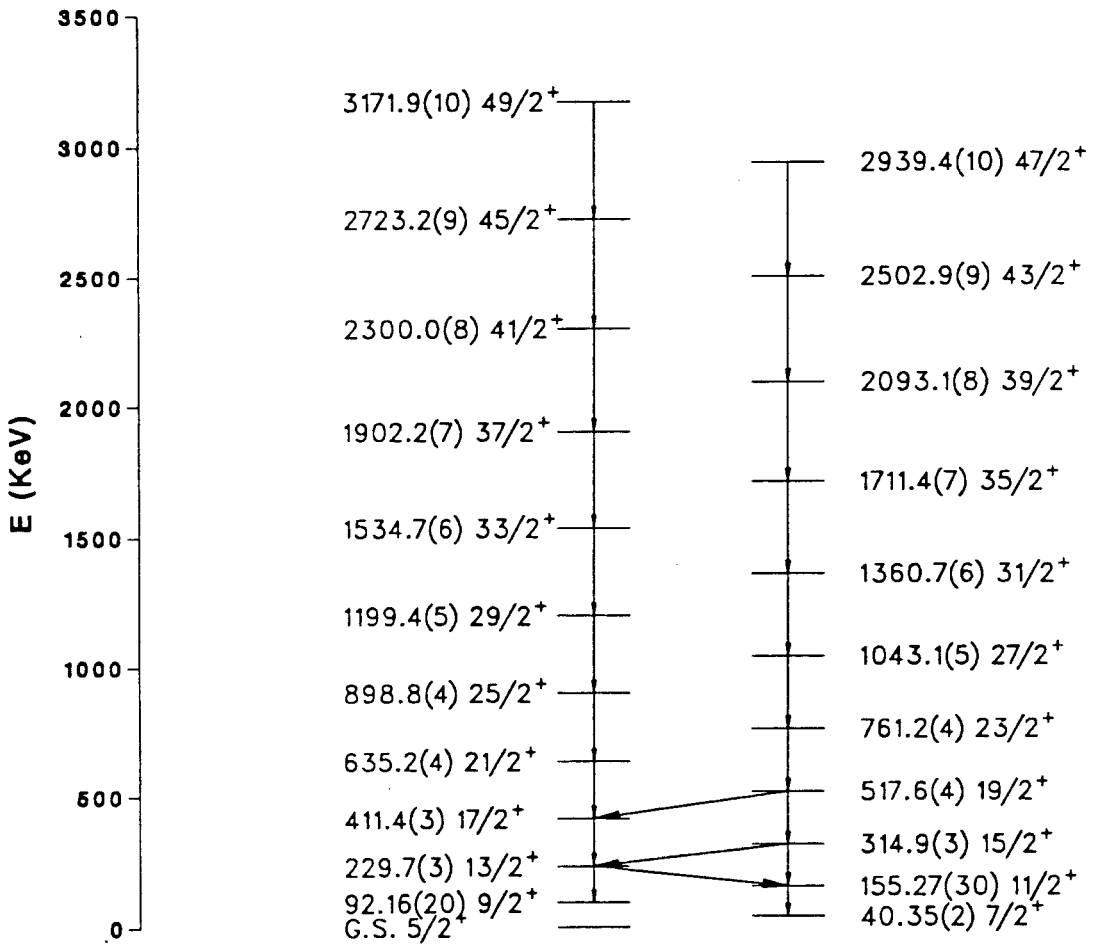

Figure 3.4: Level diagram for both signatures of the ground-state band in ^{233}U. Arrows indicate the transitions observed in these experiments. The $\frac{9}{2}^+ \rightarrow \frac{5}{2}^+$ and $\frac{17}{2}^+ \rightarrow \frac{15}{2}^+$ transitions were masked by uranium X-rays. Errors in the last digit of the level energies are shown in parentheses (eg., 92.16(20) = 92.16 ± 0.2 keV). The levels up to the $\frac{41}{2}^+$ level are based on the Nuclear Data Tables [47], and the remaining levels are obtained by adding transition energies.

the favored signature starting with the $\frac{5}{2}^+$ level and the unfavored signature starting with the $\frac{7}{2}^+$ level. The $E2$ transitions connecting levels within a signature are the crossover transitions because a level from the other signature is skipped. The $\frac{M1}{E2}$ transitions connecting the signatures are cascade transitions. The staggering between the signatures is just the energy difference between levels I and $I+1$, ie., $E_{\frac{7}{2}^+} - E_{\frac{5}{2}^+}$ for instance. The arrows in Figure 3.4 indicate the transitions that were observed in these experiments. Level energies up to the $\frac{41}{2}^+$ level were taken from [47], and higher level energies were obtained by summing the fitted transition energies. The $\frac{9}{2}^+ \rightarrow \frac{5}{2}^+$ and $\frac{17}{2}^+ \rightarrow \frac{15}{2}^+$ transitions were masked by uranium X-rays. It should be noted that the highest spin known previously was $\frac{41}{2}^+$ from Coulomb excitation with Kr projectiles [47], whereas in our work with ^{206}Pb projectiles levels up to $\frac{49}{2}^+$ are observed. Both the (α,3n) reaction of reference [41] and the ^{58}Ni Coulomb excitation experiment populated the $\frac{31}{2}^+$ level.

It has been theoretically predicted that backbending should be observed near $30\hbar$ in the even-even uranium nuclei [48]. However, backbending in the actinide region has only been observed in ^{242}Pu and ^{244}Pu nuclei [38]. Figure 3.5 shows a plot of moment-of-inertia ($\Im$) vs. cranking frequency (ω) for ^{233}U.

The transition energy is related to the cranking frequency by $\frac{E_i - E_f}{\Delta I} = \hbar\omega$. The moment-of-inertia has been calculated several ways; using the transition energy, $\Delta E = E_i - E_f$;

$$\frac{2\Im^{(1)}}{\hbar^2} = \frac{I_i(I_i+1) - I_f(I_f+1)}{\Delta E}, \tag{3.1}$$

where I_i and I_f are the initial and final spin states, respectively; and using the first difference of transition energies,

$$\frac{2\Im^{(2)}}{\hbar^2} = \frac{2\Delta I}{\Delta(\hbar\omega)}, \tag{3.2}$$

where $\Delta(\hbar\omega) = \Delta(\frac{\Delta E}{2})$. The moments-of-inertia, $\Im^{(1)}$ and $\Im^{(2)}$, are generally referred to as the "kinematic" and "dynamic" moments-of-inertia, respectively.

A brief examination of the moment-of-inertia plots (Figure 3.5 and Figure 3.6) shows a steadily increasing moment-of-inertia, with nothing dramatic in the way of upbending or backbending. This change in the moment-of-inertia is probably a combination of alignment and a decrease in the pairing gap, Δ, rather than a change in deformation. Recently, Helgesson and Hamamoto have explored the effects of triaxiality on the moments-of-inertia [49] in the rare earth region, and have shown smooth yet significant effects as a function of γ_d in the region $-60° \leq \gamma \leq 0°$. For $N = 90, A = 152$ the moment-of-inertia $\Im_x$

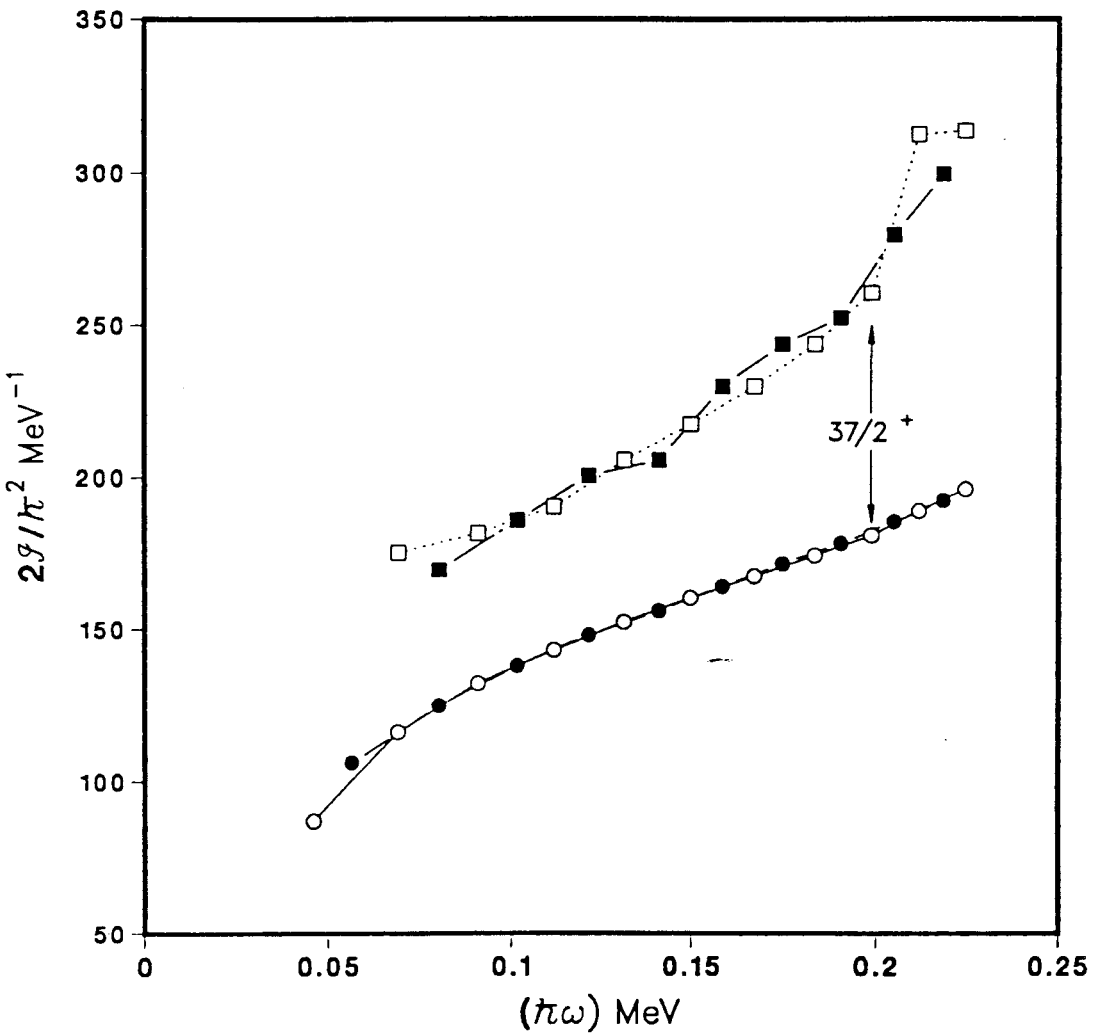

Figure 3.5: Plot of $\Im$ vs. ω for ground-state band in ^{233}U. The moment-of-inertia, $\Im$, was calculated using equations (3.1) [o and •], and (3.2) [open and solid squares] in the text. The open symbols are for the $\frac{5}{2}^+$ signature and the solid symbols are for the $\frac{7}{2}^+$ signature. The errors in the moment-of-inertia are smaller than the plotted points.

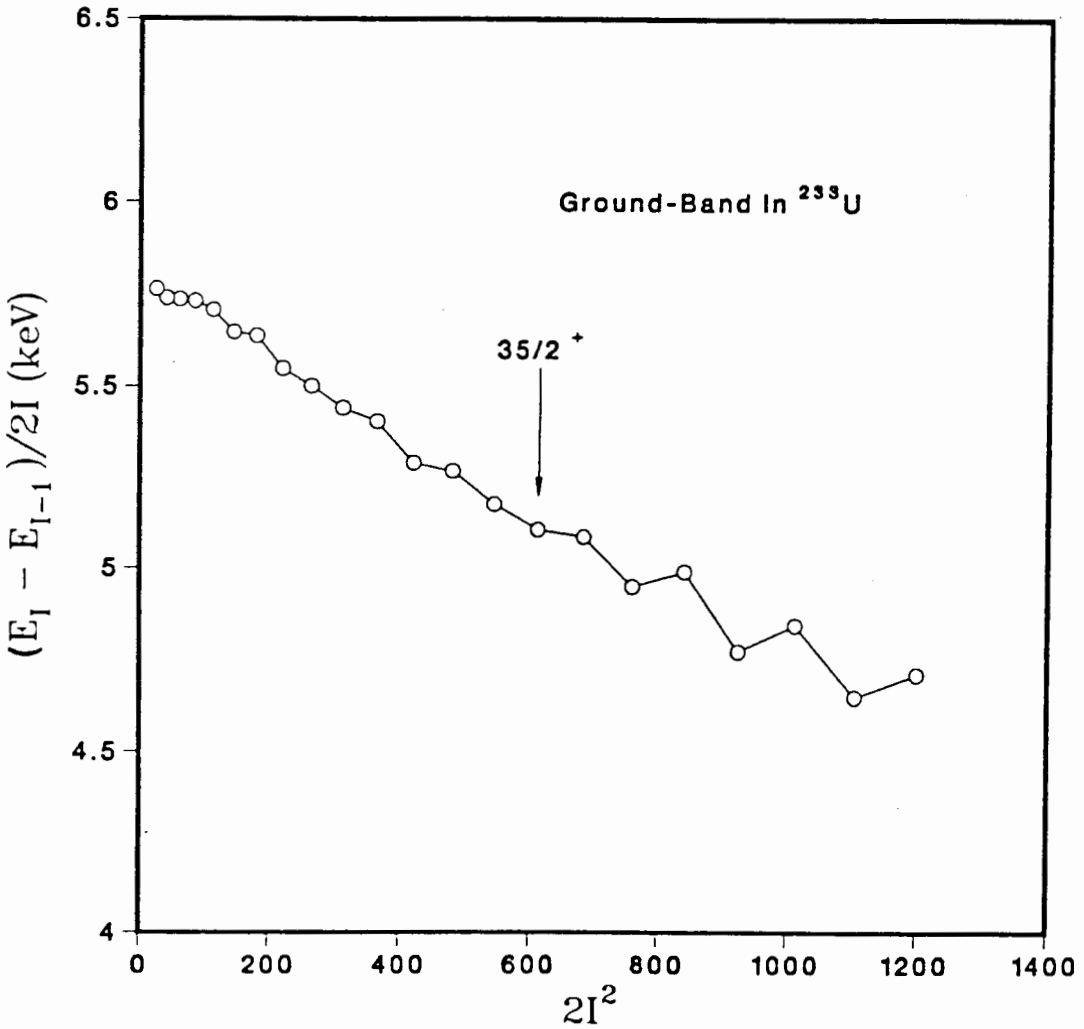

Figure 3.6: Plot of $\frac{E_I - E_{I-1}}{2I}$, the inverse moment-of-inertia $(\frac{\hbar^2}{2\mathcal{J}^{(1)}})$ for $\Delta I = 1$ transitions, vs. $2I^2$ showing the magnitude of the staggering term.

decreases by a factor of two from $\gamma = 0°$ to $\gamma = -60°$ (see their Figure 1). Thus, a small amount of triaxiality may be important in interpreting the change in the moment-of-inertia. In addition, the rotational level spacings appear to be very regular (see Figure 3.4), and the plot of the inverse moment-of-inertia ($\hbar^2/(2\Im^{(1)})$) for $\Delta I = 1$ transitions vs. $2I^2$, as shown in Figure 3.6, indicates the staggering term is small. However, on closer examination of Figure 3.6, it appears that the stagger reverses in sense part way up the rotational ground-state band (at about spin $\frac{35}{2}^+$). Additionally, in Figure 3.5 there is a change in slope of the $\Im^{(2)}$ plot in the same region ($\sim \frac{37}{2}^+$). This spin is only about $\frac{2}{3}$ that of the predicted position of band crossings for neighboring even-even nuclei. These subtler features are perhaps indicating a soft band crossing or strong band mixing.

A single-particle level Nilsson calculation using P. Möller's code PEMOM [50] shows the ground-state configuration of the odd neutron to be $\frac{5}{2}[633]$ (standing for the usual asymptotic quantum numbers $K[Nn_z\Lambda]$) derived from the $\nu 2g\frac{9}{2}$ orbital mainly. A series of Cranking calculations using RSM [51] were then performed to study the neutron configuration as a function of spin. The Cranking model is well known and was not developed or modified in this thesis. A more complete discussion of Cranking can be found elsewhere

[52]. In this thesis the basis used is indicated in Table 3.2 with a core of 32 protons and 50 neutrons. The quadrupole and hexadecapole deformations, β_2

Table 3.2: Orbitals used as basis for Cranking model calculations

neutrons

$\pi = +$	$1i\frac{11}{2}, 1i\frac{13}{2}, 2g\frac{7}{2}, 2g\frac{9}{2}, 3d\frac{3}{2}, 3d\frac{5}{2}, 4s\frac{1}{2}$
$\pi = -$	$1j\frac{13}{2}, 1j\frac{15}{2}, 2h\frac{11}{2}, 2f\frac{5}{2}, 3p\frac{1}{2}, 3p\frac{3}{2}$

protons

$\pi = +$	$1i\frac{11}{2}, 1i\frac{13}{2}, 2d\frac{3}{2}, 3s\frac{1}{2}$
$\pi = -$	$1h\frac{9}{2}, 1h\frac{11}{2}, 2f\frac{5}{2}, 2f\frac{7}{2}, 3p\frac{1}{2}, 3p\frac{3}{2}$

and β_4, the pairing gap parameters, Δ_n and Δ_p, and the chemical potentials, λ_n and λ_p, were fixed at angular momentum zero, $\omega = 0$, at the values of Kumar and Baranger [53]. The deformations and pairing parameters were kept fixed for all spins, but the chemical potential was allowed to vary. No number projection was done, because the number of valence particles is rather large compared to the number of core particles, λ does not vary much, and the need to pull particles from the core is minimal. Thus the total number of valence particles was kept correct on average. For each angular momentum,

the cranking frequency ω was determined by the usual cranking condition

$$\langle J \rangle + \omega \Im_c = [I(I+1)]^{-\frac{1}{2}} \tag{3.3}$$

where $\langle J \rangle$ is the angular momentum of the valence particles along the rotational axis and $\Im_c/\hbar^2 = 10$ MeV^{-1} is the moment-of-inertia of the core. Many calculations were performed to compare results when β, Δ, λ, and $\Im_c$ values were varied. Figure 3.7 presents the results for the standard Kumar and Baranger parameters ($\beta_2 = 0.240, \beta_4 = 0.142, \Delta_p = 0.900, \Delta_n = 0.680$) and for a case where $\beta_2 = 0.300$, as they reasonably well reproduced the first few energy level spacings of the ground rotational band. The fit at higher spins is not as satisfactory, perhaps because the deformation parameters were not allowed to vary as one goes up the band. The calculation with the increased β_2 tends to fit the lower spin region better, but again has the problem of too much alignment at higher spins. Other calculations were performed to try to fit the high-spin energy levels by increasing the deformation and pairing parameters and neglecting what happened at lower spins, but no satisfactory fit was obtained. The ground state configuration is mainly a mixture of $\frac{5}{2}$[633] (66%) and $\frac{5}{2}$[622] (20%) in agreement with the Nilsson calculation. However, at $I = \frac{49}{2}^+$, the configuration is mainly $\frac{1}{2}$[651] (41%), indicating alignment. Ta-

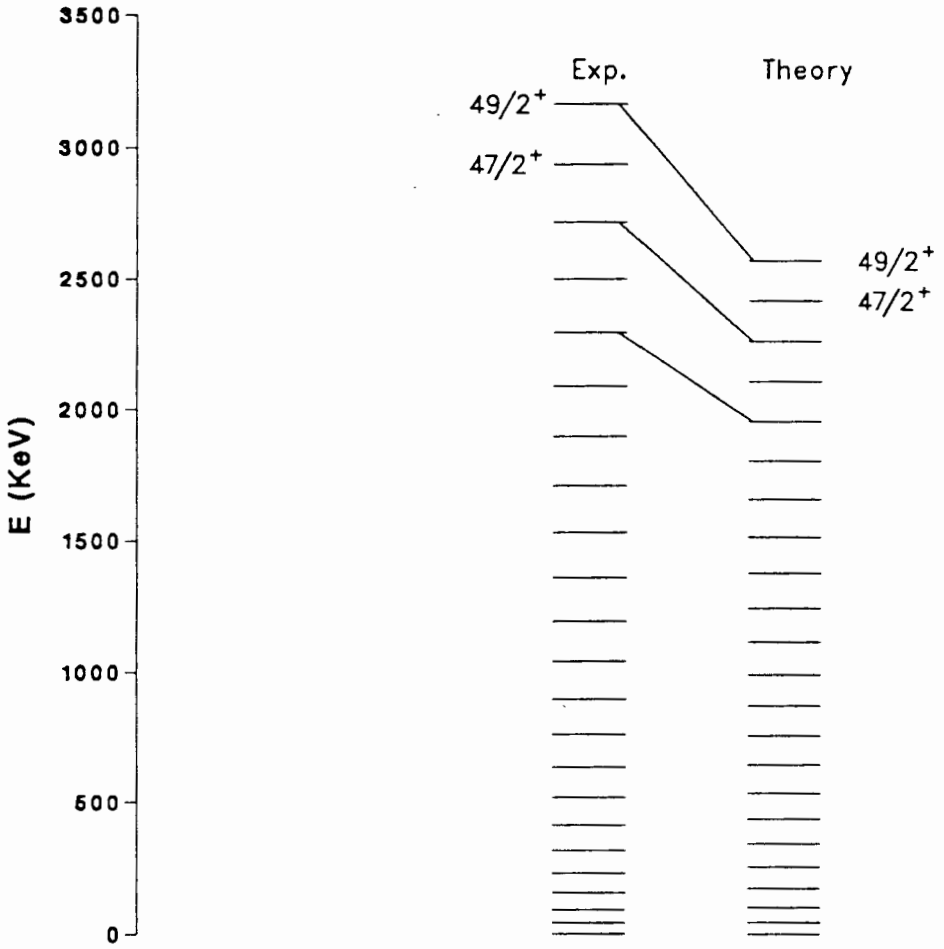

Figure 3.7: A comparison between experimental energy levels and theoretical energy levels for the ground rotational band in ^{233}U. The theoretical energy levels are calculated using the cranking model described in the text and the standard Kumar and Baranger parameters.

ble 3.3 shows the major portions of the wavefunctions (amplitude squared > 16%) as a function of spin. Alignment sets in for the theoretical calculations

Table 3.3: Main parts of the ground-state band wavefunction for ^{233}U in Cranking model

I^π	$K[Nn_z\Lambda]$	Prob.	I^π	$K[Nn_z\Lambda]$	Prob.
$\frac{5}{2}^+$	$\frac{5}{2}[633]$	0.197	$\frac{7}{2}^+$	$\frac{5}{2}[633]$	0.185
	$\frac{5}{2}[622]$	0.663		$\frac{5}{2}[622]$	0.613
$\frac{9}{2}^+$	$\frac{5}{2}[633]$	0.166	$\frac{11}{2}^+$	$\frac{5}{2}[622]$	0.466
	$\frac{5}{2}[622]$	0.543			
$\frac{13}{2}^+$	$\frac{5}{2}[622]$	0.398	$\frac{15}{2}^+$	$\frac{5}{2}[622]$	0.345
				$\frac{1}{2}[651]$	0.195
$\frac{17}{2}^+$	$\frac{5}{2}[622]$	0.301	$\frac{19}{2}^+$	$\frac{5}{2}[622]$	0.269
	$\frac{1}{2}[651]$	0.230		$\frac{1}{2}[651]$	0.260
$\frac{21}{2}^+$	$\frac{5}{2}[622]$	0.242	$\frac{23}{2}^+$	$\frac{5}{2}[622]$	0.221
	$\frac{1}{2}[651]$	0.285		$\frac{1}{2}[651]$	0.307
$\frac{25}{2}^+$	$\frac{5}{2}[622]$	0.203	$\frac{27}{2}^+$	$\frac{5}{2}[622]$	0.187
	$\frac{1}{2}[651]$	0.326		$\frac{1}{2}[651]$	0.342
$\frac{29}{2}^+$	$\frac{5}{2}[622]$	0.175	$\frac{31}{2}^+$	$\frac{5}{2}[622]$	0.162
	$\frac{1}{2}[651]$	0.355		$\frac{1}{2}[651]$	0.367
$\frac{33}{2}^+$	$\frac{1}{2}[651]$	0.378	$\frac{35}{2}^+$	$\frac{1}{2}[651]$	0.387
$\frac{37}{2}^+$	$\frac{1}{2}[651]$	0.393	$\frac{39}{2}^+$	$\frac{1}{2}[651]$	0.399
$\frac{41}{2}^+$	$\frac{1}{2}[651]$	0.404	$\frac{43}{2}^+$	$\frac{1}{2}[651]$	0.407
$\frac{45}{2}^+$	$\frac{1}{2}[651]$	0.411	$\frac{47}{2}^+$	$\frac{1}{2}[651]$	0.412
$\frac{49}{2}^+$	$\frac{1}{2}[651]$	0.413			

around $I = \frac{21}{2}^+$ (here the $\frac{1}{2}[651]$ orbital becomes dominant).

As can be seen in Figure 3.8, the aligned angular momentum extracted from the calculation is much greater than experimentally observed, a problem with

some calculations with the cranking model. As the experimental data indicate rather small alignment varying smoothly at higher spins, a calculation was performed to suppress band crossings (or similarly a change in the character of the band). Increasing Δ enlarges the gap between orbitals. Letting $\Im_c/\hbar^2 =$ 50 MeV^{-1} reduces the amount of angular momentum carried by the valence particles, thus weakening the interactions between the orbitals. Both effects should conspire to suppress band crossings. Increasing Δ and $\Im_c$ changes the $I = \frac{5}{2}^+$ configuration to 17% $\frac{1}{2}[640], 35\%$ $\frac{1}{2}[651]$, and 21% $\frac{1}{2}[600]$, a configuration with a small amount of angular momentum carried by the odd-neutron. It should be noted that the $K = \frac{1}{2}$ character of these lower spin states in this particular calculation is exactly as observed in the rotational band fits below, and it is the source of the staggering terms found essential in the fitting schemes. At $I = \frac{49}{2}^+$, the configuration is 17% $\frac{1}{2}[651], 17\%$ $\frac{3}{2}[651]$, and 23% $\frac{3}{2}[642]$ indicating a band crossing, a feature that is persistent in all calculations. Since the cranking model does not fit the experimental energy levels very well, other rotational band fitting methods are presented below.

It has long been known that in the perturbation limit the effect of Coriolis band mixing ($K \neq \frac{1}{2}$) in odd-A deformed nuclei is to renormalize the moment-of-inertia, while leaving the $I(I+1)$ level spacing form unchanged. In the

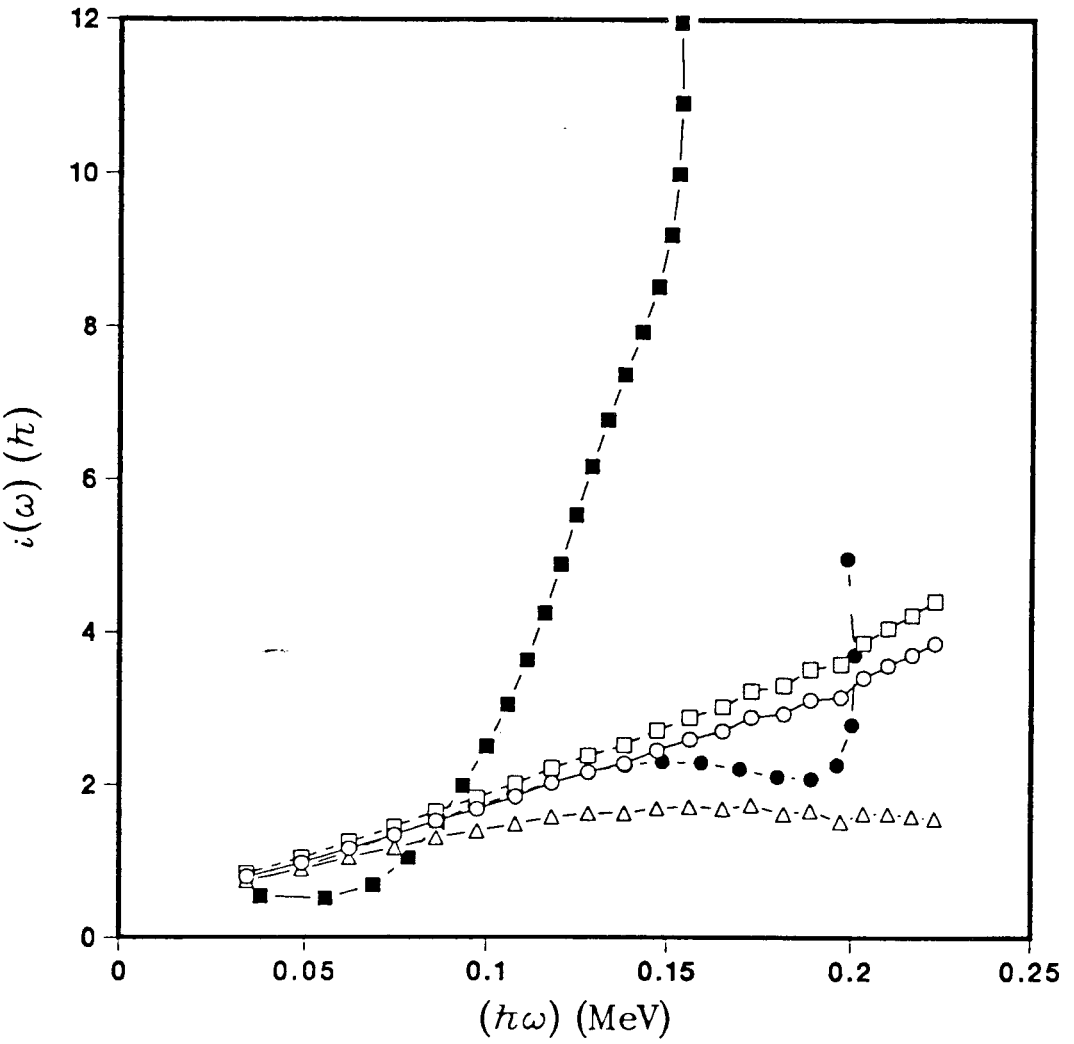

Figure 3.8: A comparison of extracted aligned angular momentum for the ground rotational band in ^{233}U between experiment and cranking model calculations. The open symbols are the experimental values derived from the three reference states discussed in the text (o is average of ^{232}U and ^{236}U, open squares is ^{236}U, and open triangles is ^{234}U). The closed symbols are cranking model calculations using the standard parameters given in the text (closed squares) and increased β_2 parameter (•).

other limit of two-band Coriolis mixing matrix elements large compared to zero order band separation, we get a constant aligned spin, i_α,

$$E(I) = \frac{\hbar^2}{2\Im}(I - i_\alpha)^2, \tag{3.4}$$

with i_α = intrinsic mixing matrix element $\langle K+1 \mid j_x \mid K \rangle$. The aligned spin formulation is equivalent to the introduction of a linear I term into the power series expansion for energy levels. We extract i_α using the method of Bengtsson and Frauendorf [54]. The projection of the total angular momentum on the axis of rotation is given by

$$I^x(I) = \sqrt{(I + \frac{1}{2})^2 - K^2} \tag{3.5}$$

where K is the projection of I on the symmetry axis. The cranking frequency is determined by

$$\omega(I) = \frac{E(I+1) - E(I-1)}{I^x(I+1) - I^x(I-1)}. \tag{3.6}$$

The aligned angular momentum is then

$$i_\alpha(\omega) = I^x(\omega) - I^x_{ref}(\omega), \tag{3.7}$$

where the reference

$$I^x_{ref}(\omega) = \omega\Im_0 + \omega^3\Im_1, \tag{3.8}$$

and $\Im_0$ and $\Im_1$ are determined from nearest even-even neighbors. For the results presented in Figure 3.8, three reference states are chosen. The first reference state has $\Im_0$ and $\Im_1$ taken from the weighted average of ^{232}U and ^{236}U (^{234}U was excluded as $\Im_1$ is at a local maximum in that nucleus), and are $67.2\hbar^2/\mathrm{MeV}$ and $448\hbar^4/\mathrm{MeV}^3$, respectively. The other two reference states have moments-of-inertia taken from ^{234}U ($\Im_0 = 68.4\hbar^2/\mathrm{MeV}, \Im_1 = 630\hbar^4/\mathrm{MeV}^3$) and ^{236}U ($\Im_0 = 65.9\hbar^2/\mathrm{MeV}$, $\Im_1 = 425\hbar^4/\mathrm{MeV}^3$) only. Figure 3.8 shows that the aligned angular momentum is a rather smoothly increasing as a function of spin. The rather sudden alignment observed in ^{238}U and ^{235}U in Ref. [53] is not observed here. As can be seen, the average of ^{232}U and ^{236}U is very similar to ^{236}U only as reference. The ^{234}U has a significant difference at high spins, where i_α saturates, due to the fact that ^{234}U is known to have a lot of neutron S-band character. This suggests that perhaps at high spins in ^{233}U, there is a lot of neutron S-band character that isn't present at lower spins. The cranking calculation tends to overestimate the amount of aligned angular momentum.

Clearly the aligned angular momentum is not constant; thus, the simple limiting case of equation (3.4) is not valid. Our rotational band fitting scheme was then guided by attempts to fit to the simple limiting case (see equation (3.9) below) and then to fit the more complex intermediate cases, using semi-

empirically derived fitting functions.

Rotational band fitting was more difficult than initially expected. Initial attempts to fit the band with:

$$E = a_0 + \sum_{i=1}^{\infty} a_i [I(I+1) - K^2]^{i/2}. \tag{3.9}$$

and doing separate fits to the two signatures to avoid explicit introduction of a staggering term related to Coriolis interaction with "anomalous" $K = \frac{1}{2}$ bands, proved to be unsatisfactory in dealing with this reversing of the stagger previously noted. Fits were then attempted using explicitly introduced staggering terms and functions of the form:

$$E(I) = D + \sum_{i=odd} A_i I^i + \sum_j B_j [I(I+1)]^j + (-1)^{I+\frac{5}{2}} C_{\frac{5}{2}} \frac{(I+\frac{5}{2})!}{(I-\frac{5}{2})!} \tag{3.10}$$

where $A_i, B_j, C_{\frac{5}{2}}$, and D are the fitted parameters, and the $C_{\frac{5}{2}}$ term is a staggering term between the two signatures ($K = \frac{5}{2}$ band). The residuals of fits of this form were fairly good at the high end of the band, but systematically in error at the low end. Also, the fits did indicate that the staggering term was quite small, as previously noted from examination of Figure 3.5. Nevertheless, even though the overall fit quality was acceptable, satisfactory explanation of the reversing of the stagger was missing, and a more complex fitting function

was postulated:

$$
\begin{aligned}
E(I) &= D + B_1[I(I+1)] + A_1 I[1 - \exp\{\frac{-(I+1)}{I_d}\}] \\
&+ A_3 I^2(I+1)[1 - \exp\{\frac{-(I+1)}{I_d}\}] + B_{S1}(-1)^{I-\frac{1}{2}}\frac{(I+\frac{5}{2})!}{(I-\frac{5}{2})!} \\
&+ B_{S2}(-1)^{I-\frac{1}{2}}[1 - \exp\{\frac{-(I+\frac{5}{2})(I-\frac{3}{2})}{I_d^2}\}]\frac{(I+\frac{3}{2})!}{(I-\frac{3}{2})!} \qquad (3.11)
\end{aligned}
$$

where $B_1, A_1, A_3, B_{S1}, B_{S2}$, and D are the fitted parameters, and like terms in equation (3.10) have the same coefficients in equation (3.11). I_d is some critical spin where the Coriolis mixing tends to become more important (at low spins, the A_1 and A_3 terms become smaller as the Coriolis mixing is less). As can be seen in equation (3.11), consistent with our formulation of Coriolis band mixing in the perturbation limit, there is an $I(I+1)$ term. The A_1 term is analogous to the introduction of the linear I term in the power series from inclusion of i_α, and A_3 is the I^3 term. Both A_1 and A_3 have exponential factors modifying them so that they have the proper low-spin limiting form of $[I(I+1)]^n$. B_{S1} and B_{S2} are staggering terms introduced from higher order coupling into two $K = \frac{1}{2}$ bands with opposite-sign decoupling constants. It is the competition between these two terms that could fit the reversing of the stagger noted in Figure 3.5.

Equations (3.9), (3.10), and (3.11) were all used to attempt to fit the

rotational band – totaling about 25 fits. The results of the fits from equation (3.10) and equation (3.11) are presented in Table 3.4. As can be seen, the

Table 3.4: ^{233}U rotational band fit parameters (keV)

Eq. (3.10)	D	A_1	A_3	B_1	B_2 ($\times 10^5$)	$C_{\frac{5}{2}}$ ($\times 10^7$)	χ^2_ν †
1	−46.29	−3.51	−0.05	6.39	−4.8	−2.3	0.114
2	−45.15	−4.01	−0.05	6.45	—	−2.2	0.109
3	−46.81	−3.46	−0.05	6.40	—	—	0.724
Eq. (3.11)	D	A_1	A_3	B_1	B_{S1} ($\times 10^7$)	B_{S2} ($\times 10^5$)	χ^2_ν †
4	−49.99	−5.55	−0.05	6.61	−1.84	2.29	0.110
5	−50.09	−5.47	−0.05	6.60	—	11.7	0.119
6	−49.97	−5.57	−0.05	6.61	−2.27	—	0.105
7	−50.62	−5.05	−0.05	6.57	—	—	0.707

† χ^2 per degree of freedom assuming standard deviations on energies from Table 3.1; that the χ^2_ν values are much less than unity indicates that the standard deviations on the energy levels are too conservative for the energy level differences governing the fitting

fits using equation (3.11) were marginally better (χ^2_ν is slightly lower). The significance of B_{S1} and B_{S2} were tested. We did not include I_d explicitly for variation, as that makes the least squares non-linear. Fittings were tried for values of I_d of 3.5 and 4.5, chosen by inspection of Figure 3.6. The latter value gave lower χ^2_ν.

The fit results indicate that B_{S1} and B_{S2} do indeed have opposite signs.

The apparent reversal of the staggering pattern in the ^{233}U ground-state band gives an interesting clue to the underlying Coriolis band mixing and its dependence on spin. Staggering, the energy shift between the different signature groups in a band, may be attributed to Coriolis coupling in some order to $K = \frac{1}{2}$ excited bands, which have the decoupling term giving staggering in lowest order. Bohr and Mottelson [55] give a power-series expression for the staggering term in a band of any K. For $K = \frac{3}{2}$ the staggering energy term is from a second-order perturbation; for $K = \frac{5}{2}$, from fourth-order; for $K = \frac{7}{2}$, from sixth-order; etc. We wish to address the problem at higher spins, where the perturbation theory form must be modified. Tri-axiality (gamma deformation) can couple the $\frac{5}{2}$ band with $\frac{1}{2}$ bands in first order. Hence, the staggering term may be a clue to gamma deformation.

In the case of two Coriolis-mixed bands with $K \neq 0$ it is well-known that at the low spin perturbation limit the $I(I+1)$ spacing is not altered but only the moments-of-inertia are renormalized. In the high-spin limit of Coriolis matrix elements large compared to the band separation, we get the aligned coupling expression with energies of equation (3.4), with the aligned angular momentum i_α equal to the perpendicular component of the odd-particle total

angular momentum,

$$i_\alpha = \sqrt{[j(j+1) - \Omega(\Omega+1)]}. \tag{3.12}$$

The aligned limiting expression has a linear term in spin I, as well as the quadratic term. This suggests that band energy fitting expressions need odd powers of I at higher spins but should have only even powers of I [or powers of $I(I+1)$] at lowest spin. This problem became apparent to us in examining the residual errors from band fitting with expressions including a linear I term.

The two-band mixing energies are analytical solutions of the quadratic equation from diagonalization of the 2×2 matrices. Fitting with such expressions has been done using non-linear least squares [56].

For analyzing the ^{233}U band power series we choose a slightly different approach, guided by the above experience. By inserting a factor $[1 - \exp(I/I_d)]$ in front of the odd-powered spin terms, we get the desired behavior of only even powers in the expansion at the low end of the band, and the odd powers that go with aligned spin at the higher angular momenta. The problem of band fitting then becomes non-linear in the term I_d, but it is still easy to use, with terms that have physical significance. We may identify I_d with that spin at which the Coriolis matrix element of the leading band coupling becomes

equal to the band separation. A more complete discussion of odd-A band fitting can be found in reference [57].

How does this apply to the staggering terms? It suggests that in addition to the Bohr-Mottelson perturbation term there might be terms with the above exponential factors to give the lower-power dependence at higher spins, where some Coriolis band coupling saturates. For a unique-parity orbital within a shell there will be only one $K = \frac{1}{2}$ band within the shell to which it can Coriolis-couple. Thus, we would expect in such cases that the sense of staggering would be of a single sign. In the ^{233}U case, the ground-state band of $K = \frac{5}{2}^+$ is a normal-parity orbital, and there are several $K = \frac{1}{2}$ bands within the shell available for Coriolis coupling, bands which have decoupling parameters of either sign. Consider a near-lying $K = \frac{1}{2}$ band with weak Coriolis coupling down to ground and a higher-lying $K = \frac{1}{2}$ band with strong Coriolis coupling and opposite sign decoupling parameters. The lower band would dominate the staggering term at lower spin because of the smaller energy denominators in the perturbation expression, but at higher spin it would saturate, and the higher-lying band coupling would dominate. ^{164}Er is a nucleus in which both positive and negative parity bands exhibit a reversal of staggering [58].

Quasiparticle (single particle) energy levels (Routhians) were extracted

from the ^{233}U ground-state band energy levels using the standard methods of Bengtsson and Frauendorf [59]. The Routhian is defined as:

$$e' = E'(A,\omega) + \Delta - \frac{1}{2}\left[E'_{ref}(A+1,\omega) + E'_{ref}(A-1,\omega)\right], \tag{3.13}$$

where $E'(A,\omega)$ is given by:

$$E'(A,\omega) = E'(I) = \frac{1}{2}\left(E(I+1) + E(I-1)\right) - \omega(I)I_x(I), \tag{3.14}$$

$I_x(I)$ is expressed by:

$$I_x(I) = \sqrt{(I+\frac{1}{2})^2 - K^2}, \tag{3.15}$$

and $\omega(I)$ is:

$$\omega(I) = \frac{E(I+1) - E(I-1)}{I_x(I+1) - I_x(I-1)}. \tag{3.16}$$

The pairing gap parameter, Δ, is chosen in the standard way where:

$$\Delta = 0.12\hbar\omega_o \tag{3.17}$$

and $\hbar\omega_o = \frac{41}{A^{\frac{1}{3}}}$. The reference state is chosen as an average of neighboring even-even nuclei.

$$E'_{ref} = -\frac{1}{2}\omega^2\Im_0 - \frac{1}{4}\omega^4\Im_1 + \frac{1}{8}\hbar^2/\Im_0 \tag{3.18}$$

Figure 3.9 shows the experimental Routhians, e', as a function of $\hbar\omega$ for three sets of reference states, (1) ^{232}U and ^{234}U averaged, (2) ^{232}U only, and

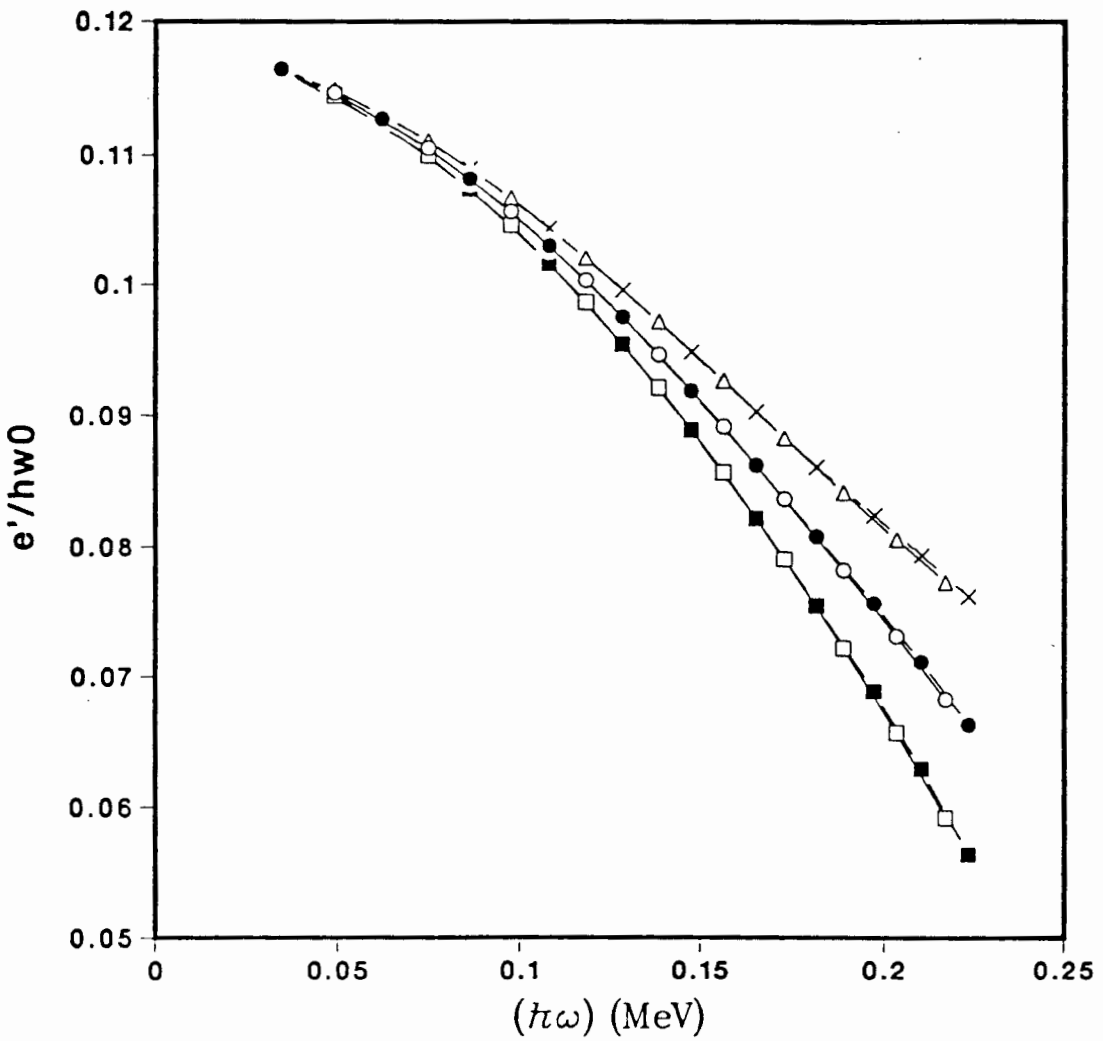

Figure 3.9: Experimental Routhians for the ground-state band in ^{233}U. The open symbols are for the $\frac{5}{2}^+$ signature and the closed symbols and X's are for the $\frac{7}{2}^+$ signature. Three reference states are shown: (1) ^{232}U and ^{234}U (open circles and •), (2) ^{232}U only (open and closed squares), and (3) ^{234}U only (open triangles and X's). The choice of reference states does not affect the results much.

(3) ^{234}U only. The Routhians, for all cases, decrease smoothly with increasing ω, and both the favored and unfavored signature of the band tend to lie on one curve. This is consistent with the minimal signature splitting noted previously.

Another cranking calculation was performed to examine the single particle levels. Figure 3.10 shows e' as a function of $\hbar\omega$ for a calculation with $N = 5, 6, 7$ neutron oscillator shells as a basis. At $\hbar\omega = 0$, the level at $e'/\hbar\omega_o = 0.1$ is the $\frac{5}{2}^+[633]$ ground state. The first excited level is the $\frac{1}{2}^+[631]$ and the second excited level is the intruder state $\frac{7}{2}^-$. Several interesting things should be noted. Firstly, the ground-state band $\frac{5}{2}^+$ level exhibits very little signature splitting, even at moderately high spins ($\hbar\omega/\hbar\omega_o = 0.03$). Secondly, the excited $\frac{1}{2}^+$ band does exhibit much stronger signature splitting at high spins as is expected. Additionally, it appears as if one signature of the $\frac{1}{2}^+$ band crosses both signatures of the $\frac{5}{2}^+$ band. This band crossing occurs at approximately the spin where the anomaly was noted in the moment-of-inertia figures, and would validate the explanation given above regarding the influence of the $K = \frac{1}{2}$ bands on the signature splitting. Please note, that at higher ω, one signature of the $K = \frac{1}{2}^+$ band is above and one below the $K = \frac{5}{2}^+$ band (both signatures). Finally, however, note that this still does not completely explain the data. No reversal of staggering, as indicated by a crossing of

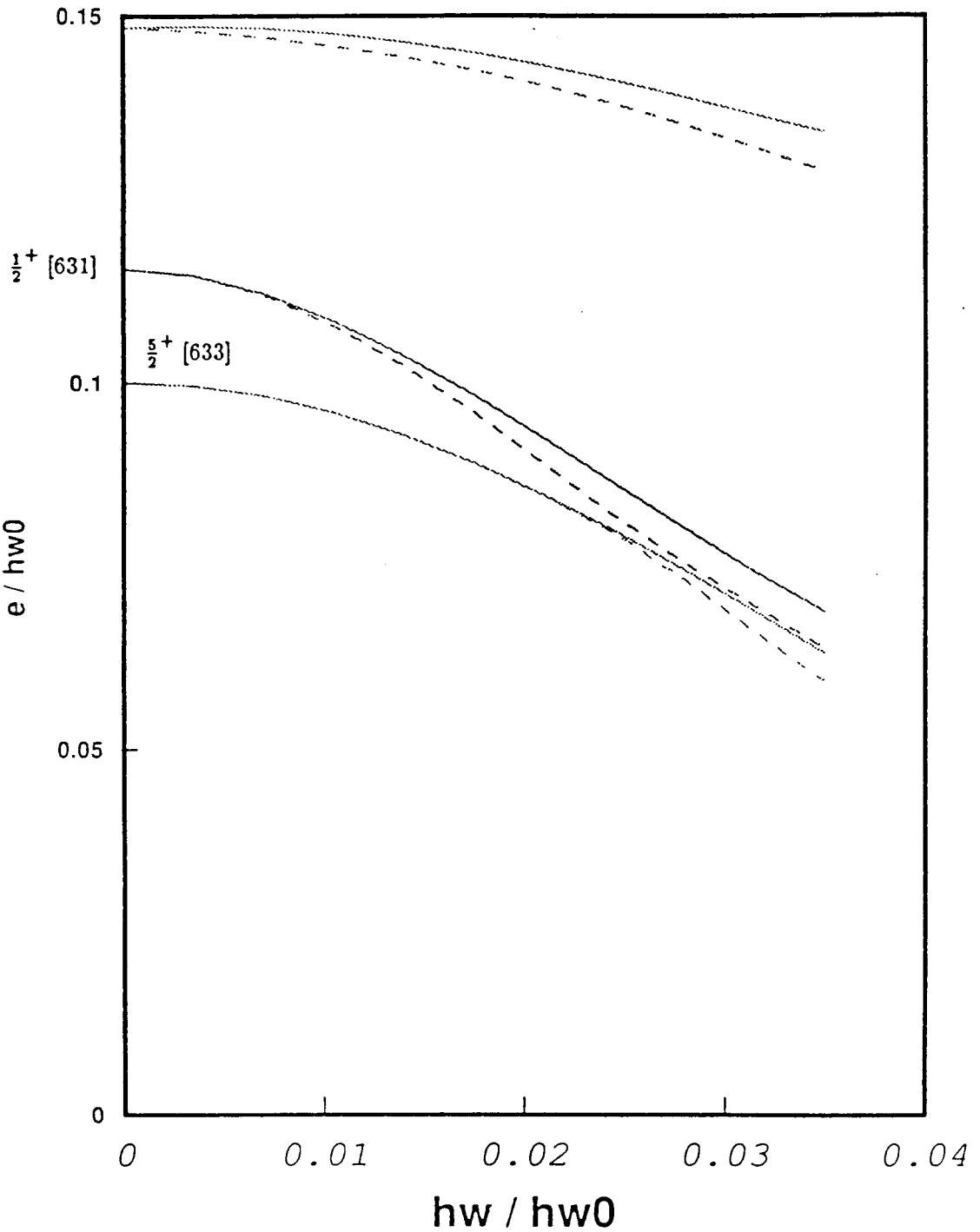

Figure 3.10: Routhians from cranking calculation for the ground-state band in ^{233}U. The lowest level at $\hbar\omega = 0$ is the $\frac{5}{2}^+$ ground state, the next excited level is the $\frac{1}{2}^+$ band. The $\frac{7}{2}^-$ intruder level has been removed for clarity. The favored signatures are the solid curves and the unfavored signatures are the dashed lines.

signatures in a band, is observed.

Recently, however, signature splitting reversals have been explained by invoking γ-deformation or triaxial nuclear shapes [60]. Hamamoto shows for the $j = \frac{13}{2}$ shell in the rare-earths that for $\gamma = 0°$, the single particle levels just exhibit the normal splitting of favored and unfavored signatures (her Figure 1a), but for $\gamma = +20°$ (her Figure 2a), the signatures cross $K - \frac{1}{2}$ times as a function of increasing ω. Thus, a cranking calculation with a slight γ-deformation was performed. The results are shown in Figure 3.11 for a case where $\gamma = 3°$ (small γ-deformation) and $N = 5, 6$ neutrons are included. Again, at $\hbar\omega = 0$ the ground-state level is the $\frac{5}{2}^+[633]$, and the first excited state is the $\frac{1}{2}^+$ level. A larger signature splitting is observed for the $\frac{1}{2}^+$ band at higher spins, as would be expected. However, several interesting differences occur. Firstly, the size of the splitting of signatures in the $\frac{5}{2}^+$ band, while still small, is larger than that for the case of no γ-deformation. Secondly, the negative signature of the $\frac{1}{2}^+$ band interacts strongly (and repels) the negative signature of the $\frac{5}{2}^+$ ground-state band in the spin region where the anomalies in the moment-of-inertia were noted. In addition, there is no band crossing, but certainly a band interaction which must result in the change of character

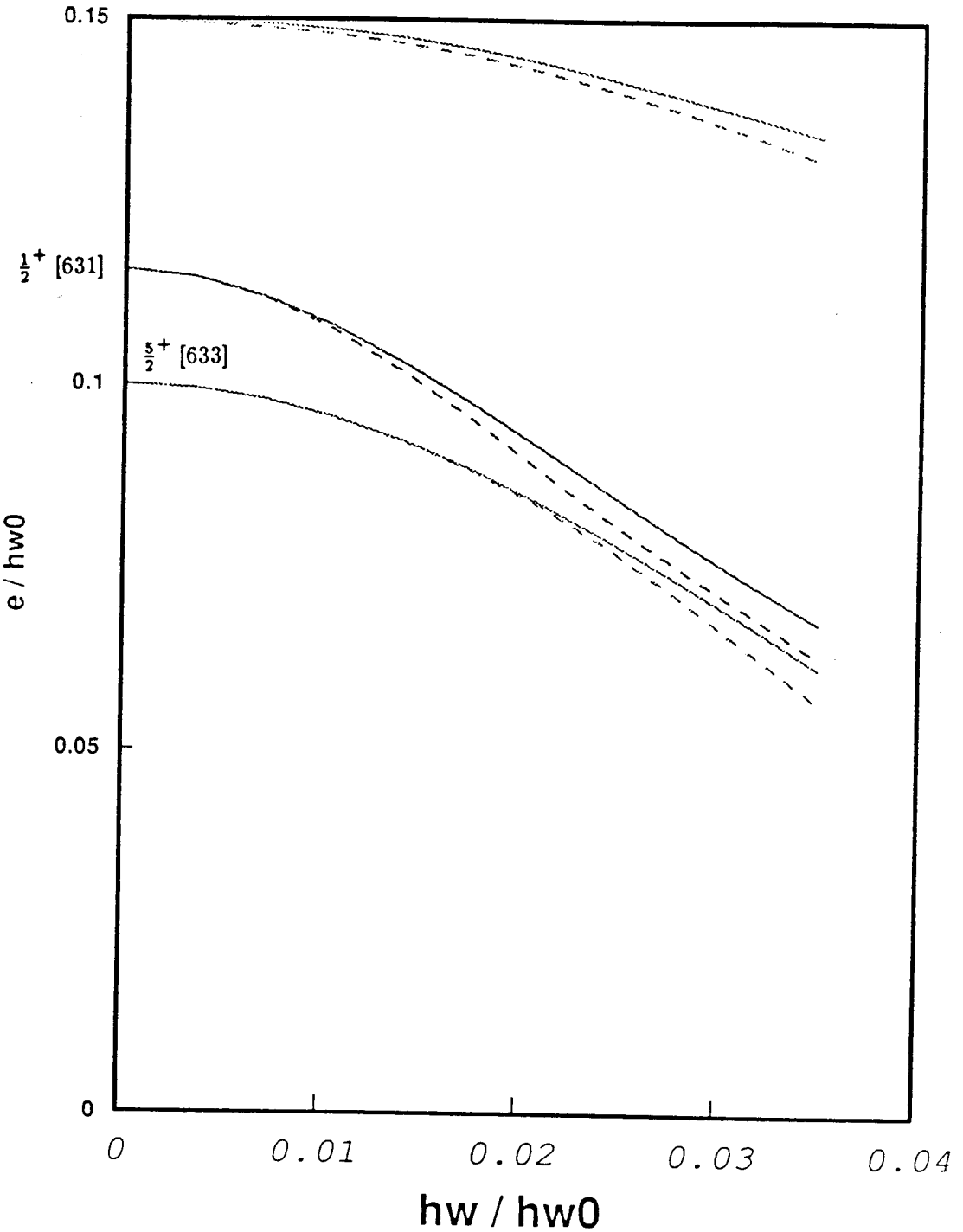

Figure 3.11: Routhians from cranking calculation for the ground-state band in ^{233}U including a slight γ-deformation. The levels and symbols are the same as in Figure 3.10.

of the $\frac{5}{2}^+$ band. Finally, at slightly higher spins, the favored and unfavored signatures of the $K = \frac{5}{2}^+$ band cross, indicating a reversal of the staggering. This is in qualitative agreement with the data.

In conclusion, it seems that a slight triaxial shape deformation explains the anomalies in the moment-of-inertia and the reversal of staggering in the ground-state band in ^{233}U. It might also explain the g-factor information presented below. While none of the experimental evidence is overwhelming, this difficult-to-fit nucleus with these subtle effects seem to be best explained by a slight triaxiality induced at higher spins.

E0 transitions between $K^\pi = 0^+$ bands in ^{232}U, ^{234}U, and ^{236}U have been measured by others [61]. The E0 transition energies between an excited $K = 0$ rotational band and the ground-state band in ^{232}U show the bands to be converging slightly with increasing spin (about 63 keV closer at spin 10^+ than at spin 0^+). However, in ^{234}U the excited-band and the ground-state band are more parallel (only 14 keV closer) indicating no real evidence for bandcrossing at these lower spins. Nevertheless, if the bands interact strongly, band crossings are difficult to detect (there is no sharp change in the level spacings). Recent experiments [62] studying the heavy-ion, one-neutron transfer reaction

product ^{234}U do indicate a possible band crossing in ^{234}U at about spin 20^+, that is, near the same spin region as the $\Im^{(2)}$ irregularity noted above in ^{233}U. These data further support the theoretical interpretation extracted from the Routhians.

Additional information can be obtained from the lower energy Coulomb excitation experiment with ^{58}Ni projectiles. Several lower energy cascade transitions were observed, besides the dominant E2 crossovers. The transition rates for gamma decay can be expressed in terms of the reduced transition probabilities [63]):

$$W(M1) = 1.71 \times 10^{13}(E_\gamma)^3 B(M1)\,\mathrm{sec}^{-1} \tag{3.19}$$

$$W(E2) = 1.23 \times 10^{13}(E_\gamma)^5 B(E2)\,\mathrm{sec}^{-1}, \tag{3.20}$$

where E_γ is in MeV. The cascade-to-crossover photon intensity ratio is given by:

$$\frac{I_c}{I_x} = \frac{W(M1) + W(E2; I \rightarrow I-1)}{W(E2; I \rightarrow I-2)} \tag{3.21}$$

where

I_c = intensity of cascade γ-ray

I_x = intensity of crossover γ-ray.

The reduced transition probability B(M1) is given by [64]:

$$B(M1) = \frac{I_0^2}{4.19}\langle I\ 1\ K\ 0 \mid I\ 1\ I-1\ K\rangle^2 (g_\Omega - g_R)^2 \tag{3.22}$$

where

g_Ω = g-factor of odd neutron

g_R = g-factor of core

I_0 = ground-state spin ($\frac{5}{2}^+$ for ^{233}U)

I = spin of nucleus

K = projection of spin on symmetry axis

$\langle\ \mid\ \rangle^2$ = square of the Clebsch-Gordan coefficient

and the reduced transition probabilities $B(E2; I \rightarrow I-1)$ and $B(E2; I \rightarrow I-2)$ are given by [65]:

$$B(E2; I \rightarrow I-1) = \frac{5}{16\pi} e^2 Q_0^2 \langle I\ 2\ K\ 0 \mid I\ 2\ I-1\ K\rangle^2 \tag{3.23}$$

$$B(E2; I \rightarrow I-2) = \frac{5}{16\pi} e^2 Q_0^2 \langle I\ 2\ K\ 0 \mid I\ 2\ I-2\ K\rangle^2 \tag{3.24}$$

where

Q_0 = intrinsic quadrupole moment.

Combining equations (3.19)-(3.24), a relationship relating gyromagnetic factors and the quadrupole moment to experimentally measured quantities can be obtained:

$$\left(\frac{g_\Omega - g_R}{Q_0}\right)^2 = \frac{0.4317}{I_0^2}\frac{\langle I\ 2\ K\ 0 \mid I\ 2\ I-2\ K\rangle^2}{\langle I\ 1\ K\ 0 \mid I\ 1\ I-1\ K\rangle^2} \cdot \left\{\frac{I_c}{I_x}\frac{E_x^5}{E_c^3} - E_c^2\frac{\langle I\ 2\ K\ 0 \mid I\ 2\ I-1\ K\rangle^2}{\langle I\ 2\ K\ 0 \mid I\ 2\ I-2\ K\rangle^2}\right\} \text{barns}^{-2} \quad (3.25)$$

where

E_x = Energy of crossover γ-ray

E_c = Energy of cascade γ-ray.

The magnetic moment μ can be related to the g-factors as follows [57]:

$$\mu = \frac{I_0^2}{I_0+1}g_\Omega + \frac{I_0}{I_0+1}g_R. \quad (3.26)$$

Cascade-to-crossover ratios for three low $\frac{M1}{E2}$ mixed transitions were determined, and if one assumes that Q_0 is relatively constant over this range of spins, then $g_\Omega - g_R$ can be extracted as one goes to higher spins. For ^{233}U, Q_0 =11.55 barns [66], $\mu = \pm 0.54$, and $I_0 = \frac{5}{2}^+$(ref. [67]). Table 3.5 gives complete results for indicated cascade-to-crossover ratios extracted from the data. The $\frac{17}{2}^+ \rightarrow \frac{15}{2}^+$ transition is masked by uranium X-rays; thus, its $\frac{I_c}{I_x}$ ratio is determined by a linear interpolation. The projected values of $\frac{I_c}{I_x}$ shown in Table 3.5 are derived from Clebsch-Gordan coefficients and the lowest mixing ratio as reference (the 40.35-keV $\frac{7}{2}^+ \rightarrow \frac{5}{2}^+$ transition which has $\frac{M1}{E2}$ ratio of 3.226) [ref. [68]]. The $(\frac{g_\Omega - g_R}{Q_0})^2$ value derived from projected $\frac{I_c}{I_x}$ ratios is

Table 3.5: Apparent g-factors deduced from cascade-to-crossover transition ratios for ^{233}U

$\frac{M1/E2}{E2}$ Ratio	$\frac{I_c}{I_x}$(proj.)	$\frac{I_c}{I_x}$(exp)	$(\frac{g_\Omega - g_R}{Q_0})^2$ ($\times 10^4$barns^{-2})	$\mid g_\Omega - g_R \mid$
$\frac{\frac{13}{2}^+ \to \frac{11}{2}^+}{\frac{13}{2}^+ \to \frac{9}{2}^+}$	0.18	0.28 ± 0.010	10.7 ± 0.46	0.38 ± 0.05
$\frac{\frac{15}{2}^+ \to \frac{13}{2}^+}{\frac{15}{2}^+ \to \frac{11}{2}^+}$	0.11	0.13 ± 0.013	7.05 ± 0.90	0.31 ± 0.05
$\frac{\frac{17}{2}^+ \to \frac{15}{2}^+}{\frac{17}{2}^+ \to \frac{13}{2}^+}$	0.09	$0.08 \pm 0.010^\dagger$	$5.60 \pm 0.50^\dagger$	$0.27 \pm 0.04^\dagger$
$\frac{\frac{19}{2}^+ \to \frac{17}{2}^+}{\frac{19}{2}^+ \to \frac{15}{2}^+}$	0.06	0.04 ± 0.005	3.10 ± 0.65	0.20 ± 0.03

† Cascade masked by uranium X-ray, $\frac{I_c}{I_x}$ obtained by interpolation

6.04×10^{-4} barns^{-2}. If one makes the assumption that the magnetic moment does not change as spin increases, one can extract individual g_Ω and g_R factors. However, the experimentally determined $(\frac{g_\Omega - g_R}{Q_0})^2$ ratios decrease rather strongly with increasing spin, implying that the effective values of $g_\Omega - g_R$, and thus the magnetic moment μ, vary with increasing spin. The simplest rotational theory estimates the rotational g-factor of the core to be just the ratio of protons to all nucleons, $g_R \simeq \frac{Z}{A} = 0.395$ for ^{233}U. The g-factors derived from the projected $\frac{I_c}{I_x}$ values are $g_\Omega = 0.13$ and $g_R = 0.42$. The changing experimental g-factors are indicative of Coriolis band mixing effects driving the increase in moment-of-inertia, as discussed above regarding the rotational band fits. The average g_R value is 0.42, slightly higher than simple theory

predicts, and the average g_Ω value is 0.13. Both g-factors are consistent with those derived and tabulated by Chasman et al. [69], $g_\Omega = 0.08$ and $g_R = 0.39$, and from projections using Clebsch-Gordan coefficients. The average value of $(\frac{g_\Omega - g_R}{Q_0})^2 = 6.61 \times 10^{-4}$ barns^{-2}, gives $\frac{g_\Omega - g_R}{Q_0} = 0.026$ barns^{-1}, which is three times larger than the value reported by Newton [70] of 0.008 for the lowest cascade-to-crossover ratio. As discussed above, the moments-of-inertia vary rather smoothly in this lower spin region, and it appears that the magnetic moment varies also.

3.3 ^{90}Zr + ^{239}Pu Reaction

The wealth of data on ^{239}Pu and ^{238}Pu will be discussed in this section. Figure 3.12 shows a total γ-ray spectrum for all 18 Ge detectors appropriately Doppler corrected. The spectrum is dominated by inelastic ^{239}Pu transitions and one-neutron transfer ^{238}Pu transitions. Very few fission events were observed. The neutron multiplicity for this reaction is shown in Figure 3.13. Events with $K_n = 0$ occurred 40% of the time. Events with $K_n = 1$ happened $\sim$ 25% of the time, and as clearly shown in Figure 3.13, events with higher neutron multiplicities were recorded ($K_n = 8$ occurred $\sim$ 1% of the time). These events

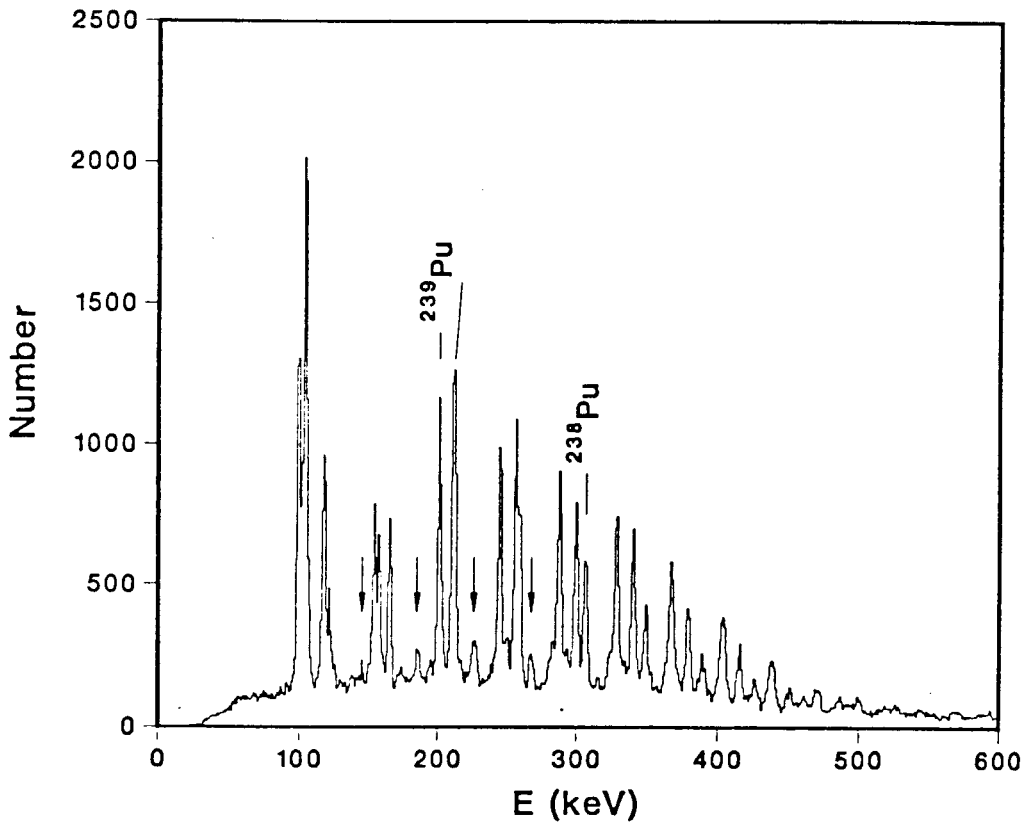

Figure 3.12: Total Ge γ-ray spectrum for the ^{90}Zr + ^{239}Pu reaction. Several ^{239}Pu peaks and one ^{238}Pu peak are marked. The peaks around 100 keV are due to Pu x-rays. Note the absence of fission background. The arrows mark the peak positions of the mystery band.

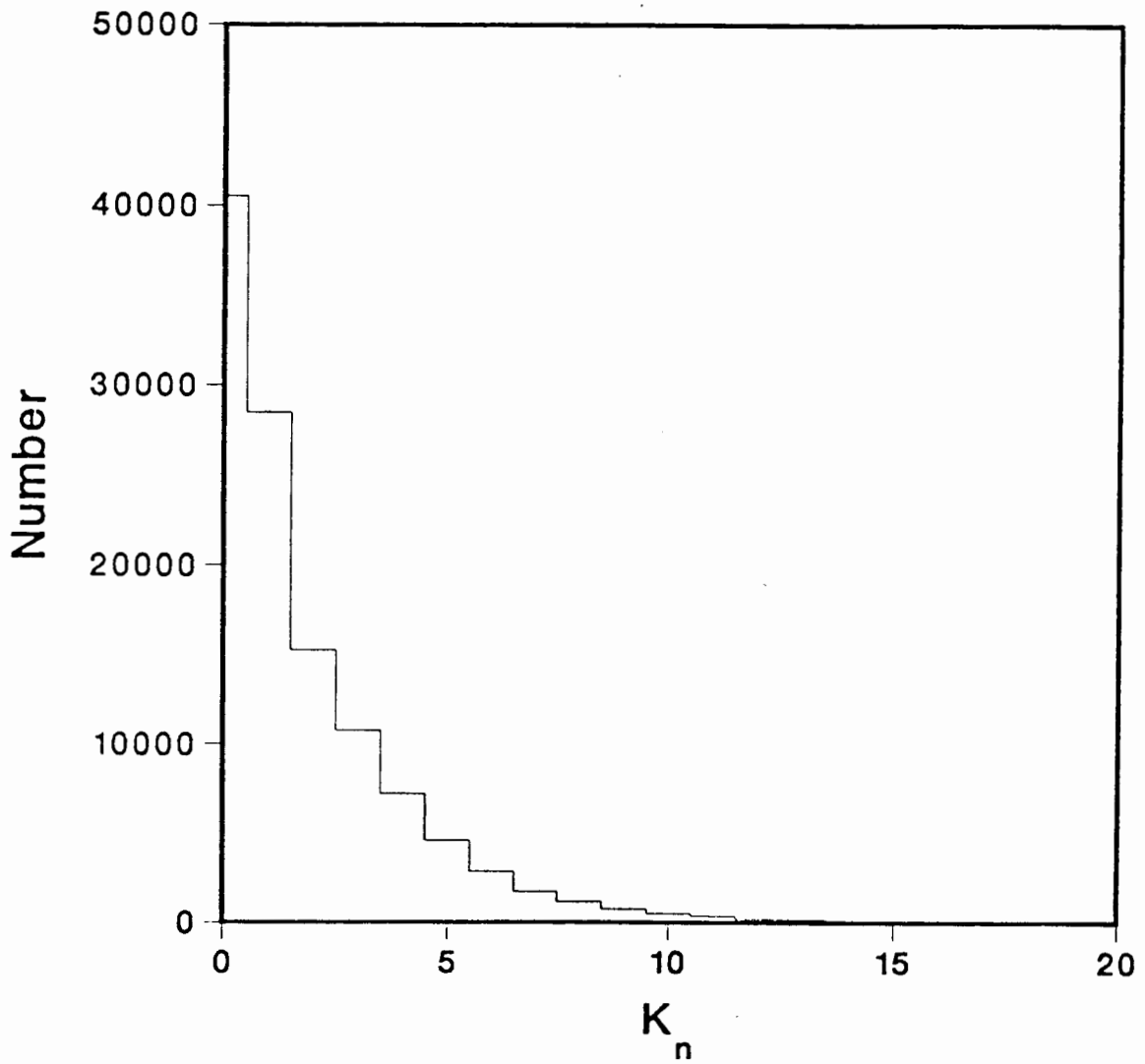

Figure 3.13: Neutron multiplicity for the $^{90}Zr + ^{239}Pu$ reaction.

are due to fission and neutron evaporation reactions, but a gate on $K_n = 0$ suppresses both neutron evaporation and fission. A series of mystery transitions is also observed in this spectrum (marked with arrows). These mystery transitions appear in a regularly spaced manner consistent with a rotational band with a similar dynamic moment-of-inertia as the ground rotational band in ^{238}Pu. They will be discussed further below.

Figure 3.14 shows a two-dimensional plot of the total γ- γ coincidence spectrum, $E_{\gamma 1}$ vs. $E_{\gamma 2}$. Dark spots indicate peak positions. The essential features of Figure 3.14 are as follows: (1) Peaks around 100 keV correspond to Pu x-rays, and are in coincidence with both ^{239}Pu and ^{238}Pu transitions, as well as themselves (multiple x-rays can be emitted per event); (2) The characteristic doublet of ^{239}Pu ground-state band transitions from both signatures is clearly observed (transitions appear like a doublet because staggering is so large); (3) ^{238}Pu transitions are clearly identifiable starting at the 307-keV $12^+ \rightarrow 10^+$ transition (lower ones are masked by ^{239}Pu peaks); (4) The 45° axis is devoid of peaks, as expected, because no particular γ-ray is in coincidence with itself; (5) The streaks between clear peaks are due to unsuppressed Compton scattering events; thus, the peaks sit on top of background ridges; (6) The mystery band mentioned previously can be clearly identified (see arrows); (7) The

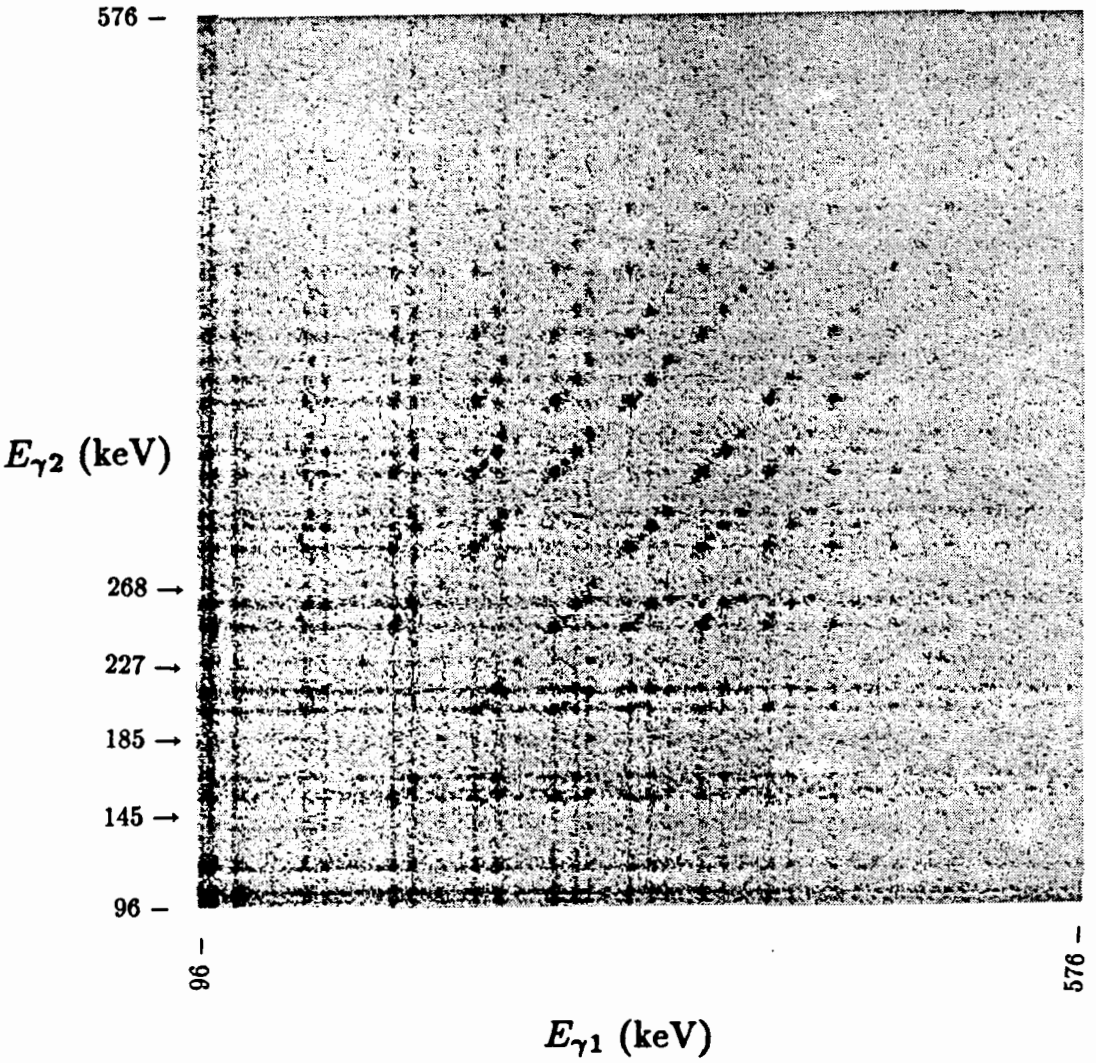

Figure 3.14: Total two dimensional Ge γ-γ coincidence spectrum for the ^{90}Zr + ^{239}Pu reaction showing relationships between γ-rays in this experiment. Both inelastic ^{239}Pu γ-rays and one-neutron transfer ^{238}Pu γ-rays are present.

mystery transition at 227 keV is in coincidence with the 307-keV $12^+ \rightarrow 10^+$ ^{238}Pu transition, indicating that the mystery transitions are in ^{238}Pu; and (8) Slices of this two-dimensional spectrum will show the rotational bands to be investigated.

Figure 3.15 shows a plot of the total (H, K) spectrum for this reaction. Projections of the H and K for the reaction are shown in Figure 3.16. Figures 3.15 and 3.16 clearly show the average multiplicity to be $3-4$ and the average total energy to be $\sim$ 1 MeV. Furthermore, there is only one maximum located at lower (H, K), indicating that perhaps the two quasi-particle transfer reaction cross-section is suppressed. The (H, K) spectrum gated on inelastic transitions will be discussed in Section 3.3.1, and (H, K) gated on transfer will be discussed in Section 3.3.2.

3.3.1 ^{239}Pu

Figure 3.17 shows a γ-ray spectrum gated on four ^{239}Pu transitions; the 201.1-keV $\frac{17}{2}^+ \rightarrow \frac{13}{2}^+$, 212.1-keV $\frac{19}{2}^+ \rightarrow \frac{15}{2}^+$, 288.3-keV $\frac{25}{2}^+ \rightarrow \frac{21}{2}^+$ and 299.7-keV $\frac{27}{2}^+ \rightarrow \frac{23}{2}^+$ transitions. The ground rotational band in ^{239}Pu is observed up to the 500-keV $\frac{49}{2}^+ \rightarrow \frac{45}{2}^+$ transition, at least $9\hbar$ higher than previously known

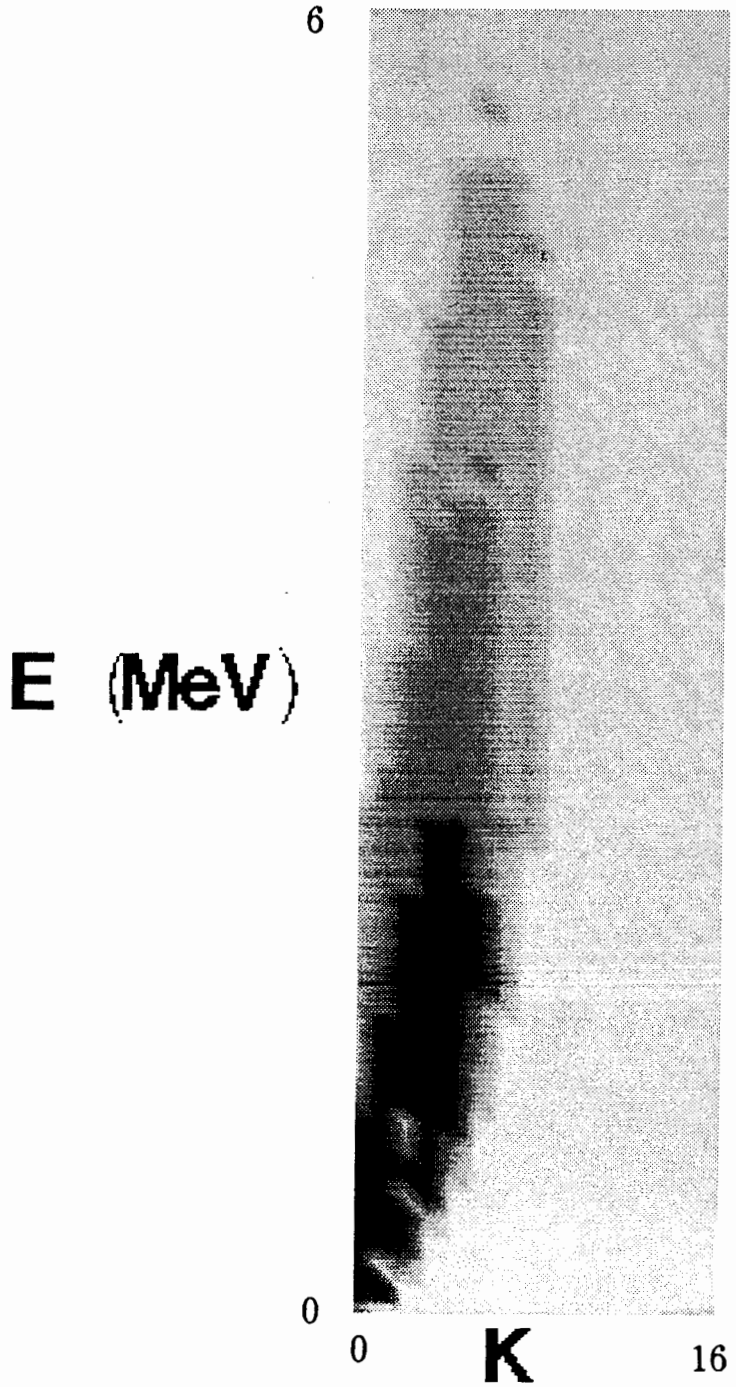

Figure 3.15: Total (H, K) spectrum for the ^{90}Zr + ^{239}Pu reaction.

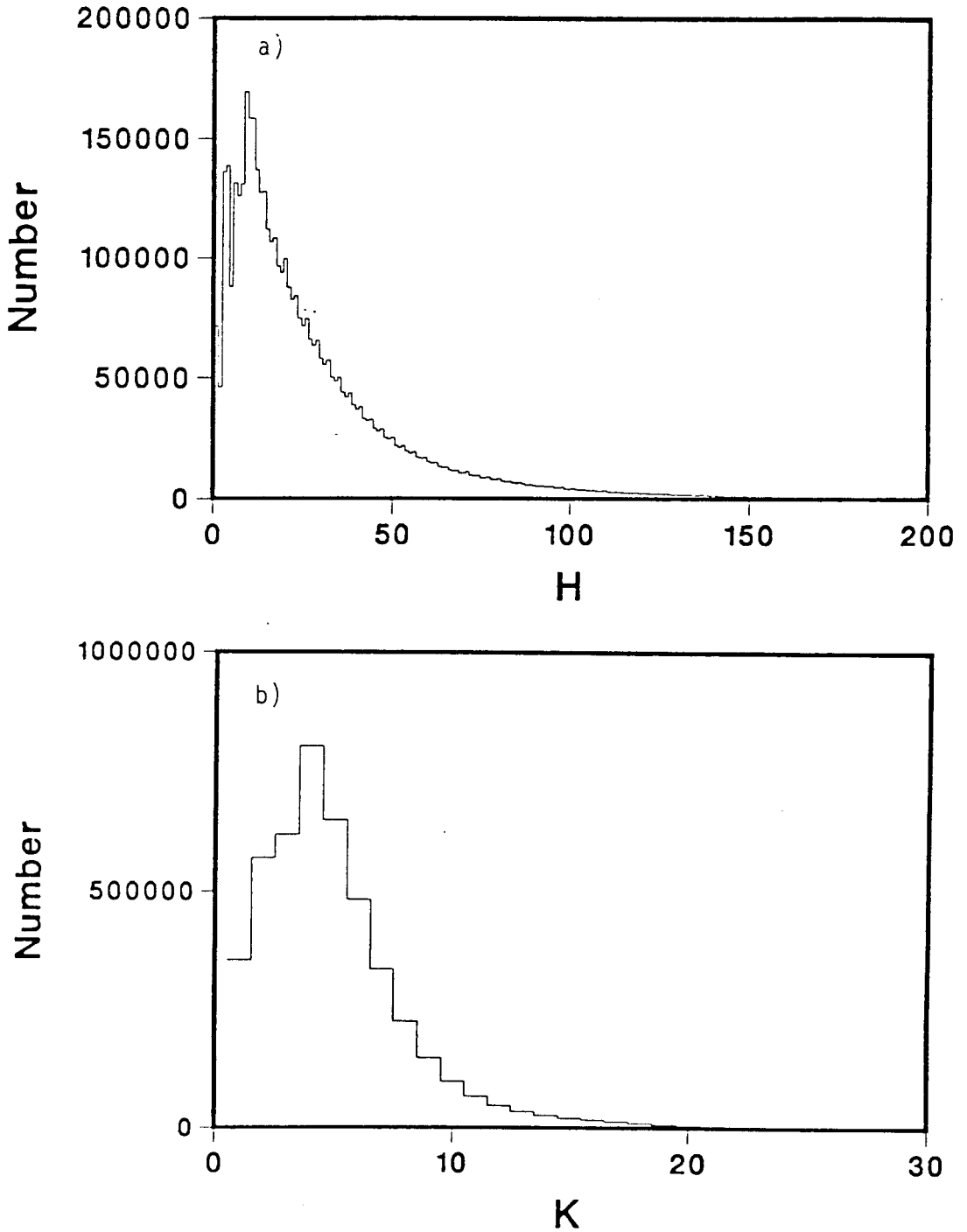

Figure 3.16: Projection of a) H and b) K for the ^{90}Zr + ^{239}Pu reaction.

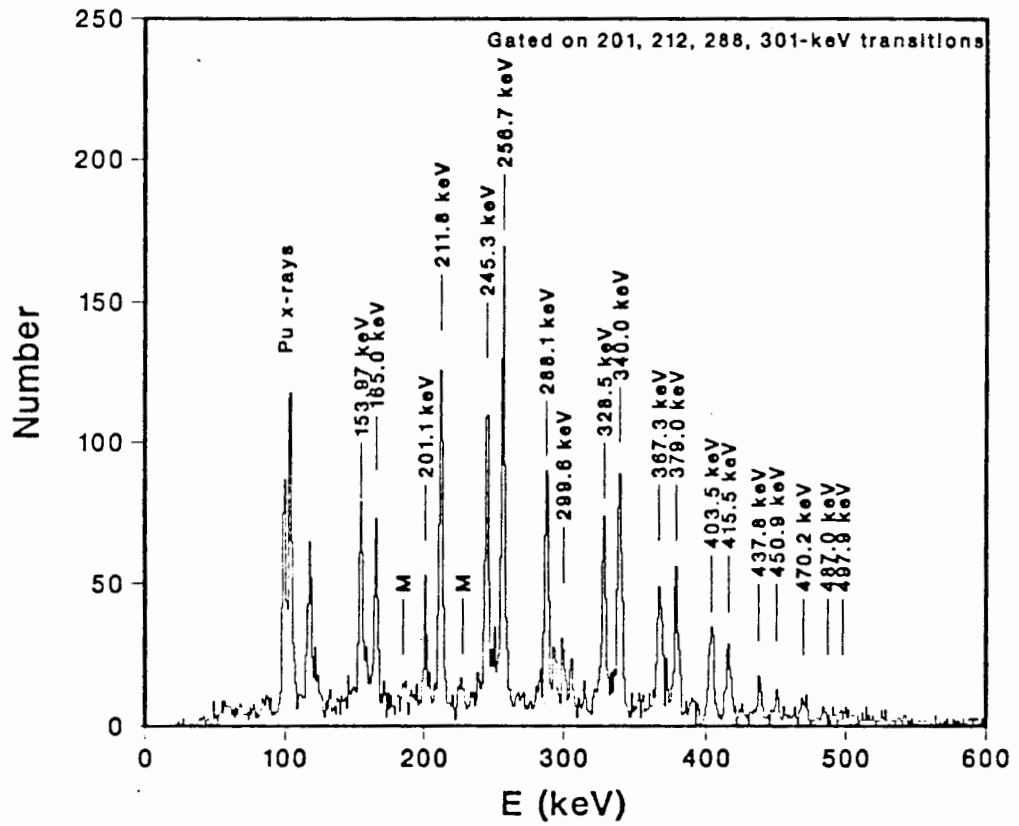

Figure 3.17: Ge γ-γ spectrum for the ^{90}Zr + ^{239}Pu reaction gated on the 201.1-keV $\frac{17}{2}^+ \rightarrow \frac{13}{2}^+$, 212.1-keV $\frac{19}{2}^+ \rightarrow \frac{15}{2}^+$, 288.3-keV $\frac{25}{2}^+ \rightarrow \frac{21}{2}^+$ and 299.7-keV $\frac{27}{2}^+ \rightarrow \frac{23}{2}^+$ transitions. ^{239}Pu transitions are marked with their corresponding energies. Two "mystery" transitions discussed in the text are marked with M's.

[41]. The band appears to be fairly regular, as shown by the transition energies given in Table 3.6. The moments-of-inertia are presented in Figure 3.18 for

Table 3.6: Observed transitions in ^{239}Pu

Transition	Energy (keV)	Transition	Energy (keV)
$\frac{11}{2}^+ \rightarrow \frac{7}{2}^+$	117.1(2)	$\frac{13}{2}^+ \rightarrow \frac{9}{2}^+$	153.97(20)
$\frac{15}{2}^+ \rightarrow \frac{11}{2}^+$	165.0(2)	$\frac{17}{2}^+ \rightarrow \frac{13}{2}^+$	201.1(2)
$\frac{19}{2}^+ \rightarrow \frac{15}{2}^+$	211.8(2)	$\frac{21}{2}^+ \rightarrow \frac{17}{2}^+$	245.3(2)
$\frac{23}{2}^+ \rightarrow \frac{19}{2}^+$	256.7(2)	$\frac{25}{2}^+ \rightarrow \frac{21}{2}^+$	288.1(2)
$\frac{27}{2}^+ \rightarrow \frac{23}{2}^+$	299.6(2)	$\frac{29}{2}^+ \rightarrow \frac{25}{2}^+$	328.5(2)
$\frac{31}{2}^+ \rightarrow \frac{27}{2}^+$	340.0(2)	$\frac{33}{2}^+ \rightarrow \frac{29}{2}^+$	367.3(4)
$\frac{35}{2}^+ \rightarrow \frac{31}{2}^+$	379.0(4)	$\frac{37}{2}^+ \rightarrow \frac{33}{2}^+$	403.5(4)
$\frac{39}{2}^+ \rightarrow \frac{35}{2}^+$	415.5(4)	$\frac{41}{2}^+ \rightarrow \frac{37}{2}^+$	437.8(4)
$\frac{43}{2}^+ \rightarrow \frac{39}{2}^+$	450.9(4)	$\frac{45}{2}^+ \rightarrow \frac{41}{2}^+$	470.2(4)
$\frac{47}{2}^+ \rightarrow \frac{43}{2}^+$	487.0(4)	$\frac{49}{2}^+ \rightarrow \frac{45}{2}^+$	497.9(4)

both signatures of the ground-state band. The kinematic moment-of-inertia $\Im^{(1)}$ has an anomaly at low spin ($\hbar\omega \approx 0.05$ MeV), but then smooths out and gently increases with increasing $\hbar\omega$. The kinematic moment-of-inertia, $\frac{2\Im^{(1)}}{\hbar^2}$, is around 85 MeV^{-1} in this rotational velocity range. The dynamic moment-of-inertia, however, shows a rather large break at $\hbar\omega \approx 0.22$ MeV, and has a much larger increase than $\Im^{(1)}$ ($\frac{2\Im^{(2)}}{\hbar^2}$ increases from $\sim$ 74 MeV^{-1} at ground state to $\sim$ 140 MeV^{-1} at the top of the band – about a factor of two increase). Figure 3.19, the inverse moment-of-inertia $\Im^{(1)}$ as a function of

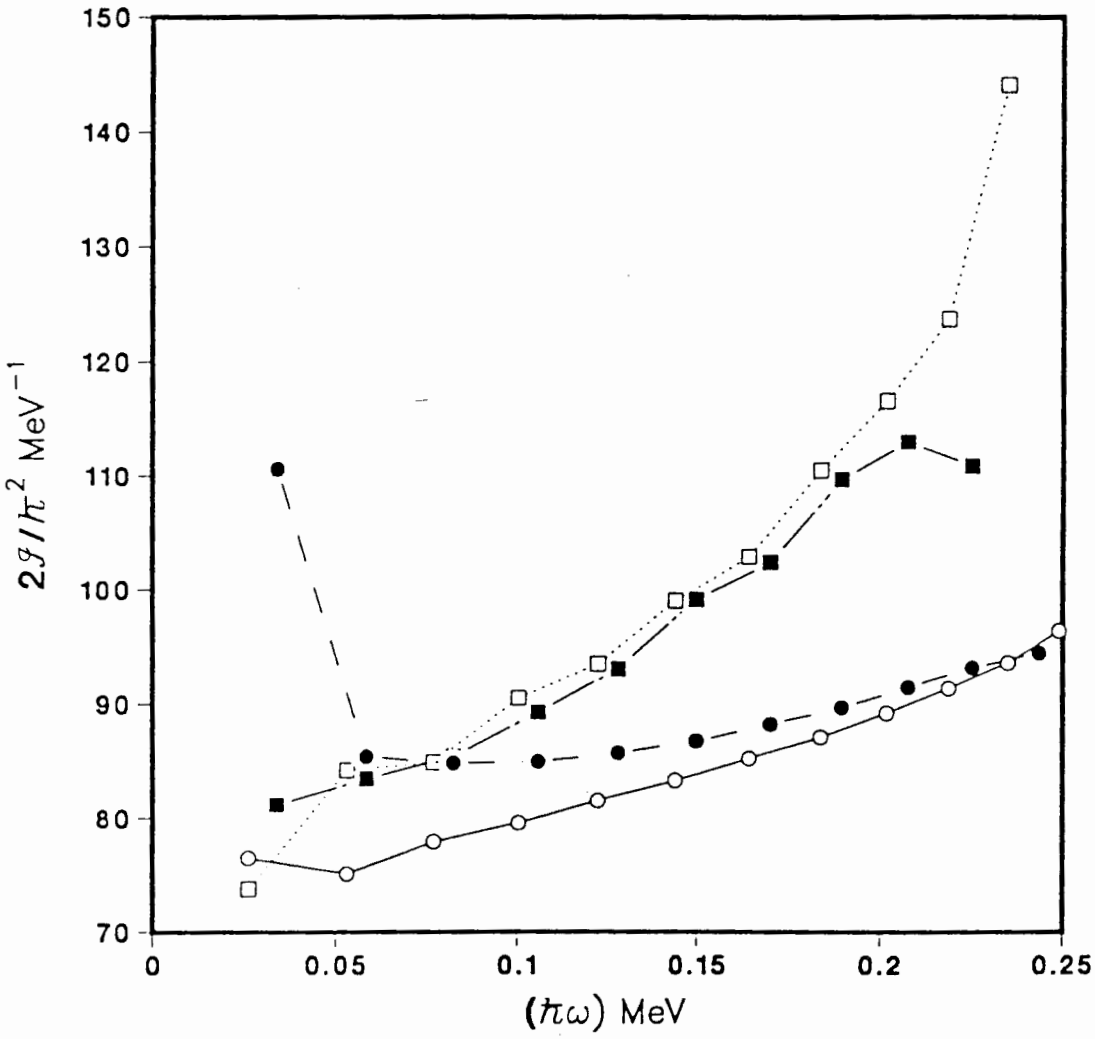

Figure 3.18: Moments-of-inertia for the ground-state band in ^{239}Pu. The open symbols are for the $\frac{1}{2}^+$ favored signature and the closed symbols are for the $\frac{3}{2}^+$ unfavored signature. The kinematic moment-of-inertia, $\Im^{(1)}$, (open circles and •) and the dynamic moment-of-inertia, $\Im^{(2)}$, (open squares and solid squares) are shown as a function of cranking frequency. An anomaly in the dynamic moment-of-inertia is observed at $\omega \approx 0.22$. The kinematic moment-of-inertia has a strange behavior at lower spins which may be alignment.

I^2, clearly shows a rather large staggering between the favored and unfavored signatures of the band, which is characteristic of a $K = \frac{1}{2}^+$ band. Note that the difference between the favored signature ($\sim$ 6 keV) and the unfavored signature ($\sim$ 17 keV) is a factor of three, much larger than the ^{233}U case discussed in Section 3.2. No clear backbending or upbending is observed, but there is a discrepancy at higher spins. However, in this region a proton backbending is expected prior (lower $\hbar\omega$) to a neutron backbend. Because rotation is a collective effect, though, such a backbend might also be observed even though neutron quasi-particle states are excited.

The aligned angular momentum (i_α) is extracted as before (see Section 3.2) and is presented in Figure 3.20 using the ^{238}Pu $\Im_0 = 67.9\hbar^2/\text{MeV}$ and $\Im_1 = 370\hbar^4/\text{MeV}^3$ for the reference state. The alignment is smooth and constant for each signature, the staggering is large as noted before, and an anomalously low i_α is observed for the $\frac{47}{2}^+$ state at $\hbar\omega \approx 0.24$ MeV. The moment-of-inertia data and the aligned angular momentum data indicate a possible band crossing point at $\hbar\omega \approx 0.22 - 0.24$ MeV.

Single particle energy level Routhians for the ground-state band in ^{239}Pu were also extracted from the data as in Section 3.2 and are presented in Figure 3.21 for a ^{238}Pu reference state ($\Im_0 = 67.9\hbar^2/\text{MeV}$ and $\Im_1 = 320\hbar^4$ /Mev^3).

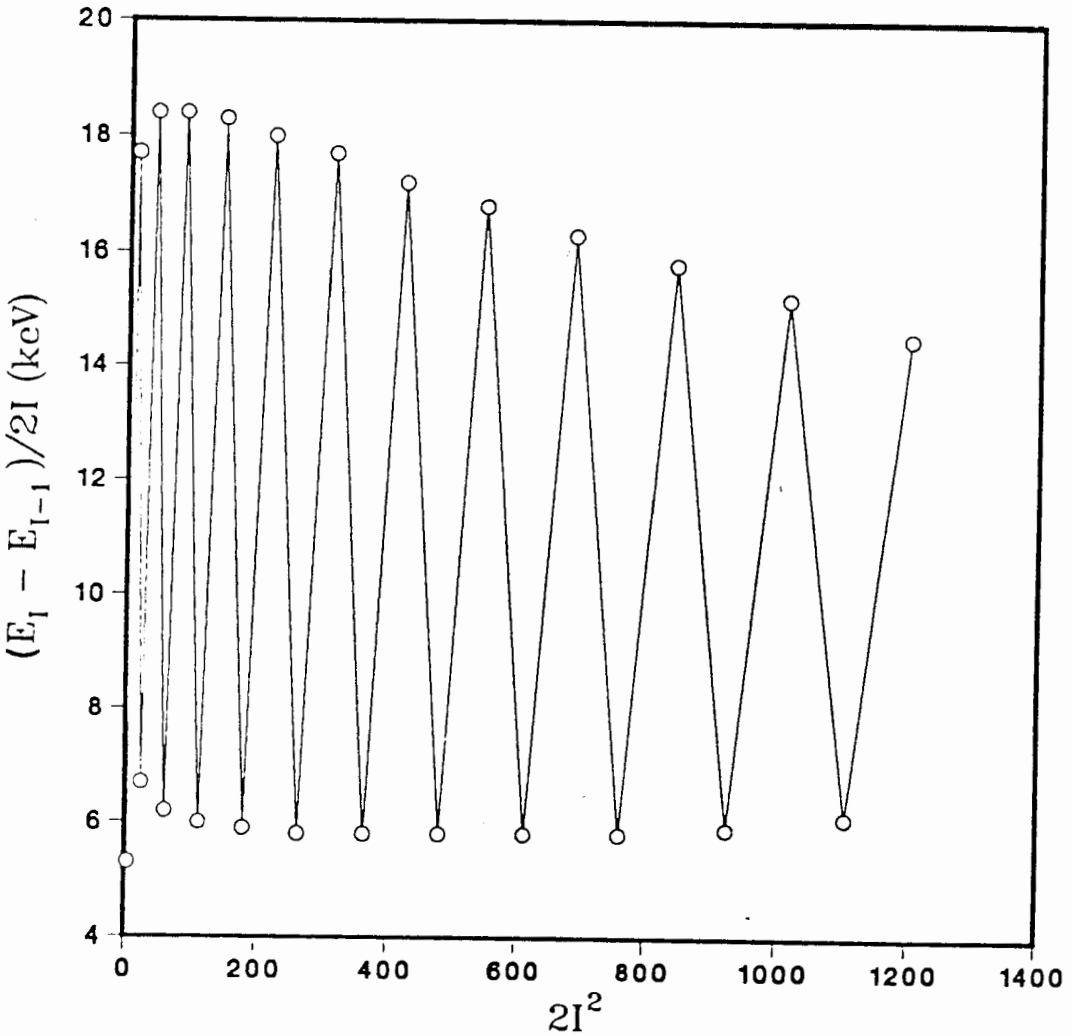

Figure 3.19: Inverse moment-of-inertia, $\Im^{(1)}$, for the ground-state band in ^{239}Pu showing the magnitude of the staggering between the favored and unfavored signatures.

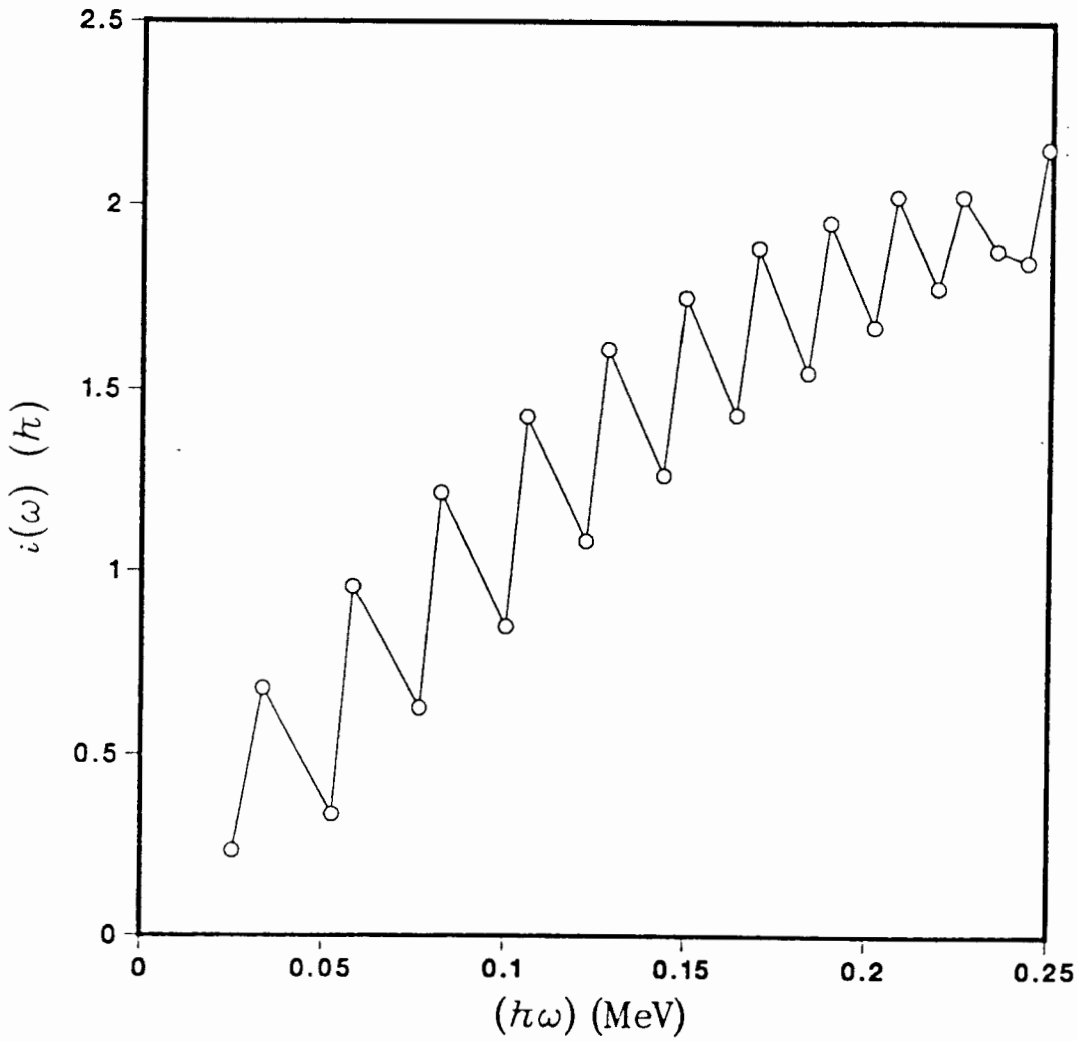

Figure 3.20: Aligned angular momentum (i_α) for the ground-state band in ^{239}Pu. Note the anomaly at $\omega \approx 0.24$. ^{238}Pu was used as the reference state, with $\Im_0 = 67.9\hbar^2/\text{MeV}$ and $\Im_1 = 320\hbar^4/\text{MeV}^3$.

The unfavored signature (•) is above the favored signature (open circles), and the splitting is very large as expected for a $K = \frac{1}{2}^+$ band. The Routhians decrease smoothly with increasing ω. The decrease is very similar to that for ^{233}U; however, from the inverse moment-of-inertia plot, there is no indication of a reversal of staggering in this nucleus.

A cranking calculation for ^{239}Pu was performed, and the $\frac{1}{2}^+$[631] ground-state band shows the expected behavior even with no γ-deformation (see Figure 3.22). The lowest level is the $\frac{1}{2}^+$ [631] ground state, with the first excited level the $\frac{5}{2}^+$ [622] and the second excited level the $\frac{7}{2}^+$ [624]. In addition, at higher spins, there seems to be a band interaction between the $\frac{1}{2}^+$[631] and $\frac{5}{2}^+$[622] bands which could explain the observed anomalies in the moments-of-inertia. Also, the $\frac{5}{2}^+$ and the $\frac{7}{2}^+$ bands show a strong interaction around $\hbar\omega/\hbar\omega_o \approx 0.018$. These bands have a first order Coriolis coupling so this is not surprising. The band mixing in this region is large. The results depend very sensitively on the location of the Fermi surface (or identically the choice of the chemical potential, λ). The conclusion, then, is that ^{239}Pu at high spins may not have a triaxial nuclear shape, or even a very small amount of triaxiality, certainly much less than observed for ^{233}U in Section 3.2.

Figure 3.23 presents the inelastic (H, K) spectrum gated on the 201.1-

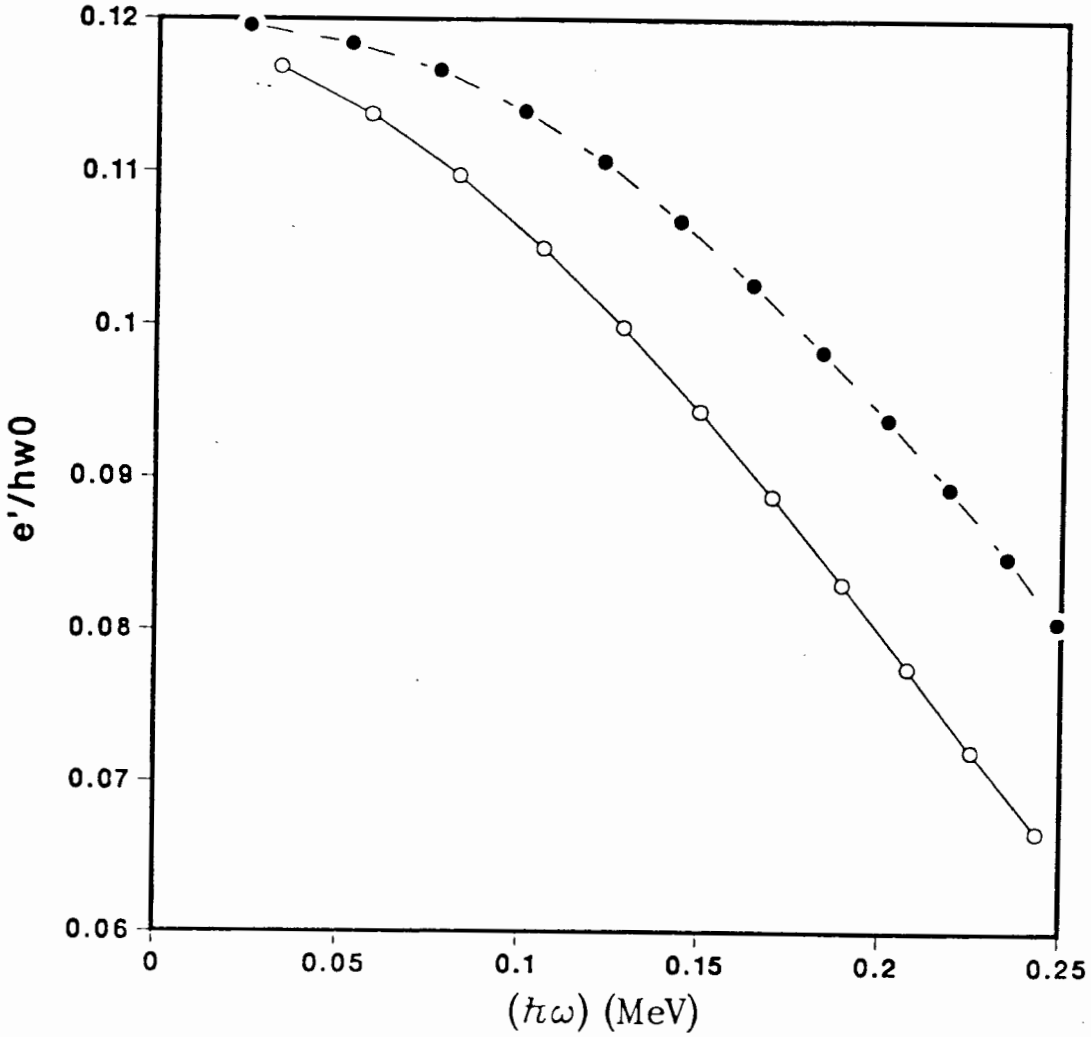

Figure 3.21: Experimental Routhians for the ground-state band in ^{239}Pu. The favored (open circles) and the unfavored signature (•) are plotted separately. Note that the splitting between signatures is large as would be expected for a $K = \frac{1}{2}$ band.

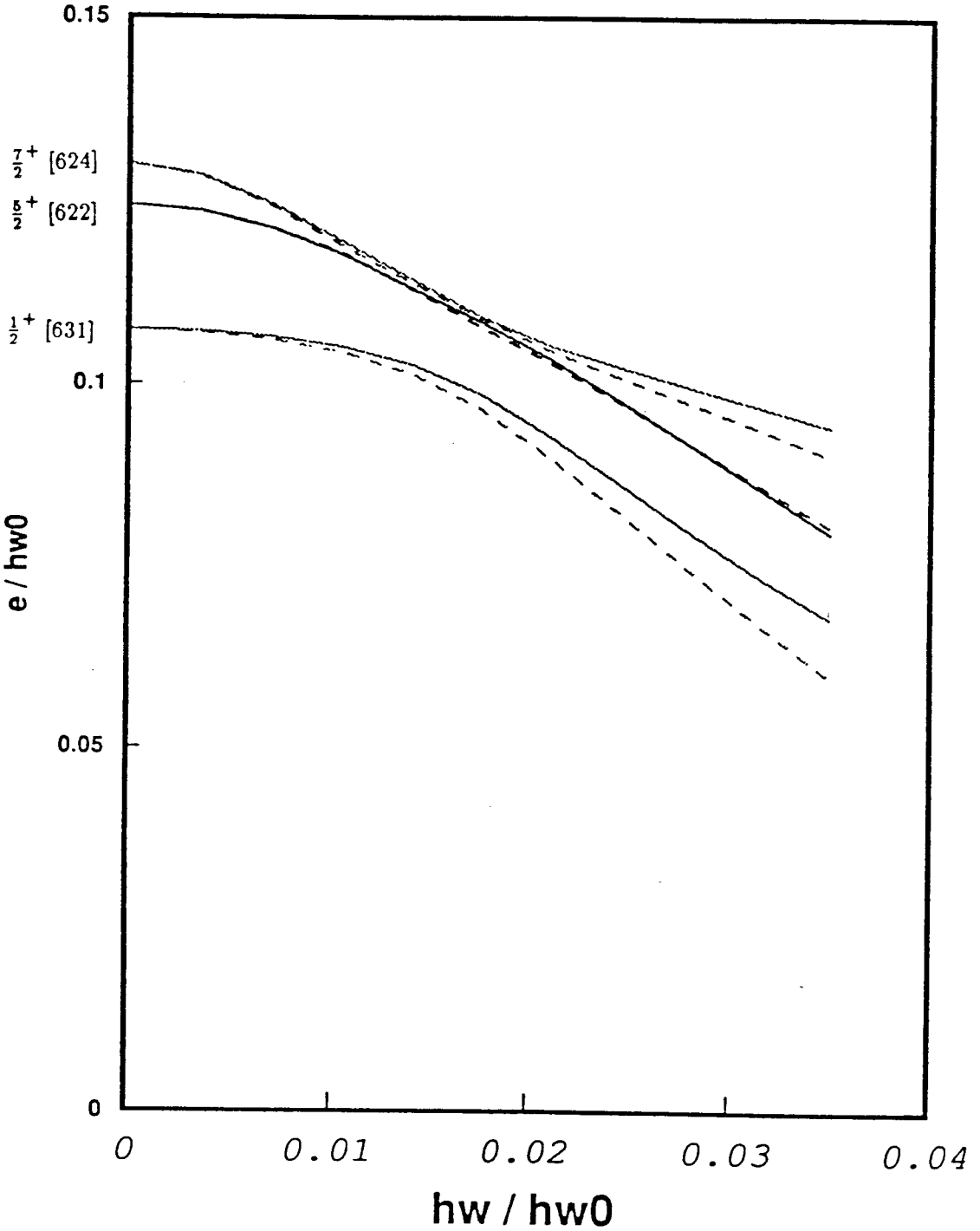

Figure 3.22: Theoretical Routhians for ^{239}Pu as a function of ω. The first level is the $\frac{1}{2}^+$ [631] ground state. The first excited level is the $\frac{5}{2}^+$ [622] and the second excited state is the $\frac{7}{2}^+$ [624]. The solid lines are the unfavored signatures and the dashed lines are the favored signatures.

keV $\frac{17}{2}^+ \rightarrow \frac{13}{2}^+$, 212.1-keV $\frac{19}{2}^+ \rightarrow \frac{15}{2}^+$, 288.3-keV $\frac{25}{2}^+ \rightarrow \frac{21}{2}^+$ and 299.7-keV $\frac{27}{2}^+ \rightarrow \frac{23}{2}^+$ transitions in the Ge detectors, and Figure 3.24 shows the H and K projections. The average multiplicity, K, is 3 and the energy, H, is $\sim$ 600 keV, centered at a typically low (H, K) for an inelastic reaction. However, as can be seen in comparison to the analogous transfer (H, K) spectrum shown in Figures 3.28 and 3.29, there is very little difference between the inelastic and transfer multiplicities and total reaction energies. Generally, transfer multiplicities and energies tend to have higher (H, K) peaks associated with the formation of two quasi-particle states when a pair of neutrons below the Fermi surface is broken. This will be discussed more completely in Section 3.3.2. Rotational population patterns for the ground-state band in ^{239}Pu are presented and discussed in Chapter 6.

3.3.2 ^{238}Pu

Figure 3.25 shows the Ge γ-ray spectrum gated on three known ^{238}Pu transitions, the 307-keV $12^+ \rightarrow 10^+$, 349-keV $14^+ \rightarrow 12^+$ and 389-keV $16^+ \rightarrow 14^+$ transitions. Lower transitions are masked by the inelastic ^{239}Pu γ-rays. The $6^+ \rightarrow 4^+$ 158-keV ^{238}Pu γ-ray appears as a shoulder on the 154-keV $\frac{13}{2}^+ \rightarrow \frac{9}{2}^+$

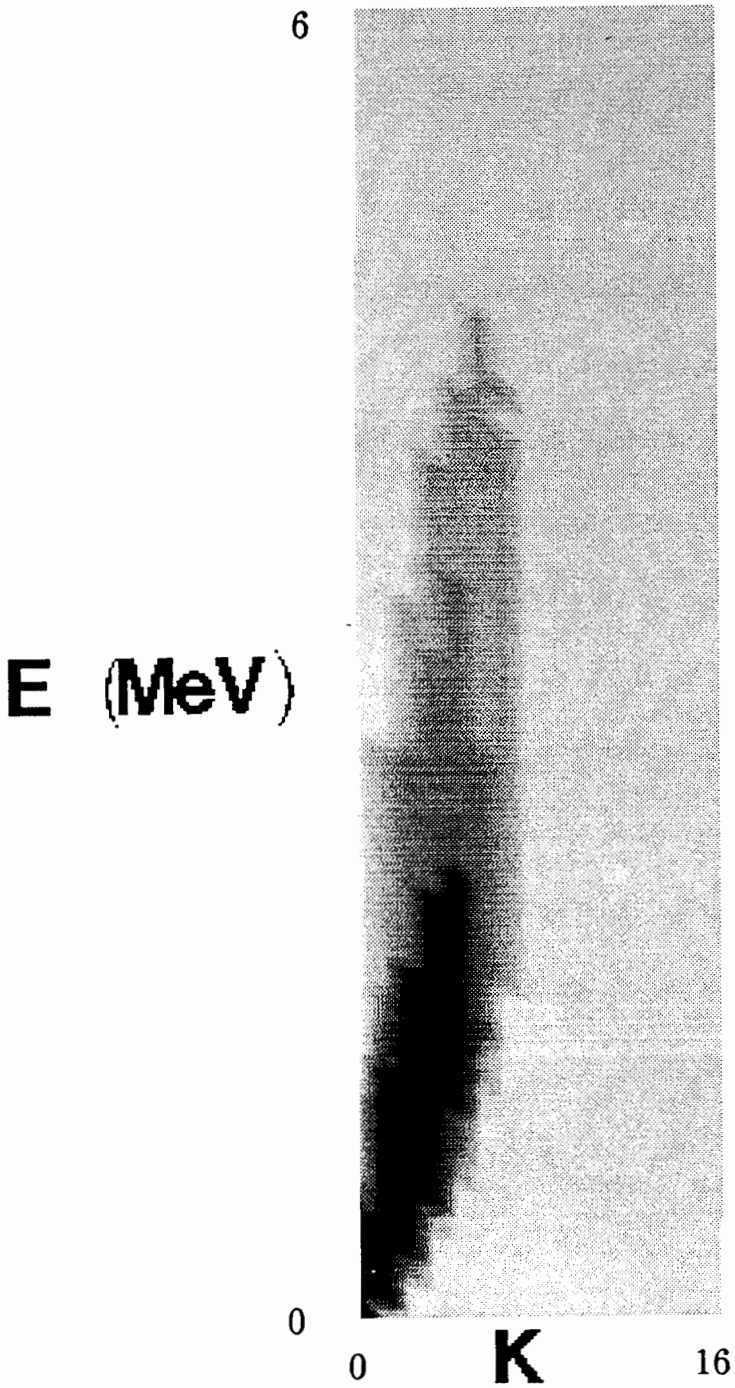

Figure 3.23: Inelastic (H, K) spectrum for the ^{90}Zr + ^{239}Pu reaction.

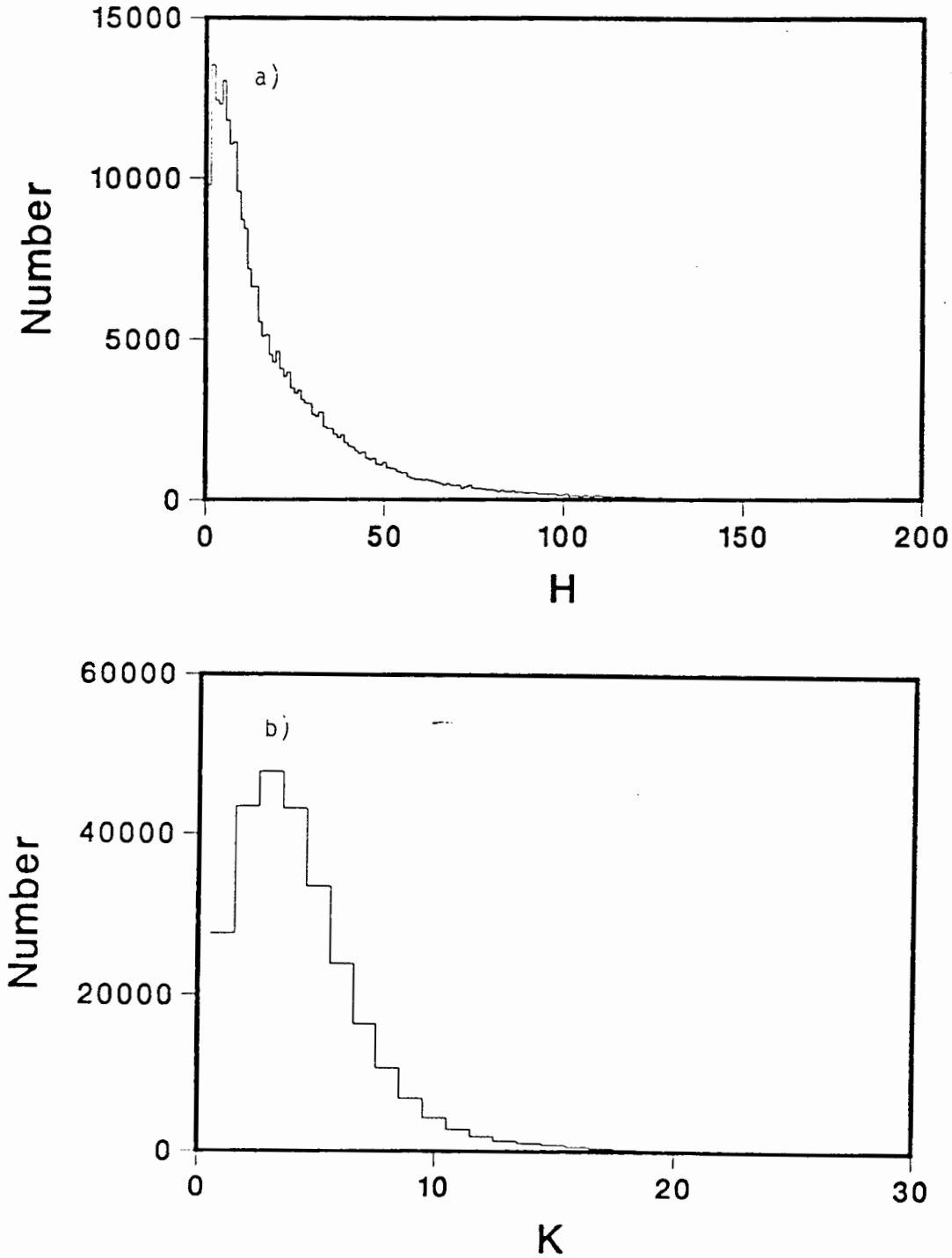

Figure 3.24: Projections of a) H and b) K for the ^{90}Zr + ^{239}Pu reaction.

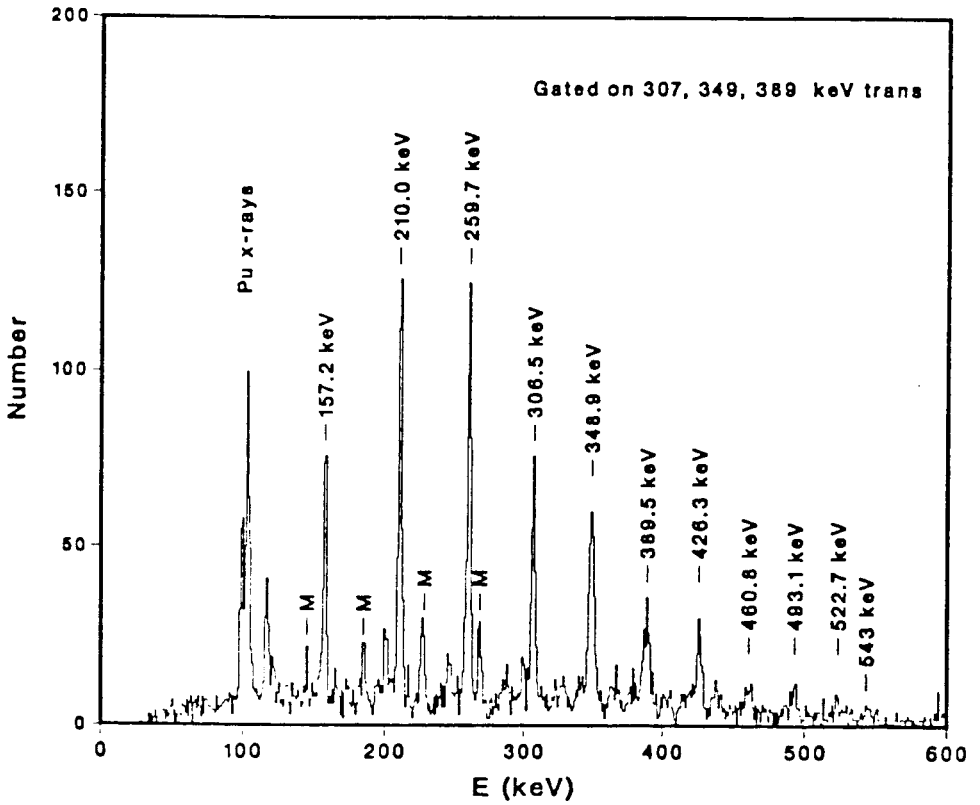

Figure 3.25: The γ-ray spectrum gated on three known ^{238}Pu transitions, the 307-keV $12^+ \rightarrow 10^+$, 349-keV $14^+ \rightarrow 12^+$ and 389-keV $16^+ \rightarrow 14^+$ transitions for the one-neutron transfer reaction. The ^{238}Pu transitions are marked with energies. The "mystery" band discussed in the text is labelled with M's.

^{239}Pu inelastic transition, too close for γ-γ gating techniques, but sufficiently separated for obtaining intensity information for the transfer reaction. The ground-state rotational band in ^{238}Pu is observed up to the 543-keV $26^+ \rightarrow 24^+$ transition (there is a candidate for the $28^+ \rightarrow 26^+$ transition if one has a little imagination). This is $10\hbar$ higher than observed in the (α,4n) work of Hardt et al. [41]. The transition energies shown in Table 3.7 are again very regular. The expected backbending [38] at about spin $30\hbar$ was not observed. The data

Table 3.7: Observed transitions in ^{238}Pu

Transition	Energy (keV)
$6^+ \rightarrow 4^+$	157.2(2)
$8^+ \rightarrow 6^+$	210.0(2)
$10^+ \rightarrow 8^+$	259.7(2)
$12^+ \rightarrow 10^+$	306.5(2)
$14^+ \rightarrow 12^+$	348.9(2)
$16^+ \rightarrow 14^+$	389.5(2)
$18^+ \rightarrow 16^+$	426.3(2)
$20^+ \rightarrow 18^+$	460.8(2)
$22^+ \rightarrow 20^+$	493.1(2)
$24^+ \rightarrow 22^+$	522.7(2)
$26^+ \rightarrow 24^+$	544.4(2)

do not rule out a backbend at higher spins.

The moments-of-inertia for the ground-state band in ^{238}Pu are presented in Figure 3.26. The kinematic moment-of-inertia is extremely regular, and

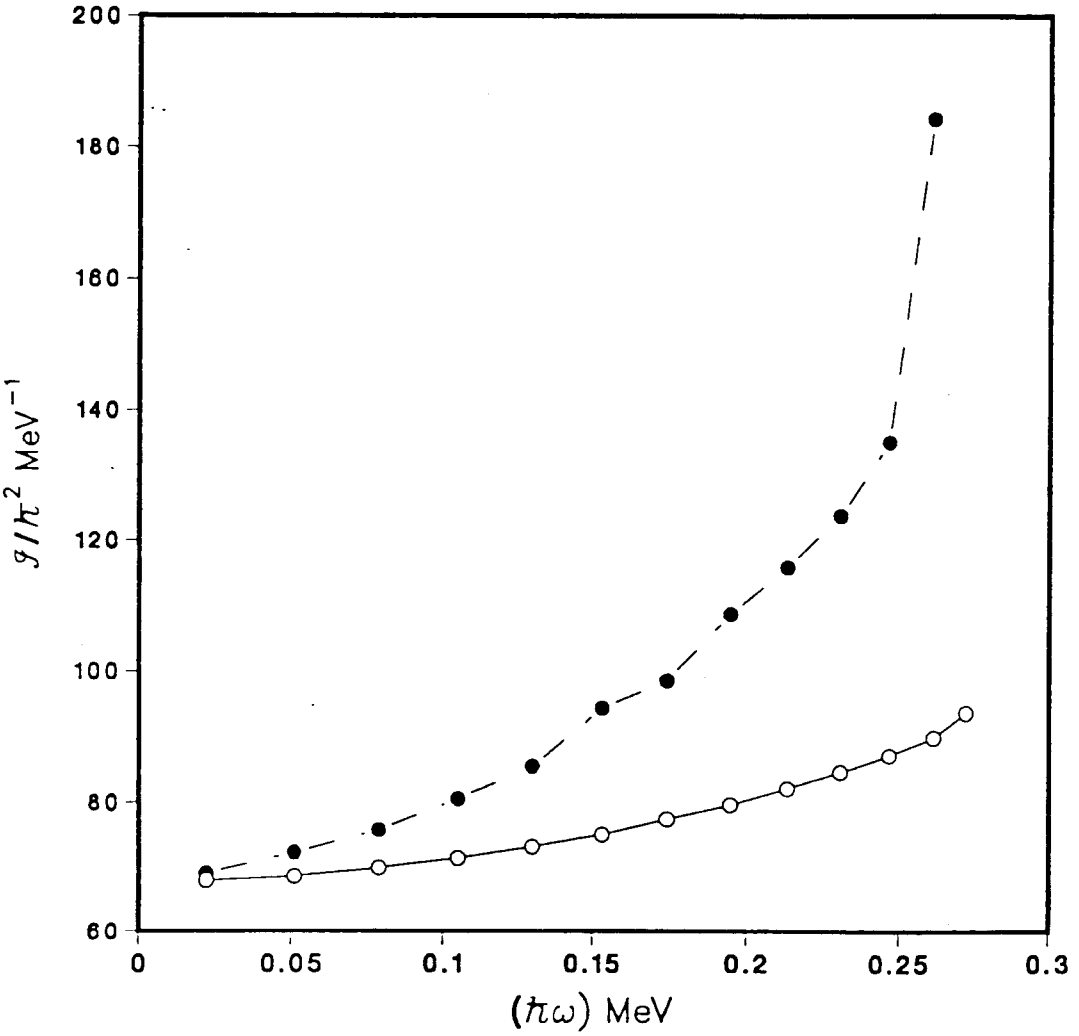

Figure 3.26: Kinematic (open circles) and dynamic (•) moments-of-inertia for the ground-state band in ^{238}Pu.

only slightly increases with increasing spin, indicating that the deformation is constant with increasing spin. However, the dynamic moment-of-inertia, a much more sensitive probe, exhibits a large increase at higher spins. In addition, the 26^+ level has an anomalously high $\Im^{(2)}$ (and $\Im^{(1)}$ is slightly higher than normal), perhaps the first indication of a backbend in this nucleus.

Single particle energy level Routhians, e', are again extracted, as in Section 3.2, and are shown in Figure 3.27. The reference state was chosen to be ^{238}Pu using $\Im_0$ and $\Im_1$ fit using the lowest five transitions. Thus, the extracted Routhians are expected to yield a horizontal line with slope = 0 (what all Routhians would be if the correct reference state were chosen). Indeed, the extracted Routhians only vary by $0.002/\hbar\omega_o(\sim 20\%)$ over the range of spins observed, whereas the Routhians for ^{239}Pu varied by a factor of two. The Routhians decrease with increasing spin, and the highest spin is anomalously low. Indeed, in the region just above the levels used to obtain $\Im_0$ and $\Im_1$, the Routhians are constant to ± 0.00001. It is only the 26^+ level which deviates by a factor of 70. Of course, single particle energy levels have relatively little meaning in a nucleus consisting entirely of pairs of particles; however, this exercise does provide an additional clue that band mixing at the highest spins observed in ^{238}Pu may be occurring. No cranking calculation was performed

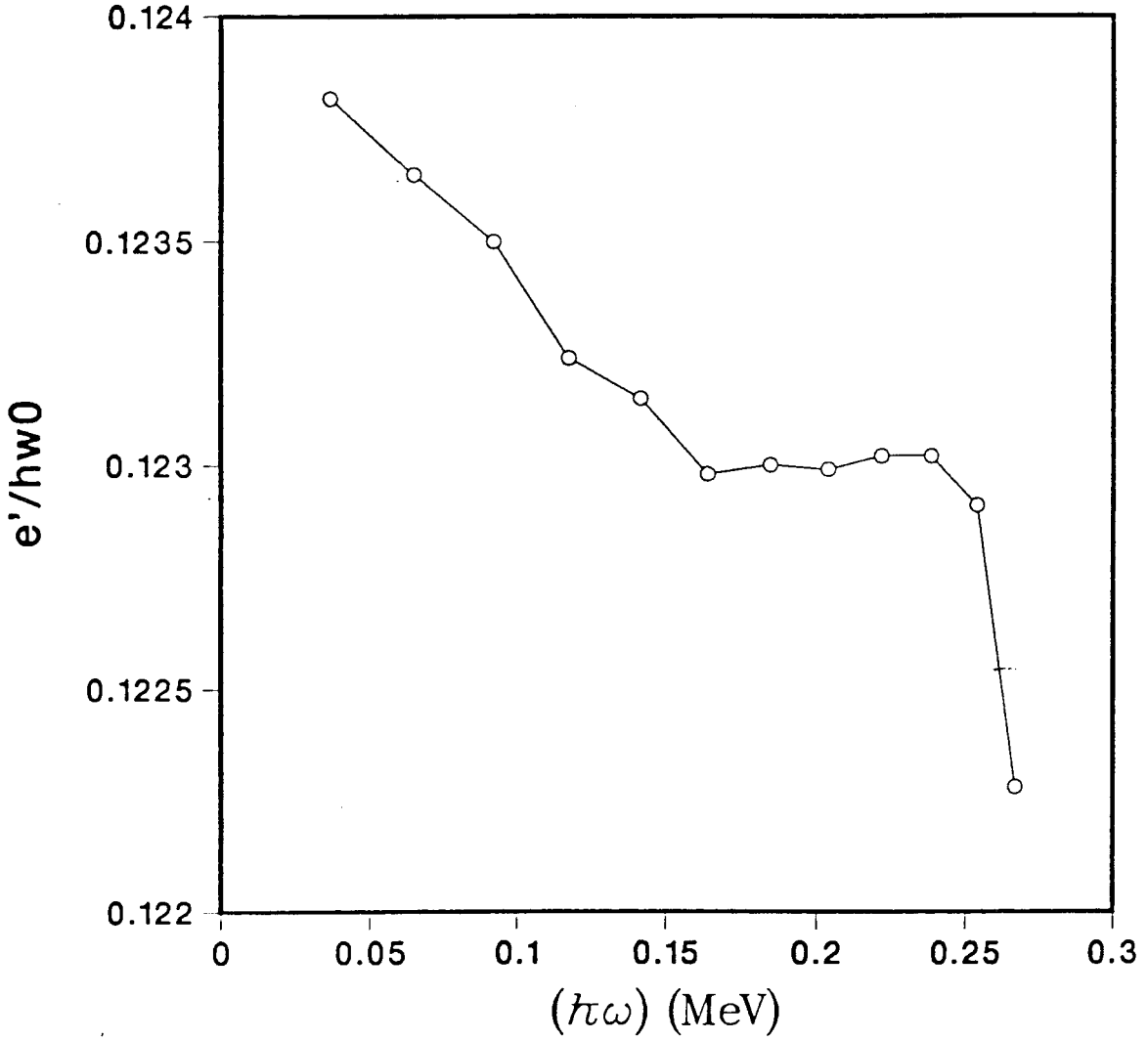

Figure 3.27: Experimental Routhians for ^{238}Pu.

as results analogous to ^{239}Pu are expected.

Figures 3.28 and 3.29 show the transfer (H, K) spectrum, and the H and K projections gated on the 307-keV $12^+ \rightarrow 10^+$, 349-keV $14^+ \rightarrow 12^+$ and 389-keV $16^+ \rightarrow 14^+$ ^{238}Pu transitions detected in the Ge detectors. The average multiplicity for the transfer reaction is $3 - 4$ and the average total reaction energy is 800 keV, both slightly higher than the inelastic reaction. No second maximum for two quasi-particle transfer is observed. The cross-section for the two quasi-particle one-neutron transfer reaction is either suppressed, or transfer of the $K = \frac{1}{2}^+$ neutron is enhanced in this reaction. It is possible that the $K = \frac{1}{2}$ neutron satisfies any Brinks selection rules much more easily than the neutrons below the Fermi surface in the $N = 7$, $\frac{7}{2}^-[743]$ or $N = 5$, $\frac{1}{2}^-[501]$ intruder levels. Additionally, the beam energy may have been coincidentally selected so as to enhance the ground-ground transfer and not the two quasi-particle transfer, as the cost to break a pair of neutrons (pairing energy) might be too high under these particular reaction conditions. This result is rather surprising, as it is the first observation of such a phenomenon; however, it is also the first $K = \frac{1}{2}$ neutron transfer studied by our collaboration.

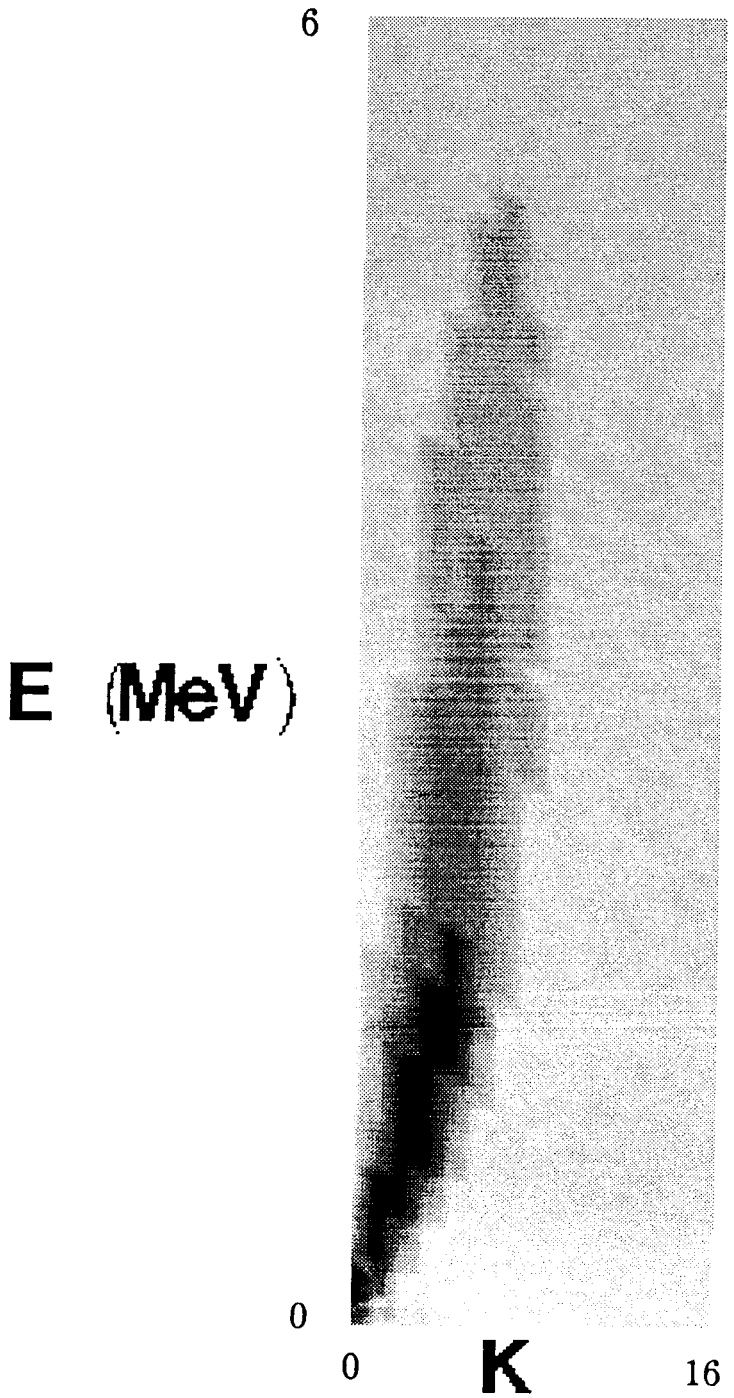

Figure 3.28: Transfer (H, K) spectrum for ^{238}Pu.

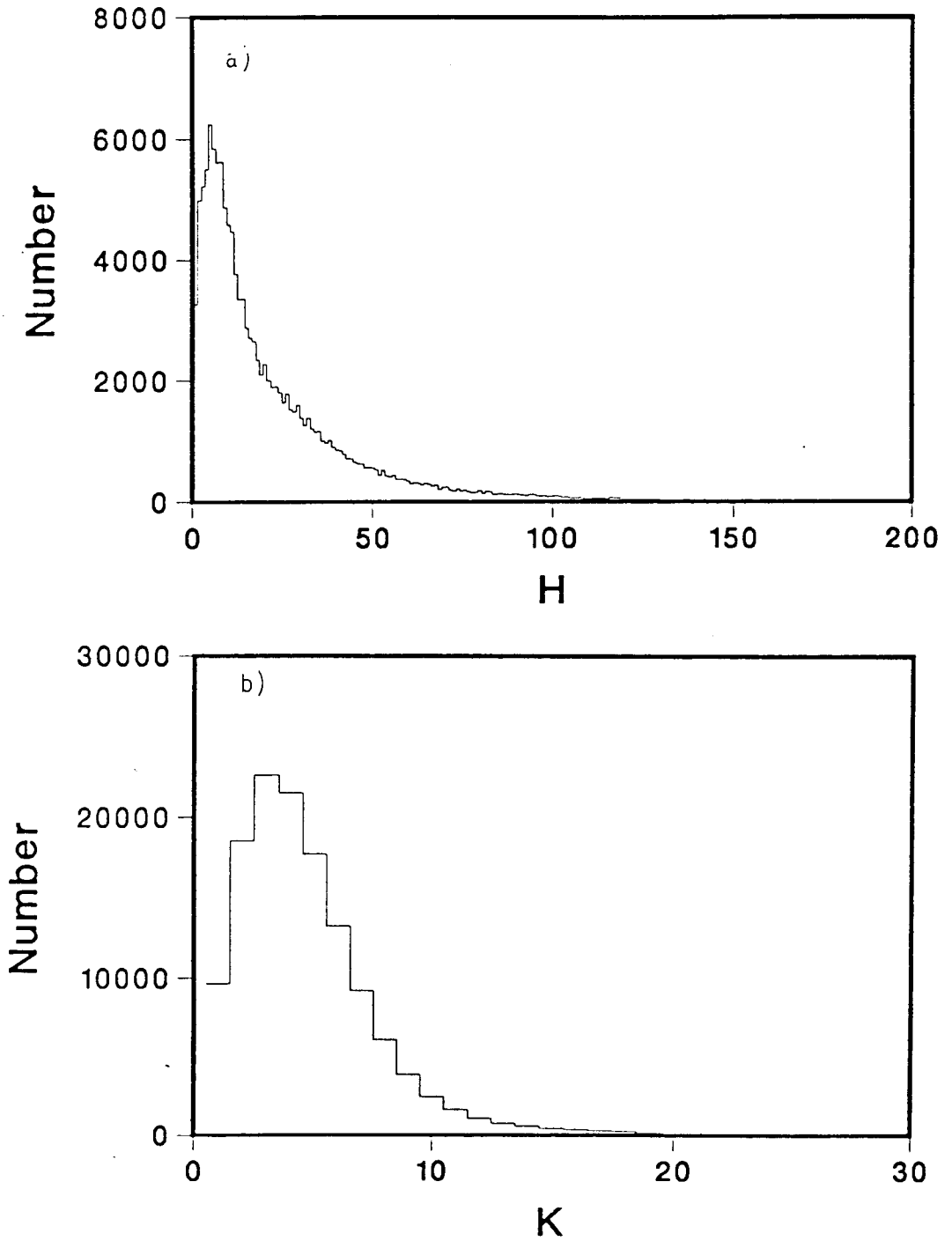

Figure 3.29: Projections of a) H and b) K for the transfer reaction.

The differential cross-section is given by:

$$\frac{d\sigma(\theta)}{d\Omega} = \left(\frac{d\sigma(\theta)}{d\Omega}\right)_{\text{elastic}} P_I \tag{3.27}$$

and

$$\left(\frac{d\sigma(\theta)}{d\Omega}\right)_{\text{elastic}} = \frac{(A_t Z_p Z_t e^2)^2 931.5 \csc^4\left(\frac{\theta_{CM}}{2}\right)}{8(197.3)^2 A_p E_{beam}}. \tag{3.28}$$

The $6^+ \rightarrow 4^+$ ^{238}Pu transition in the Ge detectors was fit as a function of scattering angle (see Appendix B for a discussion of the spectrum fitting). The γ-ray yield is then given by:

$$Y = \frac{I_\gamma(1+\alpha)}{\epsilon N_{sing}}, \tag{3.29}$$

where α is the internal conversion coefficient (summed over all energetically allowed shells) for the particular γ-ray, ϵ is the total Ge detector efficiency and N_{sing} is the number of singles. The probability is:

$$P_I = (Y_I - Y_{I+1}) \sin\left(\frac{\theta_{CM}}{2}\right). \tag{3.30}$$

Probabilities as a function of spin for the ^{238}Pu ground-state band are presented in Chapter 6.

If one assumes that one-neutron transfer can be approximated by classical Rutherford scattering, the distance of closest approach as a function of

scattering angle is:

$$D = \frac{Z_p Z_t e^2 (1 + (\sin\theta_{CM})^{-1})}{2E_{CM}}, \tag{3.31}$$

and the reduced distance of closest approach, d_0, is given by:

$$d_0 = \frac{D}{A_t^{\frac{1}{3}} + A_p^{\frac{1}{3}}}. \tag{3.32}$$

The impact parameter, b, is given by the usual equation:

$$b = \frac{Z_p Z_t e^2}{\mu v_{rel}^2} \tan\theta_{CM}. \tag{3.33}$$

The differential cross-section for one-neutron transfer at $\theta_{graze} = 140°$ in the lab is $\sim$ 80mb/sr, assuming all de-excitation flows through the 6^+ level (based on the $6^+ \rightarrow 4^+$ intensity fits). The differential cross-sections as a function of distance of closest approach, D, and reduced distance of closest approach, d_0, for lab and center-of-mass reference frames are presented in Figures 3.30 and 3.31. The reduced differential cross-sections are shown in Figure 3.32. No abnormalities are observed. However, it should be noted that the cross-section at the grazing angle is a factor of four larger than that for the ^{58}Ni(^{235}U,^{234}U)^{59}Ni reaction. Although these one-neutron transfer reactions were performed with different projectiles and different beam energies, a comparison at the grazing angle may provide some insight into the reaction mechanism. The distance of

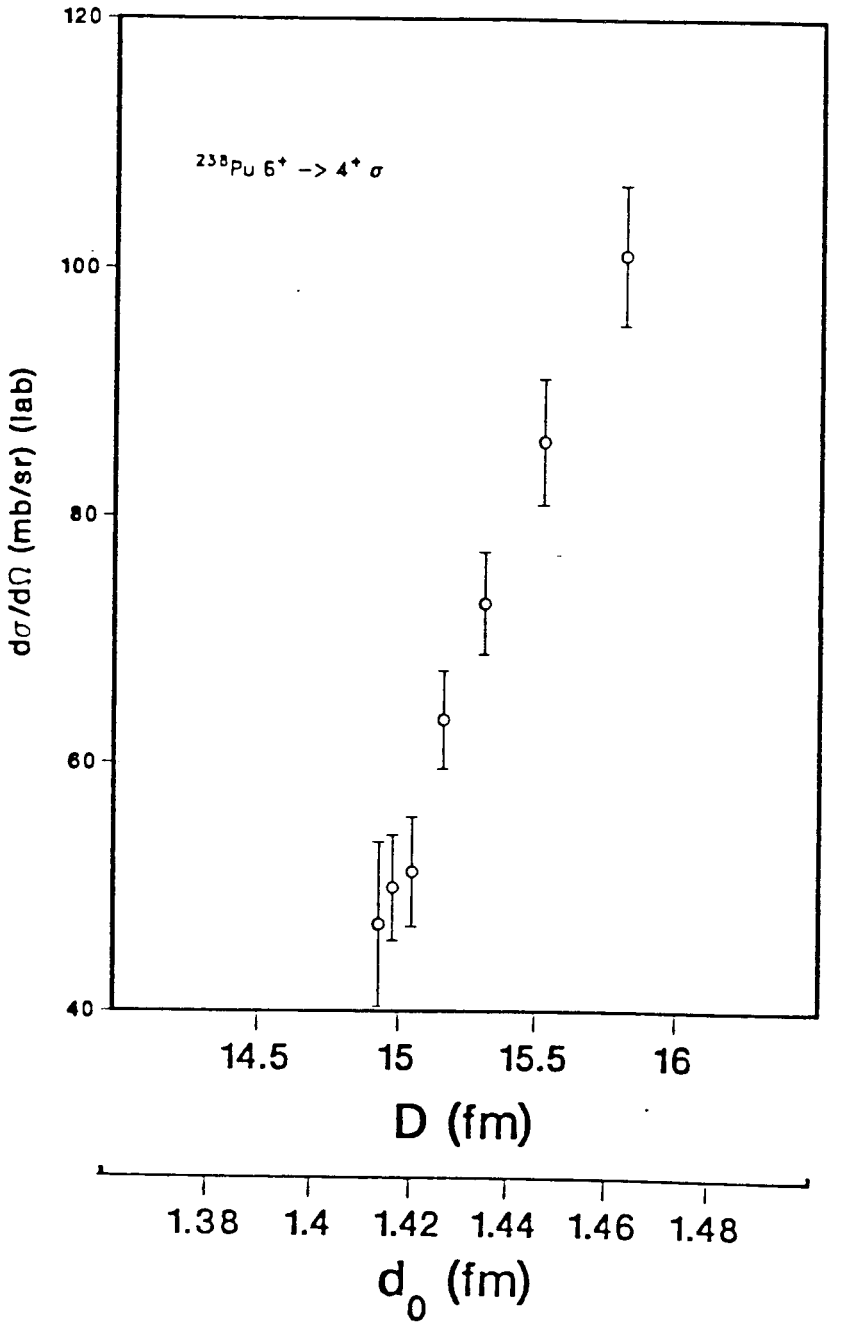

Figure 3.30: Differential cross-sections for one-neutron transfer as a function of distance of closest approach in the lab.

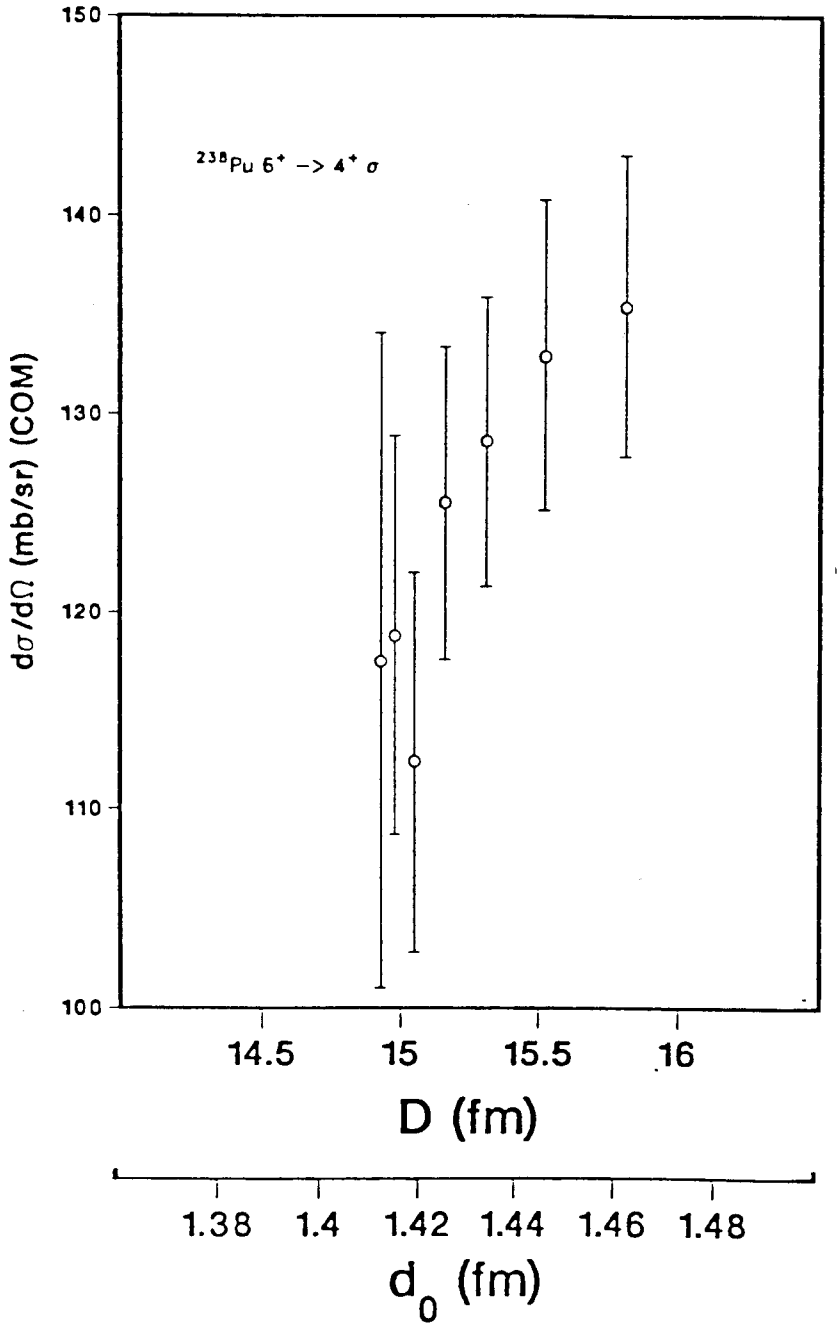

Figure 3.31: Differential cross-sections for one-neutron transfer as a function of distance of closest approach in the center-of-mass frame.

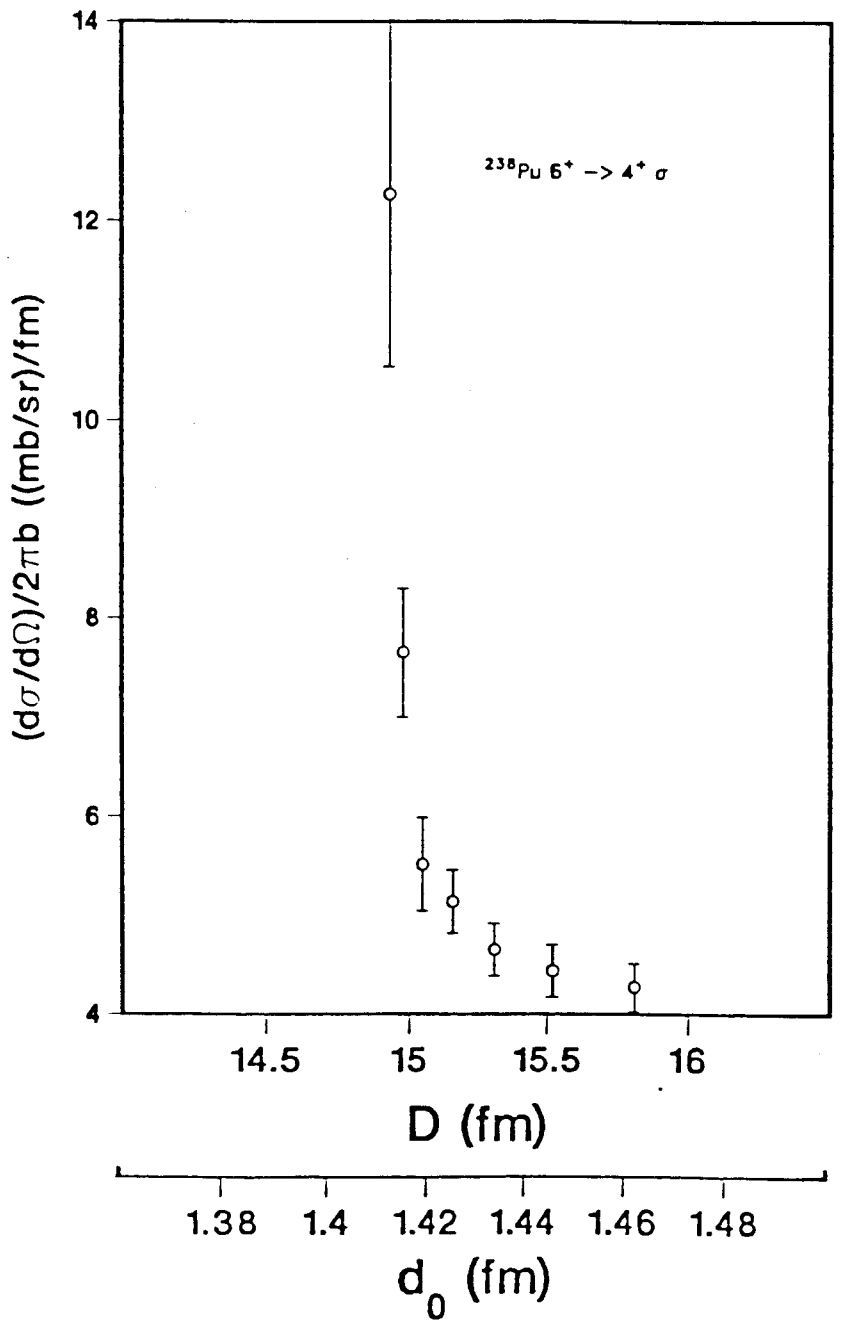

Figure 3.32: Reduced differential cross-sections for one-neutron transfer as a function of distance of closest approach in the lab.

closest approach is the same for both systems at the grazing angle (2.25 fm for ^{58}Ni + ^{235}U and 2.27 fm for ^{90}Zr + ^{239}Pu). However, the Nilsson orbitals involved in the transfer are different (the intruder $\frac{7}{2}^-$ [743] for ^{235}U ground-state and the $\frac{1}{2}^+$ [631] for ^{239}Pu ground-state), implying that nuclear structure or surface form factors may be playing an important role in these reactions. A discussion of surface form factors is included in Chapters 5 and 6.

The probability for populating the 6^+ state, as a function of D and d_0 is shown in Figure 3.33. The solid line represents a simple barrier penetration theory calculation where

$$P \propto \exp\left\{-\frac{\sqrt{2(931.5)E_{bind}}}{\hbar}R\right\} \tag{3.34}$$

and $E_{bind} = 3.442$ MeV for the $K = \frac{1}{2}$ neutron in ^{239}Pu and $R = D - R_p - R_t$, where R_p and R_t are the normal radii of the projectile and target, respectively, calculated according to the standard equation $R = r_o A^{\frac{1}{3}}$, with $r_o = 1.25$ fm. The curve is normalized to the probability at the smallest D. Figure 3.33 shows excellent agreement between the data and the simple theory, indicating this one-neutron transfer reaction is accurately described by simple Breit-Ebel theory [71]. It would be interesting to extract P_{2n} for the ^{240}Pu(^{90}Zr,^{92}Zr) ^{238}Pu reaction to see if $P_{2n}(D) = (P_{1n}(D))^2$, as simple theory predicts, or if

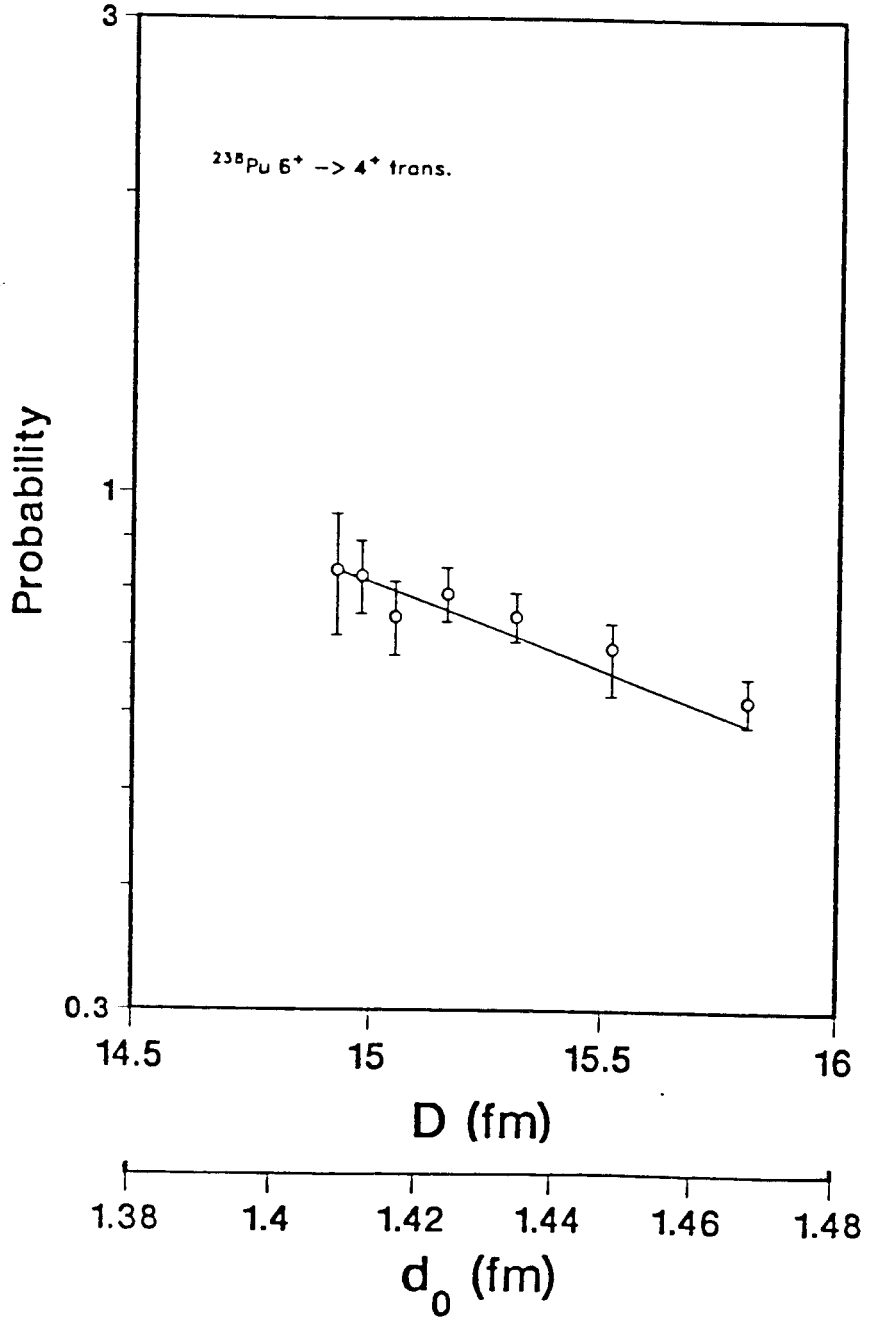

Figure 3.33: One-neutron transfer probability as a function of distance of closest approach. The solid line represents a simple theory based on equation (3.34).

an enhancement of two-neutron transfer exists, as in reference [72].

In addition to observing ground-state band transitions in ^{238}Pu and ^{239}Pu, we observed four "mystery" transitions located at 145 keV, 185 keV, 227 keV and 268 keV, respectively. These transitions are spaced about 40 keV apart, suspiciously like a rotational band with the same dynamic moment-of-inertia as the ground-state band in ^{238}Pu. As can be seen in the Ge γ-ray spectra gated on ^{238}Pu and ^{239}Pu transitions (see Figures 3.25 and 3.17), these transitions appear more strongly in the ^{238}Pu spectrum. These transitions correspond to no known γ-ray transitions in ^{237}Pu, ^{238}Pu, ^{239}Pu, ^{240}Pu, ^{241}Pu and several one-proton transfer products ^{238}Np and ^{240}Am. Also, because the γ-ray lines appear as sharp, well-defined peaks in the Pu-like Doppler shifted spectrum, this excludes any Zr-like sources (which would have a different Doppler shift), and known sources of background (which would be stationary sources in the lab). Thus, individual gates were set on these four transitions to investigate the source of these γ-rays. Figures 3.34, 3.35, 3.36 and 3.37 present the γ-γ coincidence spectra gated on individual "mystery" transitions including background subtraction.

Figure 3.34 is the γ-ray spectrum gated on the 145-keV transition. Possible peaks are marked with energies. A clear peak in the spectrum is the 268-keV

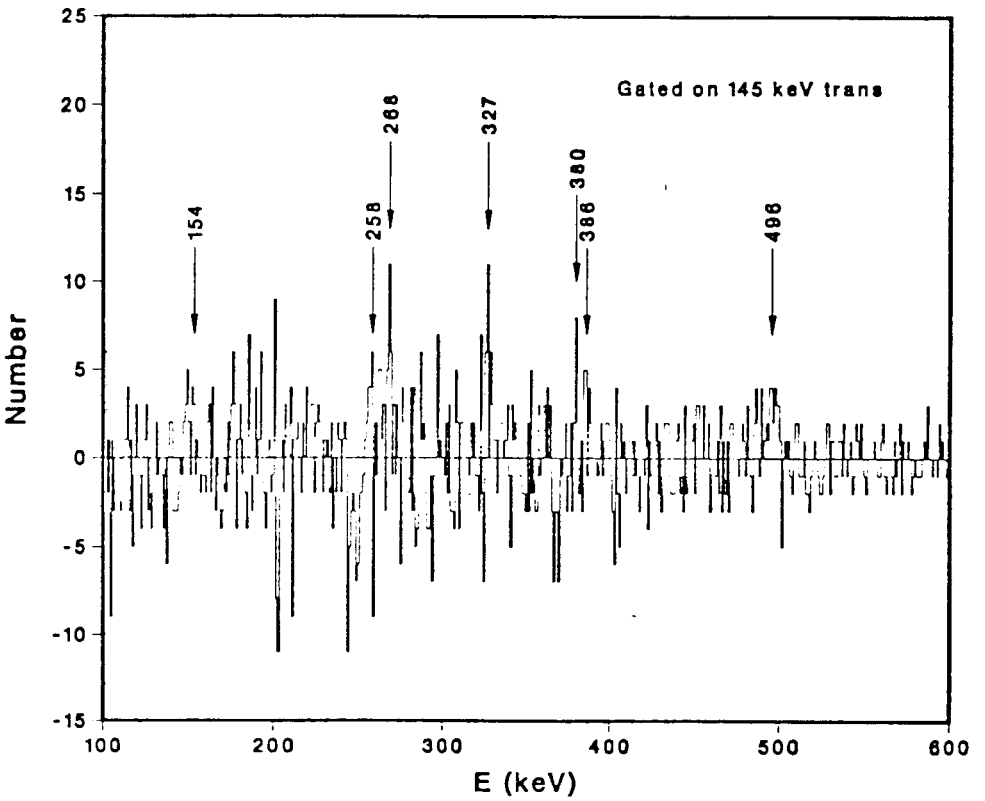

Figure 3.34: Ge γ-ray spectrum gated on the "mystery" transition at 145 keV in the ^{90}Zr + ^{239}Pu experiment.

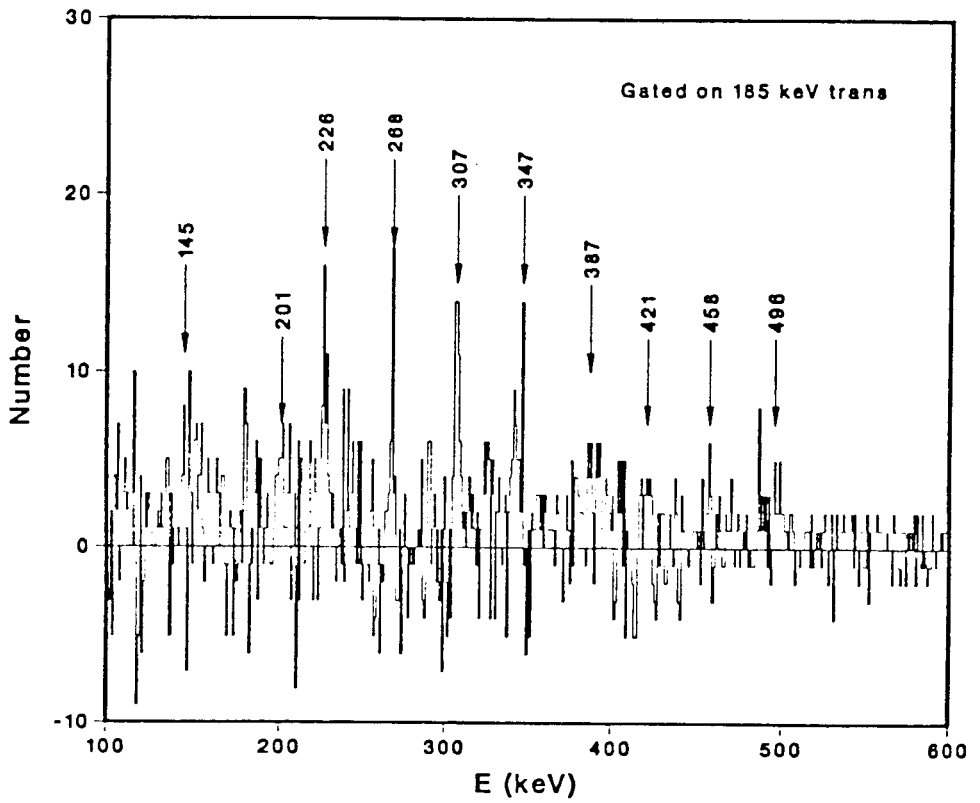

Figure 3.35: Ge γ-ray spectrum gated on the "mystery" transition at 185 keV in the ^{90}Zr + ^{239}Pu experiment.

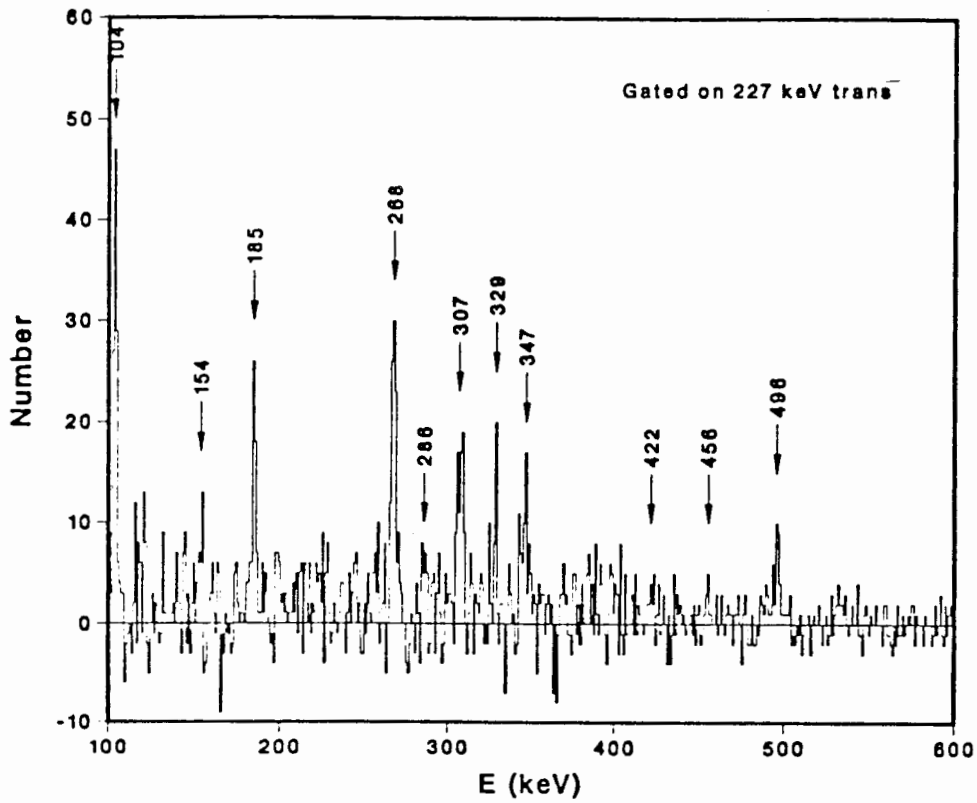

Figure 3.36: Ge γ-ray spectrum gated on the "mystery" transition at 226 keV in the ^{90}Zr + ^{239}Pu experiment.

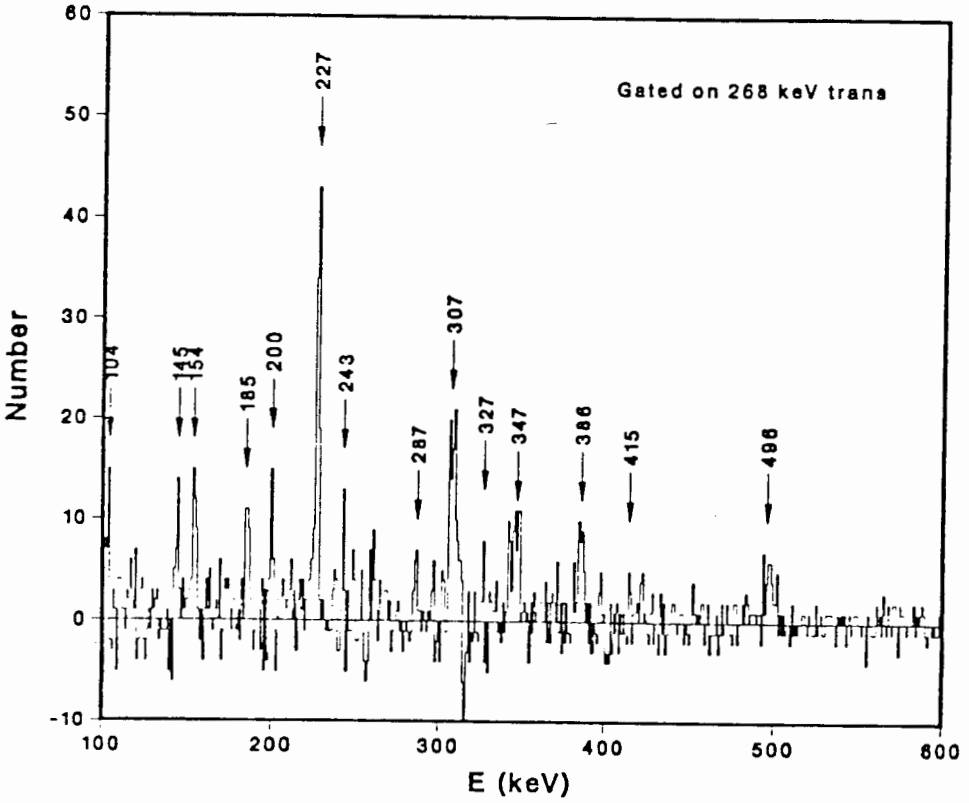

Figure 3.37: Ge γ-ray spectrum gated on the "mystery" transition at 268 keV in the ^{90}Zr + ^{239}Pu experiment.

"mystery" transition. Lack of statistics precludes a definitive statement on other γ-γ coincidences; however, possible peaks at 258-keV ($10^+ \rightarrow 8^+$ ^{238}Pu), 327-keV ($\frac{29}{2}^+ \rightarrow \frac{25}{2}^+$ ^{239}Pu), 380-keV ($\frac{35}{2}^+ \rightarrow \frac{31}{2}^+$ ^{239}Pu), 386-keV ($16^+ \rightarrow 14^+$ ^{238}Pu) and 496-keV ($22^+ \rightarrow 20^+$ ^{238}Pu) can be identified.

Figure 3.35 is gated on the 185-keV transition. Four clear peaks are observed; the 226-keV and 268-keV "mystery" transitions (the 145-keV "mystery" transition is marginally identifiable), and the 307-keV ($12^+ \rightarrow 10^+$ ^{238}Pu) and 347-keV ($14^+ \rightarrow 12^+$ ^{238}Pu) transitions. Four other ^{238}Pu transitions are partially identifiable (387-keV $16^+ \rightarrow 14^+$, 421-keV $18^+ \rightarrow 16^+$, 458-keV $20^+ \rightarrow 18^+$ and 497-keV $22^+ \rightarrow 20^+$). Also, the 201-keV $\frac{17}{2}^+ \rightarrow \frac{13}{2}^+$ ^{239}Pu transition is seen (perhaps just background). This spectrum clearly indicates that the four "mystery" transitions are indeed in coincidence, and, furthermore, that the 185-keV transition is in coincidence with ^{238}Pu transitions, implying that the "mystery" band belongs to ^{238}Pu.

However, the picture becomes less clear upon examination of Figure 3.36, gated on the 227-keV transition. Seven clear peaks are seen. The peak located at 104 keV is identified with the Pu x-rays. In addition, the 185-keV and 268-keV "mystery" transitions are observed. Three remaining peaks are assigned

to ^{238}Pu (308-keV $12^+ \rightarrow 10^+$, 347-keV $14^+ \rightarrow 12^+$ and 496-keV $22^+ \rightarrow 20^+$) and one to ^{239}Pu (329-keV $\frac{29}{2}^+ \rightarrow \frac{25}{2}^+$). There are also candidate peaks for 422-keV $18^+ \rightarrow 16^+$ ^{238}Pu, 456-keV $20^+ \rightarrow 18^+$ ^{238}Pu and 286-keV $\frac{25}{2}^+ \rightarrow \frac{21}{2}^+$ ^{239}Pu transitions. The evidence seems to indicate that the 227-keV transition belongs to ^{238}Pu (as those transitions appear much stronger in the spectrum than ^{239}Pu transitions do). However, the assignment of the peak at 497-keV to the $22^+ \rightarrow 20^+$ ^{238}Pu transition is questionable, as the transitions between 347-keV and the 497-keV peak are not readily identifiable (ie., the 497-keV peak has more intensity than expected). Nevertheless, a doublet at 497 keV or a background peak leaking through is not excluded.

Figure 3.37 shows the γ-ray spectrum gated on the 268-keV "mystery" transition, and supplies a bit more ambiguity to the assignment of the "mystery" band to ^{238}Pu. Ten clear peaks (and numerous other low statistic candidate peaks) are observed. Table 3.8 shows the assignment of the clear peaks. The strongest peaks belong to ^{238}Pu or the "mystery" band. Other candidate peaks are at 243-keV ($\frac{21}{2}^+ \rightarrow \frac{17}{2}^+$ ^{239}Pu), 287-keV ($\frac{25}{2}^+ \rightarrow \frac{21}{2}^+$ ^{239}Pu), 327-keV ($\frac{29}{2}^+ \rightarrow \frac{25}{2}^+$ ^{239}Pu) and 415-keV ($\frac{39}{2}^+ \rightarrow \frac{35}{2}^+$ ^{239}Pu) mostly belonging to the favored signature of the ground-state band of ^{239}Pu. Identification of the "mystery" band as belonging to ^{238}Pu is certainly not unambiguous (due to

Table 3.8: Peak assignments for the Ge γ-ray spectrum gated on the 268-keV "mystery" transition observed in the ^{90}Zr + ^{239}Pu experiment

E (keV)	Source
104	Pu x-rays
145	"mystery"
154	$\frac{13}{2}^+ \rightarrow \frac{9}{2}^+$ ^{239}Pu
185	"mystery"
200	$\frac{17}{2}^+ \rightarrow \frac{13}{2}^+$ ^{239}Pu
227	"mystery"
308	$12^+ \rightarrow 10^+$ ^{238}Pu
347	$14^+ \rightarrow 12^+$ ^{238}Pu
386	$16^+ \rightarrow 14^+$ ^{238}Pu
497	$22^+ \rightarrow 20^+$ ^{238}Pu

the ^{239}Pu transitions seen in some of the "mystery" transition gated spectra); however, as the ^{238}Pu peaks are stronger and consistently observed in Figures 3.34, 3.35, 3.36, and 3.37, these transitions are assigned to ^{238}Pu. The possibility of the ^{239}Pu transitions being just background accidentally leaking through the gates is not eliminated.

Therefore, the most consistent picture is that these four "mystery" transitions belong to ^{238}Pu and are part of some heretofore unobserved side-band in ^{238}Pu. The lowest octupole and beta vibrational side-bands were extrapolated to higher spins; however, neither extrapolation clearly fits the observed transitions, either in energy nor spins (based on these transitions having comparable

spins as ground-state band).

A second possibility, consistent with the γ-γ coincidence gates, is that the four "mystery" transitions belong to an as yet unobserved super-band or other excited $K = 0^+$ band, and the 496-keV transition connects the super-band to the ground-state band. Unfortunately, lack of statistics precludes a more definitive statement on this possibility.

Theoretical

Chapter 4

Introduction

In order to have a complete understanding of the processes underlying the excitation and population of rotational energy levels, either through Coulomb excitation, inelastic excitation, or neutron transfer reactions, one desires a theory that models the experimental rotational population patterns. Unfortunately, no such simple, elegant theory exists, and the state of nuclear theory in this area of nuclear structure is certainly not good or complete. Most theorists in this area concentrate on semi-classical or classical approaches to the problem, as fully quantum mechanical solutions for such heavy-ion systems require solution of the Schrödinger equation with complicated wavefunctions, and generally require a great many simplifying assumptions. Coulomb excitation, as long as beam energies are safely well below the barrier, is explained fairly well by the semi-classical approach of Alder-Winther-deBoer [73]. This

method tracks the population amplitudes of rotational levels along a hyperbolic Rutherford trajectory as integration of the time-dependent Schrödinger equations are performed. It seems to handle most dynamical effects well.

However, several complications arise once beam energies are increased, and inelastic excitation or neutron transfer reactions are investigated. Handling of the transfer matrix elements has not been fully derived, and proper inclusion of the nuclear potential has usually been ignored (or assumed to be unimportant).

Many calculations of rotational population patterns in heavy-ion collisions have been performed in the Sudden Approximation limit, where the target nucleus is assumed to remain stationary during the collision. Dynamic effects, and nuclear effects have been ignored, and the fact that the Sudden Approximation tends to overestimate the final maximum spin has been corrected by performing the calculations with a quadrupole moment reduced empirically by 20% to compensate [74]. In the actinide region, however, this factor was empirically found to be between $10 - 15\%$. Such ambiguity of results not only indicates a lack of understanding of the underlying processes, but is in itself unsatisfactory.

Other methods, such as the Coupled-Channels method [75] and the Classical Limit S-Matrix (CLSM), an alternative semi-classical approach [76],[77],[78],

do exist for calculating rotational populations but have generally been limited to lighter systems than considered in this thesis. One of the advantages to the CLSM method was that the nuclear potential could be included easily in the solutions of the equations of motion, and Coulomb-nuclear interference was described more naturally. However, it was practical only for head-on collisions (180° backscatter), problems with singularities and convergence prevented usage with very heavy systems, and the choice of energy levels and coupling matrix elements was constrained by a classical model. The Coupled-Channels approach also becomes untenable for heavier systems.

This thesis develops some methods for calculating rotational population patterns for systems as heavy as ^{206}Pb + ^{233}U and ^{90}Zr + ^{239}Pu, including nuclear potential effects [79], dynamic effects, and transfer matrix elements, that can be generalized to any scattering angle. Sudden Approximation, Monte-Carlo, and semi-classical theories are discussed, with the best calculation being from a modified Alder-Winther-deBoer method. Off-diagonal matrix elements and $\Delta L > 0$ transfer (centrifugal effects) are treated. Chapter 5 describes the theories and Chapter 6 compares the results with the experimental data. Also, these methods applied to calculation of the SQUID effects will be briefly discussed [80].

Recently, such methods have also been used by Dasso et al. [81] and [82] to calculate Diabolical pair transfer (SQUID effect). They do not include nuclear potential effects nor off-diagonal transfer matrix elements; however, they do include the S-band. Whether population favors the S-band or the ground band after the band crossing is solely dependent on the strength of the mixing matrix elements at the crossing point, something not well calculable by anyone. If the mixing is strong, the Coulomb excited population would tend to remain in the Yrast band, since $B(E2)$ matrix elements between Yrast states exceed those connecting to the band above Yrast. However, if it is weak, population could go to both bands above the virtual crossing. Mixing matrix elements are difficult to calculate theoretically, and, while we have chosen for simplicity initially not to include the S-band in the calculations, this band is certainly straightforward to include. In addition, the mixing matrix elements could be taken from experiment.

Chapter 5

Discussion of Relevant Theories

This chapter is concerned with discussing several methods used to calculate rotational population patterns for inelastic and neutron transfer reactions. The theories presented in this thesis are all still under development. Figure 5.1 defines the geometry of the physical systems under investigation. The angle θ is the scattering angle of the projectile, and χ is the orientation angle of the target axis-of-symmetry with respect to the beam axis. The rotational population pattern calculations using the Sudden Approximation are discussed in Section 5.1; and using modified Alder-Winther-deBoer methods in Section 5.2.

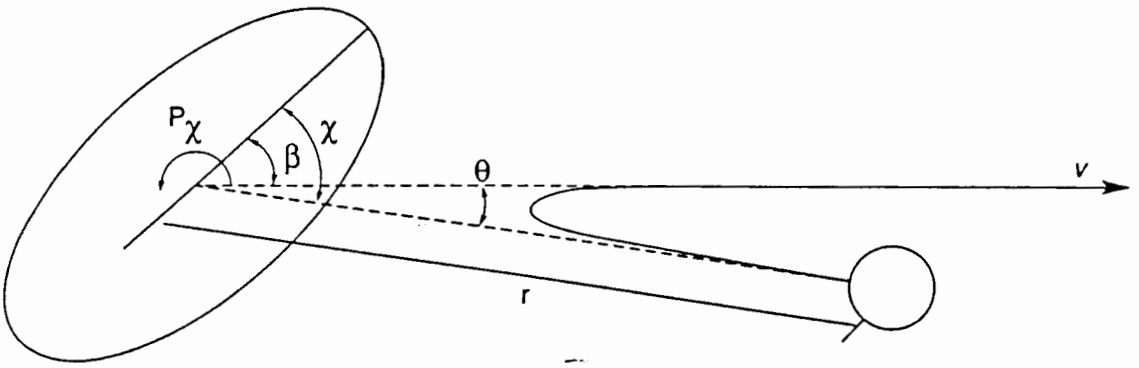

Figure 5.1: Definition of geometry of systems under investigation.

5.1 Sudden Approximation

Perhaps the simplest method that can be devised to calculate the final spin populated in a given reaction is the Sudden Approximation. As the name implies, the target nucleus is assumed not to rotate during the collision, ie., χ remains constant during the interaction. As will be seen, this approximation is valid for light systems and for obtaining an estimate of the spin at the distance of closest approach. However, other dynamical effects destroy the validity of the method for heavier systems.

The following Monte Carlo method was used to investigate the Sudden Approximation method of calculating final spin populations, and a FORTRAN code called SPIN was developed to utilize this method. Random orientation angles, χ_0, were chosen by the computer from a $\sin 2\chi_0$ distribution. In the Sudden Approximation limit, the final spin is given by:

$$I_f = 2q_2 \sin 2\chi_0 \tag{5.1}$$

where χ_0 is the initial orientation angle, and q_2, the quadrupole strength parameter, is given by:

$$q_2 = \frac{Z_p Q_0 e^2}{4\hbar v_0 a^2} \tag{5.2}$$

where Q_0 is the quadrupole moment, $e^2 = 1.44$ MeV·fm, Z_p is the charge of the projectile, v_0 is the initial relative velocity at large distance where the interaction is assumed to be negligible, and a is half the distance of closest approach,

$$a = \frac{Z_p Z_t e^2}{\mu v_0^2} \tag{5.3}$$

where Z_t is the charge of the target, and μ is the reduced mass of the system [83]. Hence, the reason for generating random orientation angles from a $\sin 2\chi$ distribution. It should be noted from equation (5.1) that the maximum final spin possible is associated with a $\chi_0 = 45°$, and thus $I_{fmax} = 2q_2$.

The change in angular momentum (assume $E2$'s connect rotational energy levels) is given by:

$$\Delta J = 2\text{NINT}\left(\frac{\Delta J_{max} \sin 2\chi_0}{2}\right), \tag{5.4}$$

where NINT is the operation of taking the nearest integer of the argument in the parenthesis. The possible final spins to be populated are then partitioned according to the Clebsch-Gordan coefficients $\langle I\ \Delta J\ I\ 0 \mid I_{int}\ I\rangle^2$, where the Clebsch-Gordan notation used is $\langle J_1\, J_2\, m_1\, m_2 \mid J_3\, -m_3\rangle^2$; I is the initial target spin, and I_{int} is the possible half integer spin to be populated. It should be noted that $\sum_{I_{int}} \langle I\ \Delta J\ I\ 0 \mid I_{int}\ I\rangle^2 = 1$ by definition. The spin then populated

is:

$$I_{pop} = I_{int} + |\Delta J - I| - 1. \tag{5.5}$$

The results are then histogrammed to generate the Coulomb excitation or inelastic excitation rotational population pattern. For neutron transfer, however, the transferred neutron has some angular momentum, i. Transfer of an aligned neutron modifies the change in angular momentum to $\Delta J - i$, as there is a loss of total angular momentum in this case. The anti-aligned neutron results in a change of angular momentum to $\Delta J + i$. The neutron angular momentum, i, is calculated using a simple two-level model. The two $j_{\frac{15}{2}}$ levels involved in transfer of a neutron in the ^{235}U case are the $\frac{7}{2}^-$ and the $\frac{5}{2}^-$ levels (the ground state of ^{235}U is $K = \frac{7}{2}^-$). The cranking Hamiltonian, $H - \frac{\hbar^2}{2\Im}\vec{I}\cdot\vec{j}$, can be solved by diagonalizing the 2×2 matrix:

$$\begin{vmatrix} E_{\frac{7}{2}} - w & \frac{\hbar^2}{\Im}\hat{I}\hat{j} \\ \frac{\hbar^2}{\Im}\hat{I}\hat{j} & E_{\frac{5}{2}} - w \end{vmatrix} = 0, \tag{5.6}$$

where $\hat{I} = \sqrt{I(I+1) - K(K+1)}$, $\hat{j} = \sqrt{j(j+1) - \Omega(\Omega+1)}$, $E_{\frac{7}{2}}$ is the energy of the $K + 1 = \Omega + 1 = \frac{7}{2}^-$ level, $E_{\frac{5}{2}}$ is the energy of the $K = \Omega = \frac{5}{2}^-$ level, $j = \frac{15}{2}$ and w is the eigenvalue to solve for. Note that the off-diagonal matrix elements are the Coriolis coupling terms. The total angular momentum

at closest approach is then:

$$R_{tot} = R_{core} + i. \tag{5.7}$$

The spin populated if an aligned neutron is transferred is:

$$I_{trans} = \mathrm{NINT}(2I_{pop} - i), \tag{5.8}$$

and that for the transfer of the anti-aligned neutron is:

$$I_{trans} = \mathrm{NINT}(2I_{pop} + i - 1), \tag{5.9}$$

where i is reduced by one unit of angular momentum to attempt to account for the fact that the anti-aligned state is not as strong as the aligned state. Transfer of an aligned neutron reduces the final angular momentum, and transfer of an anti-aligned neutron increases the final angular momentum of the product. The results are then histogrammed to obtain the neutron transfer population pattern. Typically, 10,000 random orientation angles were chosen. Additionally, to attempt to correct for the overestimation of the final spin in the Sudden Approximation, as the final spin is proportional to the quadrupole moment, Q_0, calculations were performed with Q_0 reduced by $15-20\%$. This reduction of Q_0 by 20%, however, neglects some very serious dynamical effects, which, as we shall see later, have a large effect on the final population pattern. The

most serious of these dynamical effects is that the nucleus does rotate during the collision, and thus for some choices of initial orientation angles, can over-rotate on the outward path; thus the nucleus experiences a negative torque, and the final spin achieved can be significantly lower than $2I_{CA}$. Also, the effects of the nuclear potential are ignored. The results from the SPIN code, and a further discussion of the dynamical effects are in Chapter 6.

The Sudden Approximation was also investigated using the Classical-Limit S-matrix method given by equation 46 of [84]. A FORTRAN code, SMATRIX, was written to utilize the following method. In this method, instead of choosing a random initial orientation angle, χ_0, the probability of populating final spin, I, can be calculated by numerical integration of:

$$P_{0\to I} = \sqrt{2I+1}\int_0^1 P_I(x)\exp\left(-i\frac{4}{3}q_2P_2(x)\right)dx, \tag{5.10}$$

where $P_I(x)$ and $P_2(x)$ are Legendre polynomials and $x = \cos\chi_0$. The probabilities for an even-even nucleus are obtained first. Final probabilities for odd-A nuclei are then given by:

$$P_{odd-A}(j) = \sum_{j'=I-\frac{1}{2}}^{I_{max}-\frac{1}{2}} (2j+1)\begin{pmatrix} I_t & j' & I \\ I_t & -I_t & 0 \end{pmatrix}^2 P_{e-e}(I), \tag{5.11}$$

where I is the even-even spin, I_t is the initial target spin and I_{max} is the

maximum even-even spin populated, with the array in parentheses a Wigner $3j$-symbol. The maximum spin, I_{max}, was usually chosen to be large ($\sim 40\hbar$). The probabilities for populating even-even levels and odd-A rotational levels can then be obtained for the Coulomb excitation case.

Under the assumption of equal transfer amplitudes over the spheroidal nuclear surface, neutron transfer reactions can be handled by modifying equation (5.10) as in [85]:

$$P_{TRANS}(I) = N\sqrt{2I+1}\int_0^1 P_l^m(x)a_{tun}(x)a_{abs}(x)P_I^0(x)\exp\left(-i\frac{4}{3}q_2P_2^0(x)\right)dx, \tag{5.12}$$

where N is a normalization factor given by:

$$N = (-1)^m\frac{\sqrt{2l+1}(l-m)!}{4\pi(l+m)!} \tag{5.13}$$

and l and m are the quantum numbers of the principal orbit involved in the transfer (for $i_{\frac{13}{2}}$ orbital $l = 7, m = 3$). A tunnelling factor, $a_{tun}(x)$, is given by:

$$a_{tun}(x) = \exp\left(0.052\ r(x)\right), \tag{5.14}$$

where $r(x)$ is the transfer distance at an angle $x = \cos\chi_0$. The slope factor of 0.052 was obtained by fitting the ^{116}Sn + ^{161}Dy, ^{116}Sn + ^{163}Dy and

^{58}Ni + ^{161}Dy one-neutron transfer $\ln(P)$ vs. D experimental data [86]. Equation (5.12) also includes an absorption factor:

$$a_{abs}(x) = \exp\left(\frac{\sqrt{8\pi\mu a_w}AW_0}{Z_p Z_t e^2\hbar}\exp\left(\frac{r(x)}{a_w}\right)\right), \tag{5.15}$$

where the diffuseness, $a_w = 0.54$ fm and the imaginary part of the nuclear potential, $W_0 = 25$ MeV. Probabilities for one-neutron transfer from odd-A to even-even nuclei can then be calculated by numerical integration of equation (5.12). Additional factors can be included in equation (5.12) to calculate two-neutron transfer of the SQUID effect–in fact, Canto et al. include a spectroscopic form factor, a_{spec}, in reference [85], to take into account microscopic nucleon structure in the nuclear SQUID effect. A discussion of a new SQUID calculation, and results from SMATRIX can be found in Chapter 6.

5.2 Alder-Winther-deBoer modified method

5.2.1 General Description

The general formalism of the Alder-Winther-deBoer method can be found in [73], and there exists a FORTRAN code for calculating Coulomb excitation

probabilities [87]. The projectile is assumed to move on a classical Rutherford trajectory, $r(t)$, and the structure of the projectile and target in different channels is given by the Hamiltonian:

$$H_o|n\rangle = \epsilon_n|n\rangle, \tag{5.16}$$

where ϵ_n are the eigenvalues. H_o includes no interaction between the projectile and target and thus $|n\rangle$ is a product of projectile and target wavefunctions:

$$|n\rangle = |\Psi_t\rangle|\Psi_p\rangle. \tag{5.17}$$

At any time, t, the wavefunction can be expanded in terms of these eigenstates:

$$|\Psi(t)\rangle = \sum_n a_n(t)e^{i\epsilon_n t}|n\rangle, \tag{5.18}$$

where $a_n(t)$ are time-dependent amplitude coefficients.

When the projectile and target collide, this produces an interaction potential $V(t)$ which causes excitation along the band of eigenstates. The time-dependent Hamiltonian is:

$$H(t) = H_o + V(t) \tag{5.19}$$

and the coupled time-dependent Schrödinger (TDS) equations can be written:

$$i\frac{d}{dt}a_j(t) = \sum_i \langle j|V(t)|i\rangle e^{i(\epsilon_j-\epsilon_i)t}a_i(t), \tag{5.20}$$

where $a_j(t)$ and $a_i(t)$ are the rotational state population amplitudes. Planck's constant $\hbar$ is considered unity in this expression. The Alder-Winther-deBoer method solves the TDS equations with the initial condition

$$a_n(t = -\infty) = \delta_{n0} \tag{5.21}$$

with only the lowest rotational amplitude being non-zero before the collision. The final probabilities at $t = \infty$ are:

$$P_f(\infty) = |a_f(\infty)|^2 . \tag{5.22}$$

In all cases here excitation of the projectile is neglected. This is a reasonable first approximation, as in most cases experimental projectiles have been chosen to be closed-shell nuclei (or closed-subshell), and thus they have fairly high first excited states. The interaction potential, $V(t)$, can be expanded in terms of spherical harmonics

$$V(r(t)) = \sum_{\mu\nu} V_{\mu\nu}(r) Y^*_{\mu\nu}(\hat{r}), \tag{5.23}$$

and equations (5.20) can be rewritten as:

$$i\frac{d}{dt}a_j(t) = \sum_i \sum_{\mu\nu} (-1)^{J_j - M_j} \begin{pmatrix} I_j & \lambda & I_i \\ -M_j & \mu & M_i \end{pmatrix} \langle j \| V_\lambda(r(t)) \| i \rangle e^{i(\epsilon_j - \epsilon_i)t} a_i(t), \tag{5.24}$$

where $\langle j \| V_\lambda(r(t)) \| i \rangle$ is the reduced matrix element.

5.2.2 Coulomb Excitation

For Coulomb excitation, the matrix element $\langle j \| V(t) \| i \rangle$ is determined as follows. First, the interaction is calculated in the body-fixed (rotating) frame of the target nucleus and expanded in terms of spherical harmonics:

$$V(r') = \sum_{\lambda\nu'} V_{\lambda\nu'}(r) Y^*_{\lambda\nu'}(\hat{r}'), \tag{5.25}$$

where the primes denote the rotating frame. Because the solution of the equation of motion is performed in the lab frame, the potential is transformed to the lab system by rotation $R(\Omega)$ in the Euler angles Ω:

$$V(r) = \sum_{\lambda\mu\mu'} V_{\lambda\mu'}(r) Y^*_{\lambda\mu}(\hat{r}) D^{\lambda *}_{\mu\mu'}(\Omega). \tag{5.26}$$

Integration over all Euler angles yields a matrix element:

$$\langle f | V(r) | i \rangle = \langle A_f I_f M_f | V(r) | A_i I_i M_i \rangle =$$
$$\sum_{\lambda\mu} (-1)^{I_f - M_f} \begin{pmatrix} I_f & \lambda & I_i \\ -M_f & \mu & M_i \end{pmatrix} Y^*_{\lambda\mu}(\hat{r}) \langle A_f I_f \| V_\lambda(r) \| A_i I_i \rangle, \tag{5.27}$$

where the reduced matrix element is defined as:

$$\langle A_f I_f \| V_\lambda(r) \| A_i I_i \rangle = \sum_{K_f K_i \mu'} \sqrt{2I_f + 1} \sqrt{2I_i + 1}$$
$$(-1)^{I_f - K_f} \begin{pmatrix} I_f & \lambda & I_i \\ -K_f & \mu & K_i \end{pmatrix} \langle \Phi^f_{K_f} | V_{\lambda\mu'}(r) | \Phi^i_{K_i} \rangle, \tag{5.28}$$

where $\Phi^f_{K_f}$ and $\Phi^i_{K_i}$ are the intrinsic eigenstates of the z-component of angular momentum of the target. For the simple case of a head-on collision, $\theta = \pi$, the spherical harmonic $Y_{\lambda\mu}(\hat{r}) = \delta_{\mu 0}\sqrt{(2\lambda+1)/4\pi}$ and $M_f = M_i$. Results are shown in Chapter 6.

5.2.3 Inelastic excitation

For inelastic excitation, one must include the nuclear part of the potential, $V^N(t)$ as well as the Coulomb potential, $V^C(t)$:

$$V(t) = V^C(t) + V^N(t). \tag{5.29}$$

The Coulomb potential can be written in a multipole expansion:

$$V^C_{\lambda\mu'}(r) = \frac{Z_p e^2}{r^{\lambda+1}} \frac{4\pi}{2\lambda+1} Q^{int}_{\lambda\mu'}, \tag{5.30}$$

where $Q^{int}_{\lambda\mu'}$ are the intrinsic multipole moments.

The nuclear potential is taken from the standard deformed optical model potentials:

$$V^N(r') = \frac{-(U+iW)}{1+\exp\left[(r - R_p - R_t(\hat{r}'))/a\right]}, \tag{5.31}$$

where U and W are the real and imaginary potential well depths, respectively,

and R_t can be expressed, for an axially symmetric nucleus, as:

$$R_t(\chi') = R_t \left(1 + \sqrt{\frac{5}{4\pi}}\beta P_2(\cos\chi')\right), \tag{5.32}$$

where $R_t = r_o A_t^{\frac{1}{3}}$ and β is the deformation parameter. The nuclear potential can also be written in terms of spherical harmonics and transformed to the lab frame:

$$V_{\lambda 0}^N = \sqrt{4\pi(2\lambda+1)}\frac{1}{2}\int_{-1}^{1} \frac{-(U+iW)}{1+\exp\left[(r-R_p-R_t(\chi))/a\right]} P_\lambda(\cos\chi) d(\cos\chi). \tag{5.33}$$

The reduced matrix elements, for fixed K, are:

$$\langle A_f I_f \| V_\lambda^C(r) + V_\lambda^N(r) \| A_i I_i \rangle = \sqrt{2I_f+1}\sqrt{2I_i+1}(-1)^{I_f-K} \begin{pmatrix} I_f & \lambda & I_i \\ -K & \mu & K \end{pmatrix} V_{\lambda 0}(r). \tag{5.34}$$

However, inclusion of $V^N(r)$ causes a distortion of the Rutherford trajectory. This cannot be handled exactly in the Alder-Winther-deBoer formulation. However, since the quadrupole torque from electric and nuclear forces is largest at closest approach, it is important that the Rutherford trajectory be nearly correct at closest approach. We do this by choosing an effective beam energy and target Z. Thus, a method of reproducing the turning point and

proper force at this point by reducing the lab beam energy and effective charge of the spheroidal collision partner is developed. The intrinsic quadrupole moment is fixed so that torque from electromagnetic forces remains unaltered. The turning point, r_{CA}, is found by numerically solving the equation:

$$E_{CM} = \frac{Z_p Z_t e^2}{r_{CA}} + U(r_{CA}), \tag{5.35}$$

where E_{CM} is the beam energy in center-of-mass reference frame, and $U(r_{CA})$ is the real part of the nuclear optical potential, $V^N(r)$. The radial force, F_{CA}, is simply the negative derivative of the full potential:

$$F_{CA} = \frac{Z_p Z_t e^2}{r_{CA}^2} - \left(\frac{dU}{dr}\right)_{r_{CA}}. \tag{5.36}$$

The effective charge, Z_{eff}, and the effective energy, E_{eff}, are then given by:

$$\frac{Z_p Z_{eff} e^2}{r_{CA}^2} = F_{CA} \tag{5.37}$$

and

$$E_{eff} = \frac{Z_p Z_{eff} e^2}{r_{CA}}. \tag{5.38}$$

The Alder-Winther-deBoer method run with these reduced E_{eff} and Z_{eff} parameters more closely matches [79] the full coupled channel results for ^{40}Ar + ^{160}Gd of reference [75]. Results are shown in Chapter 6.

5.2.4 Neutron Transfer

Two methods of applying modified Alder-Winther-deBoer calculations shall be described. The first method involves running the Alder-Winther-deBoer method described in the Coulomb Excitation Section (5.2.2) and multiplying the occupation amplitudes at closest approach by a transfer matrix, $T_{I'I}$. It is generally accepted that the neutron transfer process is localized in time and space around the point of closest approach, $t = 0$, in the calculation. $T_{I'I}$ is obtained by integration of:

$$T_{I'I} = T_0 \int_{-1}^{1} P_{I'}(x) a_{tun}(x) a_{abs}(x) F_{I'I}(x) P_I(x) dx, \tag{5.39}$$

where $P_{I'}(x)$ and $P_I(x)$ are Legendre polynomials, $a_{tun}(x)$ and $a_{abs}(x)$ are the tunnelling and absorption terms described in the Sudden Approximation Section 5.1, T_0 is the normalization factor between transfer from target to projectile and the time reversed reaction ($T_0 = 1$ for our cases since the ratio is unknown), and $F_{I'I}(x)$ is the angular transfer form factor at the inner turning point, r_{CA}. For example, the two-neutron angular form factor is given by:

$$F_{I'I}(x) = \langle A+2, I' | S^{\dagger}(r_{CA}) | A, I \rangle. \tag{5.40}$$

The intrinsic states $|A+2, I'\rangle$ and $|A, I\rangle$ are approximated by Cranked Hartree-Fock-Bogoliubov (CHFB) functions and $F_{I'I}(x)$ is calculated with the $S^{\dagger}(r_{CA})$

operator being a pair creation/annihilation operator (or single neutron creation/annihilation operator for one-neutron transfer). The angular form factors represent the structure of the target, specifically, the site dependence of transfer on the deformed target surface. If one neglects pairing and the dependence of the intrinsic wavefunction on the collective angular momentum, and assumes the neutron(s) are transferred to a particular Nilsson orbital (governed by the target wavefunction), $F_{I'I}(x)$ is proportional to the $|\sum Y_{lm}(\theta\phi)|^2$, where θ and ϕ are the polar angles. For example, pair transfer to the $i_{\frac{13}{2}}$ intruder shell in the rare-earths yields a form factor, $F_{I'I}(x) = |Y_{6m}(\theta\phi)|^2$, as shown in reference [88]. In this thesis, both the approximation of spherical harmonics and CHFB functions are used.

Thus, the method is to run the integration of amplitudes from $t = -\infty$ to $t = 0$, stop the calculation, multiply by $T_{I'I}$ as follows:

$$a'_I(0) = \sum_I T_{I'I}\, a_I(0) \tag{5.41}$$

and after the multiplication, continue the time evolution with the $a'_I(0)$ amplitudes. The final probabilities are given as in equation (5.22).

Because $T_{I'I}$ contains significant off-diagonal matrix elements, representing transfer of neutron(s) with angular momentum ($\Delta I = I' - I$), there are several

additional factors to be considered. First, there is a centrifugal barrier which will add to the tunnelling factor $a_{tun}(x)$. Second, there is an effect due to the finite size of the projectile. Indeed, since a heavy-ion projectile is not a point-like probe of a varying $F_{I'I}$ function, there will be some angular smearing over the surface. These effects are estimated by considering a square tunnelling barrier between the nuclear surfaces at the classical turning point. Two factors are obtained:

$$g_1(\Delta I) = \exp\left(-\left([4m_n(B_{CENT}+S)]^{\frac{1}{2}} - (4m_nS)^{\frac{1}{2}}\right)\left(\frac{r_{CA}-R_t-R_p}{\hbar}\right)\right), \tag{5.42}$$

where m_n is the neutron mass, S is the one- or two-neutron separation energy, r_{CA} is the distance of closest approach, and

$$B_{CENT} = \frac{\hbar^2\Delta I(\Delta I+1)}{4m_nR_t^2}, \tag{5.43}$$

and

$$g_2(\Delta I) = \exp\left[-\left(\frac{y\Delta I}{R_t}\right)^2\right], \tag{5.44}$$

where y, the characteristic width parameter of the tunnelling wave packet is:

$$y = (2\hbar)^{\frac{1}{2}}(4m_nS)^{-\frac{1}{4}}\left(\frac{1}{R_t}+\frac{1}{R_p}\right)^{-\frac{1}{2}}. \tag{5.45}$$

For inclusion of these factors, the $T_{I'I}$ in equation (5.39) are multiplied by g_1 and g_2. Results from these calculations are presented in Chapter 6.

The second method involves a more direct evaluation of the $\langle f|V^{tr}(r)|i\rangle$ matrix element, and does not limit the transfer to $t = 0$. For pair transfer,

$$\langle f|V^{tr}(r)|i\rangle = T_0\langle f|B^\dagger(r)|i\rangle, \tag{5.46}$$

where $B^\dagger(r)$ is a boson (Cooper pair of neutrons) creation operator. As usual, $B^\dagger(r)$ can be decomposed in terms of spherical harmonics, and thus the reduced matrix element can be written:

$$\langle A_f I_f \| V_\lambda^{tr}(r) \| A_i I_i\rangle = T_0 \sum_{K_f K_i \mu'} \sqrt{2I_f+1}\sqrt{2I_i+1}$$
$$(-1)^{I_f-K_f} \begin{pmatrix} I_f & \lambda & I_i \\ -K_f & \mu' & K_i \end{pmatrix} \langle \Phi^f_{K_f}|B^\dagger_{\lambda\mu'}(r)|\Phi^i_{K_i}\rangle, \tag{5.47}$$

where

$$B^\dagger_{\lambda\mu'}(r) = \int B^\dagger(\hat{r})Y_{\lambda\mu}(\hat{r})d^2\hat{r}. \tag{5.48}$$

These matrix elements contain information on the structure of nuclear states in the rotational band. Because these matrix elements are needed at very large radii, r, where the oscillator functions used for the calculation of the intrinsic many-body wavefunctions are not reliable, and decomposition of the intrinsic wavefuntion with respect to quantum number K requires a projection, two approximations are used. To address the problem with the wavefunctions, a

penetrability factor is introduced. Since it is difficult to express the actual wavefunction in terms of microscopic wavefunctions at large distance, r, it is approximated in this region by a wavefunction $\phi(r, E)$ of a single boson in a deformed Woods-Saxon well $U(r)$ with mass, m_B, and energy E, determined by the binding energy of the boson in the projectile. This wavefunction can then be decomposed in spherical harmonics:

$$\phi(\hat{r}, E) = \frac{1}{r} \sum_{lm} \phi_{lm}(r, E) Y_{lm}(\hat{r}), \tag{5.49}$$

and the coupled-channels equation

$$\begin{aligned} &\left[-\frac{1}{2m_b} \frac{d^2}{dr^2} + \frac{l(l+1)}{r^2} + U_0(r) - E \right] \phi_{lm}(r, E) = \\ &\quad - \sum_{\lambda > 0 \mu} \sum_{l' \mu'} U_{\lambda\mu}(r) \frac{\sqrt{2l+1}\sqrt{2\lambda+1}\sqrt{2l'+1}}{\sqrt{4\pi}} (-1)^m \\ &\quad \cdot \begin{pmatrix} l & \lambda' & l' \\ 0 & 0 & 0 \end{pmatrix} \begin{pmatrix} l & \lambda & l' \\ -m & \mu & m' \end{pmatrix} \phi_{l'm'}(r, E) \end{aligned} \tag{5.50}$$

for these wavefunctions. A matching radius, R, is chosen to be large enough to be outside the range of the potential, U, but small enough that the representation of the wavefunction in terms of ϕ is still reliable. Thus,

$$\phi_{lm}(r, E) = P_l(r, R, E) \phi_{lm}(R) \tag{5.51}$$

where the penetrability, $P_l(r, R, E)$ in the WKB approximation is:

$$P_l(r, R, E) = \exp\left[-\int_R^r \sqrt{\frac{l(l+1)}{r'^2} - 2mE}dr'\right]. \tag{5.52}$$

The reduced transition matrix element is then:

$$\langle f \| B_\lambda^\dagger(r) \| i \rangle = P_\lambda(r - R_p, R, E)\langle f \| B_\lambda^\dagger(R) \| i \rangle, \tag{5.53}$$

where the r is replaced by $r - R_p$ because the transfer takes place mostly at the surface of the projectile.

The second approximation, the high-spin approximation, for large I and small K ($K \ll I$ and $\lambda \ll I$), makes use of the semiclassical expression for the Wigner coefficient

$$\sqrt{2I_f + 1}(-1)^{I_f - K_f} \begin{pmatrix} I_f & \lambda & I_i \\ -K_f & \mu & K_i \end{pmatrix} = d^\lambda_{\mu\Delta I}(-\frac{\pi}{2}), \tag{5.54}$$

where $\Delta I = I_f - I_i$ is the angular momentum transfer and $d^\lambda_{\mu\Delta I}(-\frac{\pi}{2})$ describes a rotation of 90° around the y-axis. Thus, the reduced transition matrix elements can be written:

$$\langle A_f I_f \| V_\lambda^{tr}(R) \| A_i I_i \rangle = T_0\sqrt{2I_i + 1}\langle \Phi^f | \tilde{B}^\dagger_{\lambda\Delta I}(R) | \Phi^i \rangle, \tag{5.55}$$

where

$$\tilde{B}^\dagger_{\lambda\mu} = \sum_{\mu'} d^\lambda_{\mu'\mu}(-\frac{\pi}{2}) B^\dagger_{\lambda\mu'}. \tag{5.56}$$

The matrix elements $\langle\Phi^f|B^\dagger_{\lambda\mu}(R)|\Phi^i\rangle$, again can be found through decomposition of the angular form factor given below in terms of spherical harmonics:

$$F(R) \equiv \langle\Phi^f|B^\dagger_{\lambda\mu}(R)|\Phi^i\rangle = \sum_{\lambda\mu} a_{\lambda\mu}(R) Y^*_{\lambda\mu}(\hat{R}), \tag{5.57}$$

where $\hat{R}$ is a vector with the length of the matching radius, R. Thus,

$$a_{\lambda\mu}(R) = \langle\Phi^f|B^\dagger_{\lambda\mu}(R)|\Phi^i\rangle \tag{5.58}$$

and has the property

$$a_{\lambda\mu}(R) = (-1)^\lambda a_{\lambda(-\mu)}(R). \tag{5.59}$$

Similarly, an $\tilde{a}_{\lambda\mu}(R)$ quantized along the x-axis can be defined:

$$\tilde{a}_{\lambda\mu}(R) = \langle\Phi^f|\tilde{B}^\dagger_{\lambda\mu}(R)|\Phi^i\rangle, \tag{5.60}$$

where

$$\tilde{a}_{\lambda\mu}(R) = (-1)^\lambda \tilde{a}_{\lambda(-\mu)}(R) \tag{5.61}$$

and $\tilde{a}_{\lambda\mu}(R) = 0$ for odd values of μ. The coefficients , $a_{\lambda\mu}(R)$, can be found with some Clebsch-Gordan algebra in terms of a transition density matrix,

$F_{nn'}$:

$$a_{\lambda\mu}(R) = \sum_{nn'll'mm'} F_{nljm,n'l'j'm'} R_{nl}(R) R_{n'l'}(R) (-1)^{l+j-\frac{1}{2}+\mu}$$
$$\cdot \frac{\sqrt{2l+1}\sqrt{2l'+1}\sqrt{2j+1}\sqrt{2j'+1}\sqrt{2\lambda+1}}{\sqrt{8\pi}}$$
$$\cdot \begin{pmatrix} l & \lambda & l' \\ 0 & 0 & 0 \end{pmatrix} \begin{pmatrix} j & \lambda & j' \\ m & -\mu & m' \end{pmatrix} \begin{Bmatrix} j & \lambda & j' \\ l' & \frac{1}{2} & l \end{Bmatrix}, \tag{5.62}$$

where $R_{nl}(R)$ and $R_{n'l'}(R)$ are radial wavefunctions and the array in curly brackets is the Wigner $6j$ symbol. Finally, the reduced transition matrix element can be written as:

$$\langle A_f I_f \| V_\lambda^{tr}(r) \| A_i I_i \rangle = T_0 \sqrt{2I_i + 1} P_\lambda(r - R_p, R, E) \tilde{a}_{\lambda(I_f - I_i)}(R). \tag{5.63}$$

Note, the $P_\lambda(r - R_p, R, E)$ term includes centrifugal effects more naturally in this formalism.

For one-neutron transfer, from an odd-A nucleus to an even-even nucleus, a similar derivation can be used. Basically, one merely has to include the odd-A odd-particle with spin:

$$|\psi_i^{(t)}\rangle = |m_s\rangle |\psi_f^{(t)}\rangle. \tag{5.64}$$

Thus, the matrix elements are:

$$\langle f|V^{tr}(r)|i\rangle = \sum_{jm} C^{\frac{1}{2}\,l\,j}_{m_s\,m_l\,m} Y_{l(m-m_s)}(\hat{r})(-1)^{I_f-M_f}(-1)^{j-m}$$

$$\begin{pmatrix} I_f & j & I_i \\ -M_f & -m & M_i \end{pmatrix} \langle f\|V_j^{tr}(r)\|i\rangle, \tag{5.65}$$

and the reduced matrix element is:

$$\langle f\|V_j^{tr}(r)\|i\rangle = \sqrt{2}\sqrt{2I_i+1}\sqrt{2I_f+1}$$

$$\sum_n C^{K_f}_{nlj} R_{nl}(r)(-1)^{I_f+j-K_i} \begin{pmatrix} I_f & j & I_i \\ 0 & -K_i & K_i \end{pmatrix}, \tag{5.66}$$

where C's are Casimir coefficients and

$$R_{nl}(r) = P_l(r - R_p, R, E)R_{nl}(R) \tag{5.67}$$

according to the approximations discussed above.

Chapter 6

Comparison of Theory with Experimental Data

This chapter will compare the results of the theoretical methods discussed in Chapter 5 with the experimental data. Historically, it has been difficult to compare experimental data with theoretical calculations because experiments were run at specific beam energies, scattering angles, etc. and calculations have mostly been for head-on collisions and have neglected nuclear potential effects, scattering angle effects, etc. This is reflected in the large number of intra-theory comparisons and small number of theory-experiment comparisons. As a first comparison of data to theory, to just introduce the effectiveness of the theoretical methods in Chapter 5, a brief discussion of the SQUID effect and the results of the calculations will be presented and compared with a ^{156}Gd + ^{206}Pb experiment that is the work of Helmer et al. [89] (see Section

6.1). Then, the rotational population patterns will be presented for the ^{58}Ni + ^{233}U experiment (Section 6.2), the ^{206}Pb + ^{233}U experiment (Section 6.2), and the ^{90}Zr + ^{239}Pu experiment (Section 6.3), and compared to theoretical calculations.

6.1 Brief SQUID Results

The Superconducting Quantum Interference Device (SQUID) effect is discussed more completely in the literature [90],[91]. Briefly, it can be described as follows. Because the Coulomb force is a long range force, and nucleon transfer occurs with the highest probability at the distance of closest approach in a given heavy-ion nuclear reaction, the nucleon transfer tends to occur from rotationally excited states. If Coulomb excitation can pump in enough angular momentum to excite the target nucleus to the backbending region (or diabolical point) on the inward path of the projectile, two transfer paths exist: (1) The inward-path Coulomb excitation adds angular momentum to just below the diabolical point, nucleon transfer occurs below that point, and then the product nucleus is again Coulomb excited on the outward path of the projectile; or (2) The inward-path Coulomb excitation adds angular momentum to

just above the diabolical point, nucleon transfer occurs above that point, and then the product nucleus is Coulomb excited on the outward path. These two transfer paths quantum interfere. Nikam and Ring [92] found that the pair transfer matrix elements not only tended to sharply decrease in the region around the diabolical point, but also went negative. The experimental signature of this effect would be a sharp decrease in the population probability, and there have been several attempts to establish the region in which such an effect would manifest itself ([15],[80],[85]). Originally, because many calculations were performed in the Sudden Approximation limit, it was thought that the sharp decrease would occur at a spin twice that of the diabolical or backbending point, and little hope was held for experimental observation of the SQUID effect. The backbending point in the rare earths is $\sim 12 - 14\hbar$, thus one would need to observe at least to spin $24 - 28\hbar$, and even higher to be able to distinguish (1) a large decrease in the population probability from (2) a lack of statistics. The situation is even worse in the actinides, as the backbending point tends to be even higher in spin ($\sim 30\hbar$). Our most recent calculations [93], however, hold out the hope that perhaps a SQUID effect could be observed at lower spins (as low as $10 - 14\hbar$).

It is not the purpose of this thesis to completely discuss the SQUID effect

and the calculations, rather, it is the intention to present the results as an illustration of the theoretical model of Chapter 5 Section 5.2.4 and to compare with a recent experiment as a springboard for comparisons in the actinide region. Figures 6.1 and 6.2 show the calculated results using the method of Section 5.2.4 for the ^{208}Pb + ^{160}Dy (Figure 6.1) and ^{208}Pb + ^{158}Dy (Figure 6.2) neutron pair transfer reactions. In both, the beam energy was 1100 MeV, the population probabilities at spin 0 are normalized to unity, and the scattering angle is 180°. Figure 6.1 corresponds to a case with a diabolical point, and Figure 6.2 corresponds to a case without a diabolical point. The dotted line (square symbols) is the calculation performed for the case where the functions $F_{I'I}(x)$ (see Section 5.2.4) are set to unity, and the full line (•) corresponds to a calculation performed with the full transfer matrix $T_{I'I}$. A comparison of Figures 6.1 and 6.2 shows the large dip in population probability starting around spin 10, but enlarging at spins 14 – 16, for the case in which a diabolical point exists. From numerous other calculations with different combinations of input parameters not shown here, this dip at spin $I \approx 12\hbar$ is fairly robust.

Figure 6.3 compares the solid line (•) of Figures 6.1 and 6.2 with experimental two-neutron transfer yields in the same region in the rare earths from the ^{156}Gd + ^{206}Pb reaction. Pair transfer yields as a function of spin are pre-

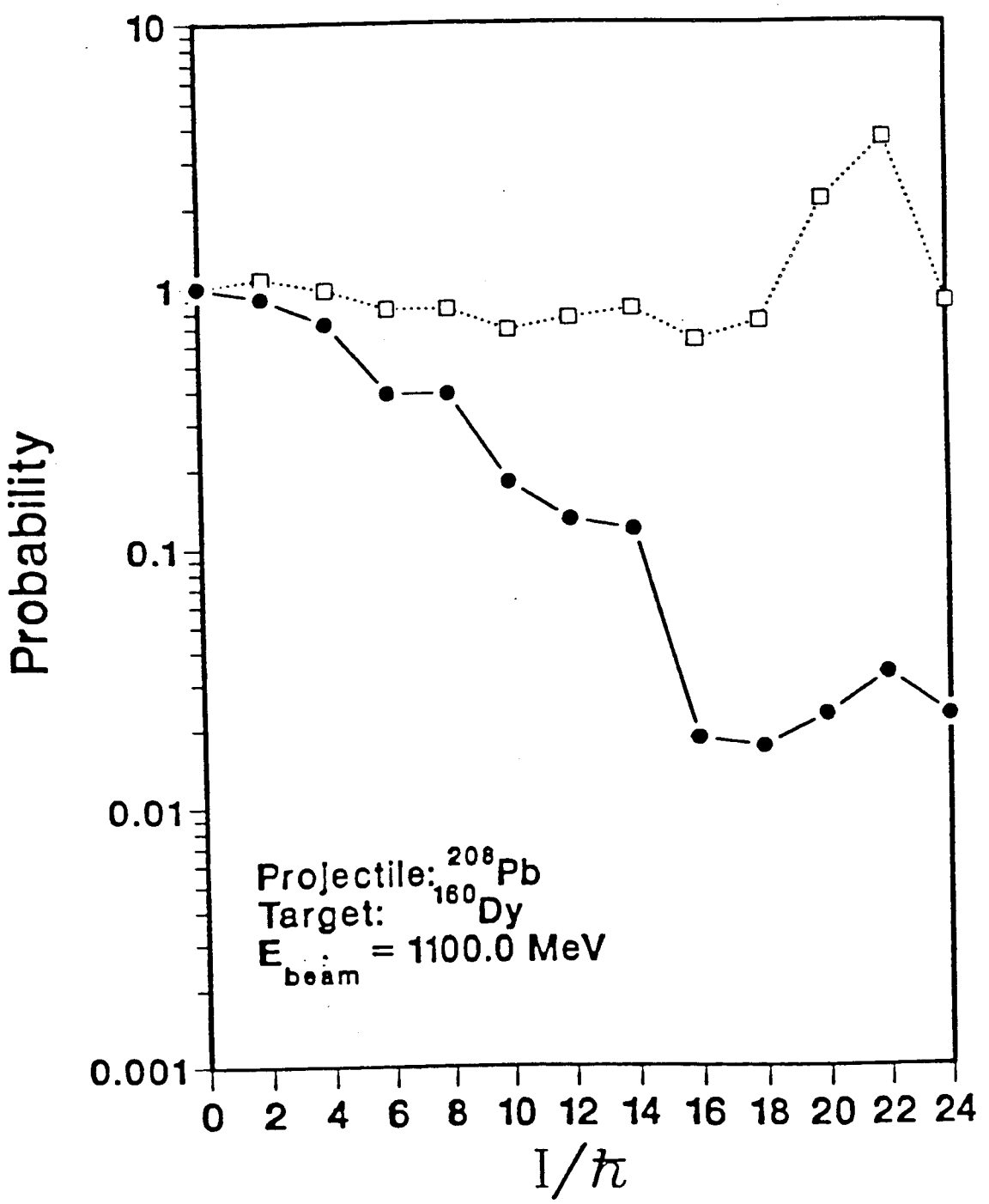

Figure 6.1: Theoretical calculation of the rotational population probability for states in the ground band in the neutron pair transfer reaction ^{208}Pb + ^{160}Dy reaction. The dotted line (open squares) is the calculation performed for the case where the functions $F_{I'I}(x)$ (see Section 5.2.4) are set to unity, and the full line (•) corresponds to a calculation performed with the full transfer matrix $T_{I'I}$.

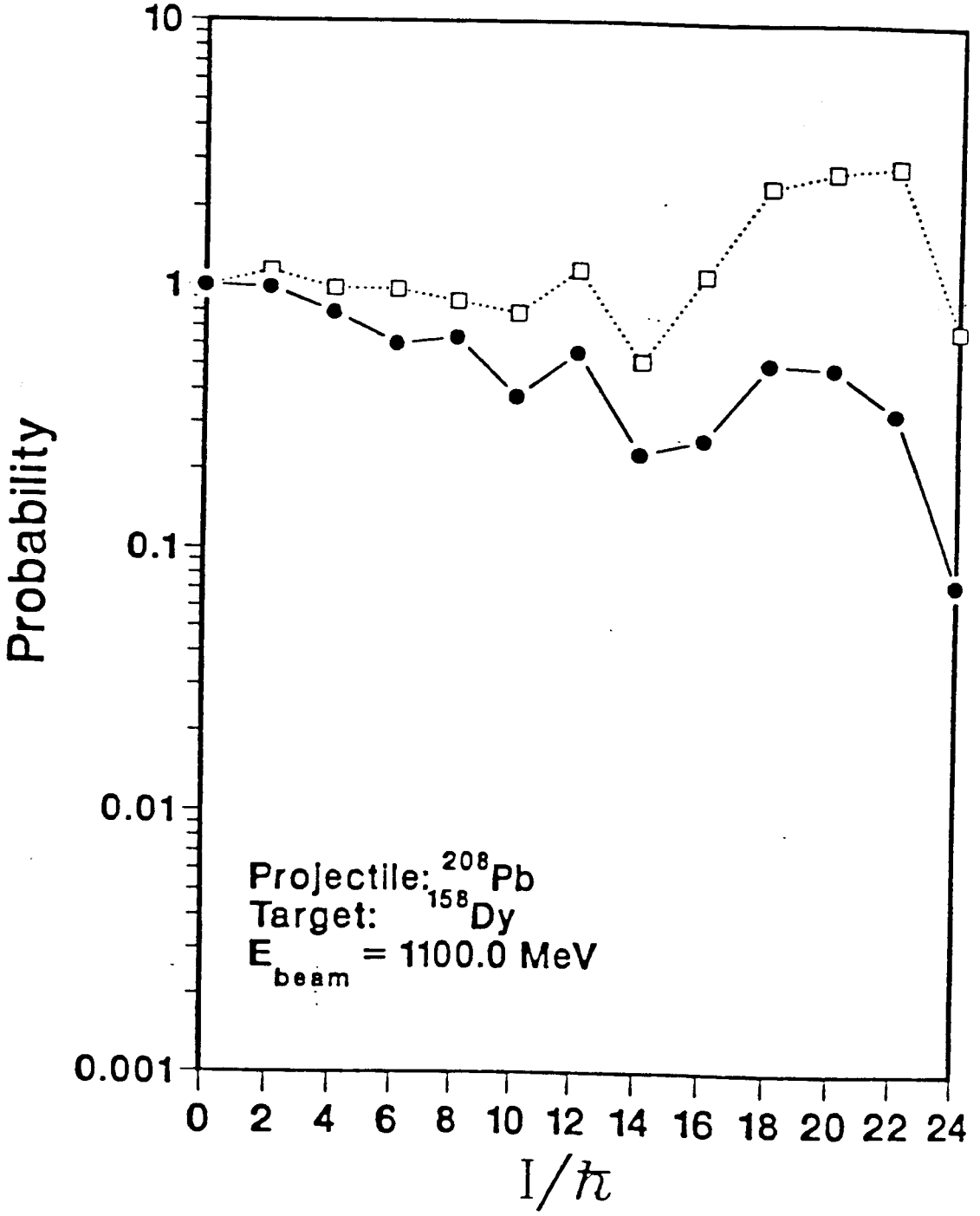

Figure 6.2: Theoretical calculation of the rotational population probability for states in the ground band in the neutron pair transfer reaction ^{208}Pb + ^{158}Dy reaction. The symbols are the same as for Figure 6.1.

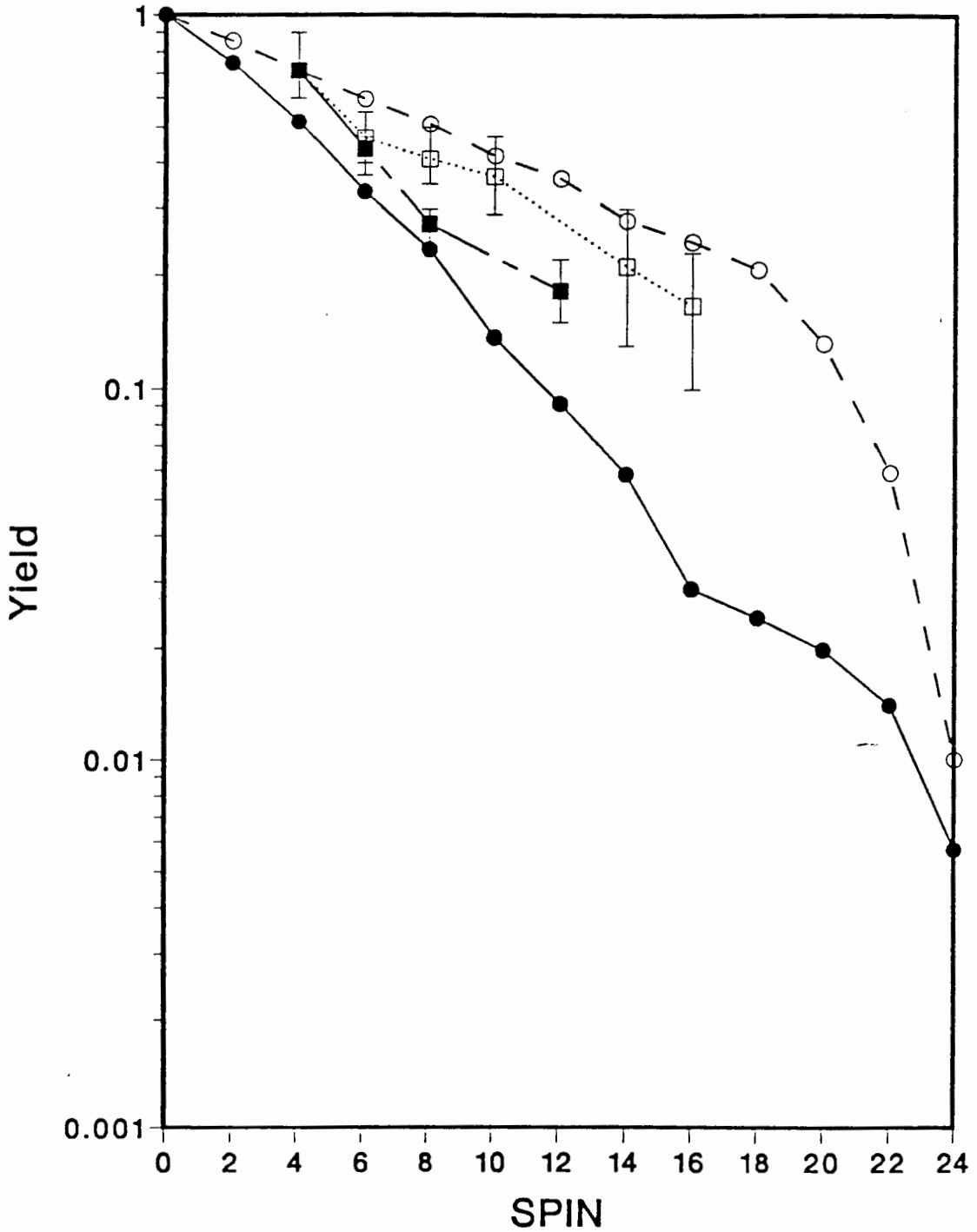

Figure 6.3: A comparison of the experimental rotational population yields extracted from the reaction ^{156}Gd + ^{206}Pb with the calculations of theory from Section 5.2.4 for the reactions ^{208}Pb + ^{160}Dy and ^{208}Pb + ^{158}Dy. The solid line (•) presents the case with the diabolical point, the dashed line (open circles) presents the case without a diabolical point, the dotted line (open squares) is data for ^{154}Gd and the chain-dashed (closed squares) is data for ^{158}Gd.

sented for both ^{158}Gd (chain-dashed line, solid squares) and ^{154}Gd (dotted line, open squares). The transfer yields for both ^{158}Gd and ^{154}Gd are between the two calculated curves, the upper curve demonstrating a non-diabolic case, and the lower curve demonstrating the diabolic case. It should be noted, however, that the experimental data are not corrected for side-feeding, which could have an effect on the final populations, and that the calculations were not done for the exact system studied experimentally. The precise position of the diabolical point depends in a sensitive way on the parameters of the model, such as deformation and pairing parameters. The present theories are not precise enough to predict the exact location of the diabolical point, and experiments may determine that it is shifted to a different neutron number from what is depicted in this case. Additionally, the statistics of the experiment were marginal (reflected in the error bars). We make no claim that these data show the SQUID effect, as the results lie between the calculated signatures, defying distinguishing between the two cases. However, it demonstrates the problems associated with theory-experiment comparisons and illustrates the quality of such comparisons.

6.2 ^{233}U Results

Figure 6.4 compares the rotational population pattern extracted from the University of Rochester (UOR) ^{58}Ni + ^{233}U Coulomb excitation experiment with several theories. The experimentally observed pattern (•) is corrected for internal conversion and cascade-to-crossover ratios. Angular distribution effects are assumed to average out. Additionally, the maximum spin observed in the experiment is assumed to be the maximum state populated. As the beam energy for this experiment (249 MeV) was well below the Coulomb barrier (325 MeV), no correction for side-feeding should be required. The population probability peaks around spin $\frac{19}{2}^+$ and drops off to $\frac{1}{10}$ of the strength by spin $\frac{29}{2}^+$. The results of the Sudden Approximation methods of Section 5.1 are shown for the Monte Carlo method (dashed line, open circles) and the S-matrix method (dotted line, open squares) and generally reproduce the maximum population spin and fall off above the rainbow. The rainbow is a quantum mechanical effect where states higher than the maximum spin and classically forbidden are populated with an exponentially decreasing probability (or an upside-down rainbow). Both methods overestimate the location of the maximum probability, an indication that the Sudden Approximation may

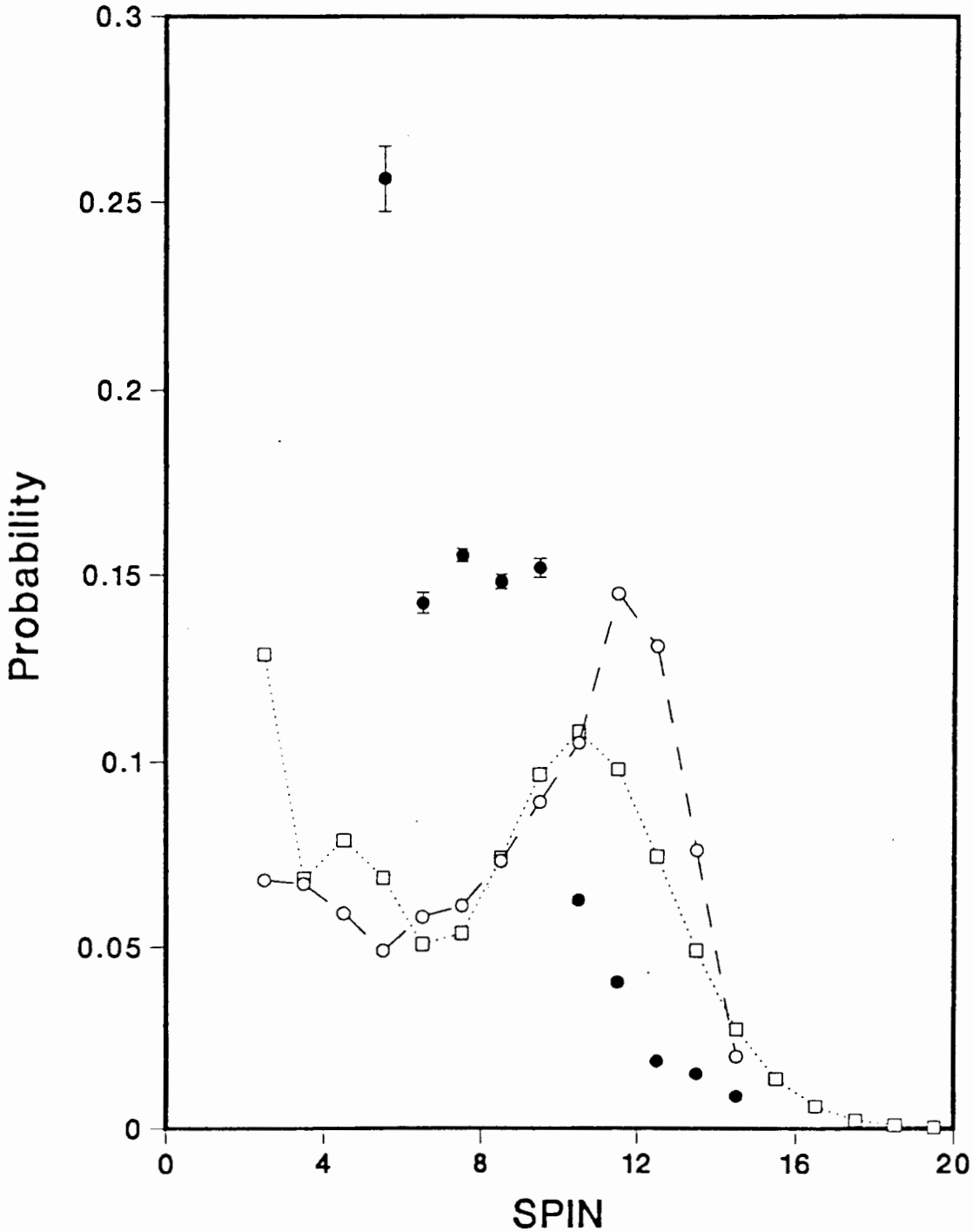

Figure 6.4: Rotational population pattern for the ^{58}Ni + ^{233}U Coulomb excitation experiment. The experimental data (•) are compared to the Monte Carlo method (dashed line, open circles) and the S-Matrix method (dotted line, open squares). Note the oscillation around spin $\frac{11}{2}^+$ in the calculation.

be having some difficulties with systems as heavy as Ni + U. The location of the maximum probability can be decreased by 2−4 units of angular momentum with a 10% reduction in the quadrupole moment, Q_0. Two initial orientation angles, χ, a large angle and a small angle, populate the same final spin, and thus, can quantum interfere. This interference pattern is known as Coulomb oscillations. The theoretical methods exhibit a Coulomb oscillation around spin $\frac{11}{2}^+$, in a region where experimental data doesn't exist. The Coulomb oscillations in the Monte Carlo method are more washed out, something that is observed in the ^{206}Pb + ^{233}U experiment also. However, such oscillations are not completely washed out in the experimental data. This, of course, generated the effort to look at other methods for calculating rotational population patterns. It should be noted that nuclear potential effects are not included in these calculations, probably not a serious approximation as the beam energy is below the Coulomb barrier. In general, these Sudden Approximation methods, while not predicting the overall magnitude of the probability correctly, seem to reproduce some of the oscillations in the rotational population pattern and roughly reproduce the location of the peak. Please note that the details of the location of the peak depend sensitively on the magnitude of the quadrupole moment and the beam energy. The quadrupole moment is not reduced by 10%

in these calculations.

Figure 6.5 compares the rotational population pattern extracted from the SuperHILAC ^{206}Pb + ^{233}U inelastic excitation experiment with theory. The experimentally observed pattern (•) is plotted with error bars and is corrected for detector efficiency and internal conversion. The most noticeable feature of the probability pattern is the presence of the large oscillations at spins $\frac{13}{2}^+$, $\frac{19}{2}^+$, $\frac{29}{2}^+$ and $\frac{37}{2}^+$, which appear to be due to Coulomb oscillations, or the interference pattern produced because two initial orientation angles χ, a small angle and a large angle, yield the same final spin. It should be noted that the data are corrected for internal conversion and cascade-to-crossover ratios, but are not corrected for side-feeding. The maximum spin observed is assumed to be the highest spin populated in the experiment. Three theoretical calculations are presented, the Sudden Approximation methods (1) Monte Carlo (dashed curve, open circles), (2) S-matrix method (dotted curve, open square symbols) and (3) the Alder-Winther-deBoer method (chain-dashed line, closed squares). The Sudden Approximation methods have the quadrupole moment Q_0 reduced by 10% to compensate for the over-estimation of the maximum final spin populated, and generally reproduce the rainbow maximum. The rainbow maximum is not observed very strongly in the experimental data,

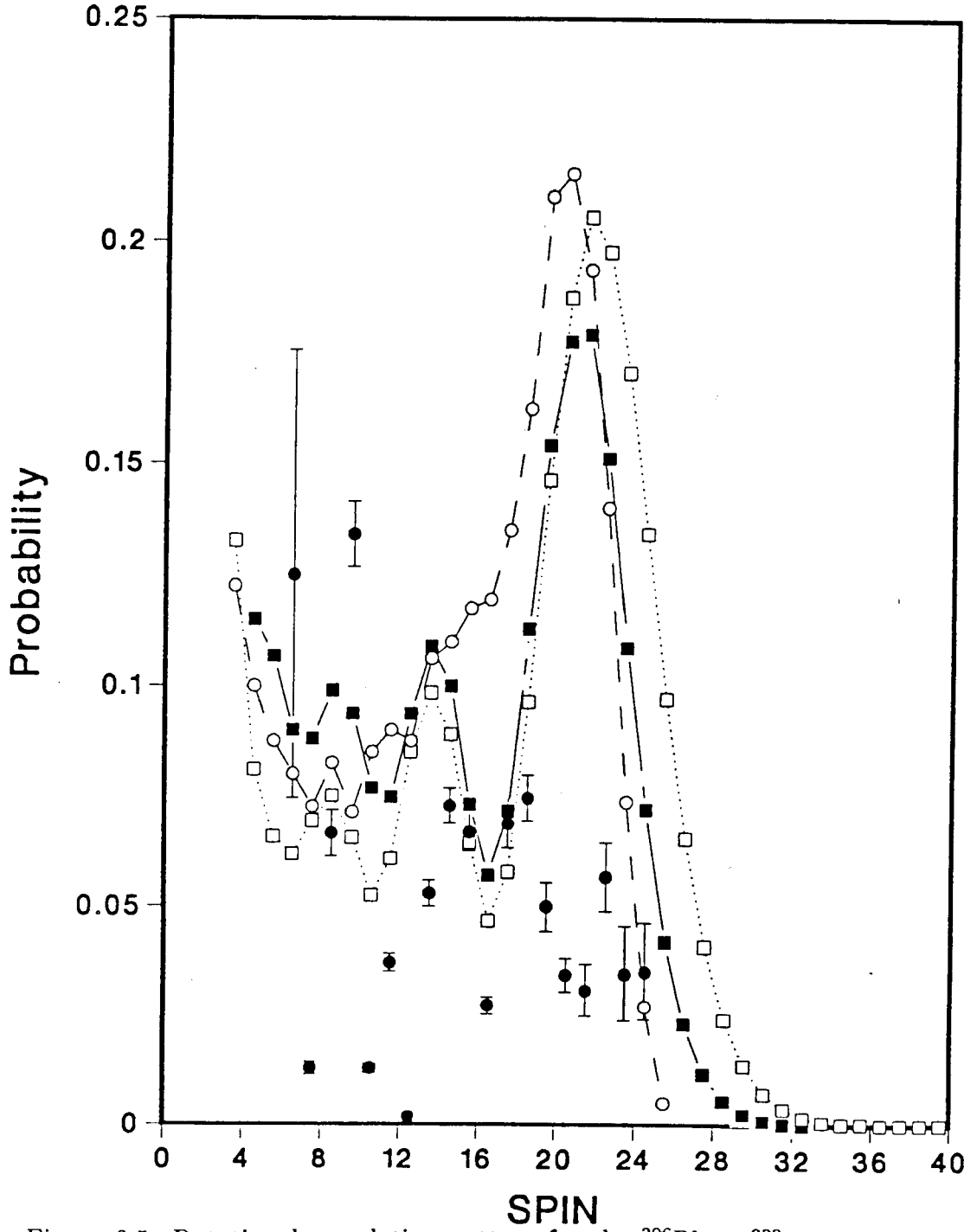

Figure 6.5: Rotational population pattern for the ^{206}Pb + ^{233}U inelastic excitation experiment. Experimental data (•) are compared with the Monte Carlo method (dashed curve, open circles), S-Matrix method (dotted curve, open square symbols) and the Alder-Winther-deBoer method (chain-dashed line, closed squares). A complete discussion of this Figure is found in the text.

consistent with the fact that the reaction is run with a beam energy near the Coulomb barrier, although the oscillation around spin $\frac{37}{2}^+$ could be identified as such. The rainbow maximum was taken from the Alder-Winther-deBoer method calculations, and one can see that the Sudden Approximation methods (with Q_0 reduced by 10%) generally agree. The Monte Carlo calculation seems to wash out the Coulomb oscillations at lower spins more than the other methods. The other two calculations agree very well on the location of those oscillations, around spins $\frac{17}{2}^+$ and $\frac{27}{2}^+$. These compare very well, in quality if not in magnitude, to those oscillations observed in the experiment around spins $\frac{19}{2}^+$ and $\frac{29}{2}^+$. However, it appears that the Alder-Winther-deBoer method offers a better comparison. Namely, a 10% reduction in Q_0 does not include dynamical effects which may be important in the final rotational population pattern (the data are not good enough to state whether this is the case or not) for such a heavy system. We have already seen this in the Pb + Dy calculations. The target is not stationary during the collision, and especially for large initial orientation χ angles ($> 60 - 70°$), the nucleus may rotate past 90° during the collision, changing the sign of the torque which may actually reduce the final spin populated. Overall, the comparison of theory with experimental data is marginal.

6.3 ^{90}Zr + ^{239}Pu Results

6.3.1 ^{239}Pu Inelastic Excitation

Figure 6.6 compares the rotational population of the ground band in ^{239}Pu in the ^{90}Zr + ^{239}Pu $\rightarrow$ ^{90}Zr$'$ + ^{239}Pu$'$ experiment with Alder-Winther-deBoer theory. The experimental data (•) is corrected for internal conversion and assuming the $\frac{49}{2}^+$ level is the highest populated in the reaction, but not corrected for side-feeding and assuming cascade-to-crossover ratios are negligible (valid at higher spins, where the E_γ factor makes $E2$ transitions more favorable than $M1$ transitions). A dip in the population probability is observed at spin $\frac{21}{2}^+$. The dashed line is a pure Coulomb excitation calculation using the Alder-Winther-deBoer method discussed in Section 5.2.2 using experimental rotational state energies for a beam energy of 500 MeV and scattering angle of 180°. For comparison, a calculation using ^{238}Pu rotational state energies and assuming the odd-neutron is fully decoupled from the core and then partitioning intensities among the $I \pm \frac{1}{2}$ states by statistical weight $2I+1$ is shown. It is very similar to the Alder-Winther-deBoer method calculation using the ^{239}Pu energy levels. However, the calculations exhibit more oscillations at lower

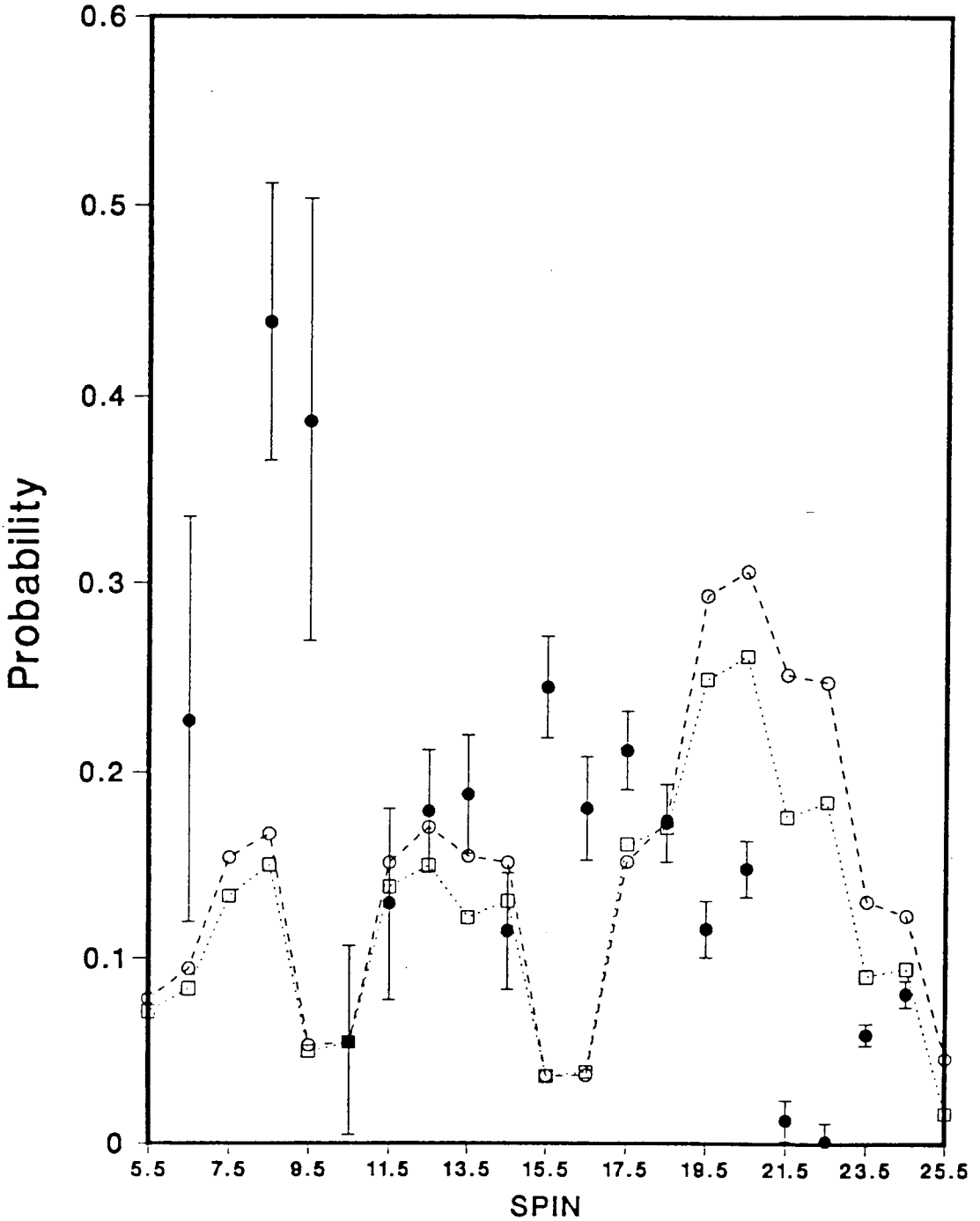

Figure 6.6: Inelastic excitation rotational population pattern in the ground band of ^{239}Pu. Experimental data (•) are compared with Alder-Winther-deBoer theories. Pure Coulomb excitation (dashed line, open circles) for ^{239}Pu is compared to a calculation (dotted line, open squares) using ^{238}Pu energy levels and partitioning final probabilities as discussed in the text. As the two theories are very similar, the approximation of a spectator odd-neutron is valid. The theory curves are normalized to the experimental data at spin $\frac{21}{2}^+$.

spins than are experimentally observed, although the dip around spin $\frac{21}{2}^+$ is qualitatively reproduced. The dip at spin $\frac{29}{2}^+$ in the data may qualitatively be associated with the dip in the theories around spin $\frac{31}{2}^+$; however, the dip at $\frac{45}{2}^+$ is not reproduced. If there was population of states higher than $\frac{49}{2}^+$ in the experiment, the last two points may be higher than normal, as some transition strength (for the higher transitions) would not be subtracted out correctly.

Figure 6.7 presents the rotational population pattern derived from spot intensities in the γ-γ coincidence spectrum gated on Yrast transitions. The experimental errors are larger because of poorer statistics. Again, the population probabilities are corrected for internal conversion, and I assume the $\frac{41}{2}^+$ level is the highest populated in the reaction and neglect cascade-to-crossover ratios. Relative spot intensities are extracted from the γ-γ coincidence spectrum by gating on individual rotational transition γ-rays for ^{239}Pu and then fitting the resulting spectrum with peaks of fixed energy and width. The peak positions and widths were obtained from fits of Figure 3.17. The Gaussian width used was 2.9 keV. The relative spot intensities are tabulated in Table 6.1 and are corrected for detector efficiency and internal conversion.

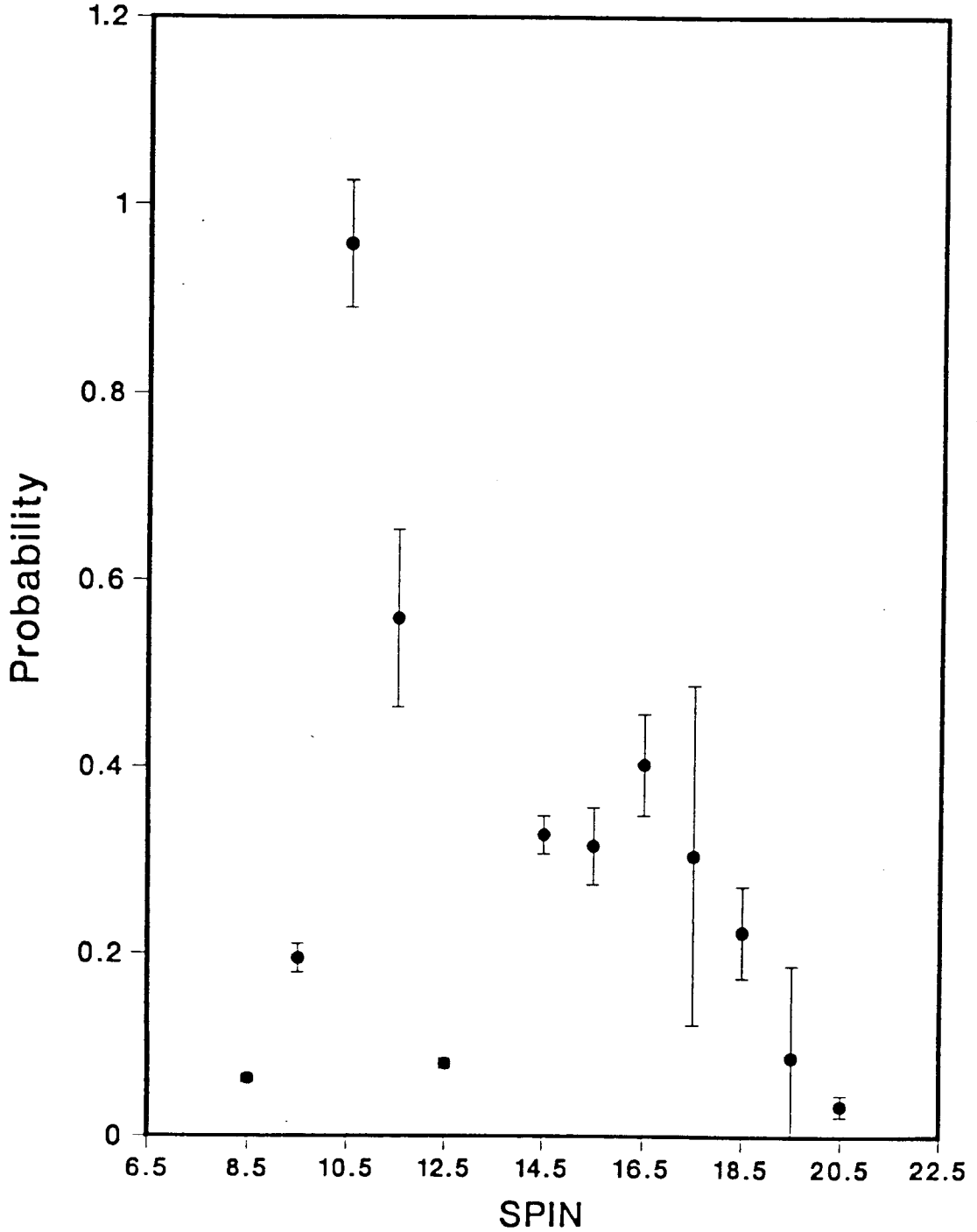

Figure 6.7: Inelastic rotational population pattern for the ground band in ^{239}Pu extracted from the γ-γ coincidence spectrum gated on Yrast transitions.

Table 6.1: Relative spot intensities for the probability of populating a given spin in ^{239}Pu including a gate to exclude side-feeding.

Trans. (keV)	154.0	165.0	201.1	211.8
154.0	-	-	276011 ±15%	94704 ±42%
165.0	-	-	24336 ±138%	166513 ±19%
201.1	226192 ±19%	-	-	-
211.8	-	153533 ±20%	-	-
245.3	122377 ±28%	61300 ±44%	308315 ±6%	24245 ±65%
256.7	-	97902 ±27%	24557 ±68%	164261 ±10%
288.1	-	32825 ±82%	150574 ±11%	45546 ±35%
299.6	-	29506 ±92%	10462 ±163%	90297 ±15%
328.5	69283 ±51%	-	100196 ±18%	16523 ±98%
340.0	-	38120 ±72%	28752 ±61%	66602 ±25%
367.3	142833 ±26%	-	100885 ±18%	-
379.0	-	-	22726 ±82%	30474 ±57%
403.5	-	24161 ±122%	45710 ±42%	16005 ±112%
415.5	-	-	-	-
437.8	53319 ±83%	-	-	-
450.9	-	-	-	-

Table 6.1: Continuation of relative spot intensities for ^{239}Pu

Trans. (keV)	245.3	256.7	288.1	299.6
154.0	145911 ±23%	56788 ±60%	18944 ±176%	-
165.0	52388 ±51%	130946 ±21%	-	-
201.1	252237 ±7%	39857 ±42%	143931 ±12%	-
211.8	10717 ±143%	125168 ±13%	20928 ±74%	59265 ±27%
245.3	-	-	84728 ±16%	-
256.7	-	-	-	51651 ±27%
288.1	87704 ±16%	-	-	-
299.6	-	87588 ±16%	10686 ±130%	-
328.5	87490 ±16%	21484 ±8%	170677 ±8%	-
340.0	17199 ±80%	134002 ±11%	-	76425 ±19%
367.3	87897 ±17%	-	81335 ±18%	-
379.0	-	10347 ±143%	-	66766 ±24%
403.5	39141 ±40%	13677 ±113%	12900 ±119%	-
415.5	-	-	-	-
437.8	72610 ±23%	-	19967 ±91%	-
450.9	-	-	-	-

Table 6.1: Continuation of relative spot intensities for ^{239}Pu

Trans. (keV)	328.5	340.0	367.3	379.0
154.0	102826 ±34%	-	102070 ±36%	-
165.0	20355 ±134%	36393 ±75%	-	-
201.1	31101 ±56%	27263 ±63%	71385 ±25%	-
211.8	30862 ±52%	69587 ±23%	16278 ±101%	32717 ±52%
245.3	79077 ±17%	16763 ±82%	60478 ±24%	10926 ±132%
256.7	-	121123 ±12%	-	22697 ±64%
288.1	150486 ±9%	-	64482 ±23%	-
299.6	-	59691 ±93%	7670 ±192%	71262 ±22%
328.5	-	15762 ±93%	84585 ±18%	-
340.0	-	-	-	69662 ±22%
367.3	72072 ±21%	-	-	-
379.0	-	49222 ±31%	-	-
403.5	-	-	39410 ±42%	-
415.5	-	-	-	-
437.8	-	-	19938 ±92%	10225 ±181%
450.9	-	-	-	-

Table 6.1: Continuation of relative spot intensities for ^{239}Pu

Trans. (keV)	403.5	415.5	437.8	450.9
154.0	-	-	-	23354 ±180%
165.0	-	-	-	-
201.1	16118 ±119%	-	-	-
211.8	24404 ±72%	12883 ±137%	-	-
245.3	31882 ±47%	-	46828 ±35%	-
256.7	-	-	-	32949 ±52%
288.1	25596 ±60%	-	9605 ±179%	-
299.6	-	-	-	-
328.5	-	-	-	-
340.0	-	8275 ±191%	-	-
367.3	-	-	-	-
379.0	-	-	-	15567 ±124%
403.5	-	-	25088 ±68%	-
415.5	-	-	-	-
437.8	-	-	-	-
450.9	-	-	-	-

Figure 6.8 shows a calculation of ^{239}Pu rotational population patterns using the methods of Section 5.2.3. The large amount of population probability at lower spins is unexplained with theory. The absorption from the nuclear potential completely suppresses population of high spins, which may be enhancing the peak at lower spins.

6.3.2 ^{238}Pu One-Neutron Transfer Results

Figure 6.9 shows the rotational population patterns for rotational states populated in the one-neutron transfer reaction ^{90}Zr + ^{239}Pu $\rightarrow$ ^{91}Zr + ^{238}Pu for beam energy 500 MeV and mean scattering angle of 140° in the lab. The closed circles (•) are for non-Yrast gated events corrected for internal conversion and detector efficiency, and the closed squares are for Yrast gated events also corrected for internal conversion and detector efficiency. In both cases, the highest transition populated was assumed to be the highest transition shown in the Figure. The relative spot intensities from the γ-γ coincidence spectrum are shown in Table 6.2. The spot intensities are obtained as described in Section 6.3.1, and are corrected for detector efficiency and internal conversion. The points at spin 6 and 8 are questionable because the corrections to the

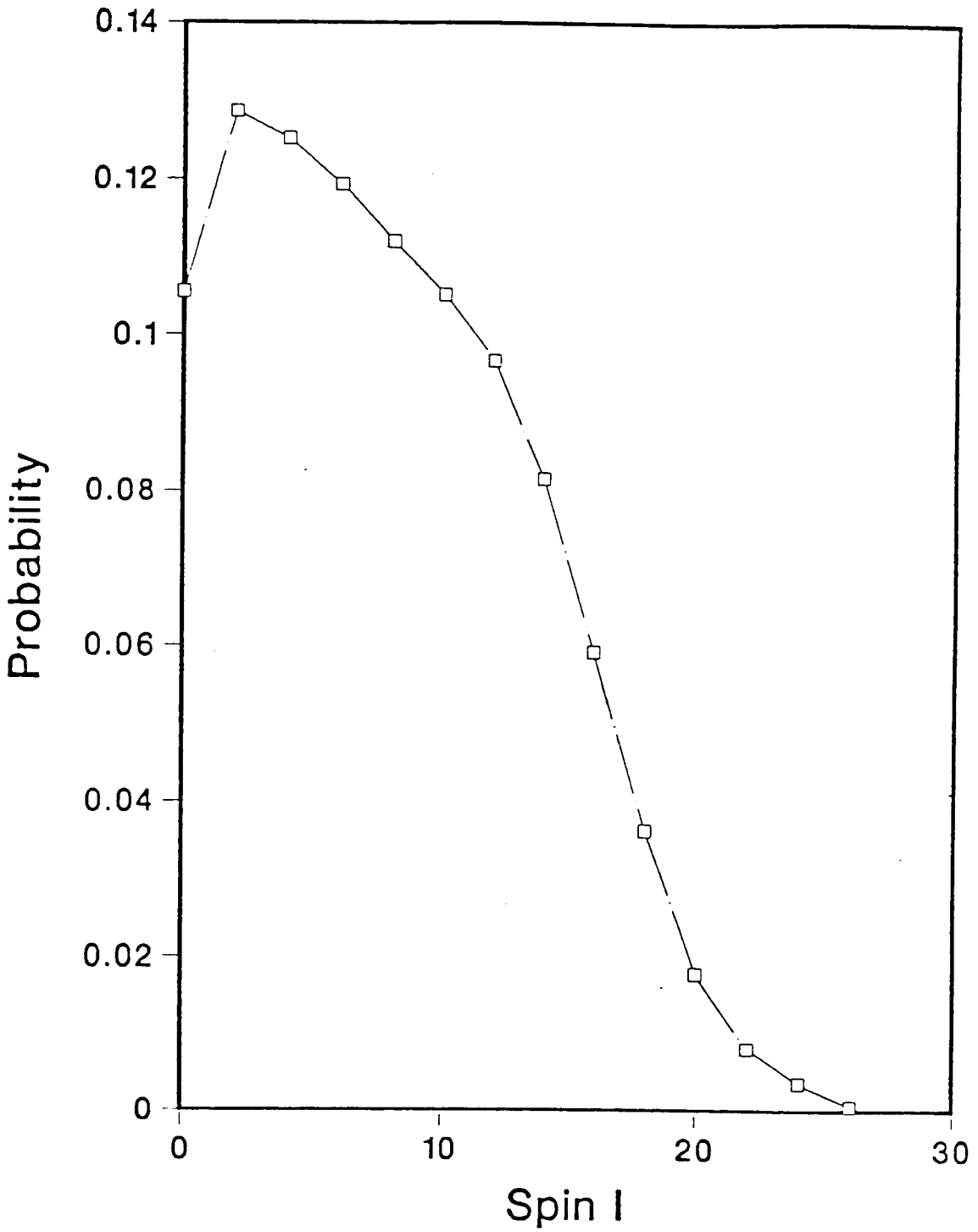

Figure 6.8: Theoretical calculation of rotational population probability for the inelastic excitation experiment $^{90}Zr + ^{239}Pu$.

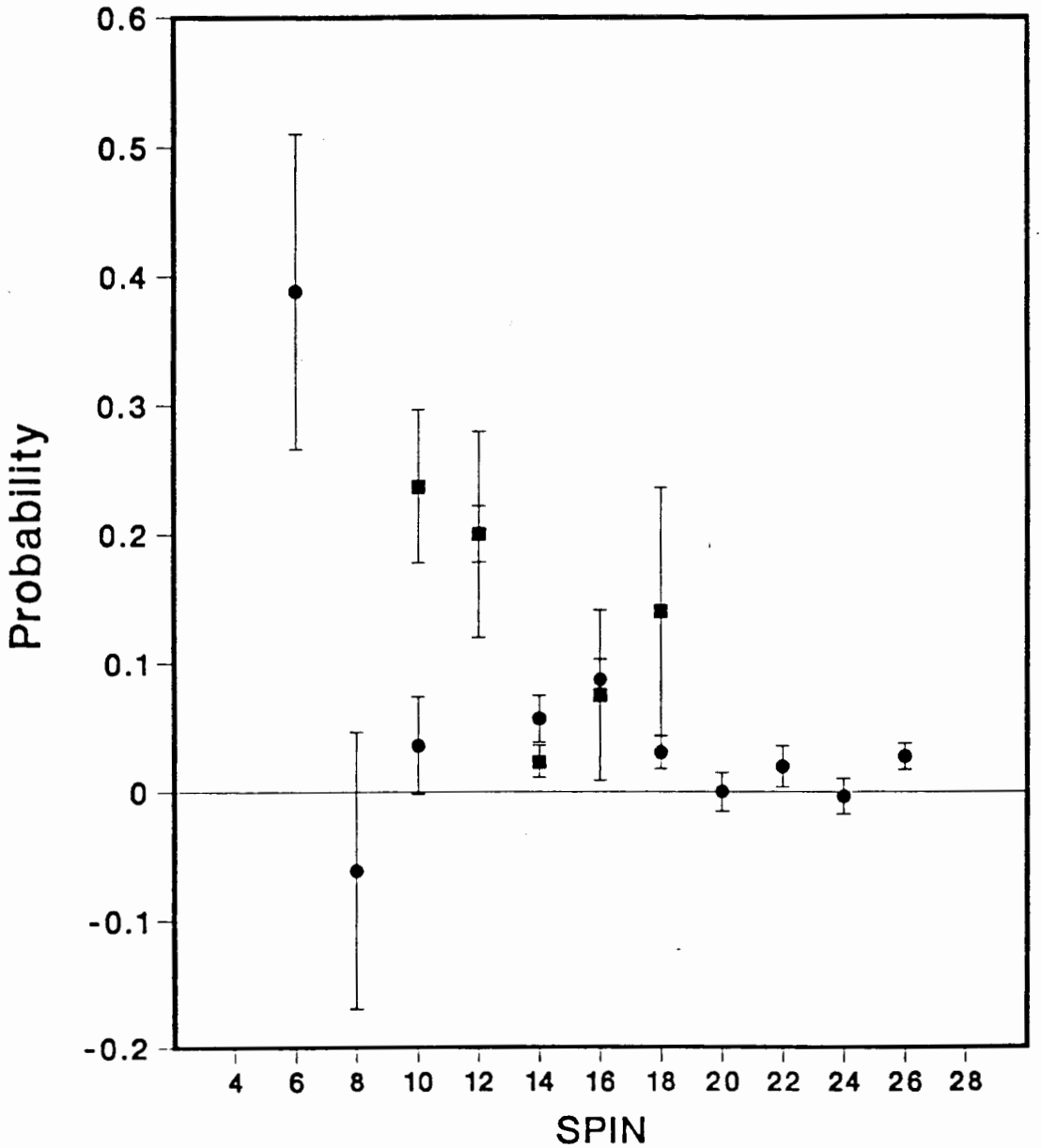

Figure 6.9: Rotational population pattern for the states populated in ^{238}Pu in the one-neutron transfer reaction. Both the probabilities of populating a certain spin excluding side-feeding (closed squares) and including side-feeding (•) are shown. The data are normalized at spin 12. The negative points arise from the subtraction of transition intensities in experiment. Their errors are consistent with the probability being equal to zero.

Table 6.2: Relative spot intensities for the probability of populating a given spin in ^{238}Pu including a gate to exclude side-feeding.

Trans. (keV)	157.2	210.0	259.7	306.5
157.2	-	44285 ±107%	43283 ±72%	47523 ±84%
210.0	76842 ±46%	-	66557 ±35%	48594 ±45%
259.7	45906 ±62%	105791 ±28%	-	31494 ±53%
306.5	73321 ±41%	50770 ±44%	41001 ±45%	-
348.9	-	-	-	17446 ±82%
389.5	22852 ±142%	17903 ±113%	33912 ±63%	28988 ±55%
426.3	-	-	8458 ±184%	25539 ±72%
Trans. (keV)	348.9	389.5	426.3	-
157.2	-	-	-	-
210.0	-	14648 ±128%	-	-
259.7	18056 ±93%	34002 ±56%	-	-
306.5	41122 ±44%	35890 ±54%	30647 ±56%	-
348.9	-	-	-	-
389.5	13282 ±119%	-	-	-
426.3	11825 ±137%	18011 ±127%	-	-

data become very large at these low spins and the errors are correspondingly larger. Thus, the predominant feature of the data is the dip in population probability at spin 14.

Several different theoretical calculations are shown in Figures 6.10, 6.11 and 6.12. Figure 6.10 shows pure Coulomb excitation (chain-dashed line, closed squares) for comparison. The solid line (•) is an Alder-Winther-deBoer calculation in which the real part of the nuclear potential is included in the coupling, the imaginary part is included in the a_{ab_3} term in the transfer matrix $T_{I'I}$, and

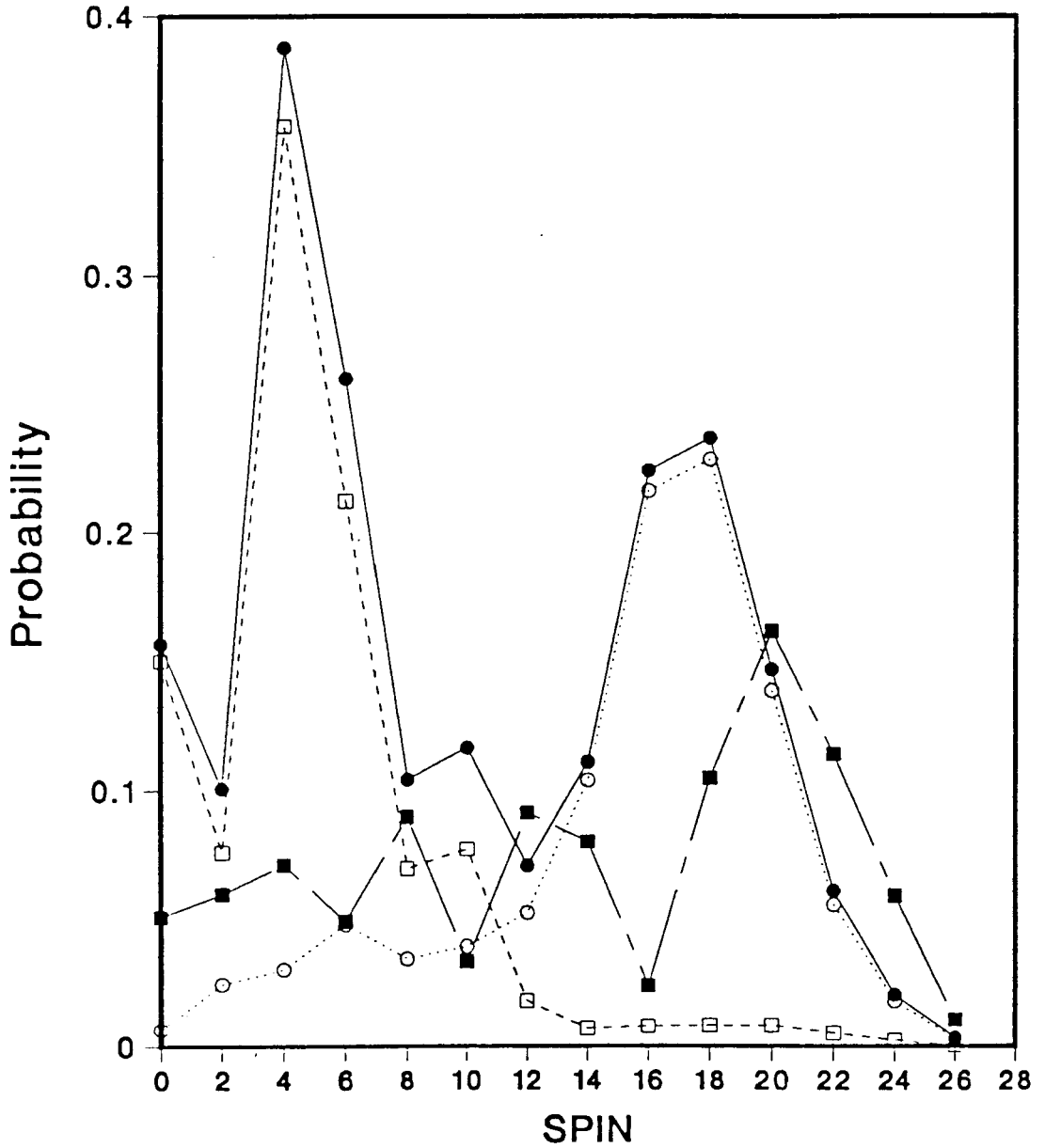

Figure 6.10: Several theoretical calculations of the rotational population patterns in ^{238}Pu from one-neutron transfer using deformation $\eta = 6$. Pure Coulomb excitation (chaindashed line, solid squares) is shown for comparison. Both the spin-up part of the wavefunction (dotted line, open circles) and the spin-down part of the wavefunction (dashed line, open squares) are individually plotted for reasons given in the text. The calculation including the total wavefunction is shown in the solid line (•).

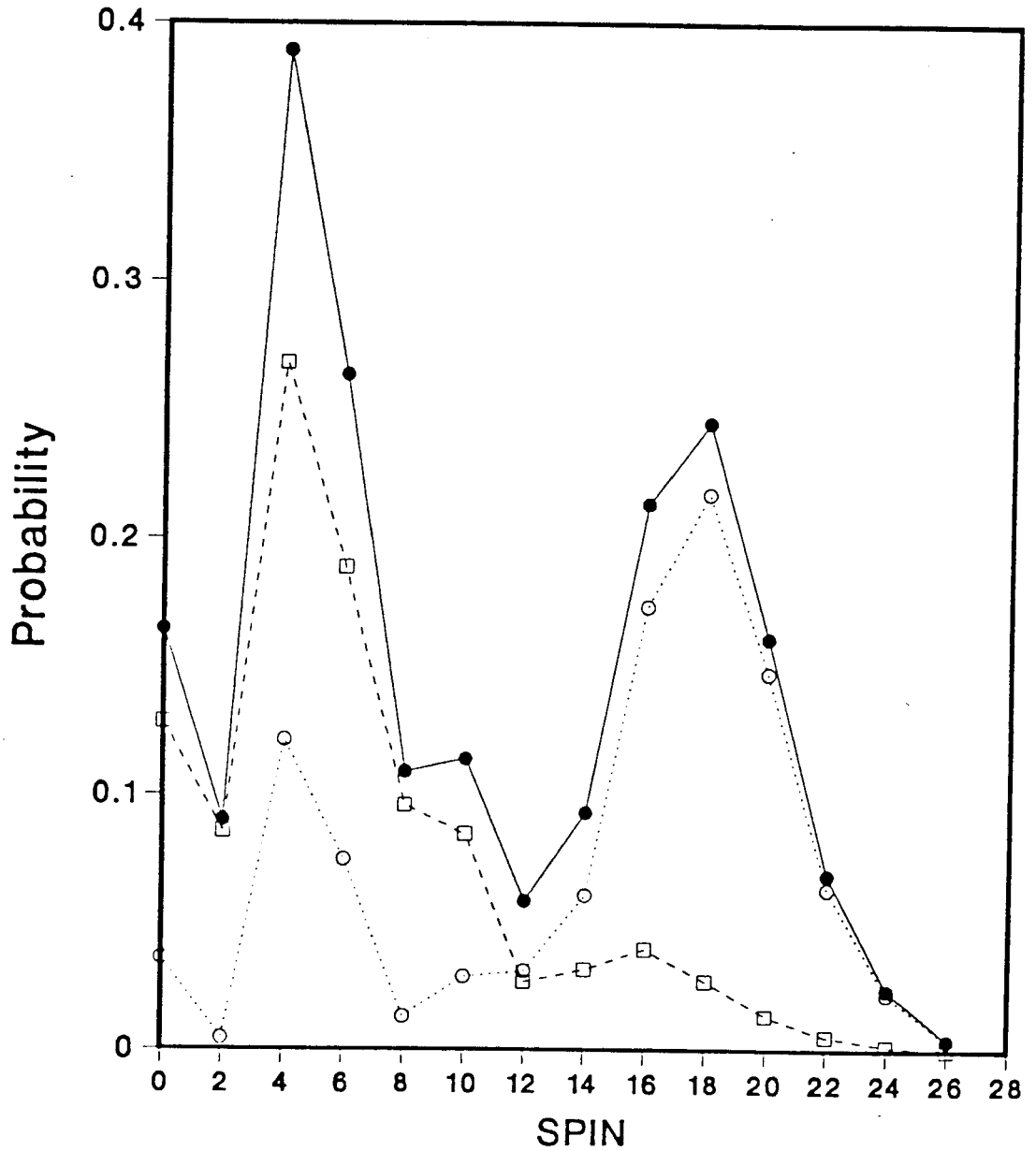

Figure 6.11: Same as Figure 6.10 but for deformation $\eta = 4$. Pure Coulomb excitation is not shown in this figure.

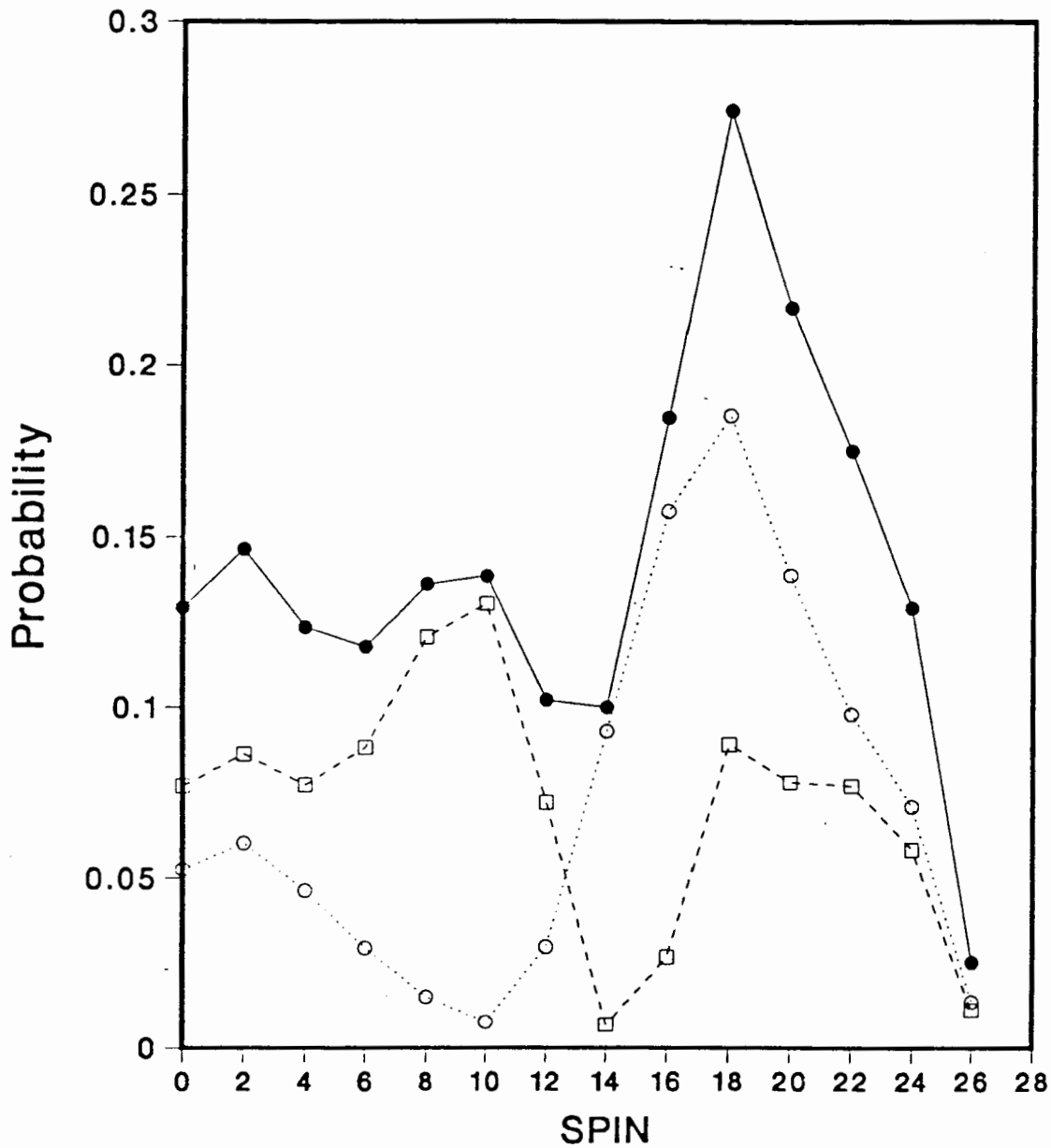

Figure 6.12: Best theoretical calculation of the rotational population patterns in ^{238}Pu from one-neutron transfer. As discussed in the text, the radial part of the wavefunction is now included in the form factor. The symbols are the same as in Figure 6.11.

a_{tun} factor is included in the transfer matrix $T_{I'I}$, effective Z and E_{beam} are used to reproduce the correct turning point and force at the distance of closest approach for 140° scattering in the lab, centrifugal barrier effects are included in the $T_{I'I}$, the odd-neutron is considered as a spectator, and the Nilsson wavefunction for the odd-neutron in ^{239}Pu is included in the surface form factor in the transfer matrix. The spin-up (dotted line, open circles) and spin-down (dashed line, open squares) parts of the wavefunction are included separately, and the probabilities are shown individually for those cases, as in principle, polarized ^{239}Pu target experiments could be performed to investigate each of those population probability patterns. The wavefunctions used were:

$$\Psi_{up} = 1.0Y_{60} + 0.879Y_{40} - 2.021Y_{20} - 1.712Y_{00} \tag{6.1}$$

and

$$\Psi_{down} = -2.746Y_{61} + 2.621Y_{41} + 2.034Y_{21} \tag{6.2}$$

where the Y's are spherical harmonics and the coefficients are from Nilsson's old tabulations [94] for diagonalization within one oscillator shell ($N = 6$). The results in Figure 6.10 are for deformation $\eta = 6$, slightly larger than the experimental deformation of ^{239}Pu. Calculations for $\eta = 4$ (slightly smaller than the actual deformation) were also performed and are shown in Figure 6.11,

with no significant difference between $\eta = 6$ and $\eta = 4$. The solid line is the total probability (sum of spin-up and spin-down probabilities). As observed in Figure 6.10, the spin-up part of the wavefunction emphasizes population of higher spins, while the spin-down part of the wavefunction emphasizes the lower spins. Additionally, there is this dip in probability at spin 14.

Figure 6.12 shows the results of a more complete calculation where the radial parts of the wavefunction are also included in the angular surface form factor in the transfer matrix. Namely, the wavefunctions become:

$$\Psi_{up} = 1.0 R_6 Y_{60} + 0.879 R_4 Y_{40} - 2.021 R_2 Y_{20} - 1.712 R_0 Y_{00} \tag{6.3}$$

and

$$\Psi_{down} = -2.746 R_6 Y_{61} + 2.621 R_4 Y_{41} + 2.034 R_2 Y_{21} \tag{6.4}$$

where the R_L functions are the sixth oscillator shell radial wavefunctions evaluated at the turning radius for the s-state (9.8 fm). This is approximately the distance of closest approach for the reaction being considered. These radial wavefunctions were calculated numerically by the "shooting method" in a spherical Woods-Saxon potential of size appropriate to ^{239}Pu but without spin-orbit coupling. These radial wavefunctions R_L(9.8 fm) are 0.248, 0.216, 0.154 and 0.075 for $L = 0, 2, 4$ and 6, respectively.

In addition, the centrifugal factor (see Section 5.2.4) is removed, as it is more naturally included in the more complete wavefunctions, and the a_{tun} factor is set to unity. The Nilsson single oscillator shell expansion is best interpreted as an expansion on a spheroid of half the eccentricity of the deformed constant density nuclear surface. The classical turning surface is also prolate due to the electric quadrupole potential. Thus, the tunnelling distance will be nearly constant. Figure 6.13 shows the a_{abs} factor and the spin-up and spin-down parts of the surface form factor as a function of $\cos(\chi)$. As can be seen in Figure 6.13, both the spin-up and spin-down form factors have a node, and they are slightly out of phase with each other. The a_{abs} factor decreases sharply for small orientation angles as expected.

As can be seen in Figure 6.12, again the spin-up part of the wavefunction emphasizes the higher spins and the spin-down part emphasizes lower spins. Additionally, the dip around spin 14 is still observed. Figure 6.14 compares the experimental probabilities with the most complete theoretical calculation, normalized at spin 10. While the magnitude of the experimental minimum is not reproduced, the calculation does qualitatively match the experimental data. Indeed, this dip is fairly robust in all of the calculations performed so far and appears to qualitatively match the experimental data. This minimum

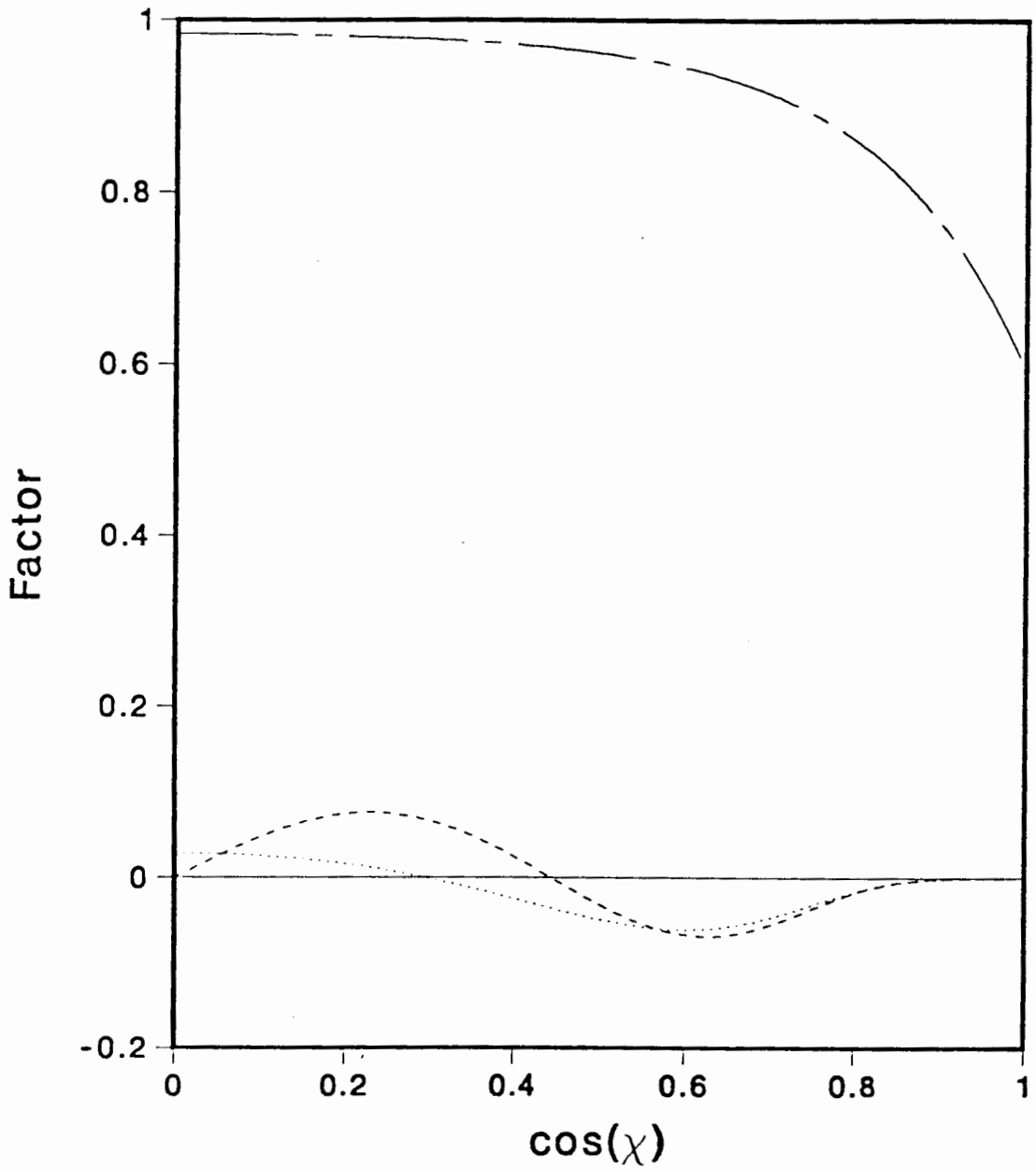

Figure 6.13: Parts of the surface form factor $F_{I'I}$ for ^{239}Pu. The chain-dashed line is the $a_{abs}(x)$ term, the dotted line is the spin-up part of the wavefunction times the absorption factor, and the dashed line is the spin-down part of the wavefunction times the absorption factor.

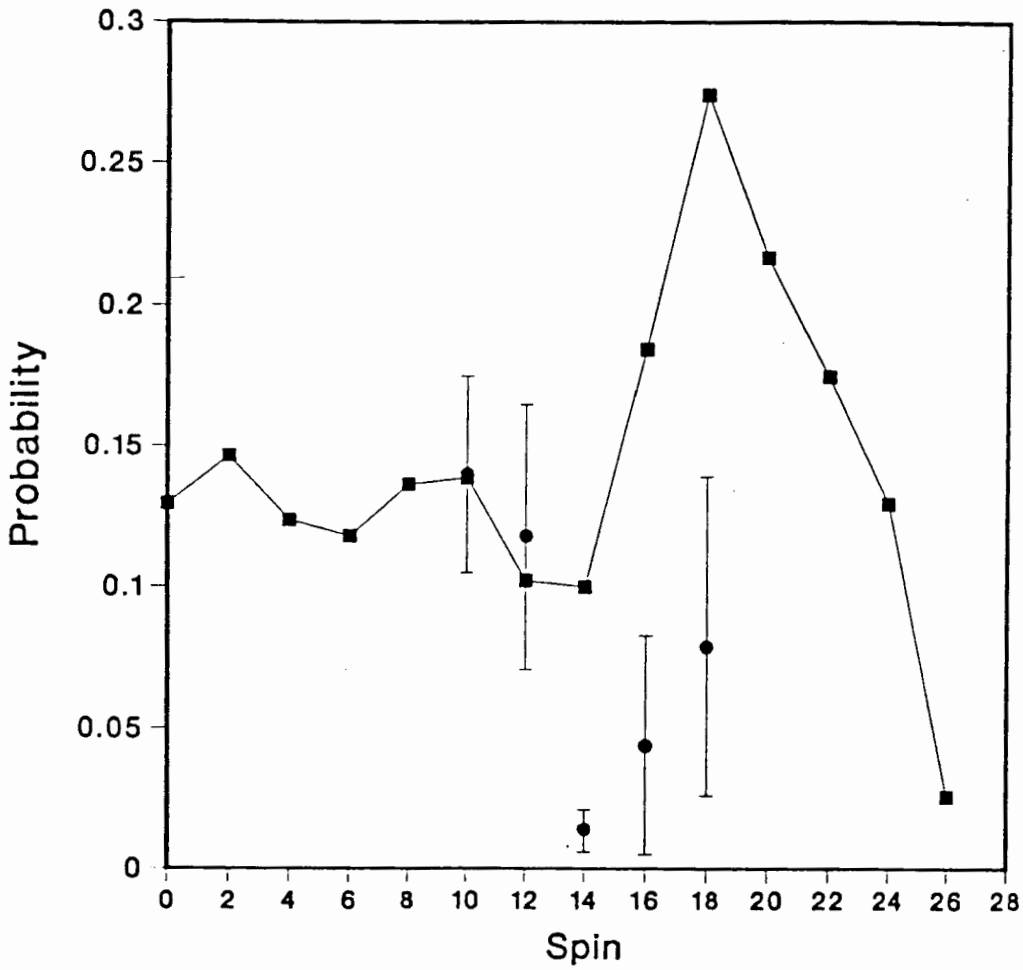

Figure 6.14: Comparison of the best theoretical calculation of the rotational population patterns in ^{238}Pu from one-neutron transfer with experimental data.

probability could be a result of a left-over Coulomb oscillation or could also be due to the different regions of spin emphasized by the spin-up and spin-down parts of the wavefunctions used in the transfer matrix. Nevertheless, this is the first comparison of experimental and theoretical rotational population patterns in one-neutron transfer to ^{238}Pu.

Several extensions can be made to the theoretical calculations: (1) the structure of the projectile could be included, (2) transfer at all distances along the Rutherford trajectory could be included, (3) the Alder-Winther-deBoer method could be generalized to other scattering angles ($M \neq 0$ terms included), and (4) a rectangular transfer matrix could be included rather than the square matrix used in the calculations described above; namely, rotational states in ^{239}Pu are Coulomb excited on the inward path, a transfer matrix linking the half-integer odd-A rotational states in ^{239}Pu and even-integer even-even rotational states in ^{238}Pu is used at closest approach, and then the states in ^{238}Pu are Coulomb excited on the outward path. However, it is anticipated that the general features of the rotational population pattern are captured in the calculations already presented above.

Chapter 7

Conclusions

This thesis has presented data on the ground-state rotational bands in ^{233}U, ^{234}U, ^{235}U, ^{238}Pu and ^{239}Pu from heavy-ion Coulomb excitation, inelastic excitation and one-neutron transfer reactions. Knowledge of high-spin states in the actinide region has been significantly enhanced, with spin states as high as 26^+ observed. A large amount of spectroscopic information (moments-of-inertia, Routhians, aligned angular momentum, g-factors, etc.) was presented. The one-neutron transfer reaction was proven to be useful in exploring high-spin states in the actinide region because the rather "cold" transfer mechanism suppresses fission (see Section 3.1).

Inelastic excitation and Coulomb excitation reactions were used to populate states in the ground rotational band of ^{233}U (see Section 3.2). The moments-of-inertia indicated no sharp backbending, but at high spins a possible soft

band crossing was observed. In addition, at high spins a reversal in the sense of the staggering between the favored and unfavored signatures of the ground-band was noted. Band fitting of the ground-band in ^{233}U proved to be very difficult. A trend in the g-factors of some of the lower spin states supported the mounting evidence of a change in the character of the ground-band with increasing angular momentum. Cranking calculations were performed. It was discovered that a slight γ-deformation or triaxiality best explained both the band crossing and the reversal of the staggering in the ground rotational band of ^{233}U.

Data were also presented for ^{238}Pu and ^{239}Pu ground rotational bands (see Section 3.3). We observed no sharp backbending in either nucleus, although a band crossing could not be ruled out. The probability of neutron transfer as a function of distance of closest approach could be explained by a simple barrier penetration model; however, an anomalous H, K spectrum indicated that transfer of the odd-neutron in the $\frac{1}{2}^+$ [631] orbital was dominant, and that transfer of a neutron from a lower Nilsson orbit, thus breaking a pair, to form a two quasi-particle state was not observed. This indicates the importance of nuclear structure in the transfer process.

For the first time, theoretical calculations of rotational population patterns

for actinide nuclei were compared with experimental data. The importance of including nuclear potential effects, dynamic effects, and nuclear structure effects was highlighted and discussed. The most reasonable agreement between theory and experiment was obtained with a modified Alder-Winther-deBoer method which included a transfer matrix at closest approach. Qualitative agreement between theory and the data was obtained, although a lot more theoretical work is needed before a complete understanding of how the one-neutron transfer process populates high-spin states is possible.

Several possible future experiments can be proposed. The two-neutron transfer reaction ^{240}Pu$(A, A+2)^{238}$Pu would be interesting to study, to perhaps measure enhancement factors for two-neutron transfer at large distances of approach in the actinide region for the first time. Additionally, a one-neutron transfer experiment ^{239}Pu(^{117}Sn,^{118}Sn)^{238}Pu has been proposed [95] to attempt to populate and observe transitions of a rotational band in shape isomeric states of ^{238}Pu. Lastly, other projectile-target combinations in the actinide region are desirable to study high-spin states and to expand the number of rotational bands in the region. The availability of radioactive nuclear beams also raises the possibility of neutron stripping reactions, and greatly enlarges the number of nuclei that could be studied. For instance, at high

spins, because Coriolis and centrifugal forces affect the high-j orbitals more as the cranking frequency increases, perhaps the super-heavy $h\frac{11}{2}$ or $k\frac{17}{2}$ neutron orbitals could be discovered in ^{249}Cm from the ^{248}Cm$(A, A-1)^{249}$Cm one-neutron transfer reaction. This, of course, would help to locate those orbitals and place restrictions on models for calculating the half-lives of super-heavy elements.

Devices such as GAMMASPHERE could greatly expand the nuclear structure studies that can be done. With a tool that allows one to look at very specific higher-fold γ-coincidences, rotational bands can be studied in intricate detail. For instance, investigation of superdeformed bands that contain $\sim 1\%$ of the strength of the ground bands discussed in this thesis becomes fairly easy.

In conclusion, this thesis presents data and theoretical calculations to attempt to interpret the data for several nuclei in the actinide region. At least a qualitative understanding of the reactions studied is presented. The future, however, portends many new experiments to study rotational levels in the actinide region.

Appendix A

Target Construction

A.1 General Apparatus

Target-making is truly an area in which science and art collide, for sometimes just following the formula was not enough to obtain a satisfactory target. The ^{233}U and ^{239}Pu targets used in this work were made using the electrodeposition method. As the target material was radioactive (mostly α decay, with some γ-rays and spontaneous fission), all operations were confined to glove boxes for safety purposes. Figure A.1 shows a side view of the electrodeposition apparatus, which consisted of a stainless-steel base-plate cathode to which the target backing is attached, glass chimney 6 mm in diameter, Pt wire anode, and electroplating solution. The target backing is spot welded to an Al target holder, which is then fastened with screws to the base-plate (in the Be

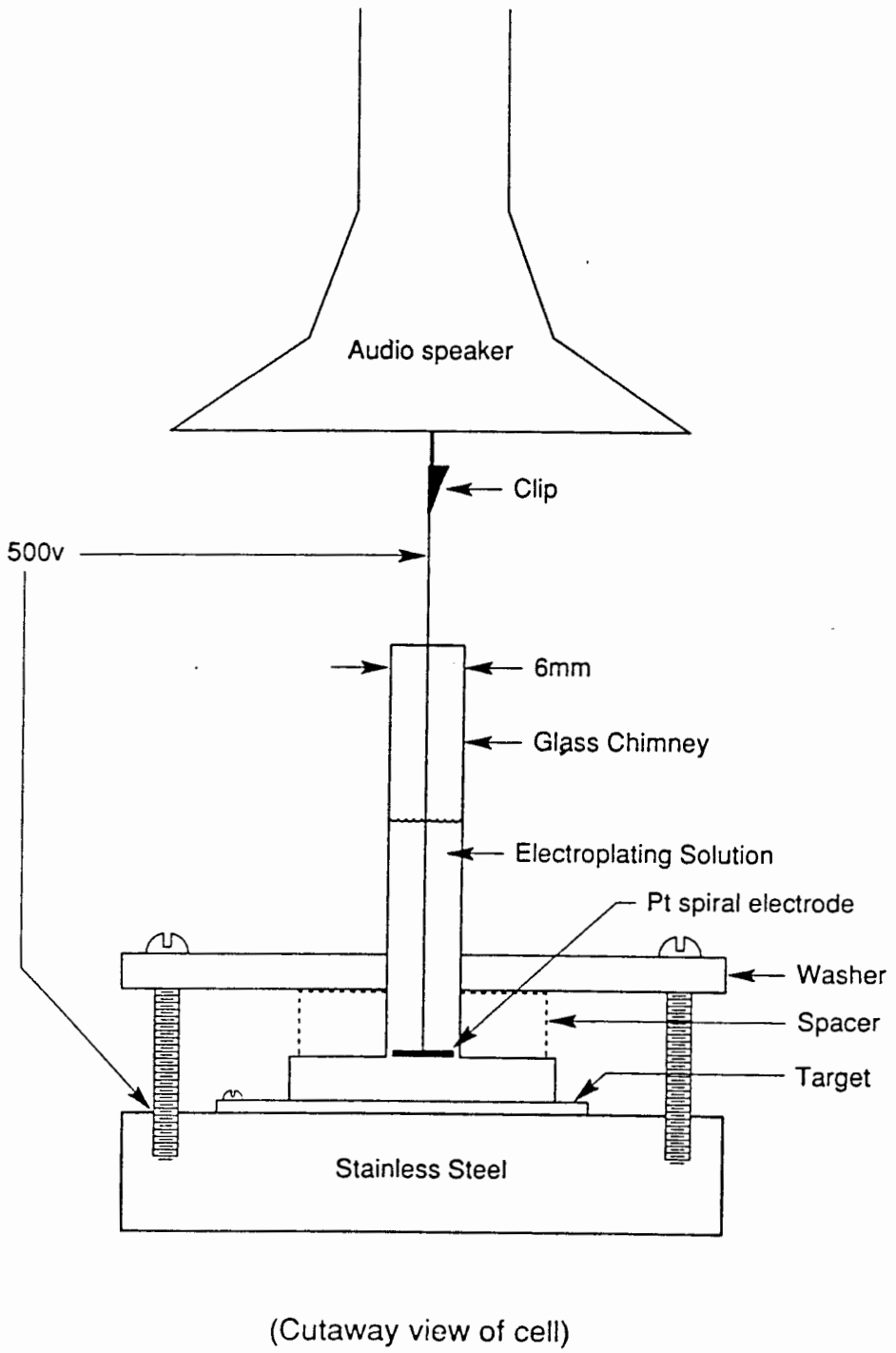

Figure A.1: Schematic of electrodeposition apparatus.

backing case, the target was epoxied to the target holder after completion). The anode is twisted in a spiral that is parallel to the target backing material, and is connected to an audio speaker driven by a low frequency audio signal to insure application of a uniform layer of target material. In addition, the vibration of the anode provides a stirring mechanism for the solution. Care must be taken to not agitate the solution too violently or the deposition of the target material will occur in ridges, thus degrading the quality of the target. The specific chemistry and electroplating procedures for constructing ^{233}U and ^{239}Pu targets are given in the following sections. Electrodeposition from organic solutions [96] was chosen for the following advantages: (1) films between $10 - 1000$ μg/cm^2 can be produced, (2) target backings which are normally etched by acids can be used, (3) uniform depositions with good adhesion to the backings are produced, (4) electrodeposition times are short, (5) high plating efficiency is ideal for use with small quantities of material, (6) and it can be used for actinides.

A.2 ^{233}U Target Preparation

Some initial sample preparation was required, so $\sim 1 - 2$ mg of ^{233}U in an unknown chemical form was dissolved in 2 ml of concentrated HNO_3 in a test tube. This solution was evaporated to dryness in a hot water bath with bubbling N_2 gas. The uranium sample was then dissolved in a small amount of 1M HNO_3 and evaporated to dryness twice more to convert the uranium to the nitrate chemical form and remove other anions like Cl^-, etc. The sample was then dissolved in $\sim$ 2 ml isopropanol and 10 λ ($1\lambda = 10^{-6}$ L) was removed, placed on a Pt foil, evaporated to dryness under an infra-red lamp, and counted in a low geometry Si α detector to determine the purity of the uranium sample and the concentration of the solution. A stock solution of $\sim$ 30μg/ml was prepared by appropriate dilution from the concentrated solution, and 1 ml of this stock solution was placed in the electrodeposition chimney. Electroplating produced a 6 mm diameter spot of uranium with approximately 100 μg/cm^2 thickness. Attempting to plate more than 100 μg/cm^2 per layer results in a non-uniform layer which does not adhere and flakes from the target backing. Target backings of Be (2 mg/cm^2) and Ni/Cu (135 μg/cm^2/4 mg/cm^2) were used for deposition of the uranium targets. 500 V was applied to the cell

for 15 – 20 min, and then the target and backing was heated in a furnace at 550°C for 15 min to convert the uranium to its oxide form and expel any excess isopropanol, water, and HNO_3. Attempting to plate faster (using a higher voltage) results in non-uniform layers and plating actually decreases if driven too hard. It is desirable to maintain current densities between 2 – 6 mA/cm^2. The target was then α-counted to determine the total thickness of the uranium deposit. The plating, heating and counting steps were repeated until the desired target thickness was achieved.

A.3 ^{239}Pu Target Preparation

The procedure for making ^{239}Pu targets is essentially the same as that for ^{233}U targets; however, the plutonium sample was in $\sim$ 2M $HClO_4$ solution, so some additional chemistry was required. Concentrated NH_4OH was added to the sample to make the solution basic and precipitate the plutonium. The sample was then centrifuged and the supernatant removed and discarded. The plutonium precipitate was then washed with NH_4OH, centrifuged, and the supernatant removed. The remaining plutonium hydroxide sample was dissolved in concentrated HNO_3 and taken to dryness in a hot water bath with

bubbling N_2. As in the uranium preparation, the plutonium is dissolved in 1M HNO_3 and evaporated to dryness twice more. The plutonium is then dissolved in 10 ml isopropanol and 0.5 ml 1M HNO_3 to avoid precipitation of the plutonium or formation of colloids. Plutonium plating efficiency was $\sim$ 80% due to the formation of polymer chains of plutonium which sticks to the glass walls, etc. Again a stock solution of $\sim 30\ \mu g/cm^2$ was prepared. The target is electroplated as in the uranium preparation, except an initial layer of $\sim 20 - 30\ \mu g/cm^2$ is made as a base for further layers (subsequent layers adhere more uniformly). Only Ni/Cu ($170\ \mu g/cm^2/4\ mg/cm^2$) backings were used. The temperature in the furnace is reduced to $\sim$ 250°C and heating is performed for 30 – 45 min, to prevent the formation of a Ni/Cu alloy in the backing. After the final electrodeposition, an additional Al target holder is epoxied to the target for structural support. The Cu is removed by dissolution in a NH_4OH/trichloroacetic acid solution forming the blue ammonia complexes of Cu, $[Cu(NH_3)(H_2O)_5]^{2+}$, $[Cu(NH_3)_2(H_2O)_4]^{2+}$, $[Cu(NH_3)_3(H_2O)_3]^{2+}$ and $[Cu(NH_3)_4(H_2O)_6]^{2+}$ (the addition of the fifth and sixth amine ligand is difficult in aqueous media). The Ni and plutonium are unaffected by the NH_4OH/trichloroacetic acid solution. A more thorough and general discussion of these electrodeposition procedures can be found in references [96] and [97].

Appendix B

FITEK Program

FITEK is a spectrum fitting code written in FORTRAN developed by Dr. Wolfgang Stöffl currently at LLNL with some debugging work and all of the documentation written by the author of this thesis. FITEK can be used to fit Gaussian or Lorentz peak shapes to almost any variety of experimental data, including exponential decay curves. In this work, FITEK was mainly used to fit peaks in Ge or NaI(Tl) spectra, although the PPAC angular calibration spectra were also fit using this code.

The program contains its own graphics package for display of the data on a cathode-ray tube tektronics monitor. Parameters can be input via a data file or manual cursor control. In addition to containing all of the normal spectrum manipulation features (summing spectra, differentiating spectra, subtracting spectra, multiplying spectra by a constant, display manipulation,

two-dimensional spectral slicing, etc.), the program allows up to a six parameter background fit, possible step-function in the background, two exponential tails associated with a peak, Gaussian or Lorentz peak shapes, energy dependent parameter fits, up to a four-parameter energy calibration, automatic residual search for missed peaks, automatic peak input and automated spectra fitting (fitting similar spectra with a command file rather than manually inputting all parameters). The fitted function is expressed with the following equation:

$$
\begin{aligned}
F(ch) \;=\; & \sum_i \{(hght(i)\, GW) + \\
& (1.0 - TD1)(hght(i)\, tlh1(ch)) \\
& \exp\left[\frac{\ln(2)(ch - x(i) + taild1(ch)\, FWHM(ch))}{tlw1(ch)}\right] + \\
& (1.0 - TD2)(hght(i)\, tlh2(ch)) \\
& \exp\left[\frac{\ln(2)(ch - x(i) + taild2(ch)\, FWHM(ch))}{tlw2(ch)}\right] + \\
& fct + \sum_{chmx}^{ch} step(ch)(spec(ch) - bck(ch+1))\}
\end{aligned}
\tag{B.1}
$$

where

$$GW = \exp\left[(-(ch - x(i))^2)(4\ln(2)(FWHM(ch))^{-2})\right], \tag{B.2}$$

$$TD1 = \exp\left[(-(ch - x(i))^2)(4\ln(2)(FWHM(ch)\, taild1)^{-2})\right], \tag{B.3}$$

$$TD2 = \exp\left[(-(ch - x(i))^2)(4\ln(2)(FWHM(ch)\, taild2)^{-2})\right], \qquad \text{(B.4)}$$

$$\begin{aligned} fct &= a + b\,(ch - center) + c\,(ch - center)^2 + d\,(ch - center)^3 + \\ &\quad e\,(ch - center)^4 + f\,(ch - center)^5, \end{aligned} \qquad \text{(B.5)}$$

and $F(ch)$ = fit function, ch = channel, i = number of peak, $x(i)$ = location of peak i, $hght(i)$ = height of peak i, $FWHM$ = full width half maximum, $taild1$ = tail distance of tail number one, $taild2$ = tail distance of tail number two, $tlh1, tlh2$ = tail heights of tails number one and two, respectively, $tlw1, tlw2$ = tail widths of tails number one and two, respectively, $center$ = center of fit area in channels, $step(ch)$ = stepheight at channel ch, $spec(ch)$ = spectrum intensity at channel ch, $bck(ch)$ = background intensity at channel ch, GW = Gaussian width formula, $TD1, TD2$ = exponential tail formula for tails one and two, respectively, and fct = polynomial background function with a, b, c, d, e and f the fit parameters.

$F(ch)$ can be rewritten as:

$$F(ch) = \sum_i \{(hght(i)GW) + AB + CD + E + F\} \qquad \text{(B.6)}$$

where

$$GW = \exp\left[(-(ch - x(i))^2)(4\ln(2)(FWHM(ch))^{-2}\right] \qquad \text{(B.7)}$$

$$A = (1.0 - GW)(taild1(ch))^2\, hght(i)\, tlh1(ch) \tag{B.8}$$

$$B = \exp\left[\ln(2)(ch - x(i) + taild1(ch))(FWHM(ch)/tlw1(ch))\right] \tag{B.9}$$

$$C = (1.0 - GW)(taild2(ch))^2\, hght(i)\, tlh2(ch) \tag{B.10}$$

$$D = \exp\left[\ln(2)(ch - x(i) + taild2(ch))(FWHM(ch)/tlw2(ch))\right] \tag{B.11}$$

$$\begin{aligned} E &= a + b\,(ch - center) + c\,(ch - center)^2 + d\,(ch - center)^3 + \\ &\quad e\,(ch - center)^4 + f\,(ch - center)^5, \end{aligned} \tag{B.12}$$

$$F = \sum_{chmx}^{ch} step(ch)(spec(ch) - bck(ch + 1) \tag{B.13}$$

As can be seen, the first portion of the equation is merely the equation for a Gaussian peak shape ($hght(i)\, GW$). The second portion is the equation for the first tail (AB). The tail function is obtained by multiplying an inverted Gaussian peak shape (A) and an exponential function (B). This tail function is common for Ge spectra. The third portion of the equation is the second tail function (CD). Again, it is an inverted Gaussian (C) multiplied by an exponential function (D). The fourth portion of the equation is the background function (E). The background function is a polynomial of up to fifth order. The final portion of the equation is the step function for the background (F). It is obtained from the difference between the spectrum and the background.

The difference between the fitted function $F(ch)$ and the actual data is minimized using a multi-dimensional matrix inversion method [98]. A matrix is constructed of initial guesses for all parameters allowed to vary in the particular fit and the first partial derivatives (gradient $\nabla F(ch)$) are obtained. The method is to then build up a sequence of matrices H_i such that

$$\lim_{i \to \infty} H_i = A^{-1} \tag{B.14}$$

The minimum point x_m is given by:

$$A \cdot x_m = b \tag{B.15}$$

and at some point x_i

$$A \cdot x_i = \nabla F(x_i) + b \tag{B.16}$$

Subtracting equation B.16 from B.15:

$$x_m - x_i = A^{-1} \cdot [-\nabla F(x_i)] \tag{B.17}$$

where $x_m - x_i$ is the step to get to the minimum and $A^{-1} \cdot [-\nabla F(x_i)]$ is known once $H \approx A^{-1}$ is obtained recursively. The recursive relationship is then

$$x_{i+1} - x_i = H_{i+1} \cdot [\nabla F(x_{i+1}) - \nabla F(x_i)] \tag{B.18}$$

and there exists an updating formula for H_{i+1} as a function of H_i, $(x_{i+1} - x_i)$, and the gradients $[\nabla F(x_{i+1}) - \nabla F(x_i)]$. This algorithm is similar to rolling a ball around on a surface until a pocket or minimum is encountered.

However, the method does have some limitations and disadvantages. The number of free variables in the fit is limited, as unrestricted variation of all parameters in one fit is likely to result in singularities or some totally unphysical and meaningless result (for instance, if the tail height and tail width are both allowed to vary, one might wander off to $\pm\infty$). In addition, some reasonable initial guesses for the parameters must be used to start the iterations.

In the FITEK code, once the iterations have converged, final values and their associated errors of all parameters are displayed (both numerically and graphically) and the fit quality information is given (χ^2_ν, local χ^2, scatter or χ^2, and the residuum). The residuum, or the difference between the fitted function and the data, can be differentiated and searched for the characteristic positive- and negative-spike of missed Gaussian peak shapes, and can indicate areas of the fitted region where unsatisfactory results are obtained.

Because a linear combination of errors is used in the matrix (easier to do than the normal sum-of-squares method), the errors obtained are slightly overestimated. To get the "true" error on a parameter of the fit, one must fix

all other parameters to their "true" values (here the best fit is typically used to obtain the "true" values since one doesn't *a priori* know the "true" values), and then step the parameter of interest slowly fifty or one-hundred times around the "true" value monitoring the scatter for each of the fits. The scatter for the fits will trace out a parabola (symmetric or asymmetric depending on the situation) with the minimum of course being the best or "true" parameter. A scatter increase of one from the minimum is the 1σ error, an increase of four is the 2σ error, etc. For example, to get the error in the peak widths, one would fix all other parameters (locations, heights, background, etc.) and step the width around the "true" value and find where the scatter increased by one.

A simulation was run to determine the magnitude of the overestimation of the errors. A raw integration method was compared with FITEK fits with free parameters and FITEK fits using the scatter method described above for two ideal Gaussian peaks of width ($\sigma = 5, 2\sigma = 10$) and heights of 100 counts and 10000 counts. The background was generated randomly and was between $40 - 50$ counts/channel. The results are shown in Table B.1.

The errors quoted in Table B.1 and throughout this thesis are 1σ errors. The difference between errors of intensities obtained from raw integration and FITEK (with free parameters) is $10-20\%$. Additionally, the difference between

Table B.1: Comparison of FITEK results and raw integration methods

Peak height	Raw int. Area − bkgd ±% err	FITEK (free param.) Int. ±% err	FITEK (free param.) FWHM ± err	FITEK (scatter meth.) FWHM ± err
100	420.4 ±5%	425 ± 6.2%	6.765 ± 0.589	6.765 ± 0.515
10000	123727.6 ± 0.2%	123642.8 ± 0.3%	11.425 ± 0.032	11.425 ± 0.027

errors in the FITEK (free parameter) and FITEK (scatter method) fits for the FWHM is about 15 − 20% again. In both cases, the FITEK (free parameter) method overestimated the errors by about 15%. One could correct all the error bars on fitted parameters by 15%; however, in this thesis the uncorrected FITEK (free parameter) errors are given in all cases except where otherwise noted. The distinction between the widths presented in Table B.1 (FWHM) and the Gaussian widths ($2\sigma = 10$) used as input data should be noted.

Bibliography

[1] I.Y. Lee, D. Cline, R.S. Simon, P.A. Butler, P. Colombani, M.W. Guidry, F.S. Stephens, R.M. Diamond, N.R. Johnson, and E.Eichler **Phys. Rev. Lett. 37** (1976) 420.

[2] P. Taras, D. Ward, H.R. Andrews, J.S. Geiger, R.L. Graham, and W. McLatchie **Nucl. Phys. A289** (1977) 165.

[3] R.M. Diamond, B. Elbek, and F.S. Stephens **Nucl. Phys. 43** (1963) 560.

[4] G.G. Seaman, E.M. Bernstein, and J.M. Palms **Phys. Rev. 161** (1967) 1223.

[5] D. Ward, O. Häusser, H.R. Andrews, P. Taras, P. Skensved, N. Rud, and C. Broude **Nucl. Phys A330** (1979) 225.

[6] F. Kearns, G. Varley, G.D. Dracoulis, T. Inamura, J.C. Lisle, and J.C. Willmott **Nucl. Phys. A278** (1977) 109.

[7] K.A. Erb, J.E. Holden, I.Y. Lee, J.X. Saladin, and T.K. Saylor **Phys. Rev. Lett. 29** (1972) 1010.

[8] B. Elbek and P.O. Tjom **Adv. Nucl. Phys. 3** (1969) 259.

[9] R.A. Broglia, O. Hansen, and C. Reidel **Adv. Nucl. Phys. 6** (1973) 287.

[10] G.B. Holm, J.R. Burwell, and W.D. Miller **Phys. Rev. 122** (1961) 1260.

[11] A. Isoya **Phys. Rev. 130** (1963) 234.

[12] M.N. Vergnes and R.K. Sheline **Phys. Rev. 132** (1963) 1736.

[13] M.W. Sachs, V. Chasman, and D.A. Bromley **Phys. Rev. 139** (1965) B92.

[14] R.M. Bock, M. Grosse-Shulte, and W. von Oertzen **Phys. Lett. 22** (1966) 456.

[15] M.W. Guidry, R.W. Kincaid, and R. Donangelo **Phys. Lett. 150B** (1985) 265.

[16] J. deBoer and D.A. Bromley "Treatise on Heavy-Ion Science" vol. 1, Chapter 3 Inelastic-Scattering Coulomb Excitation (Plenum Press, New York, 1984).

[17] M.W. Guidry, T.L. Nichols, R.E. Neese, J.O. Rasmussen, L.F. Oliveira, and R.J. Donangelo **Nucl. Phys. A361** (1981) 274.

[18] D. Cline **Ann. Rev. Nucl. Part. Sci. 36** (1986) 683.

[19] A.O. Macchiavelli, M.A. Deleplanque, R.M. Diamond, F.S. Stephens, E.L. Dines, and J.E. Draper **Nucl. Phys. A432** (1985) 436.

[20] F.W.N. deBoer, E. Grosse, W. Spreng, H.J. Wollersheim, E.G. Eckert, and Ch. Lauterbach GSI Annual Report (1984).

[21] M.W. Guidry, S. Juutinen, X.T. Liu, C.R. Bingham, A.J. Larabee, L.L. Riedinger, C. Baktash, I.Y. Lee, M.L. Halbert, D. Cline, B. Kotlinski, W.J. Kernan, T.M. Semkow, D.G. Sarantites, K. Honkanen, and M. Rajagopalan **Phys. Lett. 163B** (1985) 79 and references therein.

[22] P.A. Butler, C. Baktash, C.R. Bingham, M. Carpenter, D. Cline, B. Cox, M.W. Guidry, S. Juutinen, A.E. Kavka, W.J. Kernan, R.W. Kincaid, A. Larabee, I.Y. Lee, X.T. Liu, S.P. Sorensen, E. Vogt, and C.Y. Wu **Phys. Lett. 191B** (1987) 333 and references therein.

[23] S. Juutinen, X.T. Liu, S.P. Sorensen, B. Cox, R.W. Kincaid, C.R. Bingham, M.W. Guidry, W.J. Kernan, C.Y. Wu, E. Vogt, T. Czosnyka, D. Cline, M.L. Halbert, I.Y. Lee, and C. Baktash **Phys. Lett. 192B** (1987) 307.

[24] S. Juutinen PhD. thesis, University of Jyvaskyla, Jyvaskyla, Finland, 1988 (unpublished).

[25] W.J. Kernan PhD. thesis, University of Rochester, Rochester, New York, 1989 (unpublished).

[26] X.T. Liu PhD. thesis, University of Tennessee, Knoxville, Tennessee, 1988 (unpublished).

[27] C.Y. Wu, X.T. Liu, S.P. Sorensen, R.W. Kincaid, M.W. Guidry, D. Cline, W.J. Kernan, E. Vogt, T. Czosnyka, A.E. Kavka, M.A. Stoyer, J.O. Rasmussen, and M.L. Halbert **Phys. Lett. 188B** (1987) 25.

[28] G. Himmele, H. Backe, P.A. Butler, D. Habs, V. Metag, H.J. Sprecht, and J.B. Wilhelmy **Nucl. Phys. A404** (1983) 401.

[29] W. von Oertzen, H.G. Bohlen, B. Gebauer, R. Künkel, F. Pühlhofer, and d. Schüll **Z. Phys. A326** (1987) 463.

[30] W.J. Kernan, C.Y. Wu, X.T. Liu, X.L. Han, D. Cline, T. Czosnyka, M.W. Guidry, M.L. Halbert, S. Juutinen, A.E. Kavka, R.W. Kincaid, J.O. Rasmussen, S.P. Sorensen, M.A. Stoyer, and E.G. Vogt, to be published **Nucl. Phys. A** (1990).

[31] W. von Oertzen, B. Gebauer, A. Gamp, H.G. Bohlen, F. Busch, and C. Schüll **Z. Phys. A313** (1983) 189.

[32] K. Sapotta, R. Bass, V. Hartmann, H. Noll, R.E. Renfordt, and K. Stelzer **Phys. Rev. C31** (1985) 1297.

[33] J.O. Rasmussen, M.W. Guidry, and L.F. Canto in "Proceedings of the Niels Bohr Centennial Conference", ed. by J. Bang and J. deBoer (North Holland, Amsterdam, 1985) 167.

[34] A.E. Kavka PhD. thesis, Acta Universitatis Upsaliensis, Uppsala, Sweden, 1989 (unpublished).

[35] G.J. Gyapong, R.H. Spear, M.T. Esat, M.P. Fewell, A.M. Baxter, and S.M. Burnett **Nucl. Phys. A458** (1986) 165.

[36] T. Czosynka, D. Cline, L. Hasselgren, C.Y. Wu, R.M. Diamond, H. Kluge, C. Roulet, E.K. Hulet, R.W. Lougheed, and C. Baktash **Nucl. Phys. A458** (1986) 123.

[37] Ch. Lauterbach, J. deBoer, Ch. Mittag, F. Riess, Ch. Schandera, Ch. Briançon, A. Lefebvre, S. Hlavač, and R.S. Simon **Phys. Lett. B140** (1984) 187.

[38] W. Spreng, F. Azgui, H. Emling, E. Grosse, R. Kulessa, Ch. Michel, D. Schwalm, R.S. Simon, H.J. Wollersheim, M. Mutterer, J.P. Throbald, M.S. Moore, N. Trautmann, J.L. Egido, and P. Ring **Phys. Rev. Lett. 51** (1983) 1522.

[39] R. Kulessa, R.P. DeVito, H. Emling, E. Grosse, D. Schwalm, R.S. Simon, A. Lefebvre, Ch. Briançon, R.J. Walen, G. Seitten, and Th.W. Elye **Z. Phys. A312** (1983) 135.

[40] R.B. Piercey, J.H. Hamilton, A.V. Ramayya, H. Emling, P. Fuchs, E. Grosse, D. Schwalm, H.J. Wollersheim, N. Trautmann, A. Faessler, and M. Ploszajczak **Phys. Rev. Lett. 46** (1981) 415.

[41] K. Hardt, P. Schüler, C. Günther, J. Recht, and K.P. Blume **Z. Phys. A314** (1983) 83.

[42] K. Hardt, P. Schüler, C. Günther, J. Recht, and K.P. Blume **Nucl. Phys. A407** (1983) 127.

[43] M. Jääskeläinen, D.G. Sarantites, R. Woodward, F.A. Dilmanian, J.T. Hood, and R. Jääskeläinen **Nucl. Inst. Methods 204** (1983) 385.

[44] E. Grosse, A. Balanda, H. Emling, F. Folkmann, P. Fuchs, R.B. Piercey, D. Schwalm, R.S. Simon, and H.J. Wollersheim **Phys. Scr. 24** (1981) 337.

[45] R.S. Simon, R.P. Devito, H. Emling, R. Kulessa, Ch. Briançon, and A. Lefebvre **Phys. Lett. B108** (1982) 87.

[46] H. Ower, Th. W. Elze, J. Idzko, K. Stelzer, E. Grosse, H. Emling, P. Fuchs, D. Schwalm, H.J. Wollersheim, N. Kaffrell, and N. Trautmann **Nucl. Phys. A388** (1982)421.

[47] **Nuclear Data Sheets 59** (January 1990) 276 and J. deBettencourt, C. Briancon, J.R. Tibeaux, R.J. Walen, M. Jacmar, A. Gizon, and S. Andre **Bull. Acad. Sci. USSR 40** (1976) 14.

[48] J.L. Egido, and P. Ring **Nucl. Phys. A423** (1984) 93.

[49] J. Helgesson and I. Hamamoto **Phys. Scr. 40** (1989) 595.

[50] P. Möller and J.R. Nix **At. Data Nucl. Data Tables 39** (1988) 213; and P. Möller and J.R. Nix LANL Preprint LA-UR-86-3983, Nov. 7, 1986.

[51] P. Ring and H.J. Mang **Phys. Rev. Lett. 33** (1974) 1174.

[52] D.R. Inglis **Phys. Rev. 96** (1954) 1059.

[53] K. Kumar and M. Baranger **Nucl. Phys. A110** (1968) 529.

[54] R. Bengtsson and S. Frauendorf **Nucl. Phys. A327** (1979) 139.

[55] A. Bohr and B. Mottelson in Nuclear Structure, vol II (W. A. Benjamin, Inc., Massachusetts, 1975) pp. 31.

[56] J.O. Rasmussen, J. Alonso, W. Ribbe, I. Rezanka, and R. Needham **LBL NSD Annual Report** (1972) 163, T. Tamura, I. Rezanka, S. Iwata, J.O. Rasmussen, and J. Alonso **Phys. Rev. C8** (1973) 2425, and K. Krien, R.A. Naumann, J.O. Rasmussen, and I. Rezanka **Nucl. Phys. A209** (1973) 572.

[57] J. Alonso, H. Bakhru, F.M. Bernthal, J. Boutet, B. Olsen, I. Rezanka, and J.O. Rasmussen **Nucl. Phys. A160** (1971) 193.

[58] S.W. Yates, I.Y. Lee, N.R. Johnson, E. Eichler, L.L. Riedinger, M.W. Guidry, A.C. Kahler, D. Cline, R.S. Simon, P.A. Butler, P. Colombani, F.S. Stephens, R.M. Diamond, R.M. Ronningen, R.D. Hichwa, J.H. Hamilton, and E.L. Robinson **Phys. Rev. C21** (1980) 2366.

[59] R. Bengtsson and S. Frauendorf **Nucl. Phys. A327** (1979) 139.

[60] I. Hamamoto Proceedings of the Conference on Nuclear Structure in the 90's, ORNL April 23-27, 1990, and I. Hamamoto and B. Mottelson **Phys. Lett. B127** (1983) 281.

[61] W.Z. Venema, J.F.W. Jansen, R.V.F. Janssens, and J. Van Klinken **Phys. Lett. B156** (1985) 163.

[62] K. Helmer, D. Cline, M.A. Deleplanque, R. Diamond, M.W. Guidry, A.E. Kavka, W.J. Kernan, X.T. Liu, R. McDonald, A. Machiavelli, J.O. Rasmussen, F. Stephens, M.A. Stoyer, E. Vogt, and C.Y. Wu, to be published.

[63] P. Marmier and E. Sheldon in Physics of Nuclei and Particles, vol II (Academic Press, New York, 1970) p. 1322, eqs. (15-290) and (15-291).

[64] E.M. Bernstein, and J. de Boer **Nucl. Phys. 18** (1960) 40.

[65] P. Marmier and E. Sheldon, Ibid, p. 1320, eqs. (15-279).

[66] K.E.G. Löbner, M. Vetter, and V. Hönig **Nucl. Data Tables A7** (1970) 495.

[67] G.H. Fuller and V.W. Cohen **Nucl. Data Tables A5** (1969) 433.

[68] Table of Isotopes, 7th ed., ed. C.M. Lederer and V.S. Shirley (John Wiley and Sons, New York, 1978) p. 1428.

[69] R.R. Chasman, I. Ahmad, A.M. Friedman, J.R. Erskine **Rev. Mod. Phys. 49** (1977) 833.

[70] J.O. Newton **Nucl. Phys. 5** (1958) 218.

[71] G. Breit and M.E. Ebel **Phys. Rev. 103** (1956) 679.

[72] J.O. Rasmussen, M.A. Stoyer, M.W. Guidry, L.F. Canto and R. Donangelo "Proceedings from the International Symposium on Symmetries and Nuclear Structure", Nuclear Science Research Conference Series, Vol. 13, Dubrovnik, Yugoslavia, June 5-14, 1986, pp. 391.

[73] K. Alder and A. Winther "Coulomb Excitation" (Academic Press, New York, 1966).

[74] C. Price, H. Esbensen, and S. Landowne **Phys. Lett. 197B** (1987) 15.

[75] M.J. Rhoades-Brown, R. Donangelo, M.W. Guidry, and R.E. Neese **Phys. Rev. C24** (1981) 2747.

[76] H. Massmann and J.O. Rasmussen **Nucl. Phys. A243** (1975) 55.

[77] M.W. Guidry, H. Massmann, R. Donangelo, and J.O. Rasmussen **Nucl. Phys. A247** (1976) 183.

[78] R. Donangelo, M.W. Guidry, J.P. Boisson, and J.O. Rasmussen **Phys. Lett. 64B** (1976) 337.

[79] L.F. Canto, R.J. Donangelo, J.O. Rasmussen, P. Ring, and M.A. Stoyer **Phys. Lett. B248** (1990) 10.

[80] L.F. Canto, R.J. Donangelo, M.W. Guidry, A.R. Farhan, J.O. Rasmussen, P. Ring, and M.A. Stoyer **Phys. Lett. 241B** (1990) 295.

[81] J. deBoer, C.H. Dasso, and A. Winther **Z. Phys. A335** (1990) 199.

[82] C.H. Dasso and A. Winther **Phys. Lett. 242B** (1990) 323.

[83] K. Alder, Aa. Bohr, T. Huus, B. Mottelson and Aa. Winther **Rev. Mod. Phys. 28** (1956) 432.

[84] R. Donangelo PhD. thesis, University of California, Berkeley, CA, 1977 (unpublished).

[85] L.F. Canto, R. Donangelo, R.S. Nikam, and P. Ring **Phys. Lett. 192B** (1987) 4.

[86] S. Juutinen, X.T. Liu, S.P. Sorensen, B. Cox, R.W. Kincaid, C.R. Bingham, M.W. Guidry, W.J. Kernan, C.Y. Wu, E. Vogt, D. Cline, M.L. Halbert, I.Y. Lee, and C. Baktash "Progress Report on Nuclear Spectroscopic Studies", Department of Physics and Astronomy, University of Tennessee, Knoxville, TN Feb. 1986, 87.

[87] A. Winther and J. deBoer "A Computer Code for Multiple Coulomb Excitation", Caltech report (Nov. 1965), reference 8, reprinted in reference [87].

[88] L.F. Canto, R.J. Donangelo, A.R. Farhan, M.W. Guidry, J.O. Rasmussen, P. Ring, and M.A. Stoyer Symposium on Exotic Nuclear Spectroscopy, American Chemical Society (Miami Beach, Oct. 1989).

[89] K. Helmer PhD. thesis, University of Rochester, Rochester, NY, in progress.

[90] R.S. Nikam and P. Ring **Phys. Rev. Lett. 58** (1987) 980.

[91] M.V. Berry **Proc. R. Soc. (London) A392** (1984) 15.

[92] R.S. Nikam et al. **Z. Phys. A234** (1986) 241; **Phys. Lett. B185** (1987) 269.

[93] J.O. Rasmussen, M.A. Stoyer, L.F. Canto, R. Donangelo and P. Ring "Nuclear Rotational Population Patterns in Heavy-Ion Scattering and Transfer Reactions" , to be published **Z. Phys.** (1990).

[94] B.R. Mottelson and S.G. Nilsson **Mat. Fys. Skr. Dan. Vid. Selsk. 1** (1959) no. 8 and S.G. Nilsson **Mat. Fys. Medd. Dan. Vid. Selsk. 2** (1955) no. 16.

[95] P.A. Butler, D. Cline, C.Y. Wu, R. Ibbotsen, K. Helmer, M. Devlin, R.J. Poynter, I.Y. Lee, J.D. Garrett, M.W. Guidry and X.T. Liu "Second Minimum Spectroscopy Using Heavy-Ion Transfer Reactions" ORNL proposal, June 1990.

[96] D.C. Aumann and G. Müllen **Nucl. Inst. Methods 115** (1974) 75.

[97] J.E. Evans, R.W. Lougheed, M.S. Coops, R.W. Hoff and E.K. Hulet **Nucl. Inst. Methods 102** (1972) 389.

[98] W.H. Press, B.P. Flannery, S.A. Teukolsky and W.T. Vetterling "Numerical Recipes – The Art of Scientific Computing" Cambridge Univ. Press, Cambridge (1986) 307 ff.